Copyright

by

Sanjiv Edlagan Shah

2011

The Dissertation Committee for Sanjiv Edlagan Shah Certifies that this is the approved version of the following dissertation:

Feedback Control of Gas Metal Arc Braze-Welding Using Thermal Signals

Committee:

John R. Howell, Supervisor

Carolyn C. Seepersad, Co-Supervisor

Eric M. Taleff

Ofodike A. Ezekoye

Michael B. Prime

Feedback Control of Gas Metal Arc Braze-Welding Using Thermal Signals

by

Sanjiv Edlagan Shah, B.S.; M.S.

Dissertation

Presented to the Faculty of the Graduate School of
The University of Texas at Austin
in Partial Fulfillment
of the Requirements
for the Degree of

Doctor of Philosophy

The University of Texas at Austin
August, 2011

Dedication

I dedicate this project to my wife, Katie and my daughter, Abigail for their constant support and belief in me. Additionally, I dedicate this project to my father, mother, my brother and sister for their encouragement and instilling in me the drive and desire to succeed in anything to which I apply myself.

Acknowledgements

First and foremost, I would like to acknowledge the members of my dissertation committee all of whom guided my thinking and brought unique perspectives to my work. I am sincerely grateful for the direction and advice provided by my advisor, Professor John R. Howell. His patient and his immense breadth and depth in Engineering and Science have made my time at the University of Texas developmental, influential and educational. I am a wiser person and better engineer due to my experience with Dr. Howell.

I also deeply appreciate the help and advice from, my co-advisor, Dr. Carolyn Conner Seepersad, her expertise in metamodels and statistical methods gave me the opportunity to conduct novel research in advanced manufacturing. Additional gratitude goes out to the other members of my committee, Dr. Eric Taleff whose keen experimental insight and attention to detail helped me to develop my experimental protocol, Dr. Ofodike Ezekoye whose deep knowledge in numerical modeling and heat transfer aided me in the formulation and execution of my temperature models, and Dr. Michael Prime whose background in structural mechanics has greatly enhanced my knowledge in residual stress and residual stress measurement. From each, I have received unique and helpful instruction as well as exemplars for my new profession.

I would also like to acknowledge all the past students that have helped in the development of this research without whose contributions, this research would not come to fruition. From the Seepersad design group I would like to thank Pete Backlund for designing and building the welding test station and helping me to develop the experiments that were performed and George “Ray” Ely for the formulation of the metamodels that were used in this research. In addition, I would like to acknowledge all of the undergraduate researchers that helped on this project, Ashley Browning, Richard Rhodes, Kristen Kaufman and Jenny Lo whose help with metamodeling allowed me to finish this project.

From the Beaman Group I would like to thank and acknowledge P.J. Casey, Cameron Booth, Dongwoo Kim and Zheng Li for their contributions and help that they gave me regarding control theory and sensing.

I would also like to thank Jason C. Lee and Carlos Rios-Perez for their help and contributions to this research as well as their camaraderie and friendship, it made the most difficult parts of this research very enjoyable.

Outside of this research project there were several people that supported me through their friendship and encouragement. They deserve recognition as well. From the Webber Energy Group I would like to thank, Stuart Cohen, Jared Garrison, Melissa Lott, Kelly Twomey, David Wogan, Aaron Townsend and Benjamin Gully whose conversations about feedforward control helped me to refine my control strategy. Others include Maj. Joshua Keena, Navid Ghorashian and Sertan Kutal Gokce. I have shared offices with all of you and have learned from you all through your strong work ethics and innate talent. From Dr. Ezekoye's Group I thank Uday Godse, Craig Weinschenk, Morgan Bruns, Kris Overholt and Reid Anderson. Going out to lunch with you all really enhanced my graduate school life.

Lastly and most importantly, my deepest gratitude and admiration goes to my wonderful wife who encouraged me and supported me in my decision to go to graduate school. I also attribute a great deal of my success to my parents and siblings who loved me and taught me how to succeed in all of life's endeavors. This work would never have been completed without the encouragement and support of my wife, my daughter, my parents and siblings, therefore it is dedicated to them.

Feedback Control of Gas Metal Arc Braze-Welding Using Thermal Signals

Publication No._____________

Sanjiv Edlagan Shah, Ph.D.

The University of Texas at Austin, 2011

Supervisors: John R. Howell
Carolyn C. Seepersad

In serial manufacturing processes, localized energy sources (e.g. plasma cutters, arc welders or water jets) induce material geometry transformations that yield a desired product. Simple parameter control of these energy sources does not necessarily ensure an optimal or successful part because of disturbances in the manufacturing process (material and temperature variations, etc). Currently, control in manufacturing is based on statistical process control where large databases for the manufacturing of a fixed process are available and have been compiled over several manufacturing runs. In the absence of a statistical database, and with the increased need for improved monitoring and throughput, there is need for active process control in manufacturing. In this work, Gas Metal Arc Braze-Welding (GMABW) will serve as a test-bed for the implementation of model predictive control (MPC) for a serial manufacturing process.

This dissertation investigates the integration of real time modeling of the temperature field with control algorithms to control the evolving temperature field in the braze-welded base metal. Fundamental problems involving MPC that are addressed are modeling techniques to calculate temperature fields with reduced computational requirements and control algorithms that utilize the thermal models directly to inform the controller.

The dissertation first outlines and compares analytical and computational thermal models and comparison with experimental data are obtained. A thermal model based on a metamodeling approach is used as the plant model for a classical control system and control parameters are found. Various techniques for dealing with signal noise encountered during experimentation are investigated. A proportional controller is implemented in the experimental setup that applies feedback control of the braze – welding process using thermal signals. A novel approach to MPC is explored by using a metamodel as the plant model for the braze-welding process and having the temperature trajectory dictated by the metamodel in the steady state region of the weld. Lastly, future work and extensions of this research are outlined.

Table of Contents

List of Tables xv

List of Figures xvii

Nomenclature xxiii

Chapter 1: Introduction 1

- 1.1 Overview of LANL Braze-Welding Project 2
  - 1.1.1 Problem Statement 2
  - 1.1.2 Motivation for the LANL Braze-Welding Project 2
  - 1.1.3 Thermal Surrogate Selection 4
- 1.2 Implementation of thermal surrogate to address research goals 5
- 1.3 Motivation 5
- 1.4 Research Questions Addressed by this Work 8
- 1.5 Research Introduction 9
- 1.6 Dissertation Outline 13

Chapter 2: Thermal Surrogate Selection, Literature Review and Experimental Methods 17

- 2.1 Thermal Surrogate Selection Process 18
- 2.2 Summary of LANL Braze-Welding Project 22
- 2.3 Literature Review 23
  - 2.3.1 Overview of Gas Metal Arc Welding 23
  - 2.3.2 Differences between GMAW and GMABW 27
  - 2.3.3 Governing Equation for the thermal modeling of GMABW 30
  - 2.3.4 Analytical Models 32

2.3.5 Computational Models ... 36
2.3.6 Temperature Sensing ... 40
2.3.7 Classical Control ... 42
2.4 Welding Copper and Copper Alloys ... 43
2.5 Braze- Welding Copper and Copper Alloys ... 47
2.6 Experiments on Thermal Surrogate Material with Silver-based Braze ... 48
2.6.1 Braze 505 on CuZn 90/10%wt Parameter Study ... 49
2.6.2 Braze-welding CuZn 90/10%wt with Braze 505 and preheated with Propane ... 51
2.6.3 Braze 852 on CuZn 90/10%wt Parameter Study ... 54
2.6.4 Braze-welding CuZn 90/10%wt with Braze 852 and preheated with Acetylene ... 56
2.6.5 Universal Braze Welding Parameters ... 60
Chapter 3: Experimental Validation of Thermal Models ... 62
3.1 Models Used in Experimental Comparison ... 64
3.1.1 Analytical Model ... 64
3.1.2 Numerical Models ... 65
3.1.3 Braze-Welding Experiments ... 74
3.2 Validation of Model Predictions ... 76
3.2.1 Comparision of Model Prediction with Experimental Data ... 77
3.2.2 Sensitivity Study ... 83
3.2.3 Student’s T-distribution ... 87
3.3 Conclusion ... 90
Chapter 4: Overview of MetaModels ... 93
4.1 Metamodels ... 94

4.1.1 Support Vector Regression (SVR) 97
4.1.2 Conclusion 99
4.2 FLUENT© model assumptions 99
4.2.1 Metamodel Training 104
Chapter 5: Classical Control 106
5.1 Sensitivity Study 107
5.2 PID Controllers 116
5.2.1 Proportional Control 119
5.2.2 Integral Control 120
5.2.3 Derivative Control 122
5.3 PID Control Simulations 124
5.3.1 Model based approach to finding K_p 125
5.3.2 Parameter study to find controller constants and operating point assessment 130
5.4 Filtering noise from the measured data 140
5.4.1 Regression Models to Filter Noise 143
5.4.2 Exponential Filter 146
5.4.3 Comparison Study of Regression Smoothing and Exponential Filter 151
5.5 Experimental Validation of Smoothing and Control 156
5.5.1 Experimental Hardware and Data Acquisition 157
5.5.2 Experiments on six inch long specimens 158
5.5.3 Experiments on twelve inch long specimens 171
5.5.4 Metamodel Based Control 174
Chapter 6: Conclusions 188

6.1 Thermal Modeling ... 189

6.2 Control Design and Model based tuning ... 190

6.3 Metamodel based control ... 192

Chapter 7: Future Work ... 194

7.1 Metamodeling ... 195

7.2 Analytical Modeling ... 197

7.3 Controller Development ... 200

7.4 Weld Quality ... 201

Appendix A: Experimental Set-Up ... 204

A.1 Final Design ... 205

A.1.1 Frame/Base Assembly ... 207

A.1.2 Linear Motion Table ... 208

A.1.3 Torch Mount ... 210

A.1.4 Drive Shaft Assembly ... 211

A.1.5 Motor Mount ... 213

A.2 Data Acquisiton and Motion Control ... 215

A.2.1 Temperature Measurement: Thermocouples ... 215

A.2.2 Temperature Measurement: Infrared Pyrometers ... 217

A.2.3 Temperature Measurement: Infrared Camera ... 220

A.2.4 Motion Control ... 221

A.2.5 Variable Wire Feed Rate ... 224

A.3 Final Test Station Parameters ... 226

Appendix B: Finite Difference Temperature Model 227
Appendix C: Modern Control: State Space Analysis 229
  C.1 Abstract 229
  C.2 Introduction 229
  C.3 Theory, Background and Experimental Setup 231
  C.4 Data and Results 238
  C.5 Conclusion 246
REFERENCES 248
  Thermal Modeling 248
  Welding Procedures 254
  Control 254
VITA 257

List of Tables

Table 2-1: Properties of Group II Elements (Russel and Lee, 2005)............................... 19

Table 2-2: Properties of HCP Elements (ASM, 2003) 19

Table 2-3: Material Properties from CES Edupack Search 21

Table 2-4: Recommended Filler Metals for Commercial Bronze (ASM, 2003) 22

Table 2-5: Table of analytical solutions... 36

Table 2-6: Survey of numerical solutions applied to welding problem 39

Table 2-7: Recommended preheat temperatures and electrode types for copper alloys (Lincoln, 1978) 45

Table 2-8: Recommended preheat temperatures for copper and cupro-nickel (Dawson, 1973) 46

Table 2-9: Recommended preheat temperatures for copper and copper alloys (Davies, 1977) 46

Table 2-10: Recommended preheat temperatures for copper and low zinc brass (Kearns and Weisman, 1978) 46

Table 2-11: Test parameters used for study 49

Table 2-12: Test parameters used for study 51

Table 2-13: Thermocouple placement for braze-weld with preheat study 52

Table 2-14: Torch Parameters... 52

Table 2-15: Test parameters used for CuZn 90/10%wt and Braze 852 study 55

Table 2-16: Test parameters used for CuZn and Braze 852 with preheating study.......... 57

Table 2-17: Welding test parameters used in experimental validation............................. 61

Table 2-18: Torch Parameters... 61

Table 3-1: Material Properties for CuZn10 (UNS C22000) (Larson and Taylor, 2008) .. 67

Table 3-2: Braze welding test parameters 75

Table 3-3: Thermocouple and IR pyrometer placement 76

Table 4-1: Temperature dependent thermal properties for commercial bronze (UNS C22000) (Larson and Taylor, 2008) 101

Table 4-2: FLUENT© parameters used in twelve inch model 101

Table 4-3: Fitting options and parameters used for SVR model 105

Table 5-1: Welding parameters used in the control simulation 127

Table 5-2: PID constants for idealized plant model without noise 140

Table 5-3: Comparison of error vs. stencil size for regression models and EWMA filter 152

Table 5-4: Welding test parameters used for study 159

Table 5-5: Torch Parameters 159

Table 5-6: Performance metrics for the different control schemes, $K_p = 2.36$ 183

Table 5-7: Performance metrics for the different control schemes, Kp = 3.68 185

Table A-1: Welding test station parameters 226

Table C-1: Thermocouple placement 237

Table C-2: Material Properties for CuZn10 (UNS C22000) 237

Table C-3: Welding Test Parameters 237

List of Figures

Figure 1-1: Schematic of LANL braze-welding project goal 7

Figure 2-1: HCP Crystal Structure (Best, 2006) 18

Figure 2-2: GMAW Schematic taken from (Holliday, 1993) 26

Figure 2-3: Schematic of Coordinate Systems for Braze-Welding Problem 30

Figure 2-4: Recommended edge preparations for GMAW of copper plates (Lincoln, 1978) 47

Figure 2-5: Schematic of specimen used during the Braze-welding with Preheat experiment 52

Figure 2-6: Trial 7 from top and side views after attempting to delaminate filler metal .. 55

Figure 2-7: Trial 5 from top and bottom views 58

Figure 2-8: Trial 6 from top and bottom views 59

Figure 2-9: Trial 7 from top and bottom views 60

Figure 3-1: Picture of semi-automated welding test station (Backlund, 2008; Backlund et al., 2009) 62

Figure 3-2: FDM maximum temperature 69

Figure 3-3: FLUENT maximum temperature 71

Figure 3-4: Z-direction temperature distribution (FLUENT) for an *x, y* point directly beneath the center of the heat source 73

Figure 3-5: Temperature distribution across the width of the top surface 74

Figure 3-6: Schematic of thermocouple (TC) and IR pyrometer layout 75

Figure 3-7: Plot of Temperature vs. Time for models and experimental thermocouple data 79

Figure 3-8: Plot of Temperature vs. Time for models and experimental pyrometer data 80

Figure 3-9: $\frac{\partial T}{\partial Y}$ sensitivity for half of specimen width for $\dot{Q}$=2060 W and X = 76.2mm and all values of Y 84

Figure 3-10: $\frac{\partial T}{\partial X}$ sensitivity for $\dot{Q}$ = 2060 W and Y = 9.53mm and all values of ξ 85

Figure 3-11: Graph of confidence interval of the IR Pyrometer data plotted along with FLUENT and Rosenthal temperature approximations 90

Figure 4-1: Schematic of key steps in surrogate modeling, taken from (Queipo et al., 2005) 94

Figure 4-2: Schematic representation of the surrogate modeling problem, taken from (Queipo et al.) 96

Figure 4-3: Illustration of metamodel prediction and uncertainty, taken from (Queipo et al.) 97

Figure 4-4: Schematic of twelve inch specimen (Ely, 2010) 100

Figure 4-5: Top view of twelve inch weld specimen showing pyrometer placement 100

Figure 4-6: Temperature vs. Position of metamodel training data plotted along with experimental data with Q = 1133 W and V =0.002117 m/s (5 inches per minute) 103

Figure 5-1: $\frac{\partial T}{\partial Q}$ sensitivity for half specimen width for Q=2060 W and several values of displacement from the weld head along the x-axis, $\xi = x - vt$ 109

Figure 5-2: $\frac{\partial T}{\partial K}$ sensitivity for half specimen width for Q=2060W for several values of displacement from the weld head along the x-axis, $\xi = x - vt$ 110

Figure 5-3: $\frac{\partial T}{\partial V}$ sensitivity for half specimen width for Q=2060W and several values of displacement from the weld head along the x-axis, $\xi = x - vt$ 111

Figure 5-4: $\frac{\partial T}{\partial \rho}$ sensitivity for half specimen width for Q=2060W and several values of displacement from the weld head along the x-axis, $\xi = x - vt$ 112

Figure 5-5: $\frac{\partial T}{\partial C_p}$ sensitivity for half specimen width for Q = 2060W and several values of displacement from the weld head along the x-axis, $\xi = x\text{-}vt$ 113

Figure 5-6: $\frac{\partial T}{\partial \alpha}$ sensitivity for half specimen width for Q=2060W and several values of displacement from the weld head along the x-axis, $\xi = x\text{-}vt$ 114

Figure 5-7: Schematic of PID control scheme for braze-welding 117

Figure 5-8: Description of PID Controller... 118

Figure 5-9: Temperature vs. Velocity from Rosenthal thin plate model 126

Figure 5-10: Schematic of weld specimen used in the control simulation 127

Figure 5-11: Temperature vs. Position plot for P controller with K_p = 0.02 128

Figure 5-12: Velocity vs. Position plot for P Controller with K_p= 0.02 129

Figure 5-13: Plots of Temperature, percent difference and controller output for K_p = 0.01 133

Figure 5-14: Plots of Temperature, percent difference and controller output for K_p = 0.005... 135

Figure 5-15: Plots of Temperature, percent difference and controller output for K_p = 0.001... 137

Figure 5-16: Chart of RMS error vs. Log K_p shows that operating point has lower RMS error... 139

Figure 5-17: Plot of noisy data obtained during testing.. 141

Figure 5-18: Temperature profile and controller response for K_p=0.001 and K_i=K_d=0.000001... 143

Figure 5-19: Illustration of a 4 point moving window.. 146

Figure 5-20: Illustration of a 4 point piecewise window 146

Figure 5-21: Graph of metamodel prediction, noisy data and EWMA smoothed data for α = 0.4 150

Figure 5-22: Graph of temperature vs. position along the weld specimen for the regression models and EWMA filter 153

Figure 5-23: Close-up of temperature vs. position for regression models and EWMA filter 154

Figure 5-24:Graph of RMS error vs. position along the weld specimen for the regression models and EWMA filter 155

Figure 5-25: Schematic of six inch test specimen used for validation tests 159

Figure 5-26: P controlled weld proportional control only, K_p = 1 inch per minute/ Deg C 160

Figure 5-27: P controlled weld proportional control only, K_p = 2.36 inch per minute/ Deg C 161

Figure 5-28: P controlled weld proportional control only, K_p = 11.5 inch per minute/ Deg C 163

Figure 5-29: Temperature vs. Time for PI controlled weld, K_p = 2.36, K_p = 11.5 inch per minute/ Deg C and τ_i = 0.02 165

Figure 5-30: Schematic of thin six inch test specimen for validation testing 166

Figure 5-31: Temperature vs. time for P controlled weld and an uncontrolled weld on a 1/8 inch thick specimen 167

Figure 5-32: Temperature vs. Time for P controlled weld with regression and extrapolation, K_p = 11.5, Δt = 25ms and a P controlled weld K_p = 11.5, Δt = 75ms 170

Figure 5-33: Schematic of twelve inch test specimen used for validation tests 171

Figure 5-34: Temperature and Velocity vs. Time for P controlled weld with regression and extrapolation, K_p = 11.5, Δt = 25ms 172

Figure 5-35: Temperature vs. Time for P controlled weld with regression and extrapolation, K_p = 11.5, Δt = 50ms and a P controlled weld K_p = 11.5, Δt = 200ms 173

Figure 5-36: Schematic of area of the work piece controlled by metamodel 176

Figure 5-37: Plots of temperature vs. position that show transients that connect different metamodel trajectories (top) one velocity change (bottom) two velocity changes (Ely, 2010) 177

Figure 5-38: Temperature vs. time for metamodel based controller without transient effects, K_p = 2.36.. 178

Figure 5-39: Temperature vs. time for two welding specimens that demonstrate initial transient effects 180

Figure 5-40: Temperature vs. time for initial transient from experimental data and the curvefit to estimate the time constant 181

Figure 5-41: Temperature vs. Time and Velocity vs. Time for a controlled weld using a metamodel with dynamics, K_p = 2.36 183

Figure 5-42: Temperature vs. Time and Velocity vs. Time for a controlled weld using a metamodel with dynamics, K_p = 3.68 185

Figure 7-1: Schematic of the steel traverse platform that weld specimen rests on during testing (Backlund, 2008; Backlund, Ely, Seepersad, Taleff and Howell, 2009) 196

Figure A-1: Final test station layout 206

Figure A-2: Final assembly.. 207

Figure A-3: Linear motion table 209

Figure A-4: Torch mount assembly 211

Figure A-5: Drive shaft assembly - rear view... 212

Figure A-6: Drive shaft assembly - side view 213

Figure A-7: Motor mount... 214

Figure A-8: Preliminary test data 216

Figure A-9: Infrared pyrometer mount (Ely, 2010) 219

Figure A-10: IR pyrometers mounted to the welding test station (Ely, 2010) 220

Figure A-11: Infrared camera mount 221

Figure A-12: LabVIEW user interface 223

Figure A-13: Relationship between wire feed rate and voltage (Ely, 2010) 225

Figure C-1: Schematic of Welding Problem 231

Figure C-2: Diagram of how *B* vector changes at each time step 235

Figure C-3: Thermocouple Layout (½ of actual domain) 237

Figure C-4: Measured power input during welding 239

Figure C-5: Comparison of Kalman Model with Regular Model for Q = .001*R 242

Figure C-6: Comparison of Kalman Model with Regular Model for Q = .01*R 242

Figure C-7: Comparison of Kalman Model with Regular Model for Q = .1*R 243

Figure C-8: Comparison of Kalman Model with Regular Model for Q = R 243

Figure C-9: Comparison of Kalman Model with Regular Model for Q = 10*R 244

Figure C-10: Comparison of Kalman Model with Regular Model for Q = 100*R 244

Figure C-11: Comparison of Kalman Model with Regular Model for Q = 1000*R 245

Nomenclature

T	temperature, (K)
k	thermal conductivity, (W/m.K)
t	time, (s)
C_p	specific heat, (J/kg.K)
a	width of the braze-welding specimen (m)
g	thickness of the braze-welding specimen (m)
h	convection coefficient (W/m^{2}K)
u,v,w	velocity, (m/s)
x,y,z	coordinate distance, (m)
$\dot{Q}$	heat rate of the heat source, (W)
$\dot{Q}'''$	volumetric heat source (W/m^3)
$R = \sqrt{\xi^2 + y^2 + z^2}$	radius from the weldhead (m)
I	arc current (A)
V	arc voltage (V)
Greek Symbols	
ρ	density, (kg/m^3)
α	thermal diffusivity, (m^2/s)
$\xi=x-ut$	reference frame of the moving heat source

Ψ	volume of the welded workpiece (m^3)
η	arc efficiency
ε	emissivity
σ	Stefan-Boltzmann Constant (5.67×10^{-8} W/m^2K^4)
Subscripts	
o	initial state
p	constant pressure
∞	far away from the domain
s	on the surface
r	radiation

Chapter 1: Introduction

1.1 Overview of LANL Braze-Welding Project

1.1.1 Problem Statement

In any arc welding process, localized heating creates residual stresses in and around the welded joint. The Los Alamos National Lab (LANL) is interested in answering the following two questions:

1) Does the residual stress affect failure in gas metal arc braze welded joints of beryllium?
2) If so, can we predict and mitigate the failure of the braze-welded joints?

It was the goal of The University of Texas to work towards answering these questions. This was done by designing and building a semi-automated welding test station, using it to gather experimental data from controlled gas metal arc welding tests, and developing predictive thermal models of the braze welding process.

1.1.2 Motivation for the LANL Braze-Welding Project

A methodology for improved failure prediction would be beneficial to LANL's beryllium braze-welding efforts and to the welding industry in general. It could be used not only to explain failures after they occur, but also to prevent failures by monitoring and correcting the welding conditions that lead to premature failure. An experimental and a computational approach are taken to answer this question.

A repeatable experimental setup is necessary in order to understand how weld parameters influence failure in a specimen. By creating a flexible weld station, more parameters can be tested, giving a better understanding of failure criteria. Because beryllium can be hazardous to humans, surrogate materials were chosen. The most suitable thermal surrogate is chosen by matching important thermal material properties, which differ from the properties considered when choosing a mechanical surrogate. The selection of the thermal surrogate is explained in Section 1.1.3.

Computationally, a mechanical and thermal model which closely matches the experimental results would be beneficial for future weld process design. The mechanical model will predict residual stresses in a processed part, and the thermal model will provide an accurate temperature history of the process. An accurate temperature history is important in order for the mechanical model to properly choose material data. The thermal model may be expanded into a predictive process model. The motivation behind this model is to have an active communication between temperature and process controllable parameters. In this way, an optimal welding process can be described based on temperature and then implemented by adjusting the controllable parameters such as feed rate, torch speed, torch position, voltage, and current.

The approach to the thermal problem was to develop our own simulation that would be tailored to solve the specific problem at hand. This proved to be too complex given the allotted time and resources. Thus, the computational model being developed has ceased in favor of using commercially available thermal simulation software. Data from the commercial software will be compared to classical analytical solutions and empirical data from experiments. Section 2.3.4 outlines the analytical models used for comparison with the commercial models.

1.1.3 Thermal Surrogate Selection

We are ultimately interested in discovering the effects of welding process parameters on the weld quality of braze-welded beryllium. The welding test station (Appendix A) will be used to process metal specimens and achieve this goal. Due to the dangers associated with handling beryllium, a suitable surrogate material is necessary in order to conduct the tests required for the Los Alamos braze-weld modeling research project. Both mechanical and thermal material attributes are important to consider during the selection process. Additionally, availability, weldability, and safety are among other factors which contribute to the decision-making process. Ultimately, the goal of this surrogate material search is to locate a material (or materials) that will behave similarly to beryllium during and after the braze-welding process.

1.2 Implementation of thermal surrogate to address research goals

In order to answer the questions posed by LANL and conduct research that will help to predict failure and mitigate failure in beryllium-AlSi braze-welded systems, a thermal surrogate is used extensively in the modeling and experimentation of the phenomena that occur during Gas Metal Arc Braze-Welding (GMABW). The thermal surrogate is the testbed in which the thermal behavior of the beryllium system is gauged and the vehicle on which the thermal modeling of beryllium system is validated. The goal of the LANL research is to model and predict failures in beryllium so that process paths may be identified and lay the foundation towards predictive process control for the mitigation of residual stresses in beryllium-AlSi systems. Described in Section 1.3 is the motivation of this research to address the model predictive control needs of the LANL project in order to implement a model based control in the thermal domain to mitigate the formation of residual stress.

1.3 Motivation

As an outgrowth of the LANL braze-welding project, the research presented in this dissertation is the seminal research in order to move to a predictive process approach to manufacturing control and to add a new perspective to model predictive control by using trained metamodels as plant models.

Currently, automated control in manufacturing is done stochastically. This requires an extant database that characterizes the manufacturing process of the item being constructed. These databases are compiled from several batch runs of the same process and have sufficient data to characterize the manufacturing process. These include material, geometry, run time conditions and perturbations in the manufacturing process. Having access to this database allows for changes to be made during manufacturing to ensure the desired final product.

There is a need to apply process control in manufacturing to minimize waste and ensure the quality of the final products but, in the absence of a stochastic database there must be an alternate way to apply process control. In this research, model based process control will be used to control a Gas Metal Arc Braze-Welding (GMABW) process to control the temperature developed in the workpiece during the welding process.

LANL wanted to investigate ways of improving failure prediction capabilities in braze-welds on beryllium. Residual stresses are imparted to the beryllium workpieces from the differential heating and cooling of the beryllium during braze-welding. Through this research, LANL wanted to identify suitable processing paths and move towards a model-based predictive process control that eliminates the reliance on a stochastic database. The approach was to couple structural and thermal models with experimental data and metallography to formulate a well informed process model that does not rely on information from several batch runs of the same manufacturing process.

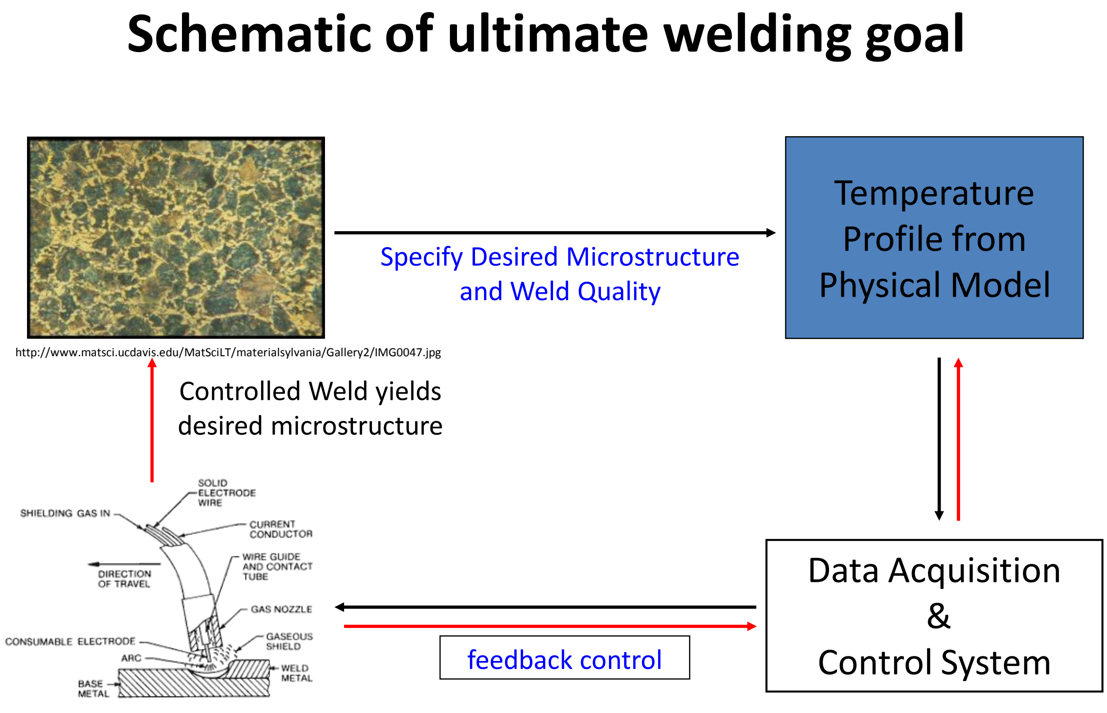
Schematic of ultimate welding goal
Specify Desired Microstructure and Weld Quality
Temperature Profile from Physical Model
http://www.matsci.ucdavis.edu/MatSciLT/materialsylvania/Gallery2/IMG0047.jpg
Controlled Weld yields desired microstructure
SOLID ELECTRODE WIRE
SHIELDING GAS IN
CURRENT CONDUCTOR
DIRECTION OF TRAVEL
WIRE GUIDE AND CONTACT TUBE
GAS NOZZLE
CONSUMABLE ELECTRODE
GASEOUS SHIELD
ARC
WELD METAL
BASE METAL
feedback control
Data Acquisition & Control System

Figure 1-1: Schematic of LANL braze-welding project goal

Shown in Figure 1-1 is the ultimate goal of this research. The essential desire is to be able to specify the desired weld quality and microstructure and the model based control system would be able to control the welding schedule precisely to achieve the desired outcome. At the same time, through the monitoring of weld parameters such as temperature, voltage, current, velocity and several others, the control system can correct the process in real time depending on the types of perturbations encountered during the braze-welding process. As a natural extension of the LANL braze-welding project, specific research questions came about that directly contribute to the overall purpose of the LANL project.

1.4 Research Questions Addressed by this Work

One of the main goals of the LANL project was to circumvent the need for stochastic databases in process control and supplant them with models capable of controlling the process. In the effort to implement models in a model based control scheme, two questions naturally arise.

1. Are the current physics based models adequate for use in physics based control of GMABW?
2. How can physical models of GMABW be effectively implemented into control systems with temperature sensing to create a physics based control methodology for GMABW?

This research investigates the efficacy of current physics based models to simulate and represent the physical effects being monitored during braze-welding. Secondly, methods to implement the physics based models in a control system are researched and tested to determine their feasibility in real time control. Lastly, novel methods of implementing newer strategies such as metamodels are investigated to gauge the improvement gained from their usage.

1.5 Research Introduction

Braze-welding is the general term applied to a welding process in which the filler metal exhibits a liquidus temperature that is less than the solidus temperature of the welded workpiece (Schwartz, 1993; Davies, 1977). In braze-welding, the filler metal is added to the joint via deposition from the filler rod or a consumable electrode using a technique similar to that used in fusion welding, rather than by capillary action as used in brazing. Since little to none of the welded material melts, bonding takes place primarily between the deposited filler metal and the hot unmelted metal of the workpiece in the same manner as conventional brazing (Kearns and Weisman, 1978).

In manufacturing, braze-welding has several advantages over conventional fusion welding such as reduced distortion due to the welding process, reduced residual stresses and the ability to bond dissimilar metals. Braze-welding also has the advantage of requiring reduced pre-heating relative to other brazing techniques (Schwartz, 1993). For these reasons braze-welding is used in the automotive industry for the fabrication of parts from sheet metal (White and Jones, 1997).

Given its industrial applications, it is important to understand the effect of the braze-welding process on the bonded part. One important characteristic of braze-welding is the temperature field that develops in the welded material. Temperature evolution in the workpiece directly affects the size of the heat affected zone (HAZ) which controls the weld joint fatigue life and the residual stresses remaining in the workpiece after braze-welding (Easterling, 1992). Knowledge of the temperature field also serves as the basis for specific approaches to welding control that use temperature as a control variable. For these reasons, it is advantageous to develop the capability of predicting the braze-welding temperature field accurately enough to enable process control.

Several efforts have been made to model the temperature field in a workpiece during gas metal arc welding (GMAW) and gas tungsten arc welding (GTAW). Unlike the present study, they do not include cross-comparisons of empirical data with analytical and numerical model predictions for a common braze-welding test case. Some researchers have compared analytical methods or numerical methods with empirical data but not a cross comparison of all three. In 1946, Rosenthal (1946) published one of the earliest analytical models of the quasi-steady temperature field surrounding a moving point source of heat. Subsequently, several improvements to Rosenthal's model have been developed (Jhaveri, Moffat and Adams, 1962; Carslaw and Jaeger, 1967; Swift-Hook and Gick, 1973; Friedman, 1975; Eagar and Tsai,1983; Goldak, Chakravarti and Bibby, 1984; Goldak, Chakravarti and Bibby, 1985; Boo and Cho, 1990; Song and Hardt, 1993; Nguyen, Ohta and Matsuoka, 1999). With the exception of Jhaveri et al. and Swift-Hook and Gick most of these improved models were validated via comparison with temperature data from experiments. As computational capabilities grew, several numerical models were formulated to capture similar phenomena.

Some computational models used finite element methods (FEM) with various representations of the heat source (Kumar and Bhaduri, 1994; Wahab and Painter, 1997; Wahab, Painter and Davies, 1998; Deng and Murakawa, 2005). Other models used finite difference methods (FDM) to model the coupled physical aspects of welding by including heat transfer and fluid flow in the weld pool (Kim and Basu, 1998; Fan and Kovacevic, 2006). Unified models used the FDM to model complicated arc coupling, melting of the electrode, weld pool dynamics, temperature evolution in the workpiece, and droplet formation, detachment, transfer, and impingement on the welded specimen (Hu and Tsai, 2007a; 2007b; 2008). Despite modeling multiple physical aspects of the welding process, most of these models were not validated with empirical temperature data (Kumar and Bhaduri; Kim and Basu; Fan and Kovacevic; Hu and Tsai). Furthermore, none of these studies compare computational and analytical models. Although one study compares various analytical methods (Bertram, 1996), very few model comparisons exist in the literature.

In this research, Rosenthal's analytical model is compared with a computational model based on a finite difference method and a computational FLUENT® model based on a finite volume method. All models are compared with experimental data describing the temperature distribution in a representative workpiece during GMABW. The objective of the study is to characterize the speed and accuracy of Rosenthal's analytical model for real-time, model-based control and to compare it with more sophisticated

FLUENT® models. These FLUENT® models are too computationally expensive to be used directly for real-time, model-based control, but they do serve as a data source for training surrogate models or metamodels, e.g., polynomial regression (Simpson, Mauery, Korte and Mistree, 1998), kriging (Simpson et al.), multivariate adaptive regression splines (Friedman, 1991), support vector regression (Vapnik, 1998), and others (Giunta, Watson and Koehler, 1998; Varadarajan, Chen and Pelka, 2000; Yang et al., 2000; Jin, Chen and Simpson, 2001;Simpson, Poplinski, Koch and Allen, 2001; Ely and Seepersad, 2009) for that purpose. Accordingly, the two models are compared with one another (and with experimental data and finite difference predictions for comparison purposes) with the objective of finding a thermal model that is simple but accurate and fast enough for real-time control.

Metamodels based on Support Vector Regression (SVR) serve as a process model for a numerical simulation of a Proportional Integral Derivative (PID) feedback control system. The simulated control system is used to find the PID constants to get the best performance out of the controller. The PID constants are tested experimentally for performance. Lastly, a unique model predictive controller is created by coupling an SVR metamodel with a PID controller. In the implementation of the model predictive controller, the metamodel choses the temperature trajectory and the PID controller drives the physical system to model based trajectory.

1.6 Dissertation Outline

This work is comprised of seven chapters and several appendices. The first chapter serves as an overview to the LANL braze-welding project and the goals of that research project. The movitation for this body of work is outlined and the research questions that this research addresses are presented. Lastly, a brief overview of work that has been conducted in the auxiliary fields of heat transfer modeling and control as they pertain to Gas Metal Arc Welding (GMAW) is presented. This background provides a basis of techniques and materials for the development of a Model Predictive Control (MPC) framework that may be applied to Gas Metal Arc Braze Welding (GMABW). Chapters Two through Seven outline the experimental setup used in the data collection, the experimental validation of the thermal models, classical control simulations with metamodels, experimental validation of temperature based welding control, and roadmaps for potential future work. A more detailed outline of these chapters is as follows.

Chapter Two presents an overview of the thermal surrogate selection process, literature review of Gas Metal Arc Welding and Braze-Welding, an overview of research that has been conducted in thermal modeling, temperature sensing and control techniques in addition to experimental procedures utilized in this research to weld copper and copper alloys. Experimental parameters, edge preparations and preheat temperatures are compiled from several welding handbooks and references. These serve as preliminary starting points for the treatment of CuZn 90/10 %wt. Also outlined in this chapter are the results of the parameter studies for brazing welding CuZn 90/10%wt with two types of silver braze.

Chapter Three presents the results of the experimental validation of the series of thermal models that were considered for real time calculation for the purpose of real time control. The experimental parameters are outlined and a comparison of three temperature models with the experimental data is presented. Based on the comparison, conclusions are drawn about the strengths and weaknesses of each model and the applicability in real time control.

Chapter Four provides a brief overview of metamodels. Support Vector Regression (SVR) metamodels that were found to be promising for modeling arc welding processes are presented and briefly discussed.

Chapter Five outlines the efforts made to combine classical PID control with a metamodel used as the plant model of the GMABW process. Determination of the proportional control constant is done via a model-based approach as a first estimate for the appropriate proportional value. The most favorable value for the proportional constant is found via a modified Ziegler-Nichols technique. Simulated control behavior is presented for the various value of the proportional constant. Methods for dealing with noisy data are presented and results from computer simulations and comparison metrics for denoising algorithms are outlined and discussed. Lastly experimental validation of the PID controlled welding simulations is presented.

Chapter Six presents an overview of the conclusions and results of this study. A summary of the findings and succinct overview of the study is presented.

The Seventh and final chapter of this work presents suggestions for potential follow on research for questions raised during this investigation. The areas of research that this investigation encompasses i.e. heat transfer modeling and control, has viable research paths that continue from the work presented here. Chapter Seven outlines a few of the possible questions and extant needs that exist in this field of research that were discovered through this study.

The appendices provide more detailed information or derivations of specific equations utilized in this work. Interested researchers wanting to gain further insight to some of the subjects covered may consult the appendices, yet there is no loss of continuity from the remainder of the work by the material covered in the appendices.

Appendix A outlines the design and capabilities of the semi-automatic welding test station upon which the all of the data collection and experimental validation is done. Pictures and notes regarding design are presented.

Appendix B details the formulation of the Finite Difference Model used to Section 3.1.2 compare against temperature data obtained from welding experiments and cross-compared with FLUENT and Rosenthal's Analytical Model.

Appendix C presents a preliminary study of a modern control model that takes into account systematic noise present in the data acquired during testing. The resulting state-space model with Kalman filter is used to examine the effects of various noise levels present in the data. From a modern control perspective this outlines the preliminary steps for the exploration of modern control techniques applied to GMABW.

Chapter 2: Thermal Surrogate Selection, Literature Review and Experimental Methods

In this chapter, the criteria for the selection of a thermal surrogate is outlined, and a literature review of the areas of welding modeling, temperature sensing and control as they pertain to Gas Metal Arc Welding (GMAW) is presented. As discussed in Sections 1.1.2 and 1.1.3, CuZn 90/10 %wt (C22000) was chosen as a thermal surrogate to mimic the thermal behavior of beryllium. As a result, the following experimental methods used to weld and braze weld CuZn (90/10 %wt), more commonly known as commercial bronze or UNS C22000 are outlined in this chapter. The experimental methods used to weld CuZn 90/10 %wt and are also applicable to the entire family of high brasses.

2.1 Thermal Surrogate Selection Process

Beryllium has a hexagonal close-packed (HCP) crystal structure, and it was thought that if the material were thermally stressed (as in a welding process) a material with the HCP structure would behave in a similar manner. The HCP crystal structure is shown below in Figure 2-1. As a result, the material search focused on group II periodic elements. Crystal structure, melting point, and thermal conductivity were of particular importance due to the effect of these properties on the mechanical and thermal behavior of the material.

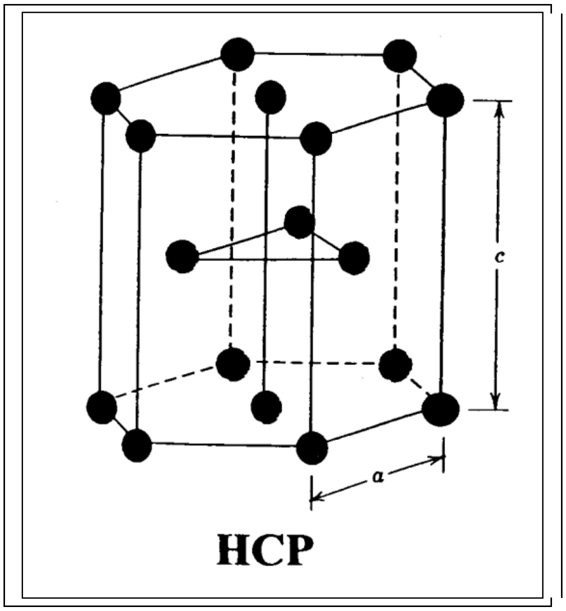

Figure 2-1: HCP Crystal Structure (Best, 2006)

Shown in Table 2-1 are the properties of group II elements. While comparing values of thermal conductivity, melting point temperature and crystal structure, it is evident that searching for suitable surrogate within the same periodic group will not yield a sufficient surrogate.

Table 2-1: Properties of Group II Elements (Russel and Lee, 2005)

Element	Valence	Crystal Structure	Density (g/cm^3)	Tm (.C)	k (W/mK)
Be	2	HCP*	1.85	1287	190
Mg	2	HCP	1.74	650	160
Ca	2	FCC	1.55	842	200
Sr	2	FCC**	2.63	777	35
Ba	2	BCC	3.51	727	18
Ra	2	BCC	5	700	19

*BCC at 1263°C

** HCP at 231°C and BCC at 623°C

The next phase of the surrogate material search was within HCP elements. As shown in Table 2-2, the elements with similar c/a ratios to beryllium had very dissimilar thermal conductivity values. As a result of the two material searches, instead of trying to find an adequate surrogate in the group II elements or HCP elements, the search focused on matching the thermal properties of beryllium since that was the behavior of interest.

Table 2-2: Properties of HCP Elements (ASM, 2003)

	Density (g/cm^3)	k (W/mK)	Tm (°C)	Phase Transformation Temperature	c/a Ratio
Be	1.850	210	1283	1270	1.57
Mg	1.738	156	650	-	1.62
Re	21.02	71.2	3180	-	1.62
Ti	4.507	21.9	1668	883	1.59
Zn	7.133	113	420	-	1.86
Zr	6.505	21.1	1852	862	1.59

The most ideal thermal surrogate would match the thermal conductivity, *k* and the thermal diffusivity, α of beryllium. The heat equation is shown in Eqn. 1 where *k* is thermal conductivity, ρ is the density and c_p is the specific heat. The main property that governs the temperature profile inside the base metal is thermal diffusivity but, often times thermal conductivity, *k* appears in the boundary conditions imposed on the workpiece. Since the evolution of the thermal profile inside the workpiece is the variable of interest, the thermal diffusivity was chosen as a selection property because of the role it plays in the heat equation.

$$\rho \cdot c_p \frac{\partial T}{\partial t} = k\left(\frac{\partial^2 T}{\partial x^2} + \frac{\partial^2 T}{\partial y^2} + \frac{\partial^2 T}{\partial z^2}\right) \tag{1}$$

The thermal diffusivity is a function of the thermal conductivity, density, and specific heat of a material and is shown in Eqn. 2:

$$\alpha = \frac{k}{\rho \cdot c_p} \tag{2}$$

By rearranging Eqn. 1 and substituting Eqn. 2, the heat equation becomes

$$\frac{\partial T}{\partial t} = \alpha\left(\frac{\partial^2 T}{\partial x^2} + \frac{\partial^2 T}{\partial y^2} + \frac{\partial^2 T}{\partial z^2}\right) \tag{3}$$

where α is the thermal diffusivity. Eqn. 3 shows that the heat equation scales with the thermal diffusivity. A material search was conducted based on the thermal diffusivity and the melting point temperature. Material properties are temperature dependent, so the thermal diffusivity of the selected surrogate material may behave differently with varying temperatures than the thermal diffusivity of beryllium. The materials search was conducted using the CES EduPack software. Shown in Table 2-3 are materials with similar thermal diffusivities, those highlighted being the closest to Be.

Table 2-3: Material Properties from CES Edupack Search

CES EduPack Materials (Properties are taking from the average of the given range)					
Material Name	ρ [kg/m^3]	k [W/mK]	T_m [°C]	C_p [J/kgK]	α [m^2/s]
Beryllium	1848	190	1283	1886	5.45E-05
Wrought aluminum pure, 1-0	2700	244	933.2	935	9.67E-05
Wrought aluminum alloy, 6082, T6	2700	172	885.7	900	7.08E-05
Phosphorus de-oxidized As h.c. Cu (UNS C14200)	8925	165.5	1340.5	380.5	4.87E-05
High conductivity copper-cadmium-tin, hard (wrought)	8942.5	227.5	1318	378.5	6.72E-05
Brass: gilding metal, CuZn10, (UNS C22000)	8712	188.5	1308	382.3	5.66E-05
Brass: gilding metal, CuZn5, (UNS C21000)	8674	232.5	1334	381.9	7.02E-05
A206	2800	121	1088.5	920	4.70E-05
Brass: CuZn40 (gravity diecast) (UNS C85500)	8100	125.5	1165	375.15	4.13E-05
Brass: high-tensile brass, CuZn27Al4.5 (wrought)	8316	113.5	1232.5	377.65	3.61E-05
Gray (Flake graphite) cast iron (BS grade 100)	7000	61	1436.5	312.5	2.79E-05
Gray (Flake graphite) cast iron (BS grade 150)	7050	57	1461.5	332.5	2.43E-05
Iron, Commercial Purity "Ingot Iron", annealed	7870	75.5	1808	450	2.13E-05
Nickel 200, Commercial Purity, soft (annealed)	8900	70	1723.5	456	1.72E-05
Rapid solidification aluminum alloy, 8019	2930	117.5	897.7	935	4.29E-05
Cast aluminum alloy, S520.0: LM10-TB	2570	88	808.2	963	3.56E-05
Cast aluminum alloy, S332.1: LM26-TE	2760	105.5	823.2	963	3.97E-05
Wrought aluminum alloy, 7055, T77511	2880	154.5	828.2	961	5.58E-05
Zinc-Copper-Titanium, "ILZRO 16"	7100	105	689.7	402.5	3.67E-05
Zinc-22%Aluminum Superplastic Alloy (Rolled)	5200	125	723.2	500	4.81E-05
Cast magnesium alloy (AS41)	1805	68	808.2	975	3.86E-05
Cast magnesium alloy, EZ33A, T5	1824	100.95	893.7	1068.5	5.18E-05

Given the similar diffusivity, thermal conductivity and melting point, Brass gilding metal with 10 percent Zinc was chosen. The American Welding Society recommends using Ag-based filler metals for brazing commercial bronze, and the table below (Table 2-4) outlines the brazing temperatures of some of these filler metals.

Table 2-4: Recommended Filler Metals for Commercial Bronze (ASM, 2003)

Filler metal	**Service temperature °C**	**Service temperature °F**	**Brazing temperature °C**	**Brazing temperature °F**
Ag	425	800	925	1700
Ag-5Al, Ag-7.5Cu	425	800	870-925	1600-1700
Ag-5Al-0.5Mn	425	800	870-900	1600-1650
Al, Al-Si (4040), Al-Mn (3003)	260	500	650-690	1200-1275
Ti-48Zr-4Be, Ti-43Zr-12Ni-2Be	540	1000	870-1095	1600-2000
Ag-9Pd-9Ga	. . .	. . .	880-920	1615-1690

Since current work at Los Alamos uses Al-Si filler metals for braze welding beryllium, it was thought that this multi-purpose filler metal would work well with commercial bronze as well.

2.2 Summary of LANL Braze-Welding Project

Commercial bronze C22000 was selected as an appropriate thermal surrogate for beryllium. The search for the thermal surrogate began by inspecting other group II elements and HCP crystal structured elements. None of these elements were similar enough to beryllium to be used as a surrogate. A search was conducted based on the thermal diffusivity, the thermal conductivity, and the melting temperature and based on these selection criteria, the commercial bronze was selected as the thermal surrogate.

2.3 Literature Review

A brief overview of the state of research is provided here to understand what progress has been made in the fields of welding modeling, temperature sensing and classic control as it applies to welding control. The fields of thermal modeling of welding processes, classical and modern control of welding and model reduction have been studied extensively in the past, yet there is a dearth of research that applies these methods and techniques to the control of Gas Metal Arc Braze-Welding control.

2.3.1 Overview of Gas Metal Arc Welding

Defined by Holliday (1993), Gas Metal Arc Welding (GMAW) is an arc welding process that joins metals together by heating them with an electric arc that is established between a consumable electrode (wire) and the workpiece. An externally supplied gas or gas mixture acts to shield the arc and molten weld pool from oxidation.

Although the basic GMAW concept was introduced in the 1920s, it was not commercially available until 1948. At first, it was considered to be fundamentally a high-current-density, small-diameter, bare-metal electrode process using an inert gas for arc shielding. Its primary application was aluminum welding. As a result, it became known as metal-inert gas (MIG) welding, which is still common nomenclature. Process developments lead to changes that included: operating at low current densities, pulsed currents and the use of reactive gases and alternate gas mixtures. As a result of these developments, the term Gas Metal Arc Welding gained formal acceptance.

GMAW has several advantages over other forms of welding, the most important of which are (Holliday, 1993):

- Electrode length does not face the restrictions encountered with shielded-metal arc welding (SMAW).
- Welding can be accomplished in all positions, when the proper parameters are used, a feature not found in submerged arc welding.
- Welding speeds are higher than those of the SMAW process.
- Deposition rates are significantly higher than those obtained by the SMAW process.
- Continuous wire feed enables long welds to be deposited without stops and starts.
- Penetration that is deeper than that of the SMAW process is possible, which may permit the use of smaller-sized fillet welds for equivalent strengths.
- Less operator skill is required than for other conventional processes.
- Minimal postweld cleaning is required because of the absence of a heavy slag.

These advantages make the process particularly well suited to high-production and automated welding applications. With the advent of robotics, gas-metal arc welding has become the predominant process choice.

GMAW also has certain limitations that may restrict its use (Holliday, 1993):

- The welding equipment is more complex, usually more costly, and less portable than SMAW equipment.

- The process is more difficult to apply in hard-to-reach places because the welding gun is larger than a SMAW holder and must be held close to the joint (within 10 to 19 mm, or 3/8 to 3/4in.) to ensure that the weld metal is properly shielded.
- The welding arc must be protected against air drafts that can disperse the shielding gas, which limits outdoor applications unless protective shields are placed around the welding area.
- Relatively high levels of radiated heat and arc intensity can hinder operator acceptance of the process.

Shown in Figure 2-2 is a schematic of the GMAW process. An arc is established between a continuously fed electrode of filler metal and the workpiece. Settings are made by the operator; the arc length is maintained between the electrode tip and workpiece at the set value, despite the changes in the gun-to-work distance during normal operation. This automatic arc regulation is achieved in one of two ways. The most common method is to utilize a constant-speed (but adjustable) electrode feed unit with a variable-current (constant-voltage) power source. As the gun-to-work distance changes, which instantaneously alters the arc length, the power source delivers either more current (if the arc length is decreased) or less current (if the arc length is increased). This change in current will cause a corresponding change in the electrode melt-off rate, thus maintaining the desired arc length.

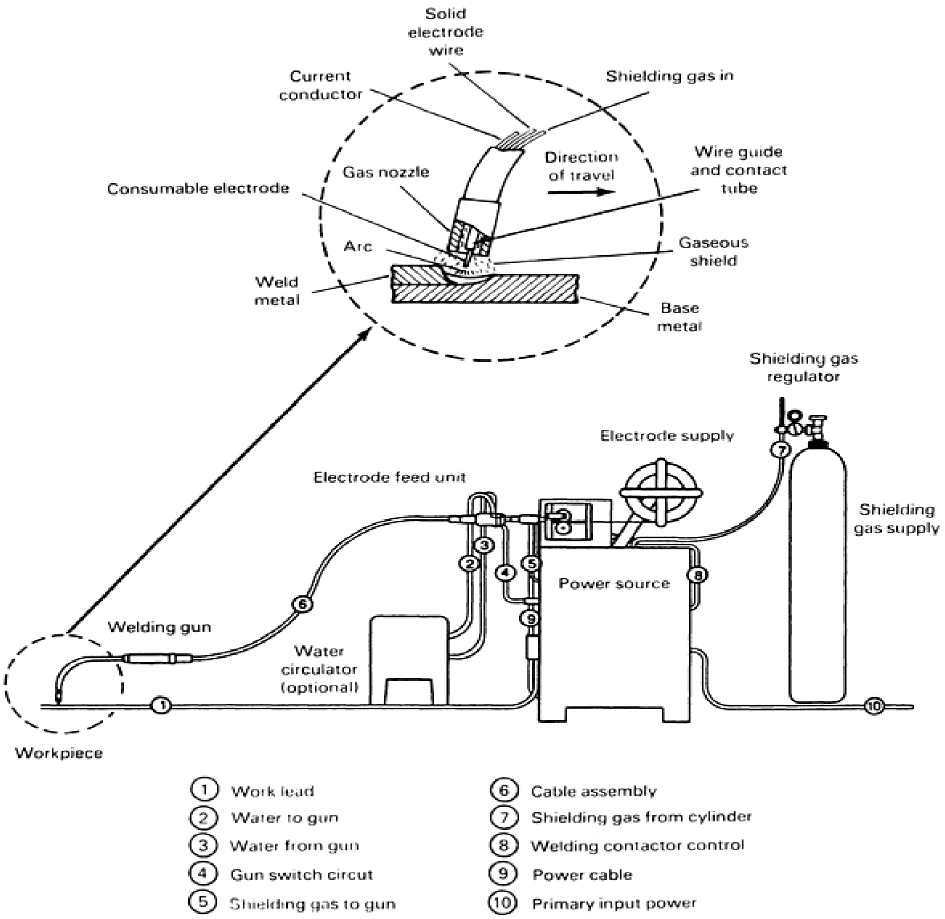
Solid electrode wire
Current conductor
Shielding gas in
Gas nozzle
Direction of travel
Wire guide and contact tube
Consumable electrode
Arc
Gaseous shield
Weld metal
Base metal
Shielding gas regulator
Electrode supply
Electrode feed unit
Shielding gas supply
Power source
Welding gun
Water circulator (optional)
Workpiece
① Work lead
② Water to gun
③ Water from gun
④ Gun switch circuit
⑤ Shielding gas to gun
⑥ Cable assembly
⑦ Shielding gas from cylinder
⑧ Welding contactor control
⑨ Power cable
⑩ Primary input power

Figure 2-2: GMAW Schematic taken from (Holliday, 1993)

The second method of arc regulation utilizes a constant-current power source and a variable-speed, voltage-sensing electrode feeder. In this case, as the arc length changes, there is a corresponding change in the voltage across the arc. As this voltage change is detected, the speed of the electrode feed unit is changed to provide either more or less electrode per unit of time. This method of regulation is usually limited to larger electrodes with lower feed speeds.

How well the GMAW process works depends on the deposition mode of the metal transfer from the electrode to the workpiece. The three basic means by which metal is transferred from the electrode to the workpiece are: short-circuiting transfer, globular transfer, or spray transfer. The type of transfer is determined by a number of factors, the most influential of which are:

- Magnitude and type of welding current
- Electrode diameter
- Electrode composition
- Electrode extension beyond the contact tip or tube
- Shielding gas
- Power supply output

2.3.2 Differences between GMAW and GMABW

The main focal point of this work is the modeling and control of Gas Metal Arc Braze Welding (GMABW). In the last section, the GMAW process was outlined, but it is important to understand the differences between arc welding and arc braze welding. Despite the identical procedures of both processes the underlying physical differences will affect the treatment in terms of modeling and control.

Defined by Schwartz (1993), brazing is a process for joining solid metals in close proximity by introducing a liquid metal that melts above 450 °C (840 °F). A sound brazed joint generally results when an appropriate filler alloy is selected, the parent metal surfaces are clean and remain clean during heating to the flow temperature of the brazing alloy, and a suitable joint design is used.

Brazing has several advantages and for certain applications may be more appropriate than welding. This has come about because of the (Schwartz, 1993):

- Development of new types of brazing filler metals (rapid solidification amorphous foils and titanium-added filler metals for ceramic joining)
- Availability of new forms and shapes of filler metals
- Introduction of automation that has brought brazing processes to the forefront in high-production situations
- Increased use of furnace brazing in a vacuum, as well as active and inert-gas atmospheres

Braze welding is a joining process in which a filler metal is melted and deposited in a specific joint configuration from the filler rod or consumable electrode using a technique similar to that used in fusion welding, rather than by capillary action that is used in traditional brazing. A metallurgical bond is obtained by a wetting action that is often accompanied by some degree of diffusion with the workpiece metal and filler metal, but since little to none of the workpiece metal melts, bonding primarily takes place between the deposited filler metal and hot unmelted workpiece metal (Kearns and Weisman, 1978). Braze welding requires heating and melting of the filler metal that has a melting (liquidus) temperature above 450 °C (840 °F). Stringent fit-up is not critical, because the filler metal is deposited in grooves and spaces and flows into gaps wider than those used for brazing. Fabricators use braze welding as a low-temperature substitute for oxyfuel welding or as a low-cost substitute for brazing. Joint designs for braze welding are the same as for oxyfuel welding (OFW) (Schwartz, 1993). Braze welding has been used to join cast iron, steels, copper, nickel, and nickel alloys.

Compared to conventional fusion-welding processes, braze welding requires less heat input, permits higher travel speeds, and causes less distortion. Deposited filler metal is soft and ductile, providing good machinability, and residual stresses are low. The process joins brittle cast irons without extensive preheating.

Although most braze welding initially used an OFW torch, copper filler metal brazing rod, and a suitable flux, present applications use carbon arc welding (CAW), gas-tungsten arc welding (GTAW), gas-metal arc welding (GMAW), or plasma arc welding (PAW) without flux in the manual, semiautomatic, or automatic modes to economically bond and deposit the filler metal in the braze weld joints (Schwartz, 1993).

A wide variety of parts can be braze-welded using typical weld joint designs. Groove, fillet, and edge welds can be used to join simple and complex assemblies made from sheet, plate, pipe, tubing, rods, bars, castings, and forgings. Sharp corners that are easily overheated and may become points of stress concentrations should be avoided. To obtain good strength, an adequate bond area is required between filler metal and the workpiece metal. Weld groove geometry should provide an adequate groove face area, so that the joint will not fail along the interfaces. Proper joint design selection will produce deposited filler-metal strengths that may meet or exceed the minimum workpiece metal tensile strengths. Because of the inert shielding gas, electrical arc methods have fewer included flux compounds and oxides at the facing surfaces. The result is higher joint strength and improved corrosion resistance. Original surfaces are restored by overlayments and subsequent machining (Schwartz, 1993).

2.3.3 Governing Equation for the thermal modeling of GMABW

Consider the braze-welding process shown in an elementary schematic in Figure 2-3, which depicts a symmetric half of the workpiece, divided along the *x*-*z* plane of symmetry. If convection and radiation are ignored, the temperature evolution in a substrate irradiated by a moving heat source is described by Eqn. 4a:

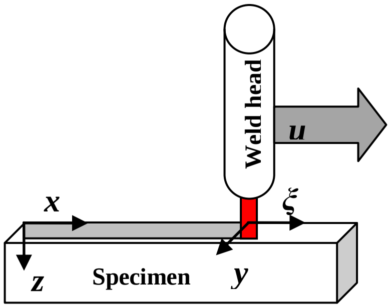

Figure 2-3: Schematic of Coordinate Systems for Braze-Welding Problem

$$\frac{DT}{Dt} = \alpha \nabla^2 T + \frac{\dot{Q}'''}{\rho C_p} \tag{4a}$$

The terms in Eqn. 4a and the following equations are outlined in the previous nomenclature section. The material derivative of temperature in the substrate is equal to the thermal diffusivity, α, times the Laplacian of the temperature, plus contributions from volumetric heat sources, $\dot{Q}'''$ such as chemical reactions that occur inside the substrate. In Eqn. 4a the volumetric heat source, $\dot{Q}'''$ will represent the heat input per unit volume into the workpiece from the welding arc. Eqn. 4a can be expanded into Eqn. 4b in Cartesian coordinates:

$$\frac{\partial T}{\partial t} + u\frac{\partial T}{\partial x} + v\frac{\partial T}{\partial y} + w\frac{\partial T}{\partial z} = \alpha\left(\frac{\partial^2 T}{\partial x^2} + \frac{\partial^2 T}{\partial y^2} + \frac{\partial^2 T}{\partial z^2}\right) + \frac{\dot{Q}'''}{\rho C_p} \tag{4b}$$

where *u, v,* and *w* represent the velocity of the heat source in the *x, y,* and *z* directions in Fig. 1, respectively. Some thermal models, such as the computational models described in Section 2.3.5, are based on the assumption of a coordinate system that is fixed with respect to the top surface of the substrate. When appropriate terms are removed for this assumption, Eqn. 4b reduces to Eqn. 5:

$$\frac{\partial T}{\partial t} = \alpha\left(\frac{\partial^2 T}{\partial x^2} + \frac{\partial^2 T}{\partial y^2} + \frac{\partial^2 T}{\partial z^2}\right) + \frac{\dot{Q}'''}{\rho C_p} \tag{5}$$

Other thermal models, such as the analytical model described in Section 2.3.4, are based on the assumption that a coordinate system is aligned with the moving heat source as pictured in Figure 2-3. When appropriate terms are cancelled for this assumption and the coordinate frame is rotated, Eqn. 4b reduces to Eqn. 6:

$$\frac{\partial T}{\partial t} - u\frac{\partial T}{\partial x} = \alpha\left(\frac{\partial^2 T}{\partial x^2} + \frac{\partial^2 T}{\partial y^2} + \frac{\partial^2 T}{\partial z^2}\right) + \frac{\dot{Q}'''}{\rho C_p} \tag{6}$$

where u is the velocity of the torch in the x direction. Eqn. 6 is based on the assumption that the weldhead moves only in the x direction.

Eqs. 5 and 6 may be solved analytically for specific types of boundary conditions, as described in Section 2.3.4. However, those analytical solutions consider only the problem of heat conduction. The temperature distribution may be influenced by other physical phenomena, such as convection, radiation, fluid dynamics in the weld pool, and temperature-dependent material properties, but those phenomena require additional equations that become intractable to solve analytically (Yang and Debroy, 1999). More sophisticated computational models, such as the computational models described in Section 2.3.5, can take these phenomena into account, but the associated execution times make them difficult to use for real-time, automated control applications. Hence, more computationally efficient analytical models are used in this research for preliminary analysis and sensitivity studies. The analytical and computational models are described in the remainder of this section.

2.3.4 Analytical Models

One of the earliest solutions of the braze-welding equation, Eqn. 6, is Rosenthal's analytical model (1946). In Rosenthal's model, the torch is modeled as a point heat source, such that the heat is assumed to be transferred from the torch to the substrate at an infinitesimally small point. The point source (torch) is assumed to move relative to the substrate, and the origin of the coordinate axes is fixed to the top of the domain as shown in Figure 2-3. Rosenthal alters the fixed coordinate system by defining a moving coordinate system aligned with the heat source. In the moving coordinate system, ξ represents the distance between a point on the substrate and the heat source, moving with velocity, u, as shown in Figure 2-3. Accordingly, x is replaced with ξ in Eqn. 5, which is related to x by the velocity of the heat source (i.e., $\xi=x-ut$). The resulting formulation is shown in Eqn. 7:

$$\frac{\partial^2 T}{\partial \xi^2}+\frac{\partial^2 T}{\partial y^2}+\frac{\partial^2 T}{\partial z^2}=-\frac{u}{\alpha}\frac{\partial T}{\partial \xi}+\cancel{\frac{1}{\alpha}\frac{\partial T}{\partial t}} \tag{7}$$

Rosenthal’s treatment of the governing equation is a quasi-steady approximation in which the temperature distribution surrounding a heat source, moving with constant velocity, is assumed to be steady with time (Rosenthal).

Rosenthal’s solution for Eqn. 7 is based on several simplifying assumptions. The substrate is assumed to be a semi-infinite solid subjected to a quasi-steady moving point source. The material properties of the substrate are assumed to be temperature-independent. The solution accounts for conduction within the solid but neglects convection, radiation, and melting/solidification. Finally, the heat source is modeled as a boundary condition. The solution is provided for three dimensional heat flow as a function of radial distance, R, from the heat source, as follows:

$$T(R) = T_o + \frac{\dot{Q}}{4\pi k R} \exp\left(-\frac{u}{2\alpha}(\xi + R) \right) \tag{8}$$

Rosenthal found that his solutions matched experimental data closely except for regions in close proximity to the heat source or near the workpiece boundaries. Rosenthal attributed the error near the heat source to the fact that it was modeled as a point source rather than a source of finite size and defined geometric distribution.

Rosenthal's solution has several advantages and limitations. The solution is simple and very fast for calculating the temperature distribution in a workpiece. Also, it retains the 3-D characteristics of the problem and seems to be relatively accurate for specific welding regimes (Christensen, Davies and Gjermundsen, 1965). However, temperature predictions become less accurate and approach infinity as the radius, R, approaches zero because the heat source is modeled as a point source (Rosenthal). In addition, the solution is a quasi-steady solution; therefore, transient effects (e.g., startup) are not represented. Also, the assumption of a semi-infinite domain causes underestimation of the temperature field in the substrate because of heat conduction away from the weld zone into an infinite heat sink. Lastly, lack of temperature-dependent properties causes inaccuracies for braze-welding applications that have a broad range of temperatures.

Other researchers have subsequently relaxed some of Rosenthal's assumptions, as outlined in Table 2-5. For example, some of the subsequent models preserve the transient term in the model to reflect the time dependence of the problem (Carslaw and Jaeger, 1967; Friedman, 1975; Eagar and Tsai, 1983 and Nguyen, Ohta, Matsuoka, Suzuki and Maeda, 1999). Additional improvements on Rosenthal's solution include: (1) coupling the heat equation with other physical phenomena and modeling the multi-physics system (Yang and Debroy, 1999) and (2) formulation and solution of the heat equation in a finite domain as opposed to an infinite domain (Friedman; Goldak, Chakravarti and Bibby, 1984; Goldak, Chakravarti and Bibby, 1985 and Boo and Cho, 1990). Furthermore, many subsequent models use different expressions to represent the heat source, thereby removing the singularity of the point source (Eagar and Tsai; Friedman; Goldak et al.; Boo and Cho; Song and Hardt; Nguyen et al.). Representation of the geometric character of the heat source is very important for the practical relevance of the thermal model, and it is one of the most difficult conditions to model accurately.

Table 2-5: Table of analytical solutions

	Year	**Heat Source**	**Boundary Conditions**
Rosenthal	1946	Point source (Quasi-Steady)	Semi-infinite solution and adiabatic planes
Carslaw and Jaeger	~1947	Point source (Transient)	Semi-infinite solutions
Jhaveri et al.	1962	Point source (Quasi-Steady)	Added corrections for plate thickness and surface radiation
Swift-Hook and Gick	1973	Line source	Semi-infinite solution with variable properties
Eager and Tsai	1983	2-D Gaussian Distribution	Semi-infinite solution
Boo and Cho	1990	2-D Gaussian Distribution	Finite thickness and top surface convection
Nguyen et al.	1999	Double Ellipsoidal	Semi-infinite solution

2.3.5 Computational Models

Although some of the models described in Section 2.3.4 provide an adequate estimate of the temperature profiles, those solutions only pertain to linear formulations of the thermal effects seen during welding. Solutions of this nature effectively decouple the thermal evolution from any other physical phenomena that contributes to the heat transport occurring in the workpiece. Coupling of physical phenomena to reflect the true multi-physics nature of welding renders the modeling problem non-linear and makes it intractable to solve analytically. Starting in the 1970's researchers began to see the necessity of including full conservation equations in the models (Jönsson, Szekely, Choo and Quinn, 1994). As computational power became more readily available, numerical solutions grew prominent and allowed for development of more sophisticated models.

Several numerical methods have included the coupled conservation equations of continuity, energy and momentum that describe the physical system being modeled. The three main methods found in the literature are Finite Difference Methods, Finite Volume Methods and Finite Element Methods. Finite Volume Methods (FVM) are similar to Finite Difference Methods (FDM) but rather than approximating the derivatives in a differential equation by a Taylor Series expansion, Finite Volume Methods use integrals of those differential equations as approximations. The Finite Volume Method may be regarded as the simplest form of a set of conservative methods called Finite Element Methods (FEM) (Ferziger, 1981).

Finite Element Methods are similar to Finite Volume Methods in that the domain is split into discrete volumes or finite elements, but differ in that the equations to be solved are multiplied by a weighting function before they are integrated over the whole domain. This approximation is substituted into the weighted integral of the equation to be solved. The solution is found by requiring that the derivative of the integral of the weighted equation be zero with respect to each nodal value in the domain. This amounts to selecting the solution out of a series of possible solutions with the minimum residual (Ferziger and Peric, 2002).

In terms of modeling fidelity, a conservative method should be used to ensure that the model is conserving energy or mass. Finite Volume Methods (FVM) or Finite Elements Methods (FEM) would be preferable over the use of Finite Difference Methods (FDM), yet FDM methods require less computational resources. Throughout the literature there has been active research done with all three numerical methods in the application to welding modeling. With the advent of widely available commercial software packages for FVM and FEM, sophisticated numerical solutions to coupled welding phenomena are well represented in the literature. Shown in Table 2-6 are some representative examples of works that have advanced the field of numerical modeling of arc welding. Because of the sheer amount of research done in this area, it is not possible to provide a comprehensive overview of all the work that has been performed. Interested readers and researchers are therefore directed to the works of Jönsson, Szekely, Choo and Quinn (1994), Mackerle (1996), Mackerle (2002) and Yaghi and Becker (2004) for a thorough and organized overview of work that has been done in the numerical modeling of arc welding.

Table 2-6: Survey of numerical solutions applied to welding problem

	Year	Heat Source	Solution Method
Friedman	1975	Gaussian Distribution	FEM
Goldak et al.	1984, 1985	Semi-Ellipsoidal and Double Ellipsoidal	FEM
Kumar and Baduri	1994	Cylindrical Metal Transfer	FEM
Wahab and Painter (with Davies)	1997, (1998)	Measured weld pool geometry used as heat source	Quasi-Steady 2-D and 3-D FEM
Kim and Basu	1998	Gaussian Distribution coupled with electromagnetics, buoyancy, surface tension and drag forces	2-D FDM transient code based on SAMPLE algorithm
Yang and Debroy	1999	Cylindrical metal transfer with turbulent fluid flow and heat transfer	3-D FDM transient, iterative solver
Taylor, Hughes, Strusevich and Pericleous	2002	Gaussian and Double Ellipsoidal heat source coupled with fluid dynamics and elasto-plastic deformation	FVM method using a commercial package, PHYSICA
Deng and Murakawa	2006	Double Ellipsoidal heat source with coupled temperature field and residual stress model	2-D and 3-D FEM using commericial package, ABAQUS
Fan and Kovacevic	2006	Electric Discharge heat source coupled heat and fluid flow with electromagnetic force	3-D FDM Volume of Fluid Method, iterative solver with SIMPLE
Hu and Tsai	2008	Electric Discharge heat source coupled heat, fluid, electromagnetic force, surface tension, plasma arc pressure and sulfur species	3-D FDM Volume of Fluid Method, iterative solver

The trend that can be noticed by the research shown in Table 2-6 is the movement from a generalized spatial distribution to represent the heat source to coupling two separate models that represent the phenomena of arc and drop formation and the transport that occurs in the workpiece.

2.3.6 Temperature Sensing

In order to apply an automatic control process to a system, it is necessary to monitor, sense or measure a process parameter. Gas Metal Arc Welding (GMAW) and Gas Metal Arc Braze Welding (GMABW) have several process variables that lend themselves to monitoring and control. In the formulation of the control problem for this work, the desired process variable to be controlled is the evolution of the temperature field during the welding or braze-welding process. Although challenging to monitor, the temperature field is directly correlated to the size of the heat affected zone and temperature gradients are directly related to the formation of residual stresses. Both of these factors are tied to weld quality. Hence, the ability to monitor and control temperature will allow for the indirect control of weld quality. There are several ways to monitor temperature; they fall into two categories, contact and non-contact.

Contact devices make physical contact with the surface to be measured. These include temperature sensitive crayons or paints that change color when they reach specific temperatures, bi-metal thermometers and thermocouples (Naidu, Ozcelik and

Moore, 2003). Of the contact thermometry methods, the thermocouple provides the most resolution. One of the earliest uses of contact thermometry for use in automatic control was when McCampbell et al. (1965) used a constantan wire that was positioned to move with the heat source and slid across the top surface of an aluminum workpiece. The junction formed between the constantan – aluminum was not used to monitor temperature but to monitor voltage from the output of the thermocouple.

Non-contact temperature measuring devices include infrared (IR) thermometers such as IR pyrometers, thermal imaging devices such as IR cameras, optical pyrometers and light pipe thermometers. Infrared thermometers fall under the category of measurement devices that measure IR radiation that is irradiated from the surface of the material being measured or directly measure irradiated power (Naidu et al., 2003). All objects having a temperature greater than absolute zero will radiate energy, E_r, which is related to the surface temperature by the Stefan-Boltzmann law as:

$$E_r = \varepsilon\sigma T_s^4 \tag{9}$$

The case in Eqn. 9 assumes that the reflected surface radiation is small compared to the emitted radiation in order to get an accurate reading of the surface temperature.

Since these methods of temperature measurement are non-contact, the temperature field of the welded solid is not altered by the measuring device. Other advantages of these methods are that infrared radiation propagates very quickly so the measuring speed of the temperature depends only on the response time of the measurement equipment. For this reason these methods of temperature measurement are well suited to real-time control (Jiluan 2003).

2.3.7 Classical Control

PID control is the most fundamental algorithm used for feedback control. The PID controller has been around since the early 1900's and is considered the classical controller (Åström and Hägglund, 1995). Greater detail of the function of the PID controller will be covered later in Section 5.2. Outlined here is an overview of how PID controllers have been utilized in the automatic control of GMAW.

One of the earliest applications of PID control in a welding process was when McCampbell et al. (1965) described the development of a servo motor control system that used feedback from a hybrid thermocouple to sense the voltage variations occurring in the workpiece during the welding process. In this implementation, the traverse speed of the weld was adjusted to maintain a constant weld penetration. Smartt and Einerson (1993) used a PI controller to control the amount of heat transfer and metal transfer from an electrode to the workpiece for a GMAW process operating in spray transfer mode. In their study, the error signal was the difference between a model-based weld current estimation and the actual measured welding current. From this feedback signal, both the wire feed speed and traverse speed were adjusted to obtain the desired current. Other uses for PID controllers in GMAW were outlined in Naidu et al. (2002). These include a 3-D positional control system for the automatic correction of path trajectory, a control system using an optical sensor for groove geometry measurements in front of the weld head, a PID controller to control the cooling rate of a welded specimen and a simple feedback controller for arc length where the process was modeled as a first order system; wire feed rate was the input and arc length was the controlled process variable.

Despite newer controllers that have been developed, the PID controller is still useful and continues to be used in contemporary control schemes. Wikle, Zee and Chin (1999) developed a control system that uses infrared point sensors to monitor heat exchange at a point and PI controller was used to maintain the net heat exchange by varying the welding current. Ngo, Duy, Phuong, Kim and Kim (2006) developed a digital GMAW control system that controls the wire feed unit and GMAW power source separately. In this work a proportional controller is used to control the power supply.

PID controllers have been used to some degree in welding control for over forty years. Their robustness and wide range applicability suits them for use in any process in which a process variable is driven to a set-point value. For these reasons, PID controllers will be considered in this work, along with model-based control.

2.4 Welding Copper and Copper Alloys

Copper has several uses throughout a wide variety of industries and is prized for its ability for conducting heat and electricity and for its reactive nature with oxygen. Because of the tendency to react with oxygen, copper of high purity forms copper oxides during welding. The copper oxides migrate toward the grain boundaries and cause copper to lose ductility (Lincoln 1978). In addition, the absorption of carbon monoxide and hydrogen at temperatures above 1300^{o}F (704^{o}C) then react with copper oxides to form water vapor and carbon dioxide to cause internal cracking and embrittlement (Lincoln). Another characteristic of copper that makes welding difficult is the naturally high thermal conductivity. When compared to steel, copper has a lower melting point (1980^{o}F (1082^{o}C) (copper) vs. 2775^{o}F (1524^{o}C) (steel)) yet it takes longer to melt a section of copper than an equivalent section of steel. As a result of the high thermal conductivity for copper, the neighboring metal directly adjacent to the welding area conducts away heat so quickly that more energy must be added to the weld area in order for that localized area to reach melting temperature. Additional consideration must be taken of the high coefficient of thermal expansion of copper in comparison to steel. As a result, copper tends to expand more during the heating cycle and contracts more during cool down which accentuates shrinkage and weld-cracking problems that occur during welding (Lincoln). For these reasons, great care must be taken to avoid inferior quality welds with pure copper and high copper alloys.

Copper and copper alloys may be welded with semi-automatic and fully automatic gas metal arc welding (GMAW) processes that utilize solid or stranded bare electrode wire (Dawson, 1973). In terms of shielding gas, Argon is the conventional shielding gas for GMAW processes. There are advantages to mixing argon with either helium or nitrogen but, even at high current densities spray transfer conditions cannot be met in a pure nitrogen or pure helium environment. As a result, up to 50% helium or 30% nitrogen mixtures with argon allow for spray transfer conditions to be met by virtue of the argon gas component. The admixture of nitrogen or helium to argon in the shielding gas allows for higher heat input which results in higher welding speed, deeper penetration, improved weld bead profile and higher deposition quality than are obtained by pure argon alone (Dawson).

The welds for this research are performed on commercial bronze (CuZn 90/10 %wt) in an effort to mimic the thermal behavior of beryllium. Although not typically welded, commercial bronze falls into the category of red brass which contains copper content greater than 83%wt (Dawson). Because of this, a good reference point for welding commercial bronze may be found in the recommendations for welding red brass or other higher copper content alloys such as Muntz Metal (CuZn 60/40% wt). Shown in the tables below are recommendations for welding copper and various copper alloys compiled from several sources.

Table 2-7: Recommended preheat temperatures and electrode types for copper alloys (Lincoln, 1978)

	Red Brass	**Muntz Metal**
copper	85%	60%
zinc	15%	40%
Electrode Type	ECuSn-C for best color match, ECuSi for best operation	ECuAl-A2 for strength, ECuSi for best operation
Preheat	400°F for 1/4" thickness	Not required

Table 2-8: Recommended preheat temperatures for copper and cupro-nickel (Dawson, 1973)

Copper	**Cupro-Nickel**
400°C for 6mm thickness and 1.6 mm wire	150°C for 6mm thickness and 1.6 mm wire

Table 2-9: Recommended preheat temperatures for copper and copper alloys (Davies, 1977)

Copper	**Copper Alloys**
400°C – 700°C depending on thickness	150°C

Table 2-10: Recommended preheat temperatures for copper and low zinc brass (Kearns and Weisman, 1978)

Copper	**Low Zinc Brass**
200° F for 1/4" thickness and 0.062" dia wire	200°F to 600°F

Typical welding operation for copper and copper alloys is direct current, reverse polarity with right-hand weld technique preferable (Dawson, 1973; Lincoln, 1978). For joint preparation, wider root openings and groove angles are required. When dealing with red brasses, a mixture of helium and argon is the preferred gas (Dawson) with ECuSn-C electrode with a preheat temperature of 400°F when welding a plate of 3/16” thickness or greater (Lincoln). When dealing with heavier plates, specifications typically call for an included angle of 70° when using ECuSn-C and 60° when using ECuSi wire (Lincoln).

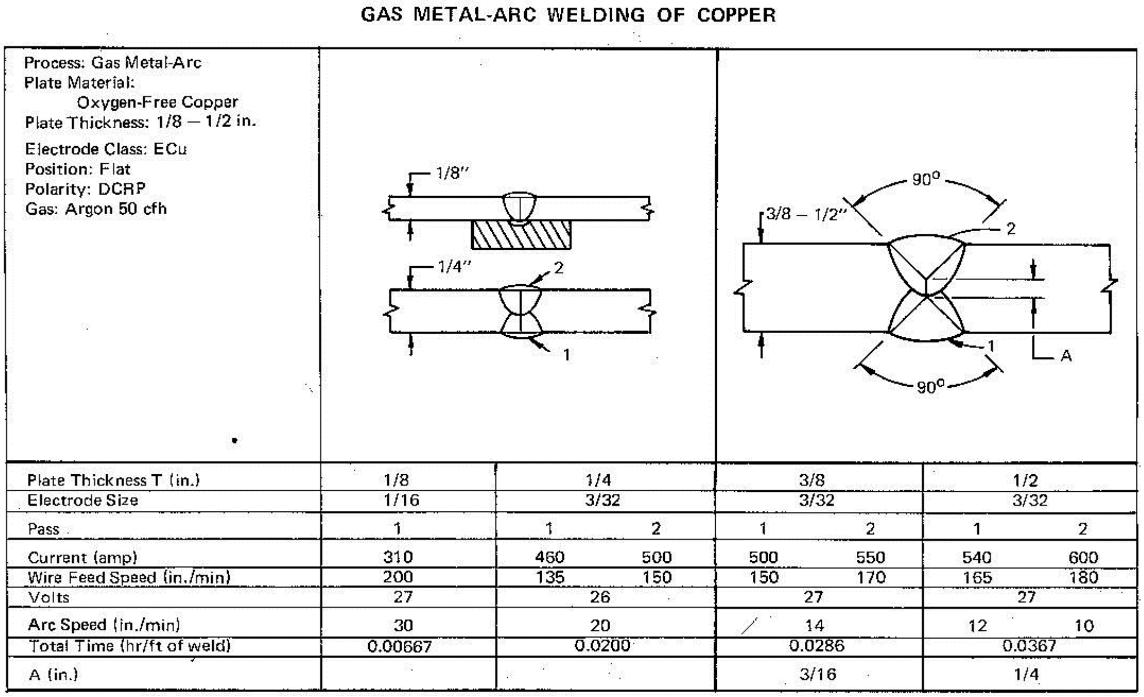
GAS METAL-ARC WELDING OF COPPER

Process: Gas Metal-Arc
Plate Material:
Oxygen-Free Copper
Plate Thickness: 1/8 — 1/2 in.
Electrode Class: ECu
Position: Flat
Polarity: DCRP
Gas: Argon 50 cfh

1/8"
1/4"
2
1
3/8 – 1/2"
90°
2
1
A
90°

Plate Thickness T (in.)	1/8	1/4		3/8		1/2	
Electrode Size	1/16	3/32		3/32		3/32	
Pass	1	1	2	1	2	1	2
Current (amp)	310	460	500	500	550	540	600
Wire Feed Speed (in./min)	200	135	150	150	170	165	180
Volts	27	26		27		27	
Arc Speed (in./min)	30	20		14		12	10
Total Time (hr/ft of weld)	0.00667	0.0200		0.0286		0.0367	
A (in.)				3/16		1/4	

Figure 2-4: Recommended edge preparations for GMAW of copper plates (Lincoln, 1978)

2.5 Braze- Welding Copper and Copper Alloys

Outlined in Section 2.3.2 were the differences between gas metal arc welding (GMAW) and gas metal arc braze welding (GMABW). As mentioned in section 2.4, the most appropriate filler metals for welding copper and copper alloys are bronze alloys, ECuSn-C (Phosphor Bronze), ECuSi (Silicon Bronze) and ECuAl-A2 (Aluminum Bronze) (Kearns and Weismann, 1978). Hence, braze welding of copper and copper alloys is sometimes referred to as *bronze welding* because of the employment of bronze filler metals. Procedurally it is the same as braze welding in that the strength and success of the joint depend on the wetting and bonding of the non-melted parent metal with a molten bronze filler metal (Dawson, 1973). From this aspect the bronze weld is more similar to a braze than a weld but retains its likeness to a weld in that the bronze weld is not driven by capillary action but derives its strength from the tensile strength of the filler metal deposited into a joint prepared in similar fashion to a fusion weld (Dawson). In the cases where the bronze filler metal used is of similar composition to the parent metal of the workpiece the resulting weld is a traditional fusion weld instead of a braze weld since melting of the parent metal will occur. Lastly, copper and copper alloys may be readily joined using appropriate filler metals and protective atmospheres (flux or shielding gas). Although copper-phosphorus filler metals are most common for brazing copper and copper alloys, silver based alloys are acceptable and often used as well (Kearns and Weismann). The use of silver based alloys is typically cost prohibitive in comparison to copper alloys. In the following experiments, silver based alloys, Braze 505 and Braze 852 are examined as braze-welding filler metals on CuZn 90/10 %wt to yield a braze-weld with structural integrity.

Outlined in the following sections experiments and results of obtaining good braze welds on CuZn 90/10%wt using silver based braze wires, Braze 505 and Braze 852.

2.6 Experiments on Thermal Surrogate Material with Silver-based Braze

From previous testing, it was determined that commercial bronze (CuZn 90/10%wt) braze-welded with AlSi would not yield a high strength bond between the two metals because of the formation of brittle intermetallic phases. As a result, experiments were performed to obtain quality braze-welds with silver based braze wires, Braze 852 and Braze 505.

2.6.1 Braze 505 on CuZn 90/10%wt Parameter Study

Shown in Table 2-11 are the test parameters used during the experiments to find optimal braze-weld parameters for Braze 505 with CuZn 90/10%wt.

Table 2-11: Test parameters used for study

Trial	Voltage	Feed (mm/s)	Speed (mm/s)	# Passes	Argon Flow Rate	Head Angle	Distance to Work Height
1	24	212 (500 ipm)	6.35 (15 ipm)	1	35 cfh	72 degrees	9.65mm (~0.38”)
2	22	212 (500 ipm)	6.35 (15 ipm)	1	35 cfh	72 degrees	9.65mm (~0.38”)
3	20	212 (500 ipm)	6.35 (15 ipm)	1	35 cfh	72 degrees	9.65mm (~0.38”)
4	18	212 (500 ipm)	6.35 (15 ipm)	1	35 cfh	72 degrees	9.65mm (~0.38”)
5	16	212 (500 ipm)	6.35 (15 ipm)	1	35 cfh	72 degrees	9.65mm (~0.38”)
6	17	212 (500 ipm)	6.35 (15 ipm)	1	35 cfh	72 degrees	9.65mm (~0.38”)
7	18	169 (400 ipm)	5.08 (12 ipm)	1	35 cfh	72 degrees	9.65mm (~0.38”)
8	18	141 (333 ipm)	4.23 (10 ipm)	1	35 cfh	72 degrees	9.65mm (~0.38”)
9	19	141 (333 ipm)	4.23 (10 ipm)	1	35 cfh	72 degrees	9.65mm (~0.38”)

10	19.5	141 (333 ipm)	4.23 (10 ipm)	1	35 cfh	72 degrees	9.65mm (~0.38”)
11	19.5	142 (335 ipm)	4.23 (10 ipm)	1	50 cfh	72 degrees	9.65mm (~0.38”)

After Trial #1 it was observed that the braze wire would vaporize immediately during testing. This led the researchers to explore lower voltages so that the braze wire would not vaporize so readily. This is reflected in Trials #2- #6. Despite the lower voltage, it was observed that the wire seemed to short-circuit on the weld pool. The lower voltage seemed to ameliorate the vaporization problem but not completely resolve it. Vapor formation of the braze wire was still observed. In order to maintain the same amount of material being deposited as in Trial #1 and to also resolve the short circuiting that was observed in Trials #2- #6, lower wire feed rates were explored. These tests are reflected in Trials #7- #10. During these trials, less short circuiting was observed but increased spattering was noted. The spattering observed was reminiscent of welding with an insufficient amount of shielding gas. In order to rule out a shielding gas issue, Trial #11 was run with the perceived best values of voltage and traverse speed and an increased volume of shielding gas.

The outcome of this experiment was that Braze 505 cannot be used in braze-weld capacity. It was determined later that the vapor that was forming during the braze-welding experiments was zinc vapor. Under the high heat input from the arc, the zinc constituents of the braze wire would vaporize and collect on the weld head thus also disrupting the shielding gas flow. The zinc vapor would be problematic in the case of temperature measurement since the zinc vapor collects on the IR pyrometers.

The manufacturer of the Braze 505 informed the research group that the braze wire was most suited to furnace brazing and torch brazing.

2.6.2 Braze-welding CuZn 90/10%wt with Braze 505 and preheated with Propane

Shown in Figure 2-5, Table 2-12, Table 2-13 and Table 2-14 are the schematic and the test parameters used during the braze-welding experiment involving CuZn 90/10%wt using Braze 505 filler wire. Direct application of knowledge gained from previous experiments has led to the current parameters used in this experiment. Specifically, to address the volatilization of the zinc constituents and to aid with the flow of molten filler metal, a lower heat input from the arc and additional preheating of the braze-weld specimen was utilized to alleviate the aforementioned effects.

Table 2-12: Test parameters used for study

Voltage	Feed (mm/s)	Speed (mm/s)	# Passes	Root Gap (mm)
16	142 (335 ipm)	3.39 (8 ipm)	1	1.59 (.0625”)

Table 2-13: Thermocouple placement for braze-weld with preheat study

	x (mm)	y (mm)
TC 1	38 (~1.5”)	25.4 (1”)
TC 2	38 (~1.5”)	25.4 (-1”)

Table 2-14: Torch Parameters

Argon Flow Rate	Head Angle	Distance to Work Height
38 cfh	71 degrees	9.65mm (~0.38”)

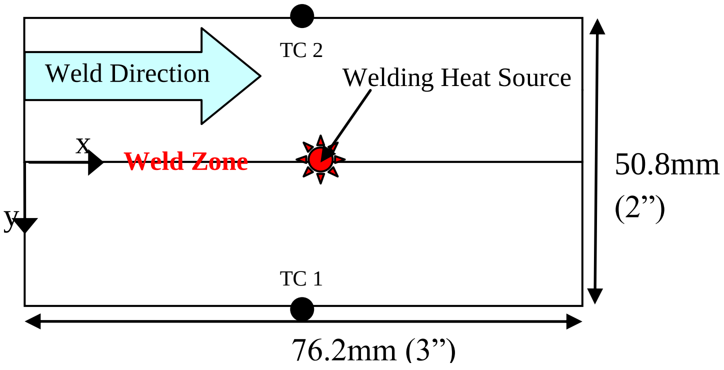

Figure 2-5: Schematic of specimen used during the Braze-welding with Preheat experiment

Procedure

- Specimen was fixtured to the welding test station with C-clamps
- One K-type thermocouple was attached to each side of the specimen as shown in Figure 2-5 at the approximate locations outline in Table 2-9
- While fixtured to the welding test station, the specimen was heated alternately from the top and bottom surface with a propane torch

- As heat was applied to the braze-welding specimen, the temperatures on both sides of the specimen were monitored via a thermocouple reader to ensure even preheating throughout the specimen.
- Specimen was heated to ~350^{o}C and braze-weld of the specimen commenced using the parameters outlined in Table 2-8 and Table 2-10.

Despite the lower voltage (16 V) and slower wire feed rate (142 mm/s (335 ipm)), there was still a fair amount of zinc being volatized during the experiment. The appearance of the weld bead obtained in this experiment was better than the beads obtained during the parameter study (Section 2.6.1). During this experiment not enough of the molten braze metal filled the 1.59 mm (1/16”) root gap which ultimately led to poor adhesion between the Braze 505 and the CuZn 90/10%wt base metal.

What was learned by this experiment was that Braze 505 is not a good filler wire candidate for a braze-welding application. Even though the heat input was nearly at its lowest setting, the zinc constituents of the braze wire still volatilized and the lower heat input even with preheating was not enough to get good adhesion between the filler metal and base metal. In future experiments, Braze 852 with CuZn 90/10%wt was used for braze welding as Braze 852 does not have the same zinc volatilization problem that Braze 505 has. In addition, the higher melting point of Braze 852 will aid in filler metal/ base metal adhesion.

2.6.3 **Braze 852 on CuZn 90/10%wt Parameter Study**

Shown in Table 2-15 are the parameters used for the experiments to explore additional heat input into braze welds with CuZn 90/10 %wt and Braze 852. Trial 1 was welded using promising parameters from previous experiments. Trials 2-4 were conducted by manually altering the wire feed rate throughout the experiment to alleviate short circuit transfer. Trial 5 experimented with altering the voltage during the experiment and produced potentially promising results at a higher voltage. Based on these results, trial 6 implemented this higher voltage and initially performed well, but the additional heat input melted the welding tip. Trial 7 (shown below in Figure 2-6) provided promising results with strong adhesion approximately halfway through the experiment after the weld reached approximately steady state temperatures. These results suggest that future experiments will require an increase in heat input; however, applying this heat by increasing voltage in conjunction with lowering the traverse speed appears to be inadequate. From this set of experiments, we concluded that supplemental heat sources will be required.

Table 2-15: Test parameters used for CuZn 90/10%wt and Braze 852 study

Trial	Voltage	Initial Feed (mm/s)	Final Feed (mm/s)	Speed (mm/s)	# Passes	Argon Flow Rate	Head Angle	Distance to Work Height
1	24	141 (334 ipm)	141 (334 ipm)	3.37 (8 ipm)	1	35 cfh	73 degrees	9.65mm (~0.38”)
2	24	212 (500 ipm)	197 (465 ipm)	6.35 (15 ipm)	1	35 cfh	73 degrees	9.65mm (~0.38”)
3	24	199 (470 ipm)	183 (433 ipm)	6.35 (15 ipm)	1	35 cfh	73 degrees	9.65mm (~0.38”)
4	24	191 (450 ipm)	174 (411 ipm)	6.35 (15 ipm)	1	35 cfh	73 degrees	9.65mm (~0.38”)
5	24.5 - 25.4	212 (500 ipm)	212 (500 ipm)	6.35 (15 ipm)	1	35 cfh	73 degrees	9.65mm (~0.38”)
6	25.5	212 (500 ipm)	212 (500 ipm)	6.35 (15 ipm)	1	35 cfh	73 degrees	9.65mm (~0.38”)
7	24	169 (400 ipm)	169 (400 ipm)	5.08 (12 ipm)	1	35 cfh	73 degrees	9.65mm (~0.38”)

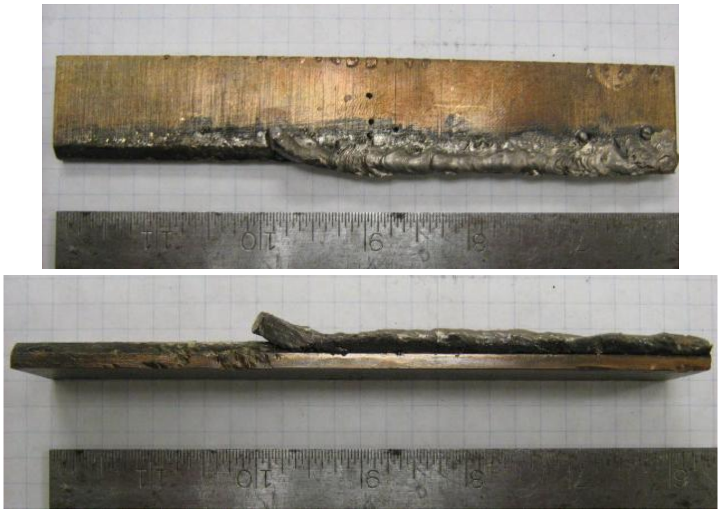

Figure 2-6: Trial 7 from top and side views after attempting to delaminate filler metal

2.6.4 Braze-welding CuZn 90/10%wt with Braze 852 and preheated with Acetylene

From previous testing, we determined that additional heat input could potentially increase the quality of our braze welds. We targeted preheating as a technique for increasing the heat input of the base metal. Shown in Table 2-16 below are the welding parameters used for our experiments with CuZn and Braze 852 with preheating. All of the experiments were performed by preheating the CuZn specimens with an acetylene torch to approximately 500° C according to thermocouples welded to the sides of the specimens. The specimens were transported to the welding test station, and we began the welds when the thermocouples cooled to approximately 400° C. Trials 1-5 were conducted on two 152.4 mm x 25.4 mm x 6.35 mm (6”x1”x0.25”) CuZn specimens. Trials 6 and 7 were performed on two 152.4 mm x 25.4 mm x 3.13 mm (6”x1”x0.125”) CuZn 90/10 %wt specimens. Modified boron flux and a root face gap of 1.59 mm (1/16”) were used on all trials.

Table 2-16: Test parameters used for CuZn and Braze 852 with preheating study

Trial	Voltage	Feed (mm/s)	Speed (mm/s)	Thickness (mm)	# Passes	Argon Flow Rate	Head Angle	Distance to Work Height
1	24	142 (335 ipm)	4.23 (10 ipm)	6.35 (0.25”)	1	36 cfh	72 degrees	9.65mm (~0.38”)
2	22.5	143 (337 ipm)	4.23 (10 ipm)	6.35 (0.25”)	1	36 cfh	72 degrees	9.65mm (~0.38”)
3	23	143 (337 ipm)	4.23 (10 ipm)	6.35 (0.25”)	1	36 cfh	72 degrees	9.65mm (~0.38”)
4	24	163 (385 ipm)	4.23 (10 ipm)	6.35 (0.25”)	1	36 cfh	72 degrees	9.65mm (~0.38”)
5	23.5	163 (385 ipm)	4.23 (10 ipm)	6.35 (0.25”)	1	37.5 cfh	73.5 degrees	9.65mm (~0.38”)
6	23.5	163 (385 ipm)	4.23 (10 ipm)	3.13 (.0125”)	1	37.5 cfh	73.5 degrees	9.65mm (~0.38”)
7	23.5	245 (578 ipm)	6.35 (15 ipm)	3.13 (.0125”)	1	37.5 cfh	73.5 degrees	9.65mm (~0.38”)

Trial 1 provided excellent adhesion, but the additional heat input melted our welding tip in the middle of the experiment. For Trials 2 and 3, we altered the voltage for trial 1 in an attempt to get an adhesion comparable to trial 1 without melting the welding tip. Neither of these experiments accomplished sufficient penetration, so trial 4 altered the wire feed rate of trial 1 in an attempt to lower the heat input. However, the increase in wire feed rate was not sufficient to prevent melting of the welding tip. Therefore, for trial 5 we decreased the voltage from trial 4 to 23.5 V. These parameters resulted in excellent adhesion without melting the welding tip. Figure 2-7 shows the specimen from trial 5 after being sectioned for metallography.

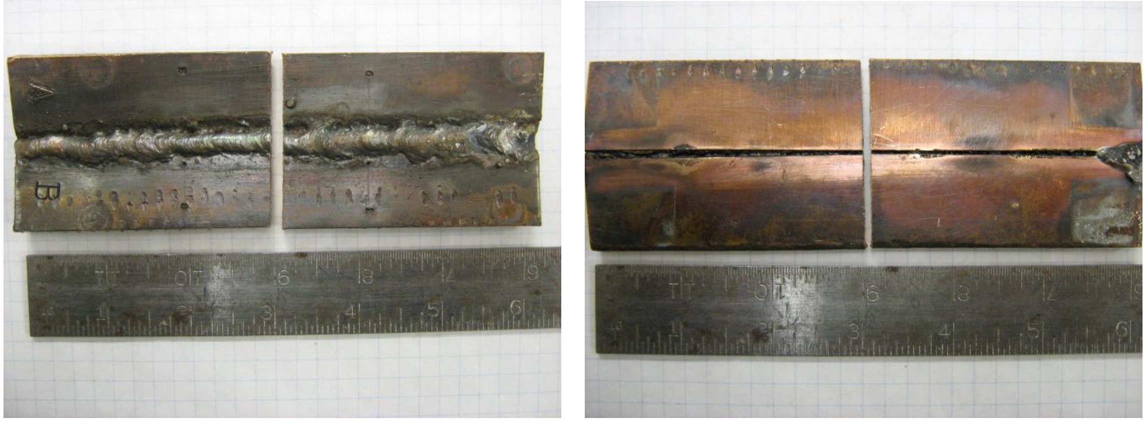

Figure 2-7: Trial 5 from top and bottom views

After achieving an excellent braze weld on the 6.35 mm (0.25”) thick specimens, for trial 6 we decided to test the same parameters on a set of two 3.13 mm (0.125”) thick specimens. The reduction in the thermal mass provided poor results due to excessive melting of the base metal (shown in Figure 2-8). For trial 7, we increased the traverse speed to 6.35 mm/s (15 inches per minute (ipm)) to reduce the heat input and increased our wire feed rate correspondingly to maintain the volume of our filler metal. The reduced heat input led to a noticeable but insufficient reduction in base metal melting (shown in Figure 2-9). Future trials on 3.13 mm (0.125”) thick specimens will need to be conducted with additional increases in traverse speed.

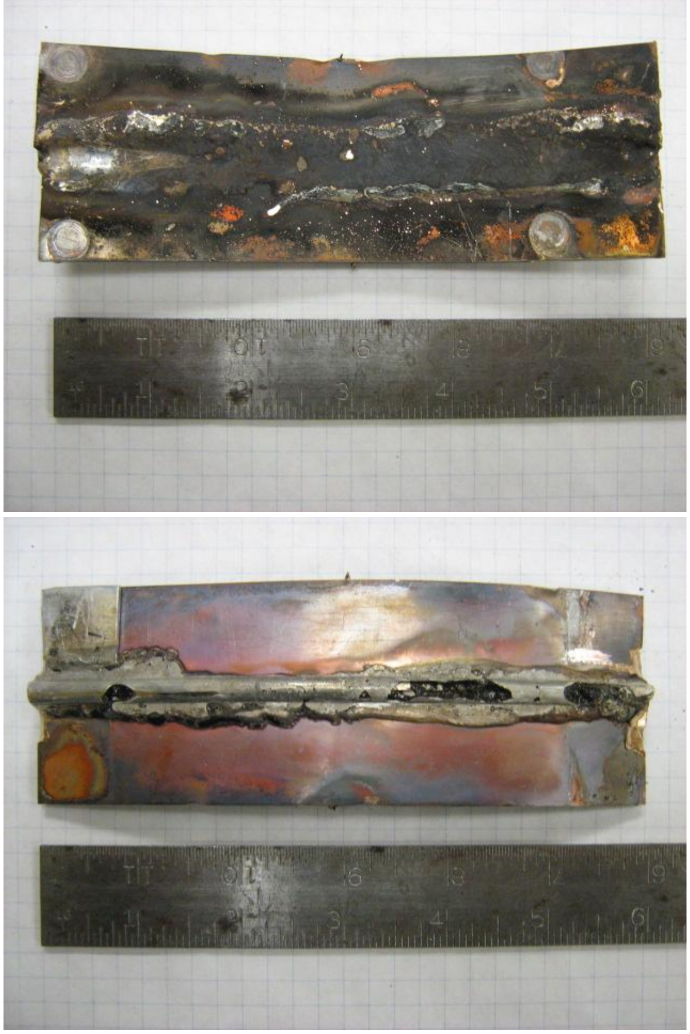

Figure 2-8: Trial 6 from top and bottom views

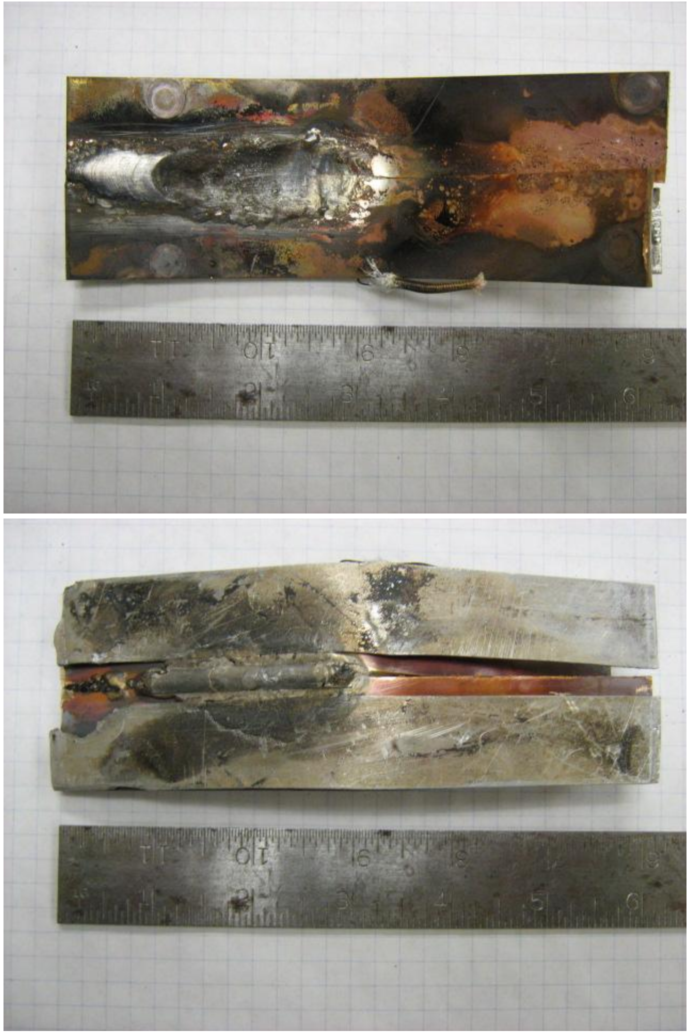

Figure 2-9: Trial 7 from top and bottom views

2.6.5 Universal Braze Welding Parameters

As discussed in Section 2.6.4 braze welding parameters were found that work well on 6.35 mm (1/4 inch) thick material, but the same parameters do not port over well to 3.13 mm (1/8 inch) thick material because of the resulting distortion to the workpiece. Shown in Figure 2-4 are some edge preparations and suggested welding parameters for bonding sections of tough pitch copper (99.99% Copper, oxygen free) (Lincoln, 1978). Although those recommendations serve as a useful heuristic for welding parameters on CuZn 90/10%wt, the braze welding done in this research uses less common filler metals such as AlSi (ER4047) and Braze 852. For this reason, a set of parameters are sought to that is compatible with both thicknesses of metal. Shown in Table 2-17 and Table 2-18 are test parameters that are amenable to both thicknesses of material. These are the test parameters that are used in the testing of the welding controller and reflected in Section 5.5.

Table 2-17: Welding test parameters used in experimental validation

Voltage (V)	Feed (mm/s)	Speed (mm/s)	# Passes	Root Gap (mm)
22	169 (400 ipm)	2.117 (5 ipm)	1	1.59 (0.0625”)

Table 2-18: Torch Parameters

Argon Flow Rate	Head Angle	Distance to Work Height
40 cfh	72 degrees	9.65 mm (~0.38”)

Chapter 3: Experimental Validation of Thermal Models

Discussed in Chapter 3 is the experimental validation of the thermal models to assess their accuracy for use in process modeling and real time control applications. All experiments were performed on a semi-automated welding test station, designed by Peter Backlund of the Seepersad design group (Backlund, 2008; Backlund et al., 2009). Shown in Figure 3-1 is a picture of the test set-up used for the acquisition of temperature data used to validate the thermal models. More details about the design and operating parameters of the welding test station are outlined in Appendix A.

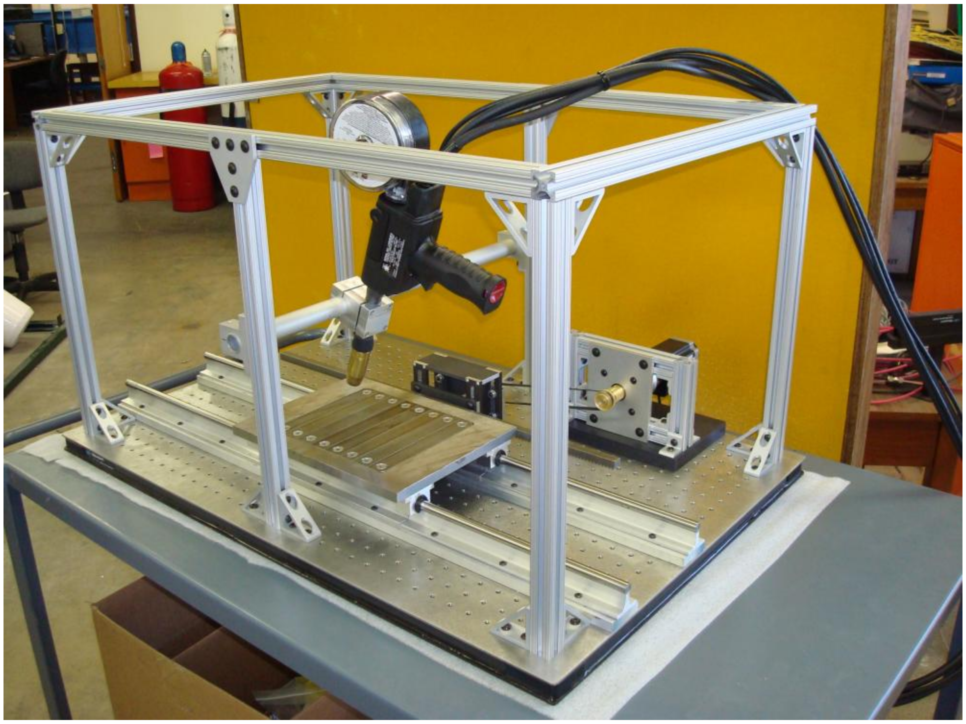

Figure 3-1: Picture of semi-automated welding test station (Backlund, 2008; Backlund et al., 2009)

In the following experiments the weldhead is held stationary and the movement of the workpiece is controlled by a stepper motor controlled by an external computer.

3.1 Models Used in Experimental Comparison

3.1.1 Analytical Model

In this study, a variant of Eqn. 8 is used as the analytical model. In this variant, the solution retains the quasi-steady and point heat source assumptions of the original solution, but the substrate is assumed to be bounded by adiabatic planes oriented parallel to the direction of motion (Rosenthal, 1946). The effective result is a domain of finite width and finite thickness and a temperature profile that is lumped in the thickness direction (i.e., a thin plate assumption). The corresponding solution is:

For $\xi \geq 0$ (locations trailing the weld head)

$$T - T_o = \frac{\dot{Q}}{C_p \rho a g u}\left[\exp\left(-\frac{u\xi}{\alpha}\right) + \sum_1^\infty \frac{2}{\mu_n}\exp\left((-\mu_n + 1)\frac{u\xi}{2\alpha}\right)\cos\frac{\pi n y}{a}\right] \tag{10a}$$

For, $\xi \leq 0$ (locations ahead of the weld head),

$$T - T_o = \frac{\dot{Q}}{C_p \rho a g u}\left[1 + \sum_1^\infty \frac{2}{\mu_n}\exp\left((\mu_n - 1)\frac{u\xi}{2\alpha}\right)\cos\frac{\pi n y}{a}\right] \tag{10b}$$

where

$$\mu_n = \sqrt{1 + \left(\frac{2\alpha\pi n}{ua}\right)} \tag{10c}$$

In Section 3.2.2, this analytical model is used to investigate the sensitivity of temperature to several important variables.

3.1.2 Numerical Models

Two computational models of the weld zone are constructed: a customized finite difference model (FDM) (Rios-Perez, 2009) and a finite volume model constructed in FLUENT® commercial software. Results from these models are compared with experimental data and predictions from the analytical model described previously. Although the primary focus of this work is to compare predictions from Rosenthal's analytical model and computational FLUENT® models with one another and experimental data, a finite difference model is included as an additional point of comparison.

Both computational techniques model a symmetric half of the workpiece by applying an adiabatic wall condition on the *x-z* surface aligned with the path of the welding torch in Figure 2-3. Radiative and convective boundary conditions are applied to exterior surfaces of the substrate, with a convective coefficient of h = 10 W/m^2 and an emissivity of ε = 0.8. The surrounding environment is treated as a non-participating medium with a uniform, steady temperature of 300 K. The energy source is a uniform heat flux distribution (square top hat or box distribution) with square dimensions of 3.18 mm and a total heat input of 2060 W. These values correspond to the dimension of a concentrated arc (Eagar and Tsai, 1983 and Nguyen et al.,1999) obtained during GMABW and the heat input obtained during the GMABW experiments, as described in Sections 3.1.3 and 3.2. Although the shape and distribution of the heat source have an important influence on the temperature distribution and history, as shown by Nguyen et al. (1999), their effects are confined to the area near the weld zone where no experimental data could be obtained for this study. This assumption was confirmed by trying square heat sources of 3.18, 7 and 10 mm in the FDM model. Temperature predictions for the various heat source distributions differed by less than 9% and 5% at 5 mm and 10 mm distances from the center of the torch, respectively. The effects of different heat source shapes were also explored in FLUENT®. At 6.35 mm from the center of the heat source, temperature predictions from conical and uniform cylindrical (top hat) heat flux distributions differed from the prediction of a uniform square distribution by less than 0.32% and 0.37%, respectively. Since the shape of the heat source had little impact on the temperature predictions, the box shaped heat source was used for numerical convenience on a rectangular grid. Experimental validation of the heat source size, shape and distribution would require temperature measurements very near the center of the weld zone.

The thermal properties of the workpiece material were obtained by the commercial testing laboratory TPRL for temperatures ranging from room temperature to 1000°C (Larson and Taylor, 2008). Temperature-dependent material properties were included initially in the FLUENT® model. However, the impact on temperature predictions was insignificant because the governing parameter of thermal diffusivity of the material exhibits very small variations over the temperature range of interest, even though the conductivity and specific heat show significant variation. Accordingly, both models use constant thermal material properties obtained at 550 K, the average temperature for which data is available. Material property values are shown in Table 3-1.

Table 3-1: Material Properties for CuZn10 (UNS C22000) (Larson and Taylor, 2008)

ρ (kg/m^3)	***k*** **(W/mK)**	**C_p (J/kgK)**	**α (m^2/s)**
7735	179.68	413.3	5.62E-05

Finite Difference Model

The Finite Difference Model (FDM) is based on Eqn. 4b and uses a 2-D, implicit method. Eqn. 4b is simplified by retaining the terms that correspond to a 2-D diffusion process and adding terms that account for radiative and convective losses from the top and bottom surfaces of the workpiece (Rios-Perez, 2009). The details of the numerical model and its derivation are found in Appendix B.

Since the FDM was developed to evaluate the relative importance of the different heat dissipation mechanisms, the radiation term is not linearized in temperature and makes this a non-linear and time dependant problem. The solution of the temperatures for the system of equations for the FDM is conducted by an iteration process using the False Position Method (Chapra and Canale, 1988).

As mentioned before, the FDM assumes the plate is thermally lumped in the z-direction i.e. there is no gradient of temperatures through the thickness of the plate;

therefore, Δz=6.35 mm (¼ inch). A square grid is used (Δx=Δy). This grid can be altered if the temperature gradient in one direction requires higher resolution.

A grid independence study was conducted to analyze the temporal variation of the maximum temperature on the surface of the workpiece. The maximum temperature on the surface of the workpiece was studied because the grid size has its most significant effect on the maximum temperature. In the *z*-direction in Figure 2-3, the plate was assumed to be thermally lumped with a grid size equivalent to the thickness of the plate. A square grid was assigned to the *x*- and *y*-directions (Δx=Δy). Three different grid sizes were analyzed: 1.5 mm (0.059 inches), 1 mm (0.039 inches) and 0.7 mm (0.028 inches) for a workpiece with *x*, *y*, and *z* dimensions of 152.4 mm (6 inches), 50.8 mm (2 inches), and 6.35 mm (¼ inch). Other model inputs were the material properties reported in Table 3-1, a heat source of 2060 W, and 6.35 mm/s (¼ inch per second) of traverse speed. The results of a grid convergence study are shown in Figure 3-2 for the three different grid sizes. As shown in the figure, the presence of oscillations in the steady state region of the temperature profile is a result of the time step, grid size and traverse speed. The heat flux was modeled such that a proportional heat flux was applied to an element partially within the heat source domain. Depending on the time step and grid size, the proportion of the element that is partially in the heat zone may change with time, causing a varying heat distribution. To avoid this phenomenon, the time step was chosen based on the grid size and traverse speed such that the weld boundary travels one element per time step. The oscillations in the peak were not completely eliminated, but they were reduced significantly. The relative amplitudes of the oscillations for an energy source overlapping with each element for 38 time steps with Δx=Δy=1.5 mm (0.059 inches), Δx=Δy=1 mm (0.039 inches) and Δx=Δy=0.7 mm (0.028 inches) was 2.5 %, 1 %, and 0.6 %, respectively. Relative amplitudes are calculated by dividing the peak-to-peak amplitude of the oscillation by the maximum temperature of the oscillation on the surface of the workpiece. A relative amplitude less than 3 % was considered acceptable for the current model; therefore, the model proved to be grid independent at Δx=Δy=1.5 mm (0.059 inches).

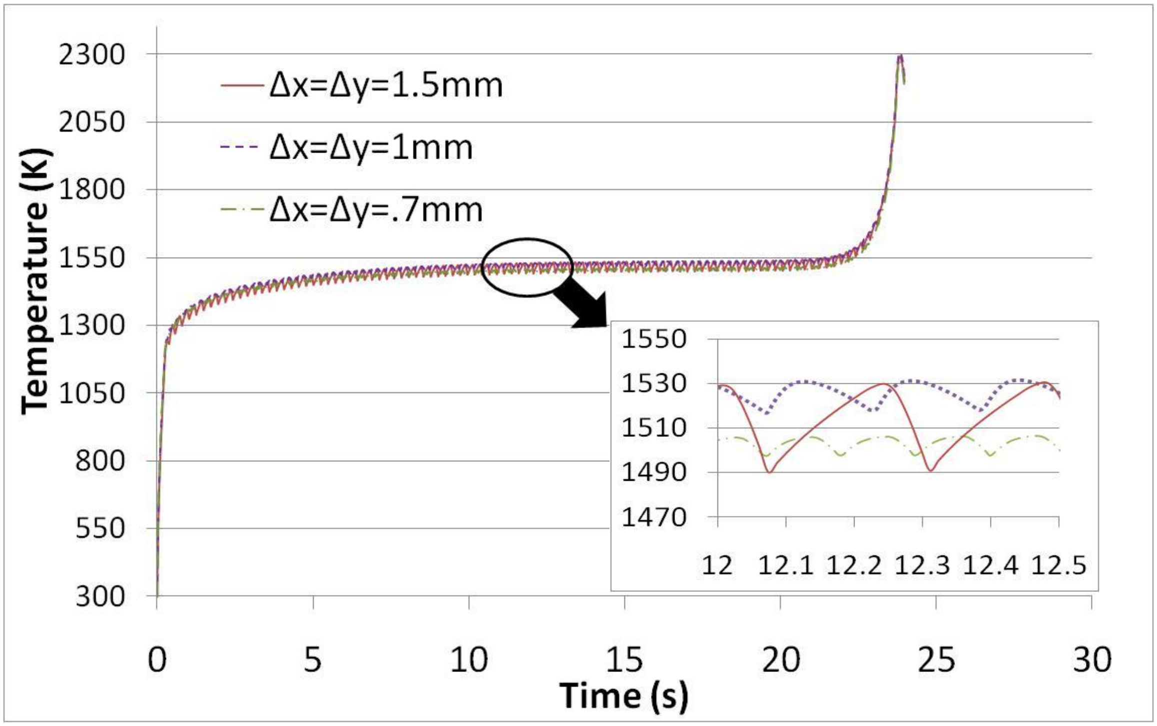

Figure 3-2: FDM maximum temperature

FLUENT® Model

A three dimensional, finite volume model was constructed in FLUENT® software for comparison with the FDM. Three different boundary conditions are specified in the FLUENT® model: (1) a symmetric boundary condition is applied to the *x*-*z* plane directly beneath the weld path; (2) radiative and convective heat fluxes are assigned to the remaining walls, with the emissivity and convective heat coefficient specified previously; and (3) additional heat flux is applied to the weldhead zone on the top surface of the specimen, using a user defined function (UDF).

The specimen geometry was meshed in GAMBIT®, a commercial software package that builds meshes for FLUENT®. To study grid independence, three sizes of cubic meshes were created: 0.635 mm (0.025 inches), 0.318 mm (0.012 inches), and 0.254 mm (0.01 inches). Material properties, applied heat flux, and traverse speed values are identical to those in the FDM study. Since the effect of grid size is most pronounced for the maximum temperature experienced by the workpiece, maximum workpiece temperatures are compared across different grid sizes.

Figure 3-3 displays these time dependent maximum temperatures for each of the three grid sizes. The maximum temperatures predicted by the two larger grid sizes, 0.635 mm (0.025 inches) and 0.318 mm (0.012 inches), differ from the smallest grid size, 0.254 mm (0.01 inches), by an average of 5.6% and 0.8%, respectively, across the time domain. The relatively small difference between the 0.318 mm (0.012 inches) and 0.254 mm (0.01

inches) grid sizes demonstrates that the 0.318 mm (0.012 inches) cubic mesh model is grid independent for the purpose of this study.

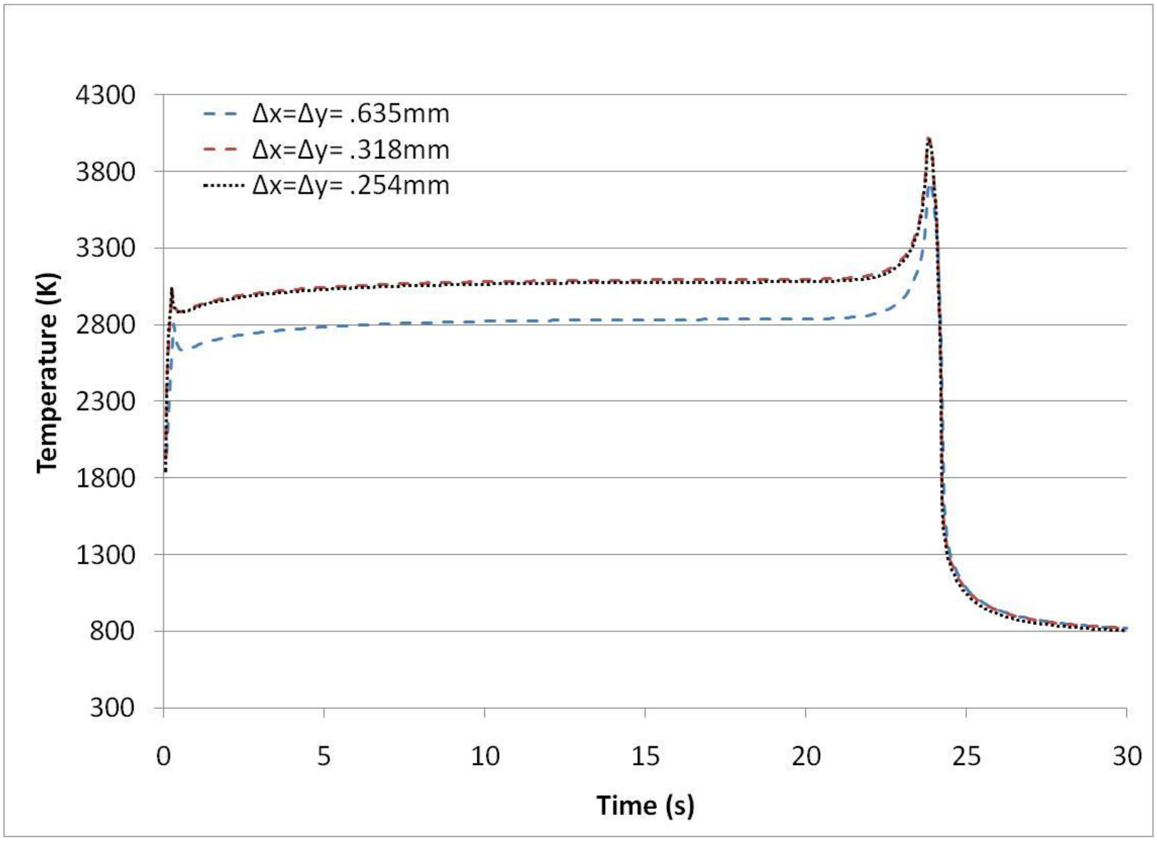

Figure 3-3: FLUENT maximum temperature

Two observations can be made of the maximum temperature plots in

Figure 3-3. Local peak temperatures are observed at 0.25 and 24 seconds. These local maxima are associated with the heat source distribution traveling onto and off of the specimen. As the heat source travels onto the specimen, it delivers a continuously

increasing quantity of heat flux to the specimen, resulting in a rapid temperature increase. Also, at both ends of the specimen, temperature spikes are caused by the reduced volume of material available for conduction. Heat dissipates faster via conduction into surrounding material than via convection and radiation into the surrounding atmosphere.

The accuracy of the lumped thickness assumption applied to the FDM model is analyzed by evaluating the temperature distribution in the *z*-direction from the FLUENT® model. The *z*-direction temperature distribution from FLUENT® is illustrated in Figure 3-4 for a point on the centerline of the specimen with the heat source distribution centered directly above it. As shown in Figure 3-5, the temperature differences between the FDM and FLUENT® models at the top surface are large near the torch. However, these temperature differences are less than 10% when *y* is greater than 5 mm. When the temperature distribution in the *z*-direction of the FLUENT® model is averaged for comparison with the lumped thickness results from the FDM, the temperature distributions are similar, even near the torch, as shown in Figure 3-5.

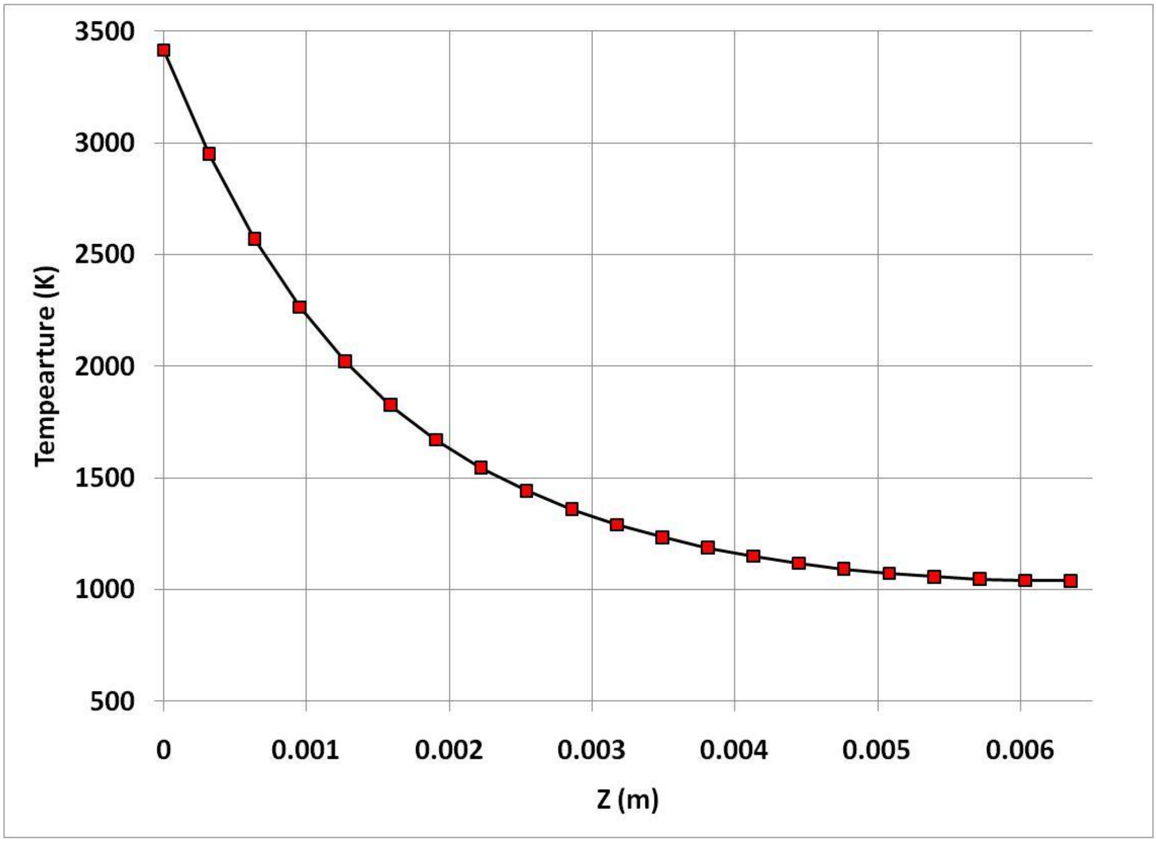

Figure 3-4: Z-direction temperature distribution (FLUENT) for an *x*, *y* point directly beneath the center of the heat source

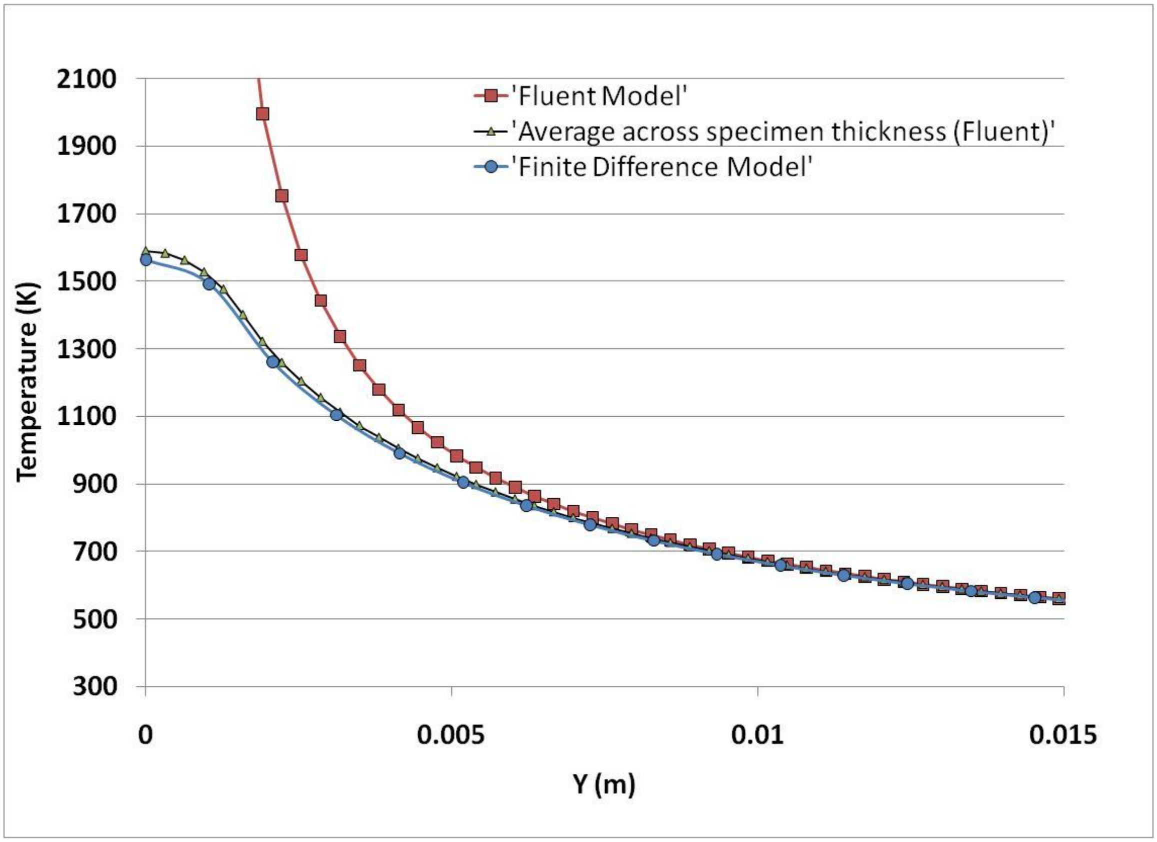

Figure 3-5: Temperature distribution across the width of the top surface

3.1.3 Braze-Welding Experiments

One rectangular piece of commercial bronze measuring 152.4 mm (6 inches) long by 50.8 mm (2 inches) wide by 6.35 mm (1/4 inch) thick was braze-welded by a GMABW process, according to the parameters outlined in Table 3-2. Two 24 gauge K-type thermocouples were mounted to the top surface of the specimen. Two Omega OS554A infrared pyrometers were mounted adjacent to the welding torch and followed a point ±6.35 mm (¼ inches) in the *y*-direction from the weld centerline and 28.9 mm

(1.138 inches) in the negative *x*-direction from the welding heat source. The thermocouple and pyrometer locations are given in Figure 3-6 and Table 3-3. The weld begins at the origin and moves along the positive *x*-direction in Figure 3-6. The welding test specimens are painted with a matte black, high temperature paint in order force the emissivity of the workpiece to aid in the collection of IR pyrometer data. Experimental results are reported in Section 3.2.1.

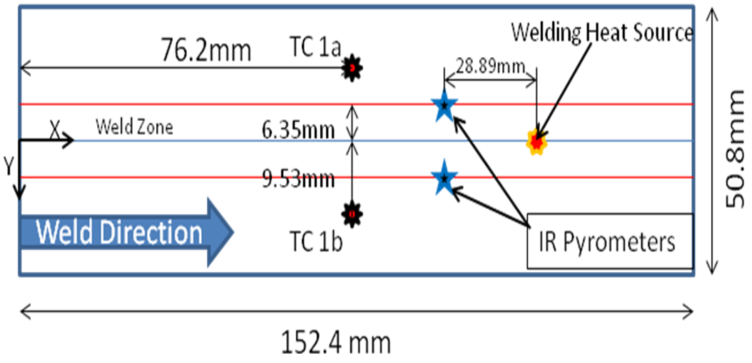
76.2mm
TC 1a
Welding Heat Source
28.89mm
X
Weld Zone
6.35mm
Y
9.53mm
Weld Direction
TC 1b
IR Pyrometers
50.8mm
152.4 mm

Figure 3-6: Schematic of thermocouple (TC) and IR pyrometer layout

Table 3-2: Braze welding test parameters

Voltage (V)	**Wire Feed Rate (mm/s)**	**Traverse Speed (mm/s)**	**Wire Diameter (mm)**
24.0	233	6.35	0.762

Table 3-3: Thermocouple and IR pyrometer placement

	X (mm)	**Y (mm)**		**X (mm)**	**Y (mm)**
TC 1a	76.2	9.53	**TC 1b**	76.2	-9.53
Pyro 1a		6.35	**Pyro 1b**		-6.35

3.2 Validation of Model Predictions

Temperature predictions from the analytical and numerical models were compared with temperature data obtained from the experiments. The results are reported in Section 3.2.1. Deviations between model-based predictions and experimental data may be attributed to both model simplifications and experimental error and uncertainty. Therefore, it is important to quantify the expected magnitude of uncertainty in the data. Of particular interest is the uncertainty in temperature data related to the precision of placement of the thermocouples and pyrometers. With the steep temperature gradients experienced near the weld zone, even a millimeter-scale error in placement could have a significant impact on temperature measurements. In Section 3.2.2, the analytical model is used to quantify the expected placement-induced uncertainty with respect to temperature measurements.

3.2.1 Comparision of Model Prediction with Experimental Data

All models (Rosenthal, FDM and FLUENT®) are used to predict the temperature history at the thermocouple locations documented in Figure 3-6 and Table 3-3. The model-based predictions and corresponding experimental data are illustrated in Figure 3-7 and Figure 3-8. The experimental data are obtained from braze-welds conducted with the parameters outlined in Section 3.1.3. Experimental temperature data are collected on both sides of the braze-welded specimen on the top surface, equidistant from weld centerline. Six sets of data are collected by repeating the experiment. The experimental data shown in Figure 3-7 and Figure 3-8 are averaged values of the six tests at each time step. For the experimental data shown in Figure 3-7 and Figure 3-8, the maximum overall standard deviations of the six sets of data were 0.72 K and 2.11 K, respectively, thereby quantifying a high level of repeatability for the physical experiments.

The rate of heat input for the computational models is calculated from experimental data. Assuming that the entire piece is lumped, the heat input rate can be estimated with a first law energy balance based on the thermal energy storage of the workpiece as outlined in Eqn. 11:

$$\rho C_p \Psi \frac{dT}{dt} = \dot{Q} \tag{11}$$

In Eqn. 11, the rate of heat input for the welded workpiece, $\dot{Q}$, is estimated by multiplying the thermal capacitance of the metal by the volume of the material, Ψ, and the derivative of temperature with respect to time. The derivative can be calculated as a function of the duration of the weld schedule and the change in the temperature of the workpiece due to the braze-welding process. If the workpiece is assumed to be thermally lumped, then the final temperature of the workpiece is estimated by its plateau temperature immediately after the weld is completed. The plateau temperature refers to the relatively constant temperature of the workpiece in the post-peak region of a plot of thermocouple temperature data over time, as seen in Figure 3-7[1]. The resulting information is used to calculate the rate of heat input as 1976 W for these experiments. Since Eqn. 11 neglects radiative and convective losses to the atmosphere, it slightly underestimates the actual rate of energy input. To correct this bias, FLUENT® models were used to estimate the radiative and convective losses during the welding pass, resulting in a corrected rate of heat input of 2060 W. The calculated rate of heat input is compared to the measured heat input from the voltage and current data to estimate the arc efficiency, η. An efficiency of approximately η=63% was calculated for these experiments. The low arc efficiency would contribute to lower power and heat input and lower temperatures throughout the specimen.

---

[1] The average temperature was chosen at a time that allowed the workpiece to reach a uniform temperature. The time chosen to use for average temperature coincided with the end of the weld schedule (24-25 seconds after arc strike). By this time the developing thermal wave inside the workpiece has finished traversing the workpiece. Thermal gradients at this point are less steep than other times in the weld schedule. This is further supported by IR camera data.

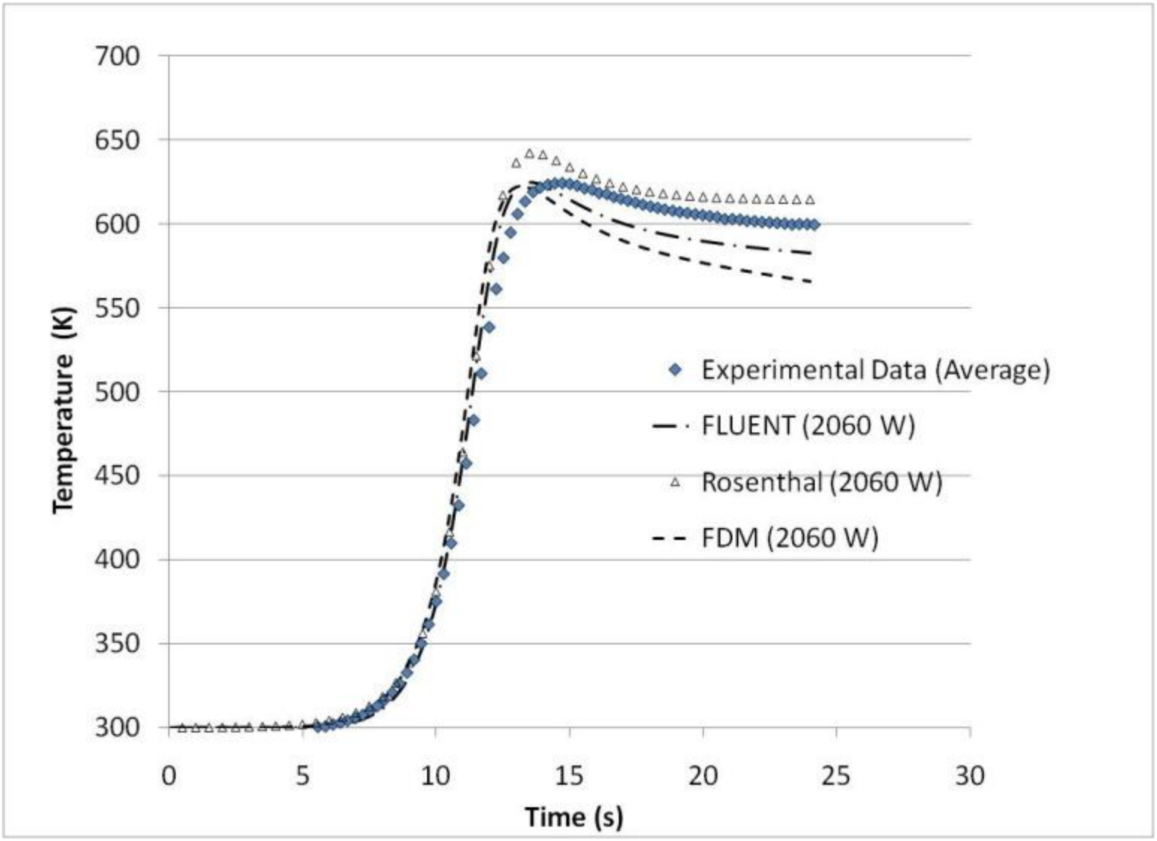

Figure 3-7: Plot of Temperature vs. Time for models and experimental thermocouple data

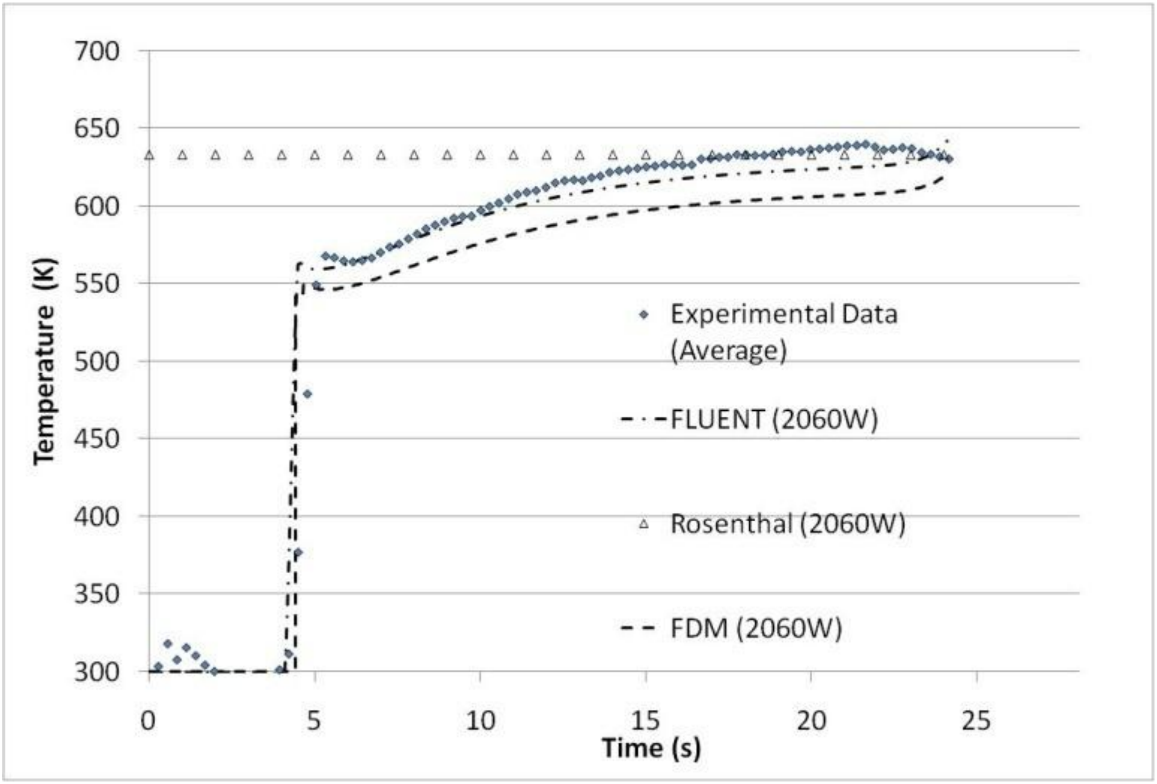

Figure 3-8: Plot of Temperature vs. Time for models and experimental pyrometer data

As shown in Figure 3-7, the FLUENT® model, Rosenthal model and FDM model predictions are in close agreement with one another and the experimental data until their predictions depart near the peak thermocouple temperature.[2] This departure can be explained by the boundary conditions and assumptions placed on each model. In the Rosenthal model, the heat source was modeled as a point source and the physical domain is bounded by adiabatic walls. The consequence is that energy losses from the plate are eliminated, which explains the higher peak temperature for the thermocouple prediction and the higher plateau (temperatures after the peak) temperatures compared with

---

[2] Peak thermocouple temperature refers to the highest local temperature measured by a thermocouple.

FLUENT® and FDM. The FLUENT® and FDM models incorporate radiative and convective boundary conditions. As a result, the tails of the FLUENT® and FDM temperature profiles decrease because of heat losses due to radiation and convection. Conduction losses to the surroundings are minimal since the welding specimen is supported by two thin slats of stainless steel. The top and bottom surfaces are exposed to more of the surroundings (losses via convection and radiation) than the amount of area in contact with the stainless steel slats. The difference in conductivity between the weld specimen and the stainless steel slats is an order of magnitude; hence the conduction losses would be less than the radiative and convective losses. The FLUENT® and FDM models assume a heat source with a spatial distribution instead of a point source. Accordingly, their peak thermocouple temperature predictions are closer to the experimental data than that of Rosenthal, since the energy from the heat source is distributed over a finite area.

Comparing the plateau temperatures of the models with the experimental data shows a maximum disparity of 17 K between the FLUENT® model and the experiment, a disparity of 22 K between Rosenthal and the experimental values and a disparity of 30 K between FDM and experimental values. The disparities in temperature for all three models lie outside of the error range predicted by the sensitivity studies (i.e., +/- 9.7 K) in Section 3.2.2 for the plateau temperature, but the FLUENT® and FDM models better predict the peak thermocouple temperature than the Rosenthal model.

In Figure 3-8, experimental data for the IR pyrometers are compared with the FLUENT®, FDM and Rosenthal models. For the power input of $\dot{Q}$ = 2060 W, both the FLUENT® and FDM models slightly under-predict the measured temperature profile. The Rosenthal model does not capture the trend of the transient experimental data because it is a quasi-steady formulation that does not take into account temperature history (i.e., the effect of the startup transient). The data points in Figure 3-8 fall outside the aforementioned error band of ± 9.7 K for the FDM and Rosenthal models. The FLUENT® data slightly underpredict the experimental data but fall within the error band of ± 9.7 K. The FLUENT® model is expected to be more accurate than the FDM model because the FDM model includes more simplifying assumptions, such as a lumped thickness assumption and an assumption that equal amounts of convective and radiative losses occur on the top and bottom surfaces of the workpiece.

In addition, a study of computational expense was performed to gauge the computation time needed to execute each model. The study was performed on a Dell PowerEdge 2950 with two dual core, hyperthreaded, Intel 3.73 GHz Xeon processors with 16 GB of shared memory, a Linux operating system, and no additional processes running simultaneously. The Rosenthal model required only 5.7 seconds of CPU time for a representative analysis. FLUENT® required 116 minutes, 22.2 seconds of CPU time and the Finite Difference Model required 175 minutes, 39.7 seconds of CPU time for equivalent analyses. These results provide a basis of comparison for the computational resources utilized by each model.

3.2.2 Sensitivity Study

The sensitivity of the temperature evolution with respect to deviations in *x* and *y* placement of the thermocouples are the quantities of interest. The quasi-steady temperature distribution in a welded material by Rosenthal (Eqn. 8) is amenable to direct analytical differentiation and is used for the sensitivity study. Eqns. 12 and 13 are the derivatives of Eqn. 8 with respect to *y* and *x*.

$$\frac{\partial T}{\partial y} = \left(\frac{\dot{Q}y}{4\pi k R^2} \right) \left(\frac{-1}{R} - \frac{u}{2\alpha} \right) \exp\left[\frac{-u(\xi + R)}{2\alpha} \right] \tag{12}$$

$$\frac{\partial T}{\partial x} = \left(\frac{\dot{Q}}{4\pi k R} \right) \left(\frac{-\xi}{R^2} - \frac{u\left(1 + \frac{\xi}{R}\right)}{2\alpha} \right) \exp\left[\frac{-u(\xi + R)}{2\alpha} \right] \tag{13}$$

In the evaluation of Eqns. 12 and 13, the material properties listed in Table 3-1 and the braze-welding parameters in Table 3-2 are employed. Figure 3-9 and Figure 3-10 display plots of the absolute value of the temperature derivative with respect to *y* and *x*.

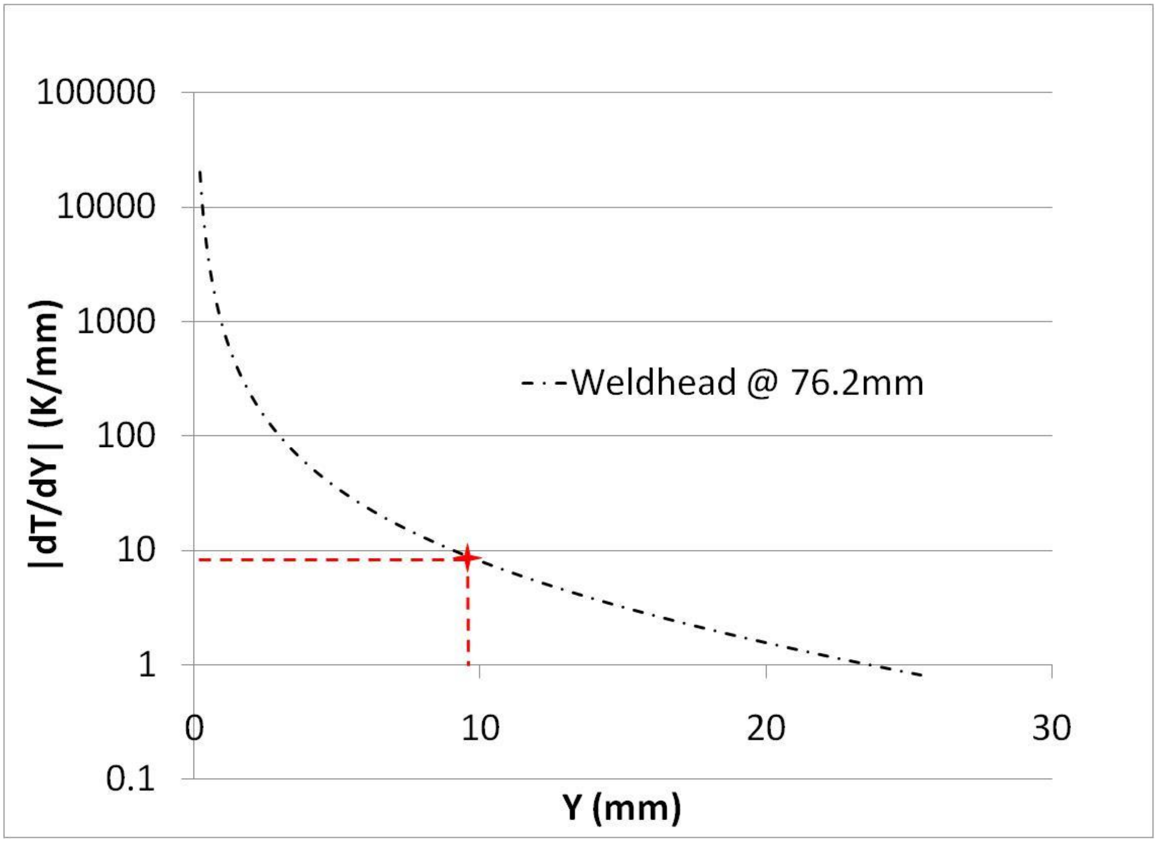

Figure 3-9: $\frac{\partial T}{\partial Y}$ **sensitivity for half of specimen width for** $\dot{Q}$ **=2060 W and** ***X*** **= 76.2mm and all values of** ***Y***

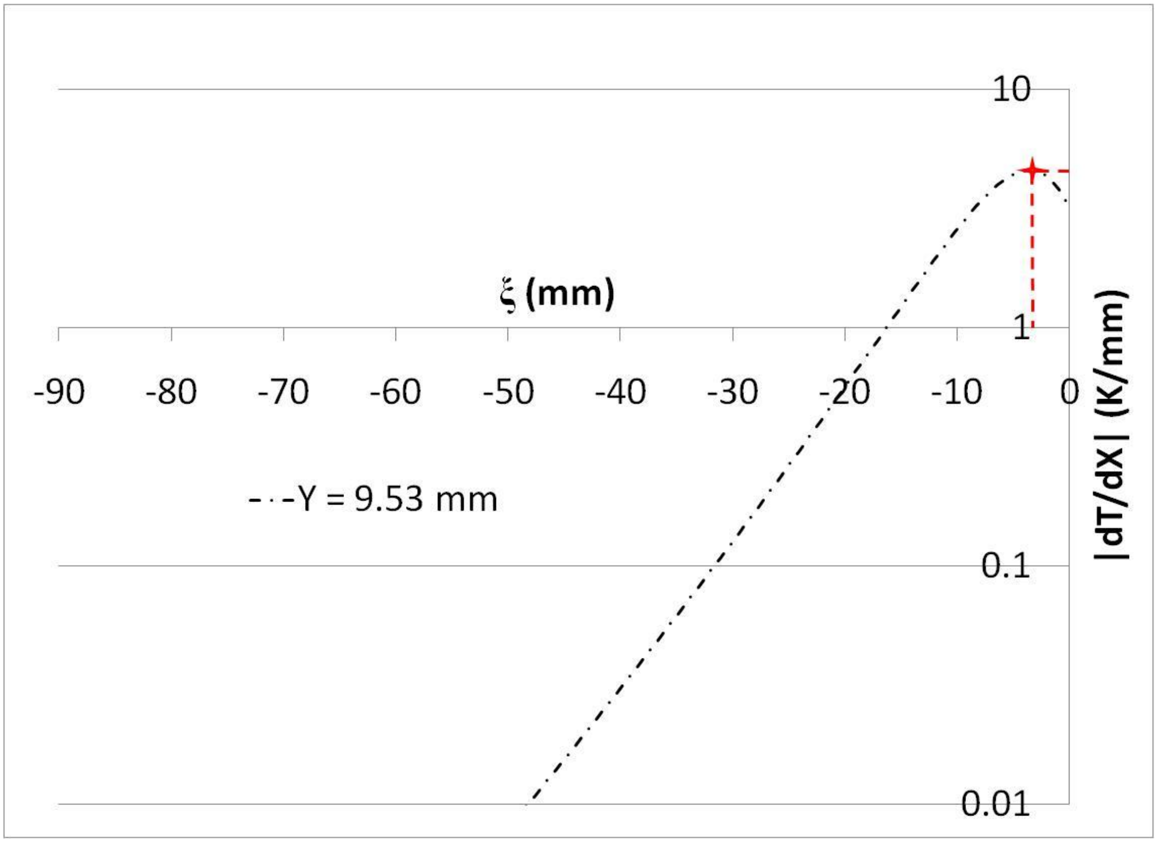

Figure 3-10: $\frac{\partial T}{\partial X}$ **sensitivity for** $\dot{Q}$ **= 2060 W and** ***Y*** **= 9.53mm and all values of** ξ

In Figure 3-9 the partial derivative of the temperature with respect to *y* is plotted for an energy input of $\dot{Q}$ = 2060 W and an *x* coordinate of 76.2 mm (3 inches), in line with the thermocouples in Figure 3-6. The weldhead is assumed to be located at *y* = 0 and *x* = 76.2 mm (3 inches), also in line with the thermocouples. Examining the plot in Figure 3-9, the point that corresponds to the location of the thermocouple on the *y*-axis, *y* = 9.53 mm (3/8 inches), is marked on the plot. The value of the partial derivative of temperature with respect to *y* at the point of the thermocouple location is used to calculate the uncertainty and error introduced by misaligning a thermocouple in the *y*-direction.

In Figure 3-10 the partial derivative of temperature with respect to *x* is plotted for an energy input of $\dot{Q}$ = 2060 W. The weldhead is assumed to be located at x = 76.2 mm (3 inches) (in line with the thermocouple locations illustrated in Figure 3-6). The line plotted in Figure 3-10 corresponds to values of the temperature gradient with respect to *x* for various values of ξ and y = ± 9.53 mm (3/8 inches). The maximum value of the curve marked in Figure 3-10 is used to calculate the uncertainty and error introduced by misaligning a thermocouple in the *x*-direction. The maximum value of the curve is used as it represents the highest deviation from the expected value of temperature and will serve as an estimate of the largest possible error introduced by misplacement of the thermocouples. Using the values marked in Figure 3-9 and Figure 3-10 to calculate the uncertainty in the temperature due to thermocouple misplacement yields a root mean square (RMS) error of ± 9.7 K for a placement error of 1 mm (0.039 inches) in both the *x* and *y* directions.

A study performed to determine the error due to estimation of the heat input found that an error of +/- 10% in the estimation in the heat input would yield a maximum percent difference error of ~5% in absolute temperature for the predictions of thermocouple temperature. In addition, an error in the estimation of the heat source would affect the aforementioned error bound (± 9.7 K) by increasing it. The current calculation of the error bound is based on a conservative estimate of the heat input. Depending on the metal transfer regime of achieved during welding, based on the welding parameters, it is possible that the heat input into the workpiece is higher. A larger source of error would come from the variance in the thermal properties used in the models. A similar study performed with an error of +/- 10% in the thermal properties yielded a maximum error of ~9-12% in absolute temperature for the calculated temperatures at the thermocouple locations.

3.2.3 Student's T-distribution

An alternate way to express the uncertainty in the measured data when the population size is small is to use a Student's T-distribution (Mickley, Sherwood and Reed, 1957; Kreyszig, 1999). This is similar to calculating the confidence interval of a sample population with a known variance, σ^2, but because of the small sample size, the population variance is unknown. In such a case, when you have small sample sizes and unknown variances, σ^2, it is still useful to calculate the confidence interval of the population, μ, in order to see the variance in the population. For instance, if a single set of data contains a finite number of values i.e. $x_1, x_2, x_3 \ldots x_i$ and the sample mean, $\bar{x}_i$, and sample standard deviation, S, have been calculated. When there is a small sample size and the standard deviation of the population, σ, is not available, then the standard deviation of the sample population, S, takes the place of the standard deviation of the population. With this in mind, we to proceed to find values of z for the distribution function of the t-distribution describe by Eqn 14. The difference between this case and one in which the variance is known is that z now depends on the sample size, n (Mickley et al.; Kreyszig).

$$F(z) = K_m \int_{-\infty}^{z} \left(1 + \frac{u^2}{m}\right)^{-(m+1)/2} du \tag{14}$$

Here, m, (=1,2,…..) is called the number of degrees of freedom of the distribution and is typically, m=n-1. The constant K_m is such that $F(\infty)$=1 and by integration, it turns out that

$$K_m = \frac{\Gamma\left(\frac{1}{2}m + \frac{1}{2}\right)}{\sqrt{m\pi}\,\Gamma\left(\frac{1}{2}m\right)}$$ where Γ is the gamma function (Kreyszig)

Calculation of the Student's T-distribution goes as follows

1. Choose the confidence level, $\gamma(95\%, 99\%, \mathit{or\ appropriate})$
2. Determine the solution, c, of the equation

$$F(c) = ½\,(1+\gamma) = F(z) \text{ of Eqn. 14} \tag{15}$$

Solution to this equation may be found in mathematical tables or handbooks as the distribution function of the t-distribution with $m = n - 1$ degrees of freedom (Kreyszig).

3. Compute the mean, $\bar{x}$, and the variance, S^2 ,of the sample population

$$\bar{x} = \frac{1}{n}(x_1 + x_2 + \ldots + x_n) \tag{16}$$

$$S^2 = \frac{1}{n-1}\sum_{j=1}^{n}(x_j - \bar{x})^2 \tag{17}$$

4. Compute $k = \frac{cS}{\sqrt{n}}$ and the confidence interval is then described as (Kreyszig):

$$CONF_{\gamma}(\bar{x} - k \le \mu \le \bar{x} + k) \tag{18}$$

Shown below in Figure 3-11 is a plot of the average experimental data for the IR pyrometers with corresponding confidence interval calculated using the Student's T-distribution with a γ = 95% along with the model predictions from the FLUENT and Rosenthal models. Figure 3-11 is similar to Figure 3-8 with the addition of the confidence interval of the experimental data. The result is the confidence interval with a confidence level of 95% falls in the ±9.7K found by using the Euclidean Norm of the Rosenthal Equation as discussed in Section 3.2.2.

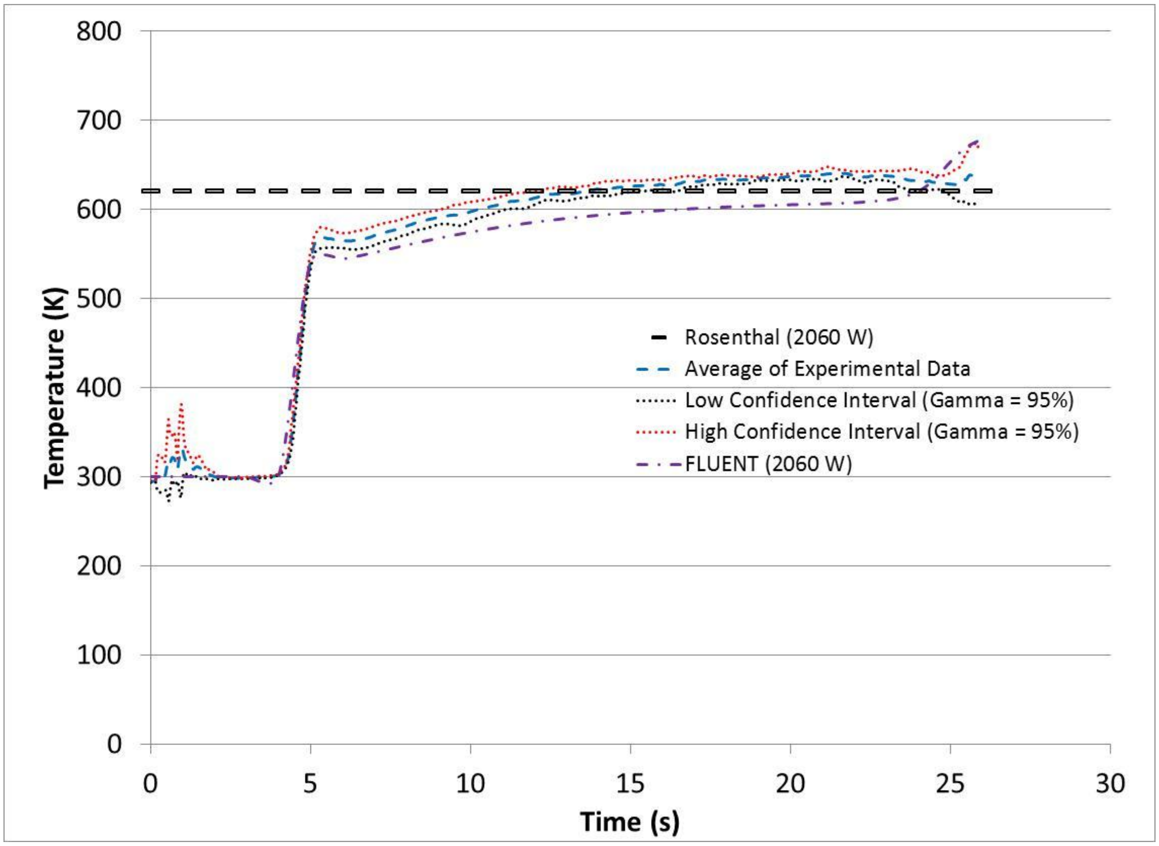

Figure 3-11: Graph of confidence interval of the IR Pyrometer data plotted along with FLUENT and Rosenthal temperature approximations

3.3 Conclusion

This study compared a finite volume method from FLUENT®, a finite difference model, Rosenthal's analytical model and experimental data from the braze-welding of commercial bronze to assess the applicability of each method for predicting the temperature distribution in braze-welding. Experimental data were taken from thermocouples and IR pyrometers and compared with the three models.

The FLUENT® model most closely predicted the temperature profile measured by thermocouples and IR pyrometers. All three models were in agreement for developing thermocouple temperatures, but FLUENT® and FDM models provided more accurate estimates of peak temperatures at thermocouple locations. Rosenthal's model over predicted peak thermocouple temperatures, partially because of the assumption of a point heat source incorporated in the model. The quasi-steady formulation of the Rosenthal model also caused it to agree poorly with the IR pyrometer data. The IR pyrometers travel along with the welding torch and register not only steady state temperatures but also transient start-up and shut-down temperatures. FLUENT® and FDM model predictions agree more closely with IR pyrometer data because they incorporate transient effects. FLUENT® models agreed even more closely than FDM models because they include fewer assumptions about temperature distributions and convective and radiative losses in the specimen.

For real time and predictive process control applications, both accuracy and prediction speed are important. Although the Rosenthal model is much more computationally efficient than the FLUENT® and FDM models, it only provides fair results for steady state temperature predictions. Other methods that take temperature history into account, such as FDM or FLUENT®, are necessary for more accurate steady-state predictions and for any form of non-steady state or transient temperature predictions. Since FDM and FLUENT® models are not computationally efficient enough for real-time control applications, surrogate modeling techniques are implemented for fitting computationally inexpensive metamodels to data obtained from FLUENT® models. Candidate surrogate modeling techniques include: polynomial regression (Simpson, Maurey, Korte and Mistree, 1998), kriging (Simpson et al., 2001), multivariate adaptive regression splines (Friedman, 1991), support vector regression (Vapnik, 1998)). The selection of the most appropriate surrogate modeling technique is typically application dependent, as evidenced by the results of several comparison studies (Simpson et al.; Giunta, Watson and Koehler, 1998; Varadarajan, Chen and Pelka, 2000; Yang, Gu, Liaw, Gearhart, Tho, Liu et al., 2000; Jin, Chen and Simpson, 2001 and Simpson, Poplinski, Koch, and Allen, 2001). Preliminary research has demonstrated the potential of surrogate modeling techniques for predictive process control of braze-welding (Ely and Seepersad, 2009).

Chapter 4: Overview of MetaModels

From the experimental validation of the thermal models outlined in Chapter 3, it was found that although the FLUENT® models were the most accurate in predicting the temperature field measured by the thermocouples and IR pyrometers, the computation time needed to run a FLUENT® model would make it prohibitive to use in real time control. Another option for the rapid calculation of temperature fields is to use metamodels in place of conventional numerical models. In this chapter, an overview of metamodels is presented along with details of specific types of metamodels that are well suited for the modeling temperature field for the expressed purpose of real time monitoring and control for Gas Metal Arc Braze Welding.

4.1 Metamodels

Metamodels are also known as surrogate models or response surface models which are essentially “models of models”. Their purpose is to emulate the behaviors of a model while retaining all the characteristics of that model and being computationally less expensive and less time consuming to evaluate. One field where surrogate models are useful is in full scale development where they take the place of high fidelity models. The metamodels utilize data drawn from high-fidelity models and use constraints and objectives from the physical problem to provide fast approximations. This allows for surrogate model based analysis and optimization to be used in real time (Jones, 2001; Queipo et al., 2005). Shown in Figure 4-1 are the key steps involved in surrogate modeling and are summarized below (Queipo et al.).

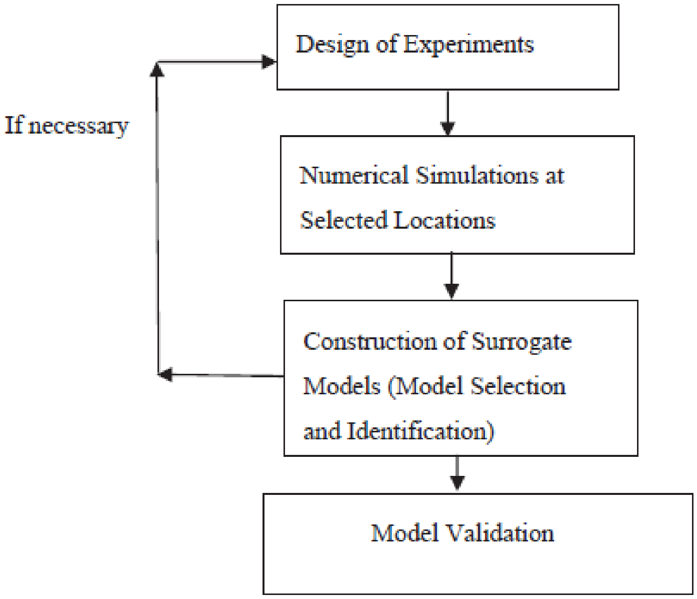
Design of Experiments
If necessary
Numerical Simulations at Selected Locations
Construction of Surrogate Models (Model Selection and Identification)
Model Validation

Figure 4-1: Schematic of key steps in surrogate modeling, taken from (Queipo et al., 2005)

1. *Design of Experiments* (DOE) – The sampling plan in design variable space of the data used to train the metamodel. This in an important step since the number of samples may be limited by the computational expense of the high fidelity model.

2. *Numerical simulations at selected locations* – Based on the DOE, the high fidelity model is run for specific cases to build a database that the surrogate model will use to base its approximations.

3. *Construction of the surrogate model* – In this step the type of surrogate model is chosen (model selection) and the corresponding parameters to be modeled are identified.

4. *Model validation* – This establishes the predictive capabilities of the metamodel without relying on available data (generalization error). This step also helps to determine the margins of operation for the metamodel.

Shown in Figure 4-2 is a schematic of the surrogate modeling problem. In essence, surrogate modeling can be seen as a non-linear inverse problem that aims to determine the continuous function, f, of a set of design variables from a limited amount of data, f_l. (Queipo et al.). The available data, f_l, can be deterministic and can represent the exact function evaluations of function f or noisy observations of function f but in general does not contain enough information to uniquely identify f.

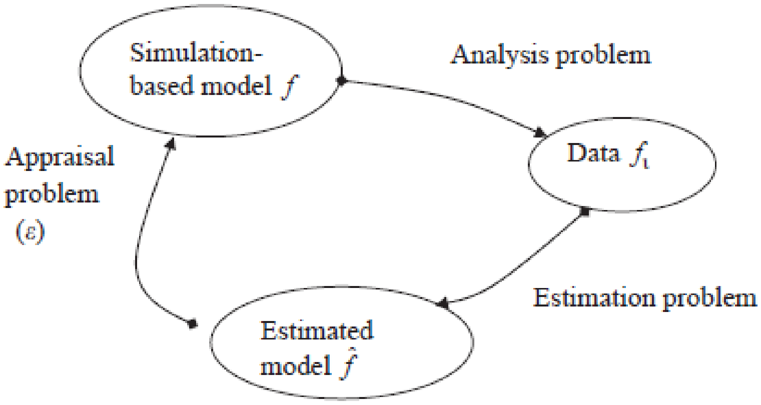
Simulation-based model f
Analysis problem
Data f_1
Appraisal problem (ε)
Estimation problem
Estimated model $\hat{f}$

Figure 4-2: Schematic representation of the surrogate modeling problem, taken from (Queipo et al.)

Hence, surrogate modeling deals with the unique problems of (Queipo et al.):

1. Constructing a model, $\hat{f}$ from the available data, f (model estimation)
2. Assessing the errors, ε attached to the model, $\hat{f}$ (model appraisal)

Using the surrogate modeling approach, the prediction of the simulation- based model output, f_p, is formulated as, $f_p(x) = \hat{f}(x) + \varepsilon(x)$. In other words, prediction of the high fidelity model is based on the surrogate model built from that data and the error attached to that surrogate model. An illustration of a surrogate model prediction and its variance, $V(f_p)$, is shown in Figure 4-3.

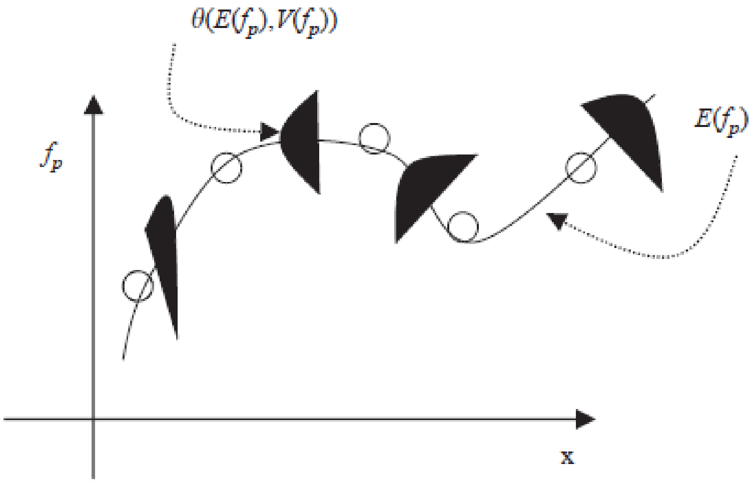

Figure 4-3: Illustration of metamodel prediction and uncertainty, taken from (Queipo et al.)

In Figure 4-3, $E(f_p)$ is the expected value of the metamodel prediction and θ is the probability density function which is a function of the model prediction, $E(f_p)$, and its variance, $V(f_p)$ (Queipo et al.).

The following sections will give a brief overview of surrogate modeling techniques that were found to be suitable for the modeling of Gas Metal Arc Braze Welding. A comparison of several techniques for the purpose of predictive process control of welding applications was reported by Ely and Seepersad (2009).

4.1.1 Support Vector Regression (SVR)

The support vector regression technique models the response with the standard form of ε-SVR (Vapnik, 1998)

$$\hat{y} = \langle w \cdot x \rangle + b \tag{19}$$

where we want to minimize w to ensure a smooth function across our design space. We minimize w with an optimization problem of the form:

$$\text{Minimize} \qquad \frac{1}{2}|w|^2 + C\sum_{i=1}^{l}\xi_i + C\sum_{i=1}^{l}\xi_i^* \tag{20}$$

$$\text{subject to} \qquad \begin{cases} y_i - \langle w \cdot x_i \rangle - b \le \varepsilon + \xi_i \\ \langle w \cdot x_i \rangle + b - y_i \le \varepsilon + \xi_i^* \\ \xi_i, \xi_i^* \ge 0,\ i = 1,2,\ldots,l \end{cases} \tag{21}$$

where x_i's are the independent variables, y_i is the dependent variable, ξ_i and ξ_i^* are slack variables, $C > 0$, ε is some tolerated deviation, and l is the number of samples. Clark *et al.* (2005) establish the merits of support vector regression over polynomial regression, radial basis functions, kriging, and MARS for 26 engineering analysis functions. Based on the average Root Mean Square (RMS) error, average error, and maximum error of the 26 problems, SVR outperformed the other four techniques, with the exception of lower maximum errors associated with kriging. The LIBSVM MATLAB code was utilized for constructing support vector regression models (Chang and Lin, 2001).

4.1.2 Conclusion

Ely and Seepersad (2009) looked at several different types of metamodeling techniques to assess the suitability of the different techniques to model temperature profiles generated during arc welding. The surrogate models were based on several metrics that included: accuracy, time to build the model, time to execute the model, scalability, multimodality and transparency. It was found that SVR and MARS were the two most promising techniques for use in real time control in terms of accuracy and speed. The following chapters provide a discussion on the use of the metamodels in a control framework.

4.2 FLUENT© model assumptions

Shown in Figure 4-4 and Figure 4-5 are the schematics of the geometry of the twelve inch specimen and the pyrometer spot placement as represented in the FLUENT© model. Similar to the model that was discussed in Section 4.1.1 and used in Section 5.3 and Section 5.4, this model differs in that the length of the weld specimen has been doubled to allow for additional studies of controller robustness and metamodel analysis. This specimen geometry was used as the basis for a new metamodel.

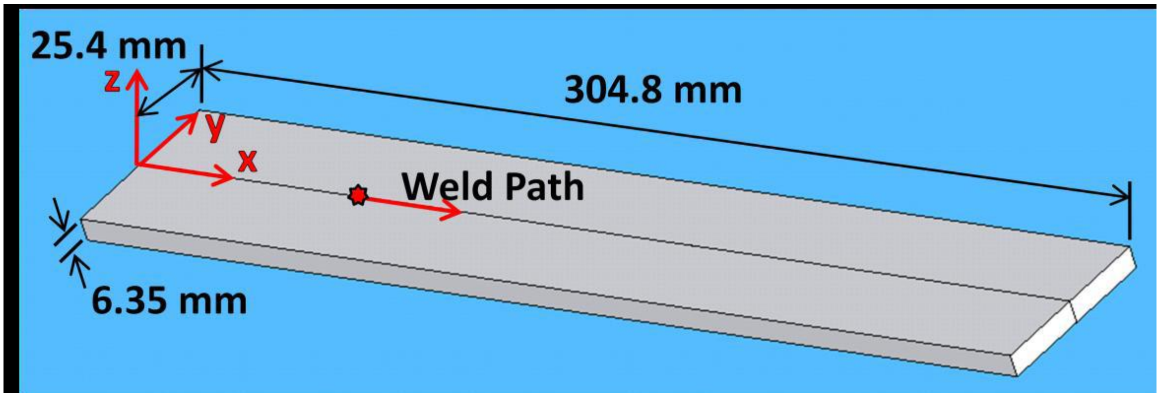
25.4 mm
304.8 mm
z
y
x
Weld Path
6.35 mm

Figure 4-4: Schematic of twelve inch specimen (Ely, 2010)

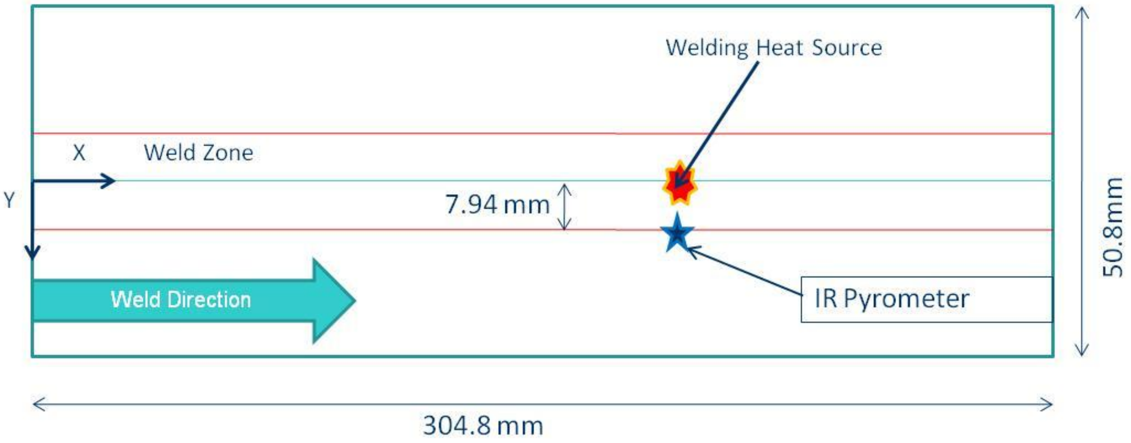
Welding Heat Source
X
Weld Zone
Y
7.94 mm
IR Pyrometer
Weld Direction
50.8mm
304.8 mm

Figure 4-5: Top view of twelve inch weld specimen showing pyrometer placement

The FLUENT$^{©}$ parameters used to compile the training data for the metamodel remained the same as those used in Section 5.3 and Section 5.4. Shown in Table 4-1 and Table 4-2 are the parameters used in FLUENT$^{©}$. Temperature-dependent material properties and boundary condition remained the same with the exception of different heat input range and an adaptive time stepping scheme that ties the time step size to mesh size and the traverse speed. This time step was chosen to coincide with the time it takes for the heat source to move from one mesh node to the next. The effects of heat conduction, convection and radiation are taken into account; the effects of fluid dynamics and electro-magnetism are ignored.

Table 4-1: Temperature dependent thermal properties for commercial bronze (UNS C22000) (Larson and Taylor, 2008)

Material Property	**Temperature Range**	**Equation**
Specific Heat (J/kgK)	296 – 553 K 553 – 593 K 593 – 1237 K	0.0824T + 368 0.272T + 261 0.0631T + 386
Density (kg/m^3)	293 – 1223 K	-0.46234T + 7989.715
Thermal Conductivity (W/mK)	296 – 1273 K	$-0.000129T^2 + 0.249T + 84.5$

Table 4-2: FLUENT© parameters used in twelve inch model

Properties	**Assumptions**
Mesh Size	.318 mm (1/80 inch)
Range of Heat Inputs	1000 to 1500 W
Range of Traverse Speed	2.12 to 12.7 mm/s (5 to 30 inches per min)
Geometry of Heat Flux Distribution	Square
Width of Heat Flux Distribution	3.18 mm (1/8 inch)
Time Step (Adaptive)	(Mesh Size)/(Traverse Speed)
Heat Transfer Coefficient	10 W/m^2K
Free Stream Temperature	300 K
External Emissivity	0.8

External Radiation Temperature	300 K

In the FLUENT$^{\copyright}$ model, the heat source moves across the top surface of the weld specimen in the positive *x*-direction and provides heat input into the work piece that causes the temperature to rise. Temperature data are taken from the FLUENT$^{\copyright}$ simulation that coincides with the pyrometer spot locations that are outlined in Figure 4-5. In order to run a series of FLUENT$^{\copyright}$ simulations that would fully cover the range of traverse speeds and heat inputs outlined in Table 4-2, a Hammersley Sequence is used to chose sets of input parameters that effectively fill the space defined by traverse speed and heat input for the values shown in Table 4-2. The pyrometer temperature data generated from the input parameters specified by the Hammersley Sequence is plotted in Figure 4-6 along with two sets of experimental temperature data for comparison. The experimental temperature data (Q = 1133, V = 0.002117 m/s (5 inches per minute)) falls within the range of heat inputs and traverse speeds of the FLUENT$^{\copyright}$ simulations.

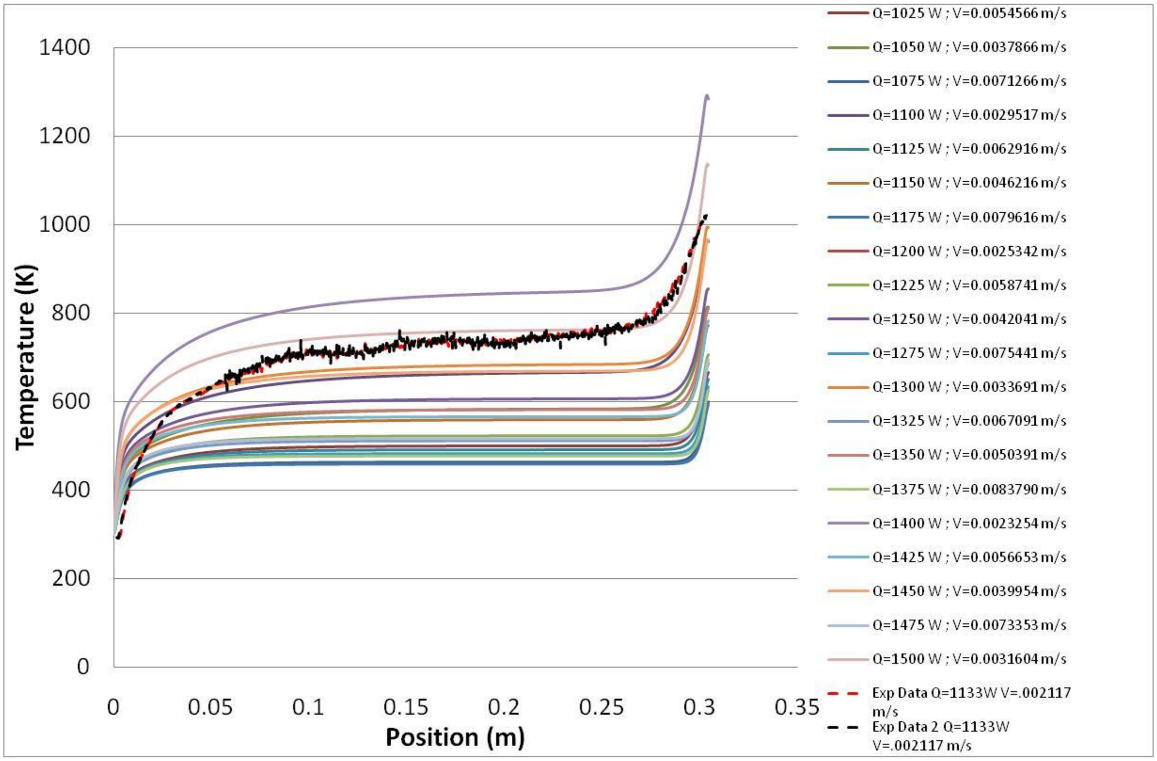

Figure 4-6: Temperature vs. Position of metamodel training data plotted along with experimental data with Q = 1133 W and V =0.002117 m/s (5 inches per minute)

Shown in Figure 4-6 is a comparison of experimental temperature data and the FLUENT© simulation data that makes up the training set of the metamodel. One trend that is apparent from comparison between the experimental data and FLUENT© simulations is that the simulations have good agreement with the experimental data in the steady state regime between 0.05m and 0.25m along the work piece. In contrast to the steady state regime, the initial transients of the metamodels and experimental data do not have good agreement. This can be explained by the difference between the boundary conditions of the FLUENT© model and the actual boundary conditions of the physical system. In the FLUENT$^{©}$ model the work piece is modeled with radiation and convection on all surfaces except for the areas that are directly impacted by the moving heat source. In the real system only the top and sides of the work piece are losing heat to the environment since the work piece actually sits on a large steel platform, this extra conduction path for the heat to escape the work piece is not modeled. In addition, the heat transfer coefficient is modeled with a low value. In reality the argon flow coming out of welding nozzle has a high velocity and is directly impinging on the work piece. These differences may have profound effects on the behavior of the physical system as compared with the model.

Because of the differences between the beginning of weld and end of weld transients in the FLUENT$^{©}$ simulations a metamodel based controller will be used for the steady state region of the weld schedule.

4.2.1 Metamodel Training

Shown in Figure 4-6 is a plot of all the training data and two sets of experiment data for comparison. The training data is used as a basis for training a Support Vector Regression (SVR) metamodel. Previously mentioned, a Hammersley sequence was used to obtain data points that fill the space of heat input, Q and traverse speed, V. Heat input ranged from 1000 to 1500 W and Traverse Speed ranged from 2.12 to 12.7 mm/s (5 to 30 inches per min) as outlined in Table 4-2. The resulting metamodel tabulates temperature as a function of traverse speed, V and heat input, Q, $T = f(V,Q)$. Shown in Table 4-3 are the parameters and options used in training the SVR model using the SVR LIBSVM Matlab code by Chang and Lin (2001).

Table 4-3: Fitting options and parameters used for SVR model

Metamodeling Technique	Fitting Method	Parameter Values
Support Vector Regression (SVR) (Chang and Lin, 2001)	• ε- SVR • Radius Basis Function kernel	• Cost = 10 • γ = 10 • ε = 0.00001 • 480 training points per data set

Chapter 5: Classical Control

In this chapter, the groundwork for incorporating the metamodels explained in Chapter 4 for classical control is described. The sensitivity study performed to determine the pertinent control variable is outlined. The framework for classical control in a discrete sense is discussed along with the studies to determine the controller constants and the methods utilized to deal with measurement noise. The control strategy presented herein employs a Support Vector Regression (SVR) metamodel as the process (plant) model. First, the metamodel is paired with a PID controller and numerical simulations of the welding process are performed to gauge the expected controller outcome and to tune and find the controller constants offline so that material and resources are not wasted while trying to tune the controller online. Once the controller constants are found from numerical methods, the parameters are validated on physical welds performed on the welding test station outlined in Chapter 3 and Appendix A. Lastly, the metamodel is paired with a tuned Proportional (P) controller and used in a novel model predictive controller in which the metamodel chooses the temperature trajectory in the steady state region of the weld and the P controller drives the physical system to adhere to metamodel based trajectory.

5.1 Sensitivity Study

To determine the effect of specific variables and parameters on a property of interest, it is essential to know which variables affect that property most significantly. In the welding process the localized high temperature of the heat source induces residual stresses and distortions. These distortions are undesirable and typically have negative effects on the structural performance. For these reasons it is important to know which welding parameters affect the temperature the most.

The easiest way to determine sensitivity is to begin with an analytical expression for the property of interest. For the physics-based control system for GMAW, the property of interest is the temperature evolution in the welded base metal. A simple analytical expression for the quasi-steady temperature distribution in a welded material is given by Rosenthal (1946) and is presented in Eqn. 8. The simplicity of this equation makes it amenable to direct analytical differentiation. The sensitivity of temperature can be determined by taking the first derivative with respect to various welding parameters and with respect to various thermo-physical properties. By examining the plots of these derivatives, the parameter that affects temperature most significantly can be identified. The partial derivative that shows the highest degree of sensitivity has the most significant effect on the change in temperature. Equations 22 – 27 are the derivatives of Eqn. 8 with respect to specific variables that appear in the equation. It is assumed that each parameter is independent of the others.

$$\frac{\partial T}{\partial Q} = \frac{\exp\left[\frac{-C_p V\rho(R+\xi)}{2k}\right]}{4\pi R} \tag{22}$$

$$\frac{\partial T}{\partial k} = \frac{C_p Q V\rho \exp\left[\frac{-C_p V\rho(R+\xi)}{2k}\right](R+\xi)}{8\pi R k^2} \tag{23}$$

$$\frac{\partial T}{\partial V} = \frac{-C_p Q\rho \exp\left[\frac{-C_p V\rho(R+\xi)}{2k}\right](R+\xi)}{8\pi R k} \tag{24}$$

$$\frac{\partial T}{\partial \rho} = \frac{-C_p Q V \exp\left[\frac{-C_p V\rho(R+\xi)}{2k}\right](R+\xi)}{8\pi R k} \tag{25}$$

$$\frac{\partial T}{\partial C_p} = \frac{-Q V\rho \exp\left[\frac{-C_p V\rho(R+\xi)}{2k}\right](R+\xi)}{8\pi R k} \tag{26}$$

$$\frac{\partial T}{\partial \alpha} = \frac{Q V \exp\left[\frac{-V(R+\xi)}{2\alpha}\right](R+\xi)}{8\pi R \alpha^2 k} \tag{27}$$

As in Eqn. 8, T is temperature; k is thermal conductivity; ρ is density; C_p is specific heat; V is the velocity of the heat source in the x-direction; x, y, z are the Cartesian coordinates of the physical domain of the problem; $\xi = x - vt$ is the reference frame attached to the moving heat source; Q is the heat rate of the point source; and the R is the radius drawn around the heat source where $R = \sqrt{\xi^2 + y^2 + z^2}$. Figure 5-3 is the sensitivity plot of the parameter (velocity) that affects temperature most significantly.

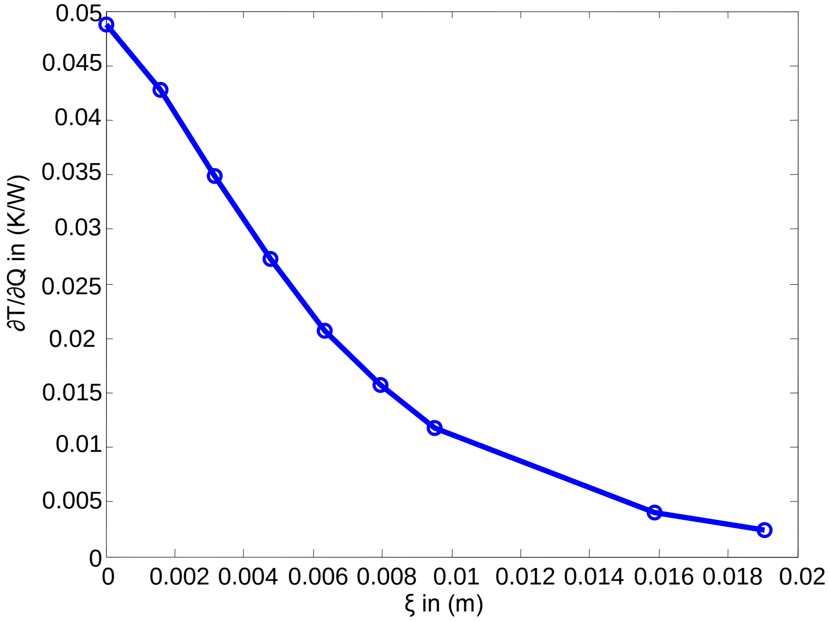

Figure 5-1: $\frac{\partial T}{\partial Q}$ sensitivity for half specimen width for *Q*=2060 W and several values of displacement from the weld head along the *x*-axis, $\xi = x\text{-}vt$

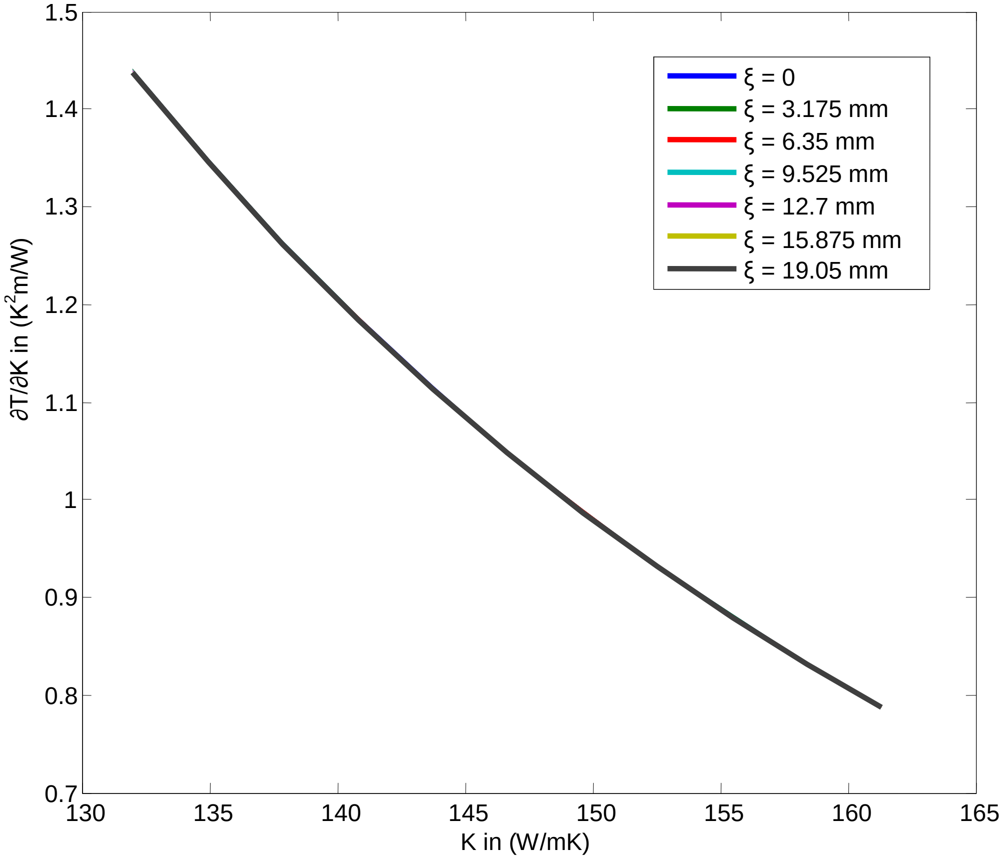

Figure 5-2: $\frac{\partial T}{\partial K}$ **sensitivity for half specimen width for *Q*=2060W for several values of displacement from the weld head along the *x*-axis, *ξ*= *x*-*vt***

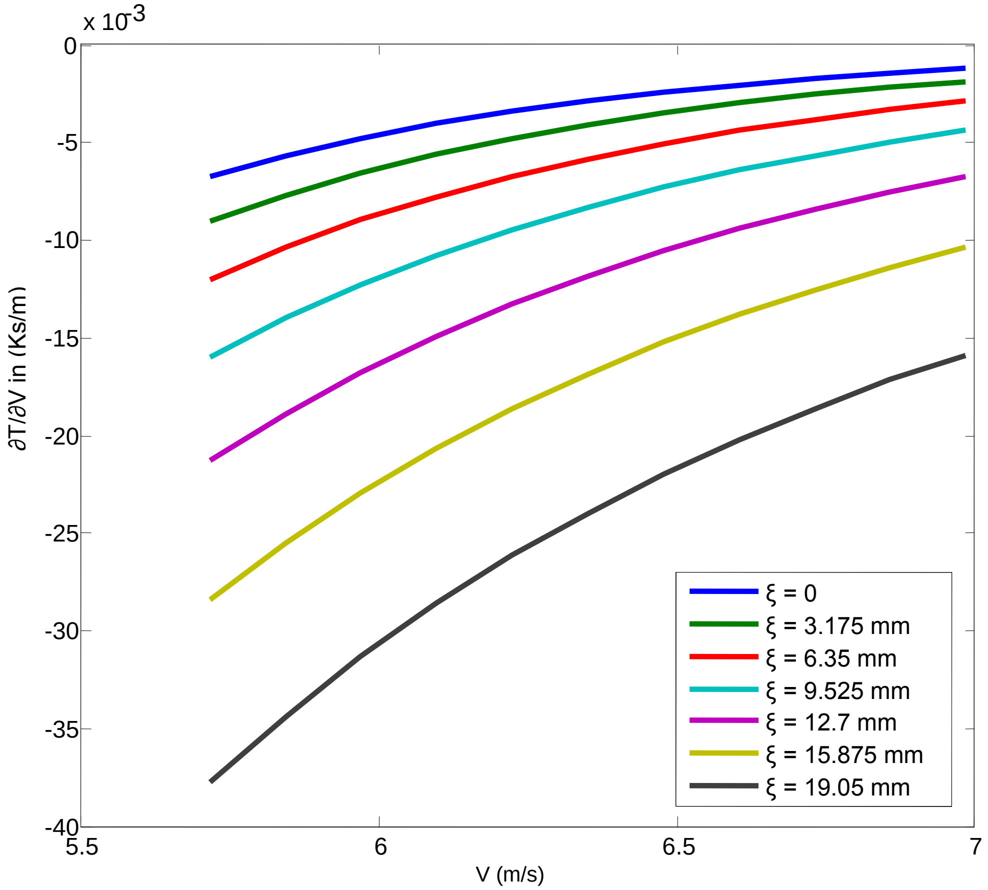

Figure 5-3: $\frac{\partial T}{\partial V}$ sensitivity for half specimen width for *Q*=2060W and several values of displacement from the weld head along the *x*-axis, *ξ*= *x*-*vt*

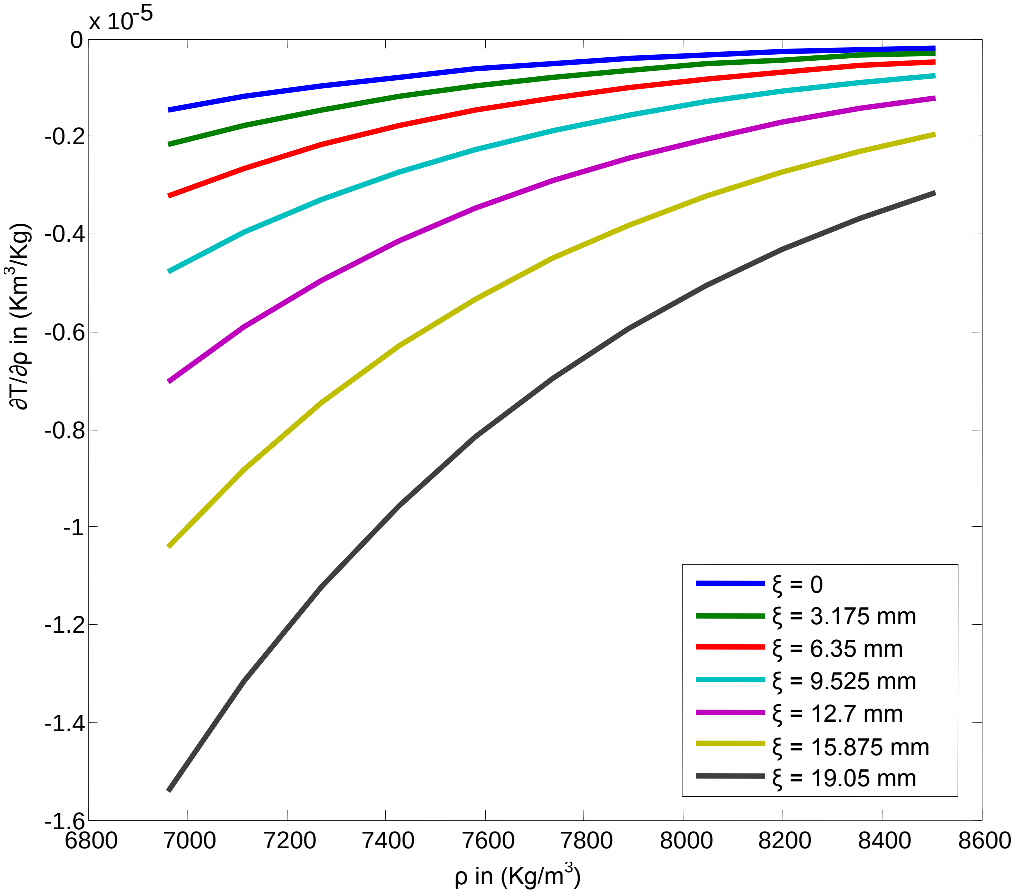

Figure 5-4: $\frac{\partial T}{\partial \rho}$ **sensitivity for half specimen width for *Q*=2060W and several values of displacement from the weld head along the *x*-axis, *ξ*= *x-vt***

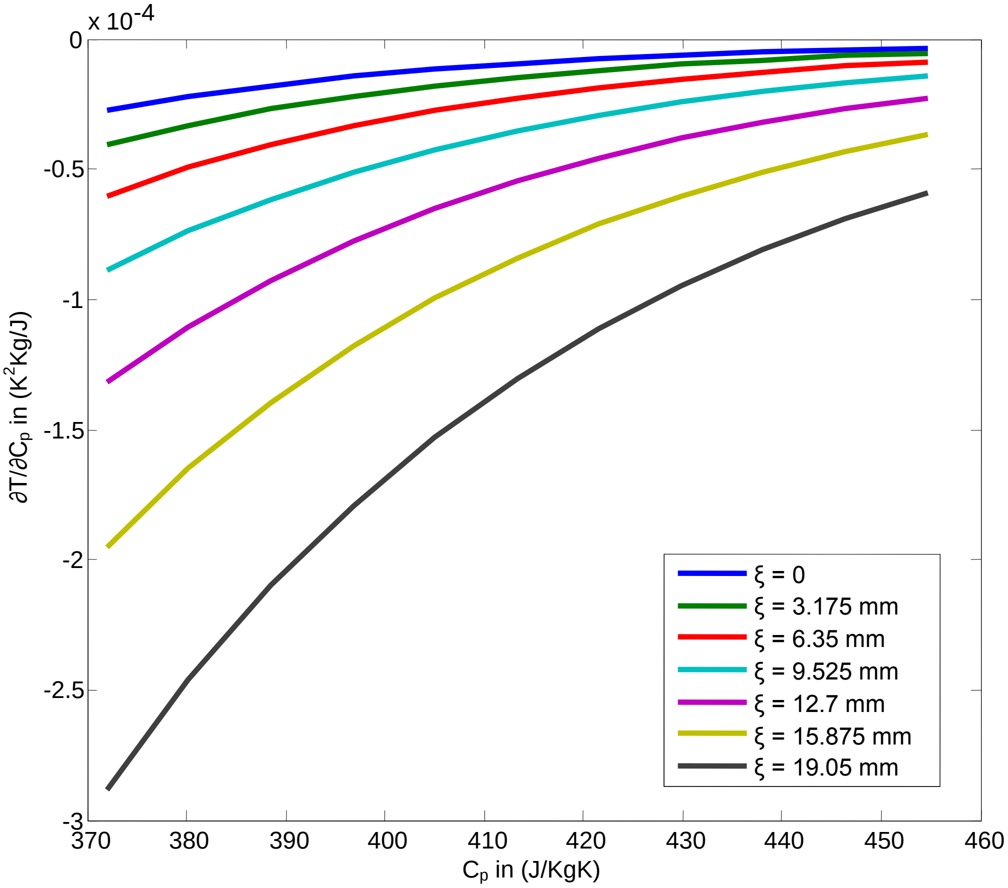

Figure 5-5: $\frac{\partial T}{\partial C_p}$ **sensitivity for half specimen width for** Q **= 2060W and several values of displacement from the weld head along the** x**-axis,** $\xi = x\text{-}vt$

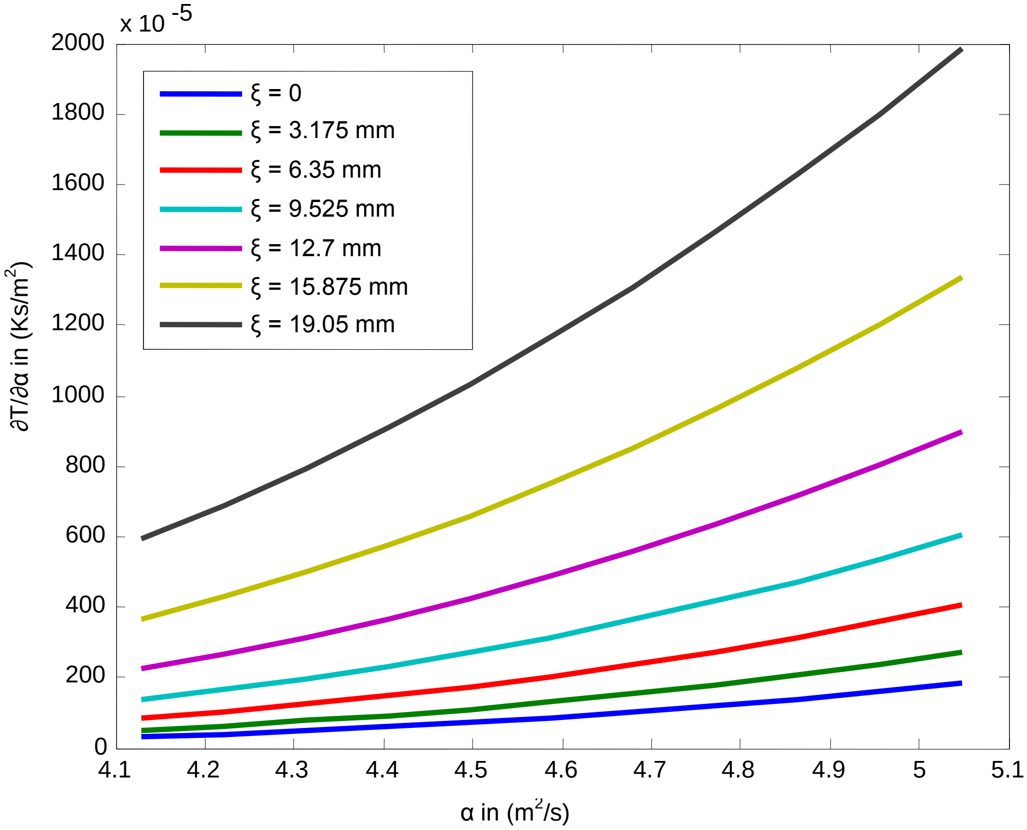

Figure 5-6: $\frac{\partial T}{\partial \alpha}$ sensitivity for half specimen width for *Q*=2060W and several values of displacement from the weld head along the *x*-axis, $\xi = x - vt$

Figure 5-3 is a graph of temperature sensitivity versus velocity of the weld head. All data are based on a steady state temperature profile (Rosenthal Equation) where the weld head is positioned 76.2 mm (3”) into a 152.4 mm (6”) workpiece. This plot is generated from Eqn 19 for points located on the welding centerline. The family of lines in Figure 5-3 represents a 19.05 mm (.75”) section of the workpiece that trails the weld head. Each line represents a specific point on the workpiece at a distance ξ (PSI) from the weldhead location on the *x*-axis and y = 9.53 mm (3/8”) from the weld centerline. Depending on the specific point and the velocity of the weld head, the peaks of the gradient occur at different locations and at different magnitudes. Using Equations 22, 23, 25, 26 and 27 to generate plots similar to Figure 5-3 will also yield families of temperature gradient curves that denote the sensitivity of the temperature to various parameters as shown in Figure 5-1 through Figure 5-6. To determine which of the parameters has the greatest effect on temperature, the highest absolute peak value is chosen and is converted into a temperature change. The gradient values from all of the different plots are compared against each other and the one that causes the greatest temperature change is the parameter that affects temperature distribution the most. For the temperature sensitivity in Figure 5-3, the maximum absolute value of the temperature gradient with respect to velocity for $\xi = 0$ is $\frac{\partial T}{\partial V} = 594\left[\frac{K}{m/s}\right]$ = $\frac{\Delta T}{\Delta V} = 594\left[\frac{K}{m/s}\right]$. To convert this value to a difference in temperature, ΔT(K) = 594 *ΔV(m/s), where ΔV is calculated from ±10% of the nominal value for the welding velocity in (m/s). Using this method to calculate temperature change and comparing the maximum values of the gradients, there are two variables that affect temperature more significantly than the others. The two parameters are the thermal diffusivity of the workpiece metal and velocity of the weld head. Since the weld head velocity is a controllable parameter it is chosen as a state variable, and thermal diffusivity is an input value into the controller.

Sensitivity studies are useful in aiding the selection of state variables or determining which variables have the most profound effect on the problem. Depending on the model being used to model the quantity of interest, sensitivity studies may not always encompass underlying implicit variables.

5.2 PID Controllers

One of the goals of this research is to use the physical models and data for real-time fault detection and control of the welding process. Investigation of proper control techniques that are applicable to braze-welding are presented. Control techniques that are appropriate for temperature control are the main focus in order to make full use of the IR temperature sensing devices integrated onto the welding test station. A first attempt to add control action to the welding test station is the use of classical control. The metamodels developed in Chapter 4 are used as the process models to relate velocity to temperature field, and a classic PID controller is used to adjust the traverse speed of the weld head to maintain temperature predicted by the metamodel. A schematic of the control system is shown in Figure 5-7.

Block Diagram of Closed Loop PID Controller

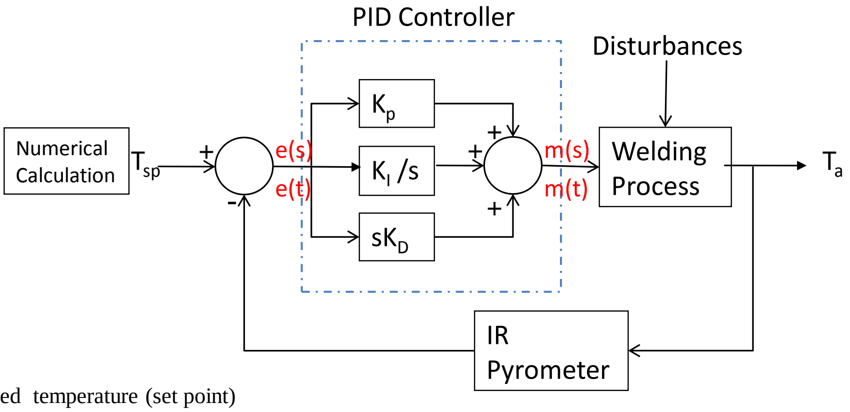
PID Controller
Disturbances
Numerical Calculation
T_{sp}
+
-
e(s)
e(t)
K_p
K_I /s
sK_D
+
+
+
m(s)
m(t)
Welding Process
T_a
IR Pyrometer

T_{sp} – Desired temperature (set point)
T_a – Actual temperature
K_p – Proportional Constant
K_I – Integral Constant
K_D – Derivative Constant
e(s), e(t) – Error Signal
m(s), m(t) – Output Signal of the controller

Controller Gain

$$G_c\ (s) = K_p\ (1+K_I/s+K_d\ s)$$

Figure 5-7: Schematic of PID control scheme for braze-welding

The control scheme shown in Figure 5-7 is the preliminary layout in which the metamodel is used in the control algorithm. In the current studies, the metamodel is used as the “welding process” model whose output will be compared to the desired set point temperature that is chosen by the welding operator. Depending on the error between the metamodel output and the set point temperature, the PID controller will perform the necessary action to reduce the amount of error between the metamodel output and the set point temperature. The following sections will outline the individual components of the PID controller and their function in terms of error reduction.

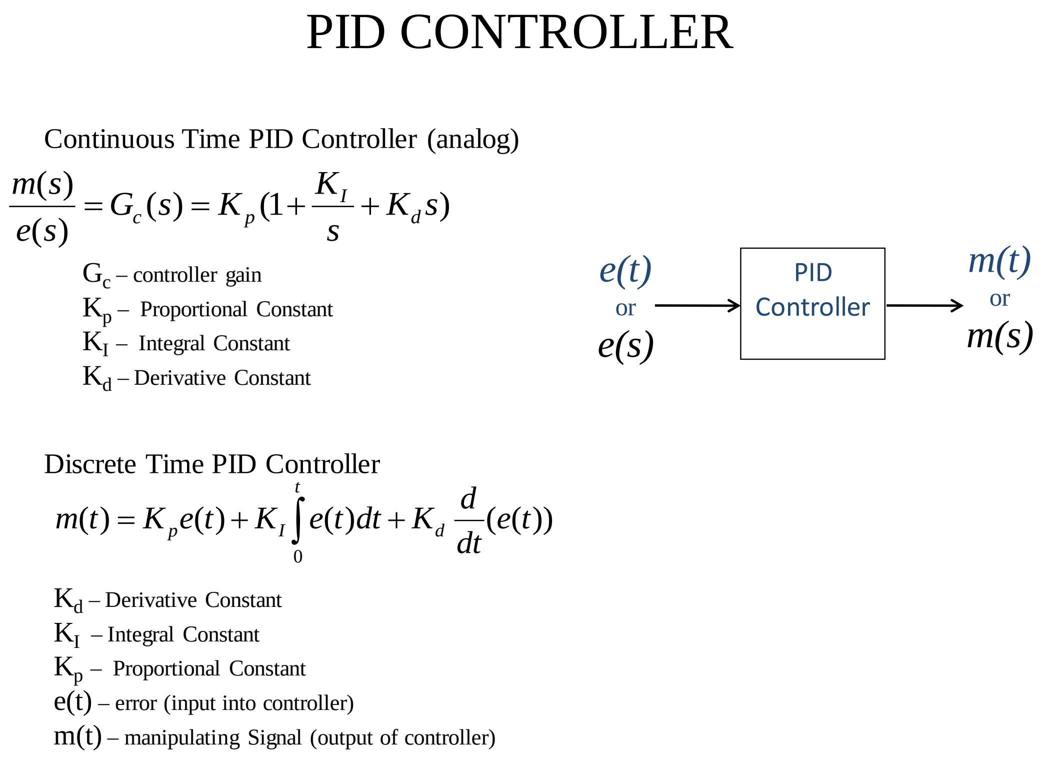

PID CONTROLLER

Continuous Time PID Controller (analog)

$$\frac{m(s)}{e(s)} = G_c(s) = K_p(1 + \frac{K_I}{s} + K_d s)$$

G_c – controller gain
K_p – Proportional Constant
K_I – Integral Constant
K_d – Derivative Constant

Discrete Time PID Controller

$$m(t) = K_p e(t) + K_I \int_0^t e(t)dt + K_d \frac{d}{dt}(e(t))$$

K_d – Derivative Constant
K_I – Integral Constant
K_p – Proportional Constant
e(t) – error (input into controller)
m(t) – manipulating Signal (output of controller)

Figure 5-8: Description of PID Controller

Shown in Figure 5-8 is a description of the PID controller both in the Laplace domain for continuous time and in discrete time. Since the SVR metamodel is trained in discrete time steps, it is most appropriate to utilize the discrete time version of the PID controller and design the control system in discrete time.

The objective of the feedback controller shown in Figure 5-8 is to reduce the error signal, *e(t)*, to zero. As shown in Figure 5-7 and Figure 5-8, *e(t)* is the error signal that goes into the controller and *m(t)* is the signal leaving the controller which alters the control variable. In our control design, the error signal, *e(t)*, is defined as:

$$e(t) = T_{sp}(t) - T_m(t) \tag{28}$$

where $T_{sp}(t)$ is the set point temperature which is the value to which the controller is trying to drive the system. It may be a constant throughout the welding schedule or may be time varying. $T_m(t)$ is the temperature measured from the IR pyrometer (controlled variable) and will be time varying throughout the weld schedule. The following sections will discuss the separate components that make up the PID controller in detail, specifically the Proportional (P), Integral (I) and Derivative (D) components and their functions.

5.2.1 Proportional Control

For proportional control, the controller output is proportional to the error signal and is described by Åström and Hagglund (1995):

$$m(t) = \overline{m} + K_p e(t) \tag{29}$$

where *m(t)* is the controller output, $\overline{m}$ is the bias (steady-state) value, also known as the operating point (in this case it is traverse velocity of the workpiece), and K_p is the proportional gain. The main concepts that govern proportional control are (Seborg, Edgar and Mellichamp, 2004):

1. The controller gain can be adjusted to make the controller output changes as sensitive as desired to respond to the deviations between the set point and controlled variable.
2. The sign of K_p can be chosen to make the output increase (or decrease) as the error signal increases (or decreases).

The proportional gain may be dimensionless or may be in units to relate the error signal to the control variable. In our system the proportional constant is expressed in units of velocity per unit temperature (inches per minute/Kelvin) in order to relate the manipulated signal (traverse velocity) to the controlled variable (IR pyrometer temperature). The main advantage of proportional control is the instantaneous control action that it provides. Once an error is detected the proportional control can immediately react and does not need to wait for a sustained error. The inherent disadvantage of proportional only control, is the steady state error (offset) that may occur after a change in set point or during a sustained disturbance (Seborg et al.; Ogata, 1987). For this reason a proportional controller is paired with integral control that reduces the amount of offset that can be encountered by proportional only control (Seborg et al.).

5.2.2 Integral Control

In integral control action, the controller output is dependent upon the integral of the error signal measured overtime and is described by (Seborg et al.):

$$m(t) = \overline{m} + \frac{1}{\tau_i}\int_0^t e(t^*)dt^* \tag{30}$$

As before, *m(t)* is the controller output, $\overline{m}$ is the controller bias, τ_i is an adjustable parameter known as integral time or reset time and has units of time. The main function of integral control action is to make sure that the process output reaches agreement with the steady state output of the system. As mentioned, a proportional-only control system will yield a steady state offset. Integral action will increase the control signal for any positive error signal and decrease the control signal for any negative error signal. The result is that a controller with integral action will always have a zero steady state error (Åström and Hagglund). The only exceptions are when the controller output saturates as caused by a disturbance or set point change so large that it is beyond the range of the manipulated variable. Typically an integral controller is not used by itself since little control action takes place until an error signal persists for a period of time. For this reason, an integral controller is normally paired with a proportional controller to form a proportional-integral (PI) controller, which is described by (Seborg et al.):

$$m(t) = \overline{m} + K_p\left(e(t) + \frac{1}{\tau_i}\int_0^t e(t^*)dt^*\right) \tag{31}$$

where the quantity, $\frac{K_p}{\tau_i}$ is referred to as the integral constant and is represented by K_i in Figure 5-7 and Figure 5-8. By inspection of Eqn. 31, integral action causes a ramp increase in *m(t)* for $t > 0$. At the point where $t = \tau_i$, the integral term will have contributed the same amount to the controller as the proportional term (Seborg et al.). In this sense the integral action has repeated the proportional action once. For this reason, the $\frac{1}{\tau_i}$ term in front of the integral may be thought of as repeats per unit time i.e. (repeats per second) and τ_i has units of time. Advantages of integral control are the reduction of the offset introduced by the proportional controller and faster response time. Inherent disadvantages of integral control include the potential reduction in stability of the feedback control system. The integral controller may cause oscillatory responses and the phenomenon known as reset windup (Ogata). Reset windup occurs when a sustained error persists for a long period of time; the integral term becomes large and the controller output eventually saturates. The integral term continues to build up while the controller is saturated and this is referred to as reset windup or integral windup. This causes large overshoots which continue to increase until the error signal changes sign. The integral term begins to decrease and becomes a damped oscillation as the control variable approaches the set point value (Åström and Hagglund).

5.2.3 Derivative Control

In derivative control action the function of the controller is to anticipate the future behavior of the error signal by considering the rate of change of the error. Consequently, this improves the closed loop stability of the controller and improves the dynamic response of the controlled variable by decreasing the process settling time. Like the integral controller, derivative control action will not cause an immediate change in the control variable; an error signal must persist for a period of time before a noticeable change takes place in the output variable (Åström and Hagglund). Derivative control is described by (Seborg et al.):

$$m(t) = \overline{m} + \tau_d \frac{de(t)}{dt} \tag{32}$$

As before, $m(t)$ is the controller output, $\overline{m}$ is the controller bias, τ_d is a parameter known as derivative time and has units of time. A derivative controller is not used by itself, since the control action is not instantaneous and the control system will always be late in correcting for an error. More importantly if the process measurement is noisy and contains high frequency and/or random fluctuations, then the derivative of the measured variable will change wildly and the derivative action amplifies the noise of the signal (Seborg et al.). As a result, derivative controllers are typically paired with proportional controllers or with proportional- integral (PI) controllers. The proportional-derivative (PD) controller is described by (Åström and Hagglund):

$$m(t) = \overline{m} + K_p\left(e(t) + \tau_d \frac{de(t)}{dt}\right) \tag{33}$$

Where the quantity, $K_p\tau_d$ is referred to as the derivative constant and is represented by K_d in Figure 5-7 and Figure 5-8. The control action of a PD controller may be interpreted as if the control is made proportional to the predicted process output, where the prediction is made by extrapolating the error by the line tangent to the error curve at time, t (Åström and Hagglund). The control signal is thus proportional to an estimate of the control error at time τ_d ahead where the estimate is obtained by linear extrapolation. The proportional-integral-derivative controller includes all of the control action terms and is described by (Seborg et al.):

$$m(t) = \overline{m} + K_p \left(e(t) + \frac{1}{\tau_i} \int_0^t e(t^*) dt^* + \tau_d \frac{de(t)}{dt} \right) \tag{34}$$

By including both the derivative and integral terms to the controller, some of the disadvantages of the integral are counteracted by the derivative action. The derivative mode counters some of the destabilizing tendencies of the integral control action. At the same time the derivative action will improve dynamic response by reducing the process settling time. For the controller simulations and analysis in the next section, the expanded, non-interacting form of Eqn. 34 will be used (Seborg et al.):

$$m(t) = \overline{m} + K_p e(t) + K_i \int_0^t e(t^*) dt^* + K_d \frac{de(t)}{dt} \tag{35}$$

5.3 PID Control Simulations

The following simulations were run to determine control parameters that yield the proper response from the control system. In the following simulations an SVR based metamodel serves as the process model to simulate the welding process. The metamodel is based on the schematic and parameters shown in Figure 5-10 and Table 5-1. The simulations and tuning are performed on idealized metamodels that do not include process noise. The tuning methodology utilized in these simulations is loosely based on Ziegler-Nichols on-line tuning methods (Åström and Hagglund; Seborg et al.). The trial and error procedure uses the continuous cycling method to obtain the value of the proportional constant, K_p after the process has reached steady state. After an acceptable value for K_p is found, then the two other constants are related to K_p in a semi-empirical manner. The following computational studies were run to determine the most practical values for K_p, K_i and K_d.

5.3.1 Model based approach to finding K_p

The first attempt to obtain the proportional constant came from using a model-based approach. By definition, K_p for our system relates the change in our manipulated variable (traverse velocity) to the change in our controlled variable (IR pyrometer measurement). In Figure 5-9, plots of temperature vs. velocity and the first derivative of temperature vs. velocity using the Rosenthal thin plate model from Eqns. 7a and 7b are shown. In theory, the inverse of the slope of a linear regression fit to the data points would serve as an estimate of the magnitude of the proportional constant. The slopes of the lines in Figure 5-9 are in units of temperature per velocity, hence the inverse of the slopes provide the proper units conversion of velocity per unit temperature.

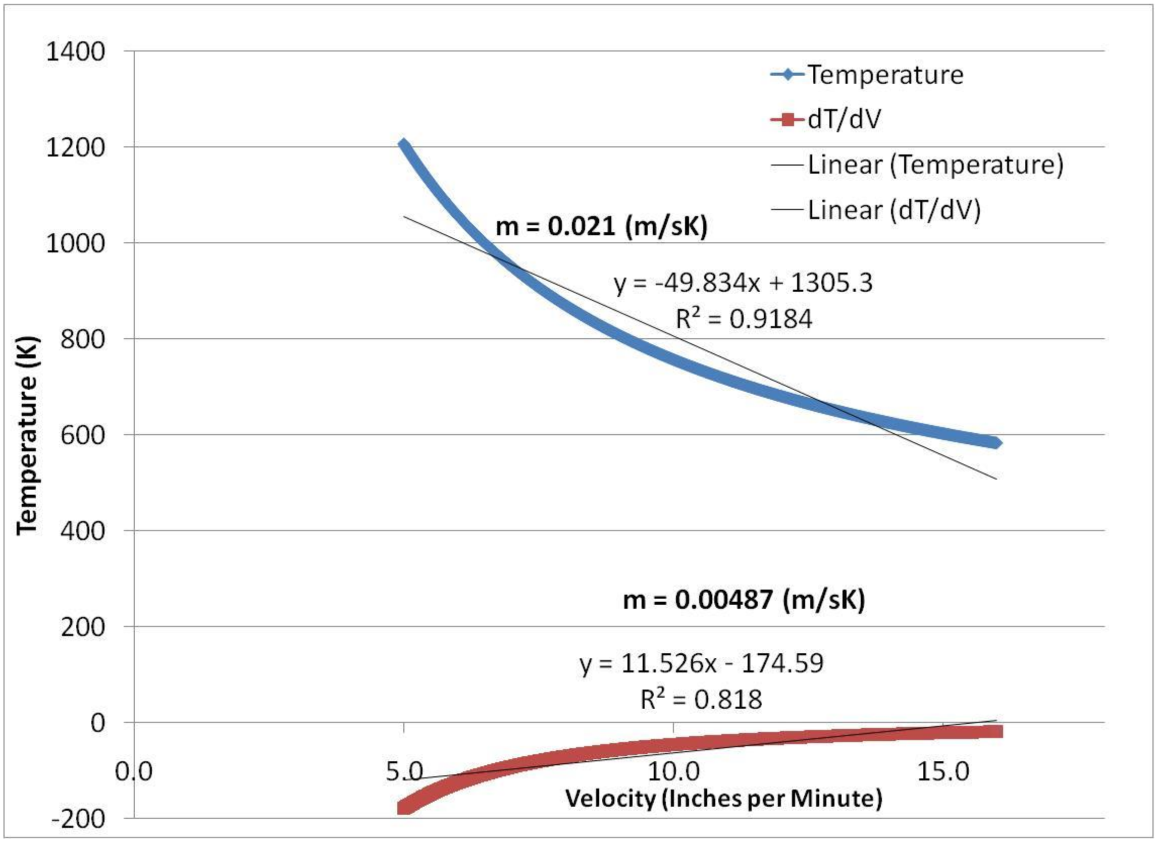

Figure 5-9: Temperature vs. Velocity from Rosenthal thin plate model

Examining the inverse of the slopes of the linear regression fits of the two lines in Figure 5-9, the estimate of K_p is between 0.02 (m/sK) (49.8 inches per minute/Deg C) and 0.00487 (m/sK) (11.5 inches per minute/Deg C). With this value, a simulation is run to see how well this estimate of K_p will work in a simulated control system. Shown in Figure 5-10 and Table 5-1 are the schematic of the domain of the weld specimen and the welding parameters used in the control simulation. Throughout the simulation, the heat input stays constant but the velocity changes as soon as the control action initiates. The value of the velocity in Table 5-1 is the value with which the simulation is initialized.

Shown in Figure 5-11 is the resulting temperature profile from the PID controller with K_p = 0.02 (m/sK) (47.24 inches per minute/Deg C) and the corresponding velocity output from the controller shown in Figure 5-12.

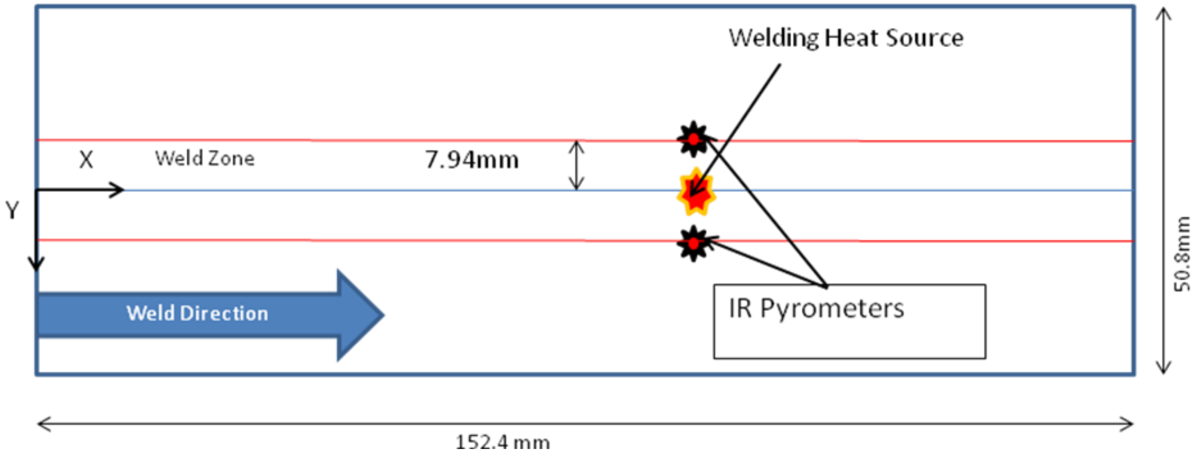

Welding Heat Source
X
Weld Zone
7.94mm
Y
Weld Direction
IR Pyrometers
50.8mm
152.4 mm

Figure 5-10: Schematic of weld specimen used in the control simulation

Table 5-1: Welding parameters used in the control simulation

Initial Velocity (mm/s)	**Heat Input (W)**	**Set point Temperature, T_{sp} (K)**
6.35	2060	635 (362°C)

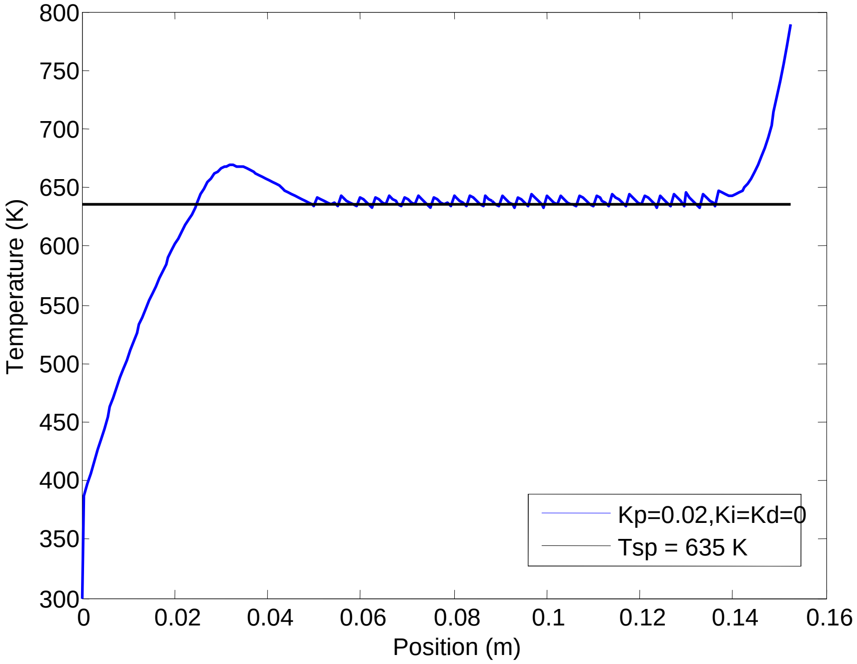

Figure 5-11: Temperature vs. Position plot for P controller with K_p = 0.02

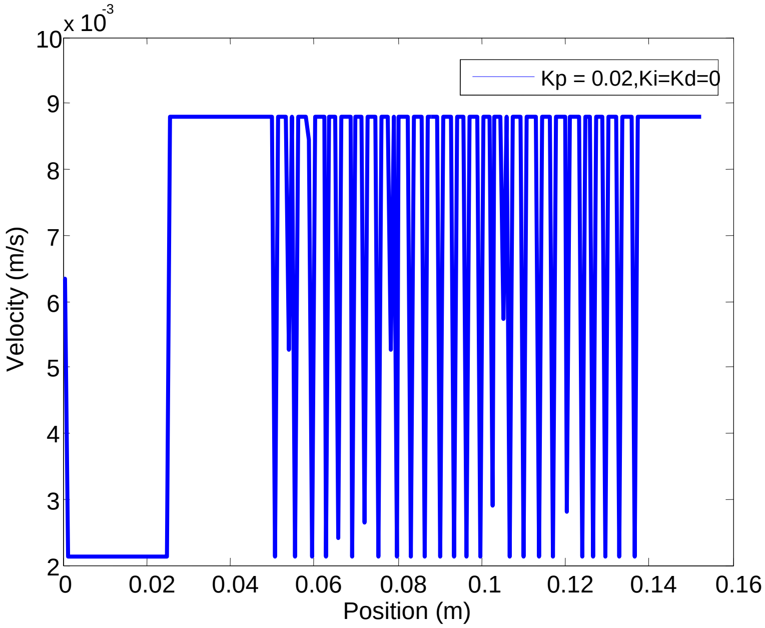

Figure 5-12: Velocity vs. Position plot for P Controller with K_p= 0.02

.

In Figure 5-11, the temperature profile exhibits oscillatory behavior once the process has reached steady state. Looking at the control output in Figure 5-12, bang-bang control action (i.e., the manipulated variable oscillating between maximum and minimum values) (Seborg et al.) can be observed by the controller output. This means that proportional constant is too large and that with every control action the controller is over correcting for the error signal that is detected. In this instance the controller is alternating between the highest and lowest speed of the traverse velocity in an attempt to reach the desired temperature. From Figure 5-12, it is determined that although the proportional constant is too high, since every control response is not on-off that the model based approach provides a good starting point to finding better control constants. The next study will focus on finding better controller constants and determining the necessity of the operating point.

5.3.2 Parameter study to find controller constants and operating point assessment

From the previous study, the model based approach to finding K_p did not yield a viable proportionality constant but provided a good starting point for finding a parameter with better performance. In this study, the same weld specimen dimension and welding parameters as outlined in Figure 5-10 and Table 5-1 are used in the control simulation. In addition, this study also compares controller performance with and without the operating point, $\overline{m}$, which is included in Eqns. 29- 35. The purpose of the operating point is to give a controller output in the event that zero error is detected. A question regarding control action comes about if the operating point is removed. For this reason, a comparison of controller performance with and without the operating point is examined to see if the control action is different (or better) in the absence of the operating point.

The metric used to compare the controller performance is based on how well the controlled temperature matches the set point temperature, T_{sp}. The method for comparison is the root mean square (RMS) error of the temperature profile over the whole workpiece. The RMS error is defined by:

$$Error_{RMS} = \sqrt{\frac{\sum_{i=1}^{n}(T_i - T_{sp})^2}{n}} \qquad (36)$$

In Eqn. 36 T_i is the value of the temperature at a discrete time and n is the number of temperature values throughout the weld schedule. Using K_p= 0.02 (m/sK) (47.24 inches per minute/Deg C), as a starting point, different values of K_p were examined for steady state temperature characteristics, controller output, and RMS error. Since K_p= 0.02 (m/sK) (47.24 inches per minute/Deg C) was found to be too high, only values of less than K_p= 0.02 (m/sK) (47.24 inches per minute/Deg C) were considered. The process of determining new proportional constants is a trial and error process. New proportional constants were considered by systematically considering some increment less than K_p= 0.02 (m/sK) (47.24 inches per minute/Deg C). The steady state temperature behavior was examined, the RMS error and percent difference was calculated and compared to gauge the amount of improvement over the previous proportional constant. Most importantly, the controller output was examined to determine how feasible the response was. Shown in Figure 5-13, Figure 5-14, and Figure 5-15 are representative examples of the improved proportional constants.

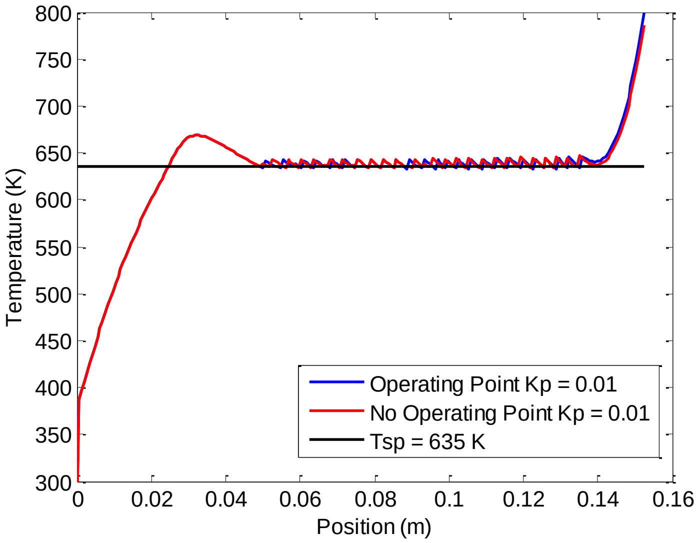
800
750
700
650
600
550
500
450
400
350
300
Temperature (K)
0
0.02
0.04
0.06
0.08
0.1
0.12
0.14
0.16
Position (m)
Operating Point Kp = 0.01
No Operating Point Kp = 0.01
Tsp = 635 K

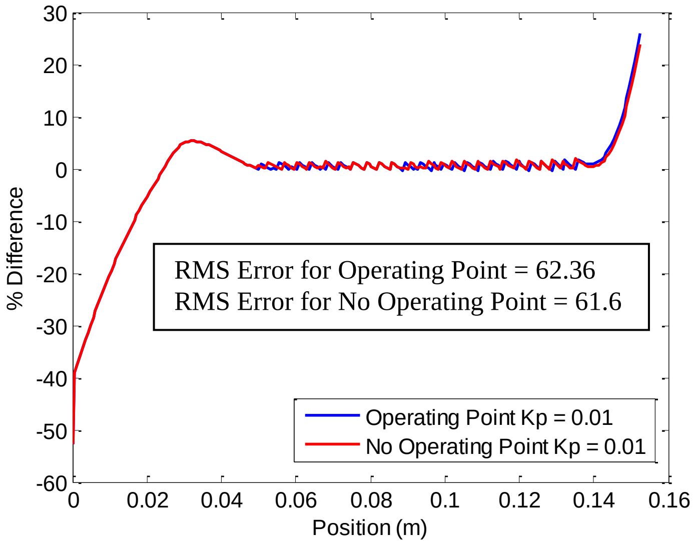
30
20
10
0
-10
-20
-30
-40
-50
-60
% Difference
0
0.02
0.04
0.06
0.08
0.1
0.12
0.14
0.16
Position (m)
RMS Error for Operating Point = 62.36
RMS Error for No Operating Point = 61.6
Operating Point Kp = 0.01
No Operating Point Kp = 0.01

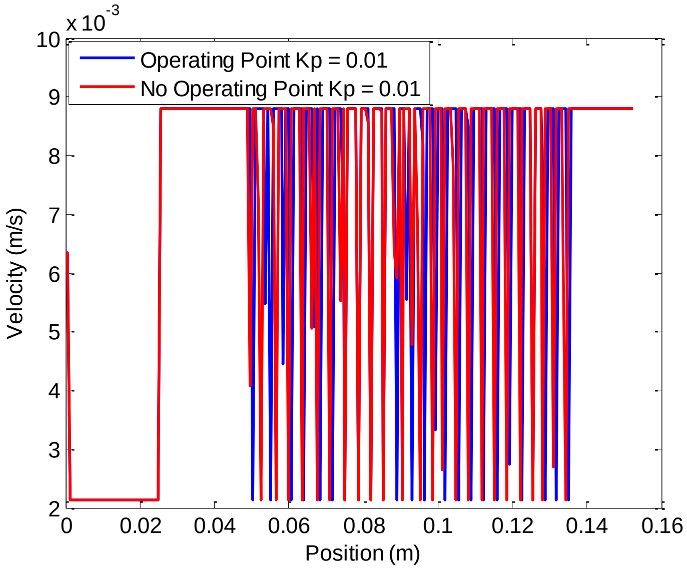

Figure 5-13: Plots of Temperature, percent difference and controller output for K_p = 0.01

Shown in Figure 5-13 are the temperature, percent difference and controller output for K_p = 0.01(m/sK) (23.62 inches per minute/Deg C). Upon inspection of the steady state temperature response there is still a fair amount of oscillation. The oscillation seems better than for K_p = 0.02(m/sK) (47.24 inches per minute/Deg C) and the RMS error values are less. Comparing the controller with the operating point against the controller without the operating point, their controller response is identical yet the temperature responses are slightly different. Of note, in the absence of the operating point, the controller made more control actions to correct for temperature. Lastly comparing the RMS error values, the controller with the operating point has slightly larger overall error across the whole workpiece.

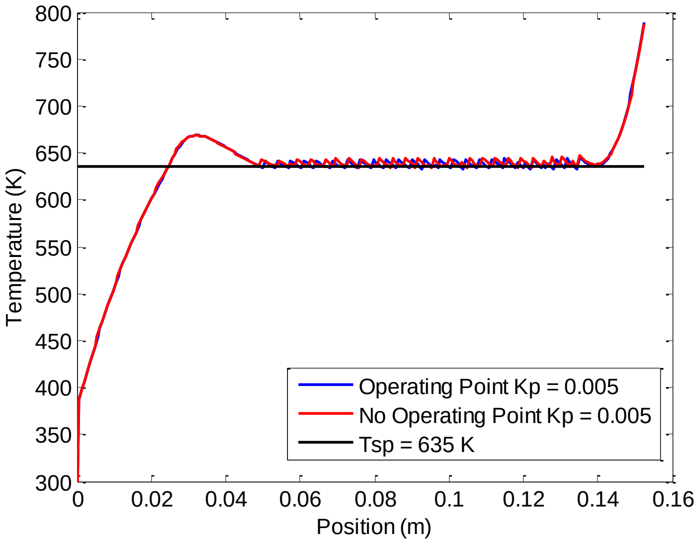
800
750
700
650
600
550
500
450
400
350
300
Temperature (K)
0
0.02
0.04
0.06
0.08
0.1
0.12
0.14
0.16
Position (m)
Operating Point Kp = 0.005
No Operating Point Kp = 0.005
Tsp = 635 K

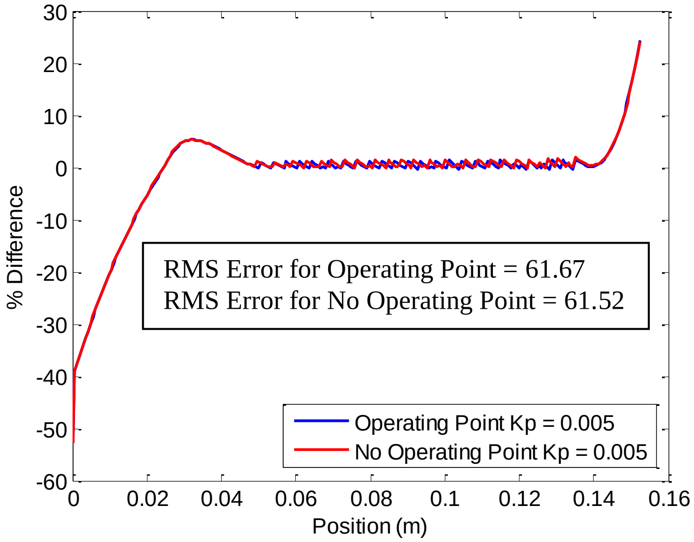
30
20
10
0
-10
-20
-30
-40
-50
-60
% Difference
0
0.02
0.04
0.06
0.08
0.1
0.12
0.14
0.16
Position (m)
RMS Error for Operating Point = 61.67
RMS Error for No Operating Point = 61.52
Operating Point Kp = 0.005
No Operating Point Kp = 0.005

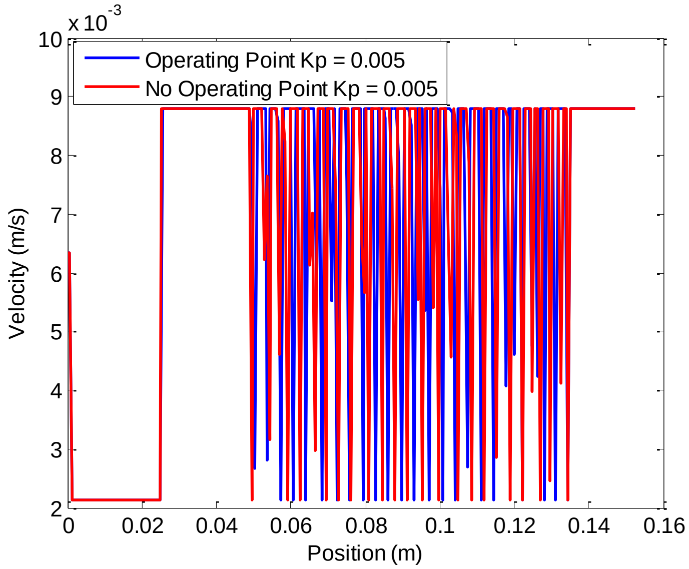

Figure 5-14: Plots of Temperature, percent difference and controller output for K_p = 0.005

Shown in Figure 5-14 are the temperature, percent difference and controller output for K_p = 0.005(m/sK) (11.81 inches per minute/Deg C). Upon inspection of the steady state temperature response there is still some oscillation. The oscillation seems about the same as the controller with K_p = 0.01(m/sK) (23.62 inches per minute/Deg C). The RMS error values are less than the case with K_p = 0.01(m/sK) (23.62 inches per minute/Deg C), yet the controller with no operating point still has a slightly smaller RMS error over the whole workpiece. Comparing the controller with the operating point against the controller without the operating point, their controller response differs between the two controllers and there is less bang-bang behavior. In this case, despite having different controller outputs their temperature responses are more similar than the case where K_p = 0.01(m/sK)

(23.62 inches per minute/Deg C). As in the last case, in the absence of the operating point, the controller made more control actions to correct for temperature.

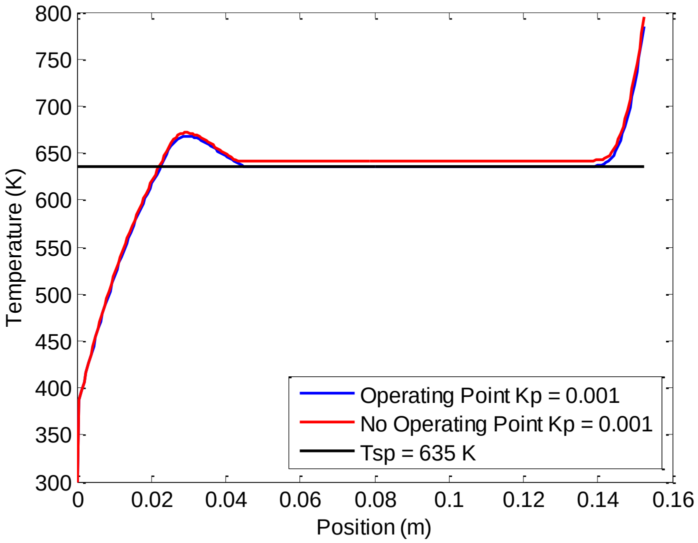

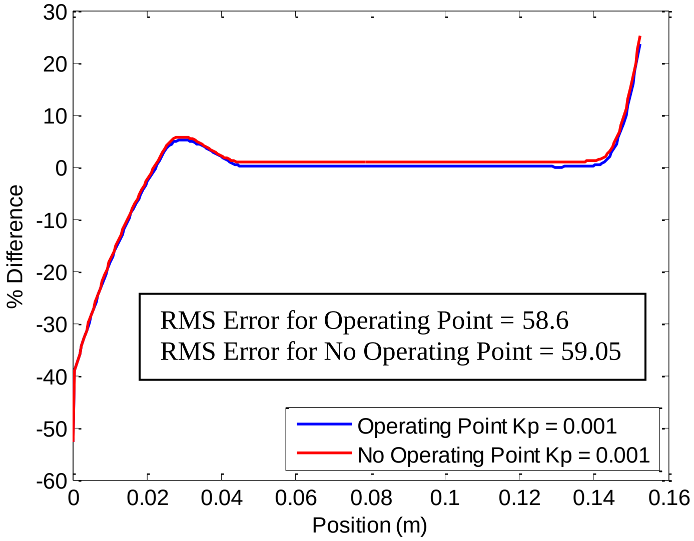

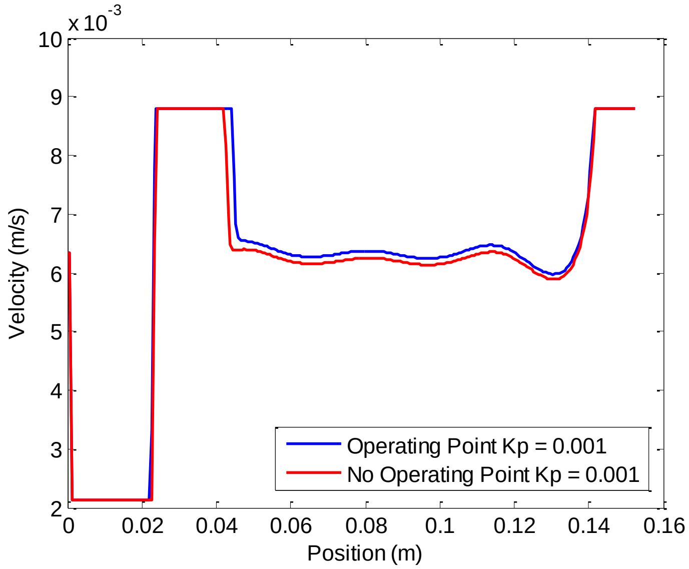

Figure 5-15: Plots of Temperature, percent difference and controller output for K_p = 0.001

Shown in Figure 5-15 are the temperature, percent difference and controller output for K_p = 0.001(m/sK) (2.36 inches per minute/Deg C). Upon inspection of the steady state temperature response there is no oscillation and the temperature responses from both controllers is smooth. The RMS error values are less than the cases with K_p = 0.005(m/sK) (11.81 inches per minute/Deg C) and K_p = 0.01(m/sK) (23.62 inches per minute/Deg C). One trend that is different in this trial is that the controller with the operating point has a lower RMS error over the whole workpiece than the controller without the operating point. Comparing the controller with the operating point against the controller without the operating point, their controller response is very similar. In this trial there is no bang-bang behavior and the controller output is smooth and non-sporadic. In this case, since the controller outputs are very similar their temperature responses are similar as well. The difference is that the controller without the operating point has more of an offset from the set point temperature than the controller with the operating point. Just as in the last case, in the absence of the operating point, the controller made more control actions to correct for temperature. Comparing all three cases from Figure 5-13, Figure 5-14 and Figure 5-15 it is apparent from the point of view of temperature response, controller output, RMS error and percent difference that K_p = 0.001 (m/sK) (2.36 inches per minute/Deg C) is the most likely proportional constant to yield a fair control response. This is further supported by a more comprehensive study of RMS error for several different values of proportional constant, K_p. Shown in Figure 5-16 is a graph of RMS error vs. Log of K_p. It is observed that the RMS error for the controller with an operating point has a local minimum at K_p = 0.001 (m/sK) (2.36 inches per minute/Deg C). The desired value of K_p is one with the least amount of error yet drives the system to the desired setpoint. The smaller the value of K_p, the smaller the amount of proportional adjustment to the system. For very small values of K_p, longer rise times and more steady state offset may be observed. For values of K_p approaching zero, the less the amount of control is applied where K_p = 0 will amount to no control. From the plot it is confirmed that for K_p = 0.001 (m/sK) (2.36 inches per minute/Deg C) the RMS error over the whole work piece is at a minimum.

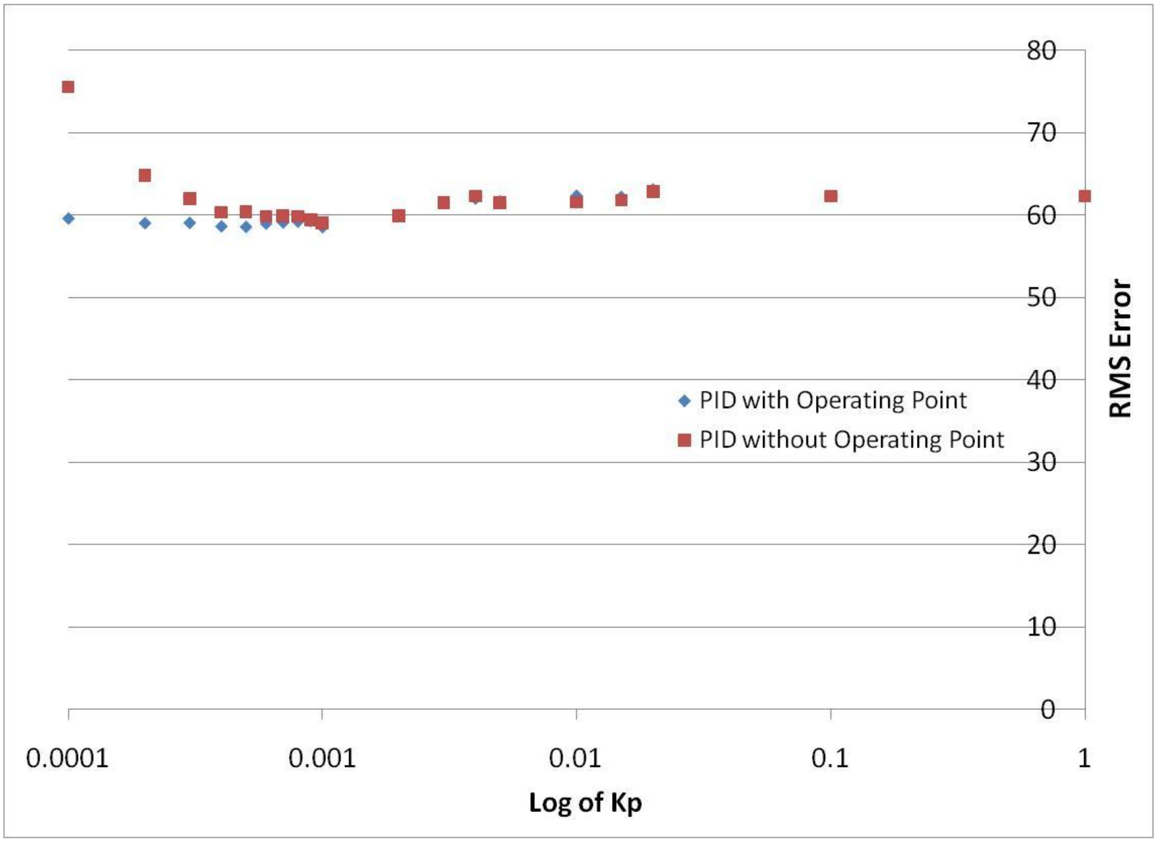

Figure 5-16: Chart of RMS error vs. Log K_p shows that operating point has lower RMS error

The results of this study conclude that a model-based approach to finding K_p is a helpful heuristic to finding a practical value for the proportional constant. It was also found that RMS error is a viable way to determine the usefulness of the chosen PID control parameters. By properly choosing K_p the other controller constants, K_i and K_d can be chosen using Ziegler-Nichols or other tuning schemes. Through a modified Ziegler-Nichols tuning method, the best controller constants were found for the idealized case where there is no noise in the plant model. The controller constants are shown in Table 5-2

Table 5-2: PID constants for idealized plant model without noise

Proportional Constant K_p	Integral Constant K_i	Derivative Constant K_d
0.001	0.000001	0.000001

5.4 Filtering noise from the measured data

In Section 5.3.2, the PID controller constants were found for the idealized plant model that did not contain noise. In the real, physical system the temperature measurement data will contain some amount of noise for which the controller will have to compensate. Shown in Figure 5-17 is noisy, raw data from the experiment outlined in section 3.1.3. The high and low experimental data values were the highest and lowest noisy data values that were observed throughout five experiments. Between the experimental trials there is an observable variance within the data collected and may fall anywhere within this envelope. Also shown in Figure 5-17 is a plot of the average of the data from five experimental trials and a plot of the average experimental data plotted along Gaussian white noise with a standard deviation, $\sigma = 15$ K. This amount of white noise was chosen since it represents the amount of possible noise that can be encountered during testing. This noise must be handled so that the robustness of the controller is maintained.

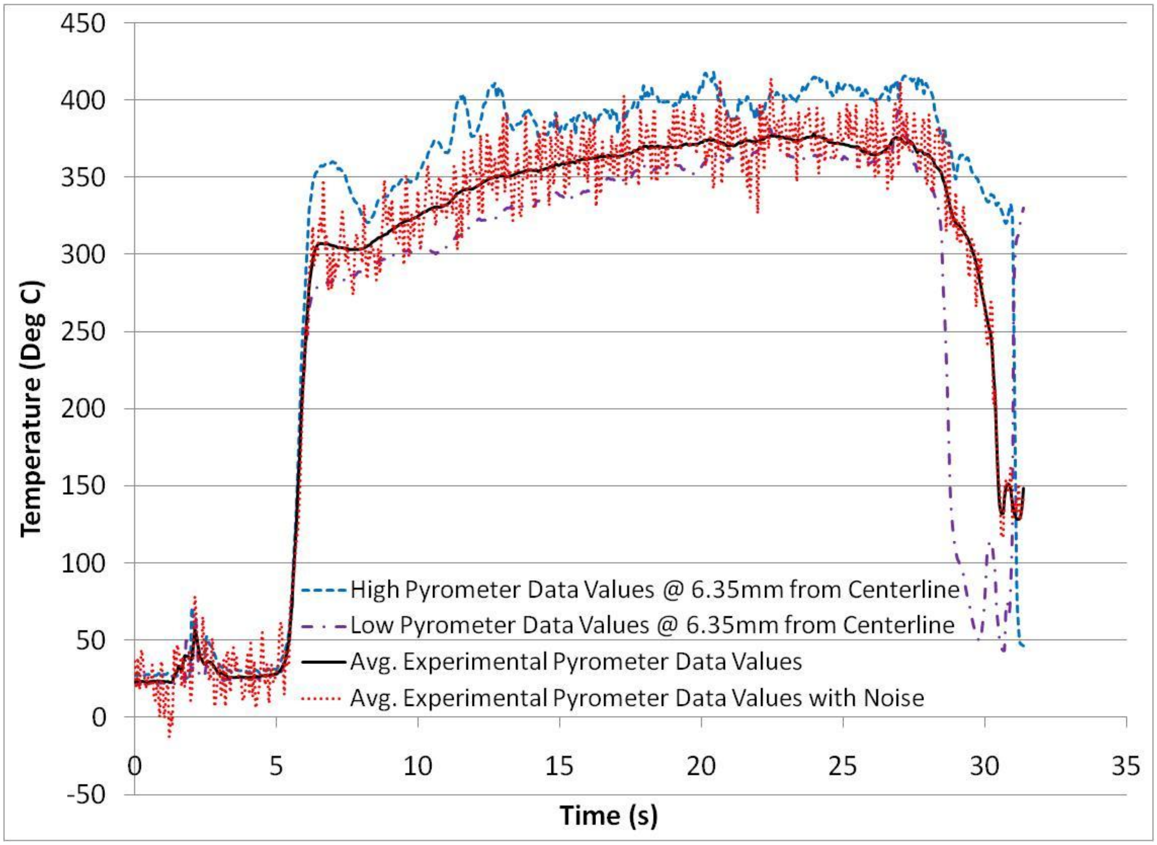

Figure 5-17: Plot of noisy data obtained during testing

In the presence of measurement noise, the PID constants from Table 5-2 do not perform as well. Gaussian white noise with a standard deviation, $\sigma = 15$ K is applied to the metamodel output to simulate noisy data and the controller compensates for the noisy measure. Shown in Figure 5-18 are the temperature response and controller output (velocity) for the idealized controller constants. Similar to some of the cases discussed in Section 5.3.2, the temperature profile and controller output demonstrate oscillatory behavior. The controller output exhibits bang-bang behavior and results in the oscillatory behavior observed in the steady state portion of the temperature response. In order for the controller to regulate temperature signal, the measurement data must be filtered or smoothed before entering the controller so that the control actions are not based on the stochastic variations in the measured temperature signal but rather the underlying signal of the temperature. The remainder of this section will investigate options for smoothing and filtering the noise in that data before sending the signal to the controller.

As previously discussed, the measurement noise inherent in our system is problematic to the controller, specifically the derivative control action. Noise present in the signal will be amplified through differentiation. As a result, the measured signal must be conditioned or filtered prior to being used in the controller (Seborg et al.).

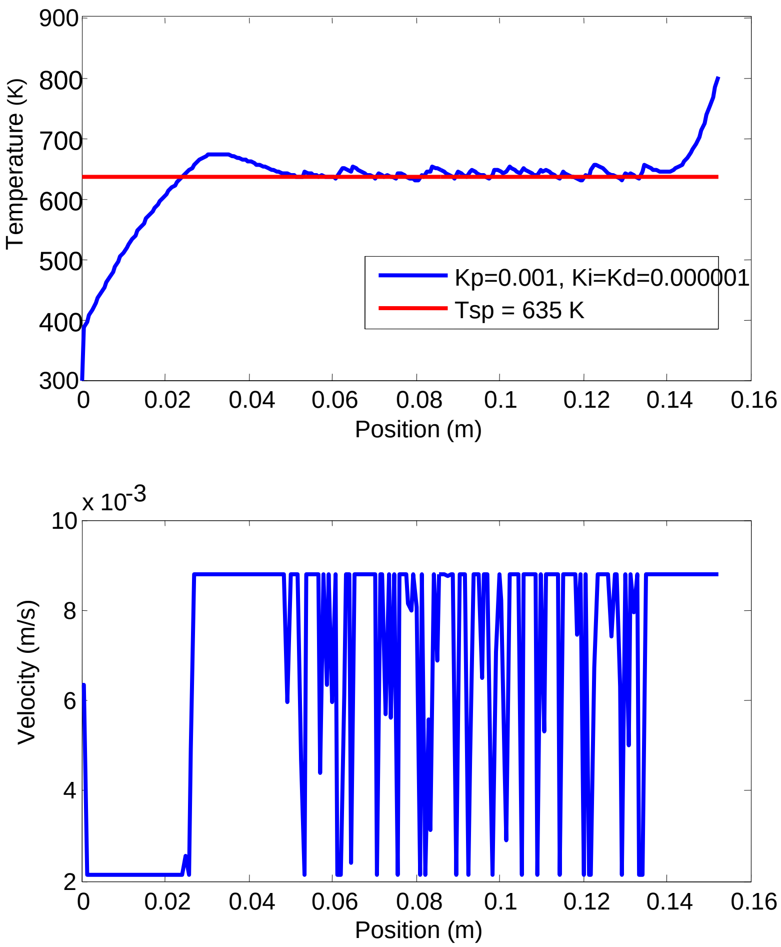

Figure 5-18: Temperature profile and controller response for K_p=0.001 and K_i=K_d=0.000001

5.4.1 Regression Models to Filter Noise

In regression analysis, the goal is to model an independent or controlled variable, *x* with respect to a dependent variable, *y*. The quantity of interest is the dependence of *y* on *x* or in other words, the regression of *y* on *x*. In an experiment, *x* is the chosen or assigned variable i.e. x_1, x_2, …. x_n and then corresponding values of y i.e. y_1, y_2, …. y_n are measured or observed (Kreysig, 1999).

For some sets of data, a simple linear regression will not provide a suitable fit. In those instances linear regression models with more than one regressor variable would be more appropriate and may provide a better fit to the data. This category of regression models is the multiple linear regression model.

One subset of multiple linear regression models is the polynomial regression model. For some cases where a linear or multiple linear regression model does not provide a good fit to the data another option is to use regressor variables of higher order. Polynomials are useful in situations where the response variable, y is curvilinear. Even nonlinear relationships can be a modeled by polynomials over small ranges of x's (Montgomery, Peck and Vining, 2001). One example of a polynomial regression model is the second order polynomial in one variable (quadratic model). It takes the form:

$$y = \beta_0 + \beta_1 x + \beta_2 x^2 + \varepsilon \tag{37}$$

In Eqn. 37 the expected value of y is described by a quadratic function in x. In general a polynomial regression model can be extended to include higher order terms to the k^{th} order and takes on the form:

$$y = \beta_0 + \beta_1 x + \beta_2 x^2 + \cdots + \beta_k x^k + \varepsilon \tag{38}$$

In this study, the order of the regression model is limited to 2^{nd} order. As a general rule for a regression model, it is recommended that the order of the model be as low as possible (Montgomery, Peck and Vining, 2001). For the implementation of Eqn. 37 in the control system, *x* is the noisy temperature data at specific discrete times (either measured or simulated) that is to be fit with a regression and *y* is the value of the smoothed, denoised temperature as a result of the regression fit. It is the temperature value, *y* that is sent to the controller and used to calculate the error signal described in Eqn. 28.

5.4.1.1 Implementation of the Regression Models

In this study, the regression models will be implemented in two ways. One way uses a moving window of predetermined size to fit a polynomial regression to the noisy data and then “use” the regression fit as input into the controller. In this implementation of the moving window, a window of size *n* will overlap *n-1* points with every movement of the window. The second method will use a piecewise polynomial fitting where the noisy data in a window of predetermined size is fit with a polynomial regression and the regression fit is used as the input to the controller for the period of the next window. This implementation of the data window differs from the moving window in that the noisy data is split into segments throughout the weld schedule and the polynomial fit is applied to each segment and the filtered data is constructed as segments similar to a spline function. Hence, a window of size *n* would only overlap the end points of the window to piece together the function. An illustration of how each method works is shown in Figure 5-19 and Figure 5-20.

$$[1\;2\;3\;4]\;5\;6\;7\;8 \rightarrow 1\;[2\;3\;4\;5]\;6\;7\;8 \rightarrow 1\;2\;[3\;4\;5\;6]\;7\;8$$

Figure 5-19: Illustration of a 4 point moving window

In Figure 5-19, the polynomial fit of the values within the window is used to control the input at last point of the current window; e.g., the fit to window [1 2 3 4] will control the input to point 5 etc.

$$[1\;2\;3\;4]\;5\;6\;7\;8 \rightarrow 1\;2\;3\;4\;[5\;6\;7\;8]\;9 \rightarrow 1\;2\;3\;4\;5\;6\;7\;8\;[9\;10\;11\;12]\;13\;14$$

Figure 5-20: Illustration of a 4 point piecewise window

In Figure 5-20, the fit to window [1 2 3 4] would be used to extrapolate into the future and be used to control input to points [5 6 7 8], etc. This results in potentially more control error, but takes less time to implement than the moving window, which requires a new regression for every data point.

The regression function used to prefilter the noisy data in the following anaylsis uses built in regression functions in MATLAB®. The functions of *polyfit* and *polyval* are used to fit the data to polynomial regression function and evaluate that polynomial for the smoothed data values.

5.4.2 Exponential Filter

One way to filter the high frequency noise associated with measurement is to use an analog filter. One example is the filter described in Eqn. 39. This class of filter is known as an exponential filter that reduces high frequency fluctuations; hence it functions as a low pass filter.

$$\tau_f \frac{dy_f(t)}{dt} + y_f(t) = y_n(t) \tag{39}$$

where, y_n is the noisy data (input to the filter), y_f is the filtered data (output of the filter) and τ_f is the time constant of the filter.

The control system and metamodels used in this work are designed in the discrete time domain; as a result the exponential filter considered is the digital version of Eqn. 39. The derivative term in Eqn. 39 is approximated by a Taylor Series expansion and is represented by a first order backwards difference in Eqn. 40.

$$\frac{dy_f(t)}{dt} \cong \frac{y_f(t) - y_f(t-1)}{\Delta t} \tag{40}$$

Substituting Eqn. 40 back into Eqn. 39 yields,

$$\tau_f \frac{y_f(t) - y_f(t-1)}{\Delta t} + y_f(t) = y_n(t)$$

Rearranging terms and moving y_f to the left hand side yields Eqn. 41a.

$$y_f(t) = \frac{\tau_f}{\tau_f + \Delta t} y_f(t-1) + \frac{\Delta t}{\tau_f + \Delta t} y_n(t) \tag{41a}$$

Defining,

$$\alpha \equiv \frac{\Delta t}{\tau_f + \Delta t} \quad \text{and} \quad 1 - \alpha \equiv \frac{\tau_f}{\tau_f + \Delta t} \tag{41b,c}$$

where $0 < \alpha \leq 1$, Eqn. 41a becomes:

$$y_f(k) = (1-\alpha)y_f(k-1) + \alpha y_n(k) \tag{42}$$

Inspection of Eqn. 42 indicates that the value of the filtered measurement, y_f, is a weighted sum of the current, noisy measurement, y_n, and the filtered measurement at the previous time step (or sampling instance). As a result, this is known as single exponential smoothing or the exponentially weighted moving average (EWMA) filter (Seborg et al.). The limiting cases for α in Eqn. 42 are:

$\alpha = 1$ → No filtering (filter output is the noisy measurement, y_n, corresponds to $\tau_f = 0$)

$\alpha \to 0$: The current measurement is increasingly ignored

Alternate expressions for Eqn. 42 may be derived if the derivative term is represented in a different manner in Eqn. 39. Higher order representations of the derivative term in forward difference, backwards difference and central difference representations may be found in Fornberg (1988). Several representations of the derivative term are examined. First and second order accuracy representations are chosen because of their ubiquity and higher even orders of accuracy are chosen for convenience. Shown in Eqns. 43-45 are higher order representations of the derivative term in Eqn. 39 that are used in this study.

3pt Stencil

$$\frac{dy_f(t)}{dt} = \frac{\frac{3}{2}y_f(t) - 2y_f(t-1) + \frac{1}{2}y_f(t-2)}{\Delta t} \tag{43}$$

5pt Stencil

$$\frac{dy_f(t)}{dt} = \frac{\frac{25}{12}y_f(t) - 4y_f(t-1) + 3y_f(t-2) - \frac{4}{3}y_f(t-3) + \frac{1}{4}y_f(t-4)}{\Delta t} \tag{44}$$

7pt Stencil

$$\frac{dy_f(t)}{dt} = \frac{\frac{49}{20}y_f(t) - 6y_f(t-1) + \frac{15}{2}y_f(t-2) - \frac{20}{3}y_f(t-3) + \frac{15}{4}y_f(t-4) - \frac{6}{5}y_f(t-5) + \frac{1}{6}y_f(t-6)}{\Delta t} \tag{45}$$

In the following section, various forms of the EWMA model are investigated to determine if a higher order representation of the derivative term in Eqn. 39 yields a higher fidelity filtered signal.

5.4.2.1 Study to find the value of α

In Eqn. 42, one variable of importance is the weighting factor, α in the exponential filter. Without this value the terms of the exponential filter will not have the proper weighting. This section outlines the result of a study performed to determine the best value for α and find the time constant of the filter, τ_f.

In this study the SVR based metamodel outlined in Section 4.1.1 was used to model the temperature evolution of a braze-welded workpiece subjected to the parameters outlined in Figure 5-10 and Table 5-1. Gaussian white noise with a standard deviation of σ = 15 K was applied to the resulting temperature distribution. The exponential filter using a moving window and based on a two point backwards difference as described by Eqn. 40 was applied to the noisy temperature distribution. Simulations were performed for values of α ranging from 0.01 to 0.99 in increments of 0.01. The goodness of fit for the exponential filter for the various values of α are compared by tabulating the RMS error (Eqn. 36) of the smoothed temperature distribution for the whole workpiece and observing the lowest RMS error value for a given α. Once the value of α is determined the value of the filter time constant, τ_f can be determined from Eqn. 41b. Shown in Figure 5-21 is a graphical result of the study. Illustrated in the plot are the metamodel temperature prediction, the prediction with added Gaussian white noise and the smoothed noise with the best found value of α. In the study the value of α with the lowest RMS error was α = 0.4.

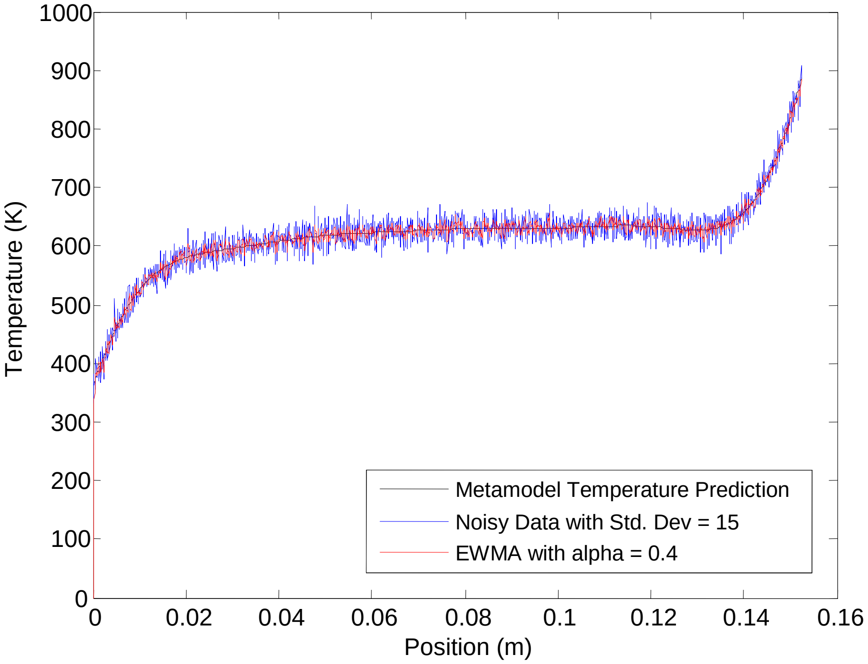

Figure 5-21: Graph of metamodel prediction, noisy data and EWMA smoothed data for α = 0.4

The filter time constant, τ_f of the exponential filter is obtained by rearranging Eqn. 41b to yield:

$$\tau_f = \frac{\Delta t - \alpha \Delta t}{\alpha} \tag{46}$$

Evaluating Eqn. 46 for a time step size, Δt = 0.01 seconds and α = 0.4, the filter time constant is found to be, τ_f = 0.015. This estimate of the filter time constant is useful if other forms of the exponential filter are used either with higher order derivative estimates or different time step sizes.

5.4.3 Comparison Study of Regression Smoothing and Exponential Filter

In this section, the noise filtering methods covered in Sections 5.4.1 and 5.4.2 are compared to assess the performance of each method. In this study the SVR based metamodel outlined in Section 4.1.1 was used to model the temperature evolution of a braze-welded workpiece subjected to the parameters outlined in Figure 5-10 and Table 5-1. Gaussian white noise with a standard deviation of σ = 15 K was applied to the resulting temperature distribution. The regression models from Section 5.4.1 are implemented with moving windows and piecewise windows applied to the noisy temperature data. Several different window sizes (stencil sizes) are considered and the RMS error for the whole workpiece is tabulated for each window size. The exponential filter is implemented using a moving window and based on different representations of the derivative term in Eqn. 39. Higher order backwards difference representations as described by Eqns. 40 and 43- 45 were applied to the noisy temperature distribution. For each case of the EWMA filter the RMS error over the whole workpiece was used as the metric for comparison. A summary of the results is shown in Table 5-3 and a graph comparing each method is shown in Figure 5-22.

Table 5-3: Comparison of error vs. stencil size for regression models and EWMA filter

Piecewise Window		**Moving Window**		**EWMA**	
Stencil Size	RMS Error	Stencil Size	RMS Error	Stencil Size	RMS Error
10	8.18	10	11.79	2	7.55
20	5.89	20	9.02	3	7.15
30	4.73	30	7.48	5	7.60
40	4.14	40	6.62	7	9.00
50	3.79	50	6.05		
60	3.72	60	5.54		

One noticeable trend in the regression schemes is that the RMS error decreases as the size of the stencil gets larger for the moving windows. This is expected since the fit of the regression will improve with a greater number of points. For larger stencils than 60 points it is possible that the overall RMS error would decrease further. The error for the EWMA reaches a minimum at a stencil size of 3 points. In practical implementation of these schemes the window size will be dependent on the number of data points the controller can store and the sampling rate that the data is taken.

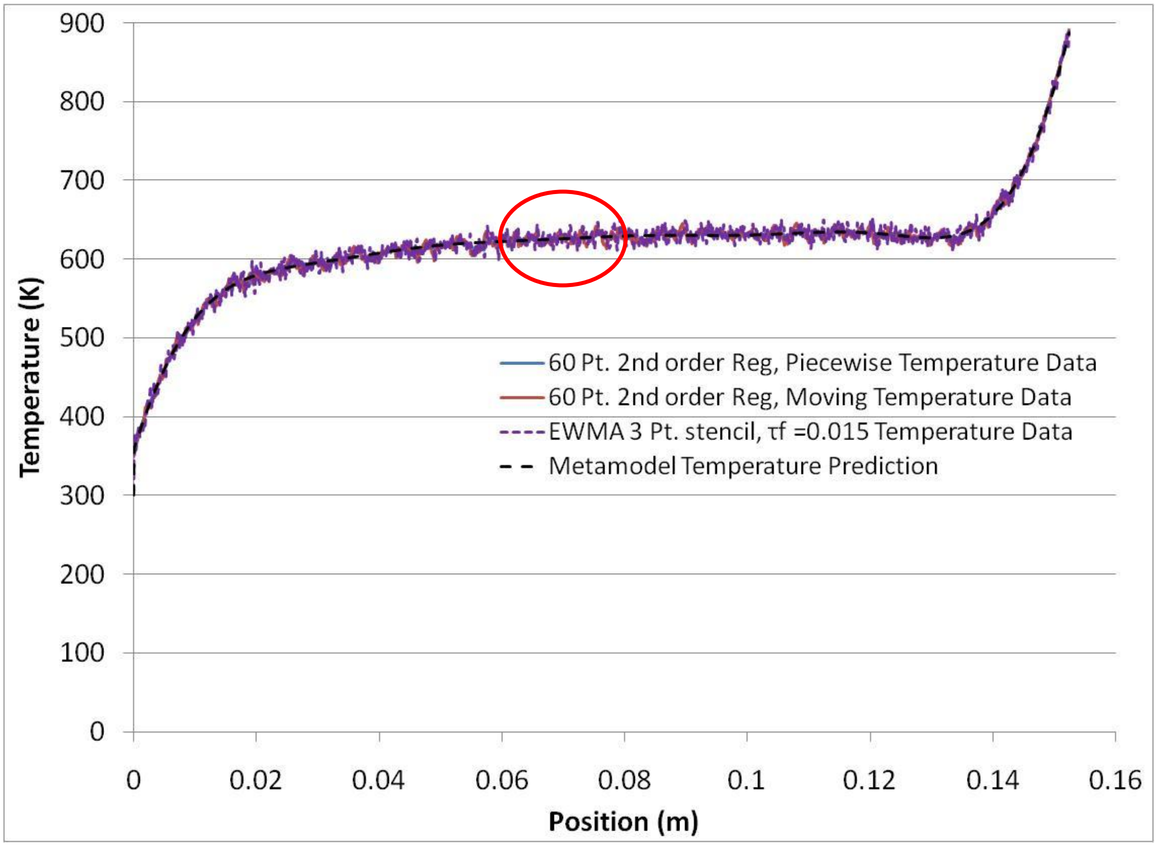

Figure 5-22: Graph of temperature vs. position along the weld specimen for the regression models and EWMA filter

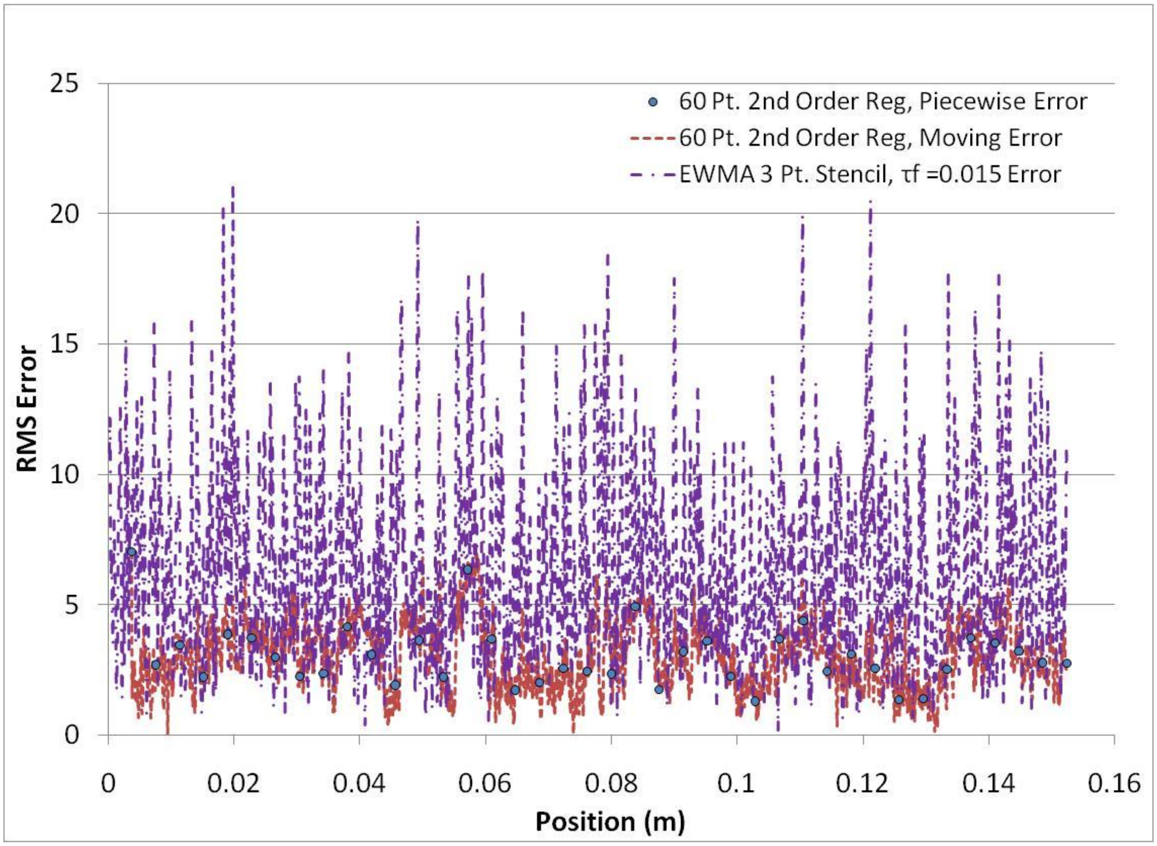

Figure 5-23: Close-up of temperature vs. position for regression models and EWMA filter

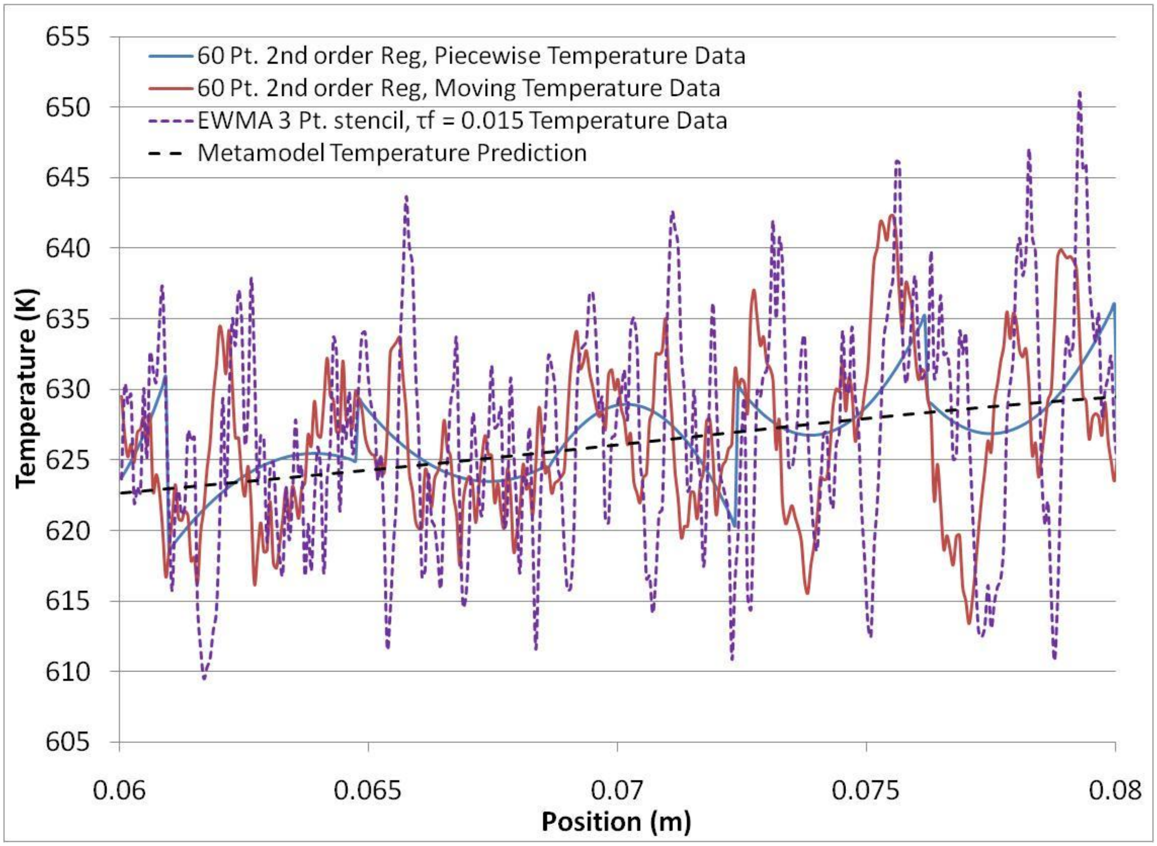

Figure 5-24:Graph of RMS error vs. position along the weld specimen for the regression models and EWMA filter

Shown in Figure 5-22 are the plots of temperature vs. position along the workpiece; shown in Figure 5-23 is a close up view of the temperature plots between the positions of *x* = 0.06m and *x* =0.08 to see the effects of the different methods. Lastly, shown in Figure 5-24 are the plots of RMS error vs. position on the workpiece. In Figure 5-22, Figure 5-23 and Figure 5-24, τf is the filter time constant found in Section 5.4.2. In the temperature vs. position plots, the underlying dotted black line shows the metamodel prediction of the temperature field and the lines overlapping it are the results of the various filtering techniques applied to the noisy data. The only methods that can be seen clearly in Figure 5-22 are the EWMA model (dotted purple line) and the 2^{nd} order moving window regression (solid red line). Those two methods exhibit greater overall error than the 2^{nd} order piecewise window regression (solid blue line). As a result, the data smoothed with the 2^{nd} order piecewise method is not seen in Figure 5-22. The overall effects of the three different methods is more apparent in Figure 5-23. This result is further demonstrated by the graph of RMS error vs. position, shown in Figure 5-24. Across the workpiece the RMS error of the 2^{nd} order piecewise window (blue circles) is lower than both the EWMA model (purple dotted line) and the 2^{nd} order moving window (dotted red line). One observation is that the EWMA model has the highest RMS error by position than either of the regression models. The following sections discuss the physical implantation of these noise filtering schemes and the experimental validation of the control system with noise filtering.

5.5 Experimental Validation of Smoothing and Control

The following sections outline the experimental validation of the theoretical simulations presented in Section 5.3. The experiments performed on six inch long specimens will be discussed in conjunction with the simulated results; then experimental results performed on twelve inch specimens is presented and discussed.

5.5.1 Experimental Hardware and Data Acquisition

Experimental validation was performed on the welding test station designed and built by the Seepersad design group. The data acquisition motor controller hardware is described below.

- PC running an AMD64 3500+ processor with 2GB of RAM
- Operating System: Windows XP SP3
- Data Acquisition and Motor Control Software: LabView 2009

Motion Control Hardware

- National Instruments: PCI 7340 motion control card
- National Instruments: NI UMI 7764 motion controller

Data Acquistion Hardware

- National Instruments: PCI 6229 M series DAQ card
- National Instruments: SCC 2345 Signal Conditioning Connector Block
- National Instruments: SCC-PWR02 Power Module
- National Instruments: SCC-TC02 K-type Thermocouple Module
- National Instruments: SCC-AI01 42-V Input module with 10Khz filter
- National Instruments: SCC-AI03 10-V Input module with 10Khz filter
- National Instruments: SCC-FT01 10-V Feed through Module
- Omega: OS554A infrared pyrometers

For data acquisition, the various modules have specific roles for the types of signals they handle. All of the SCC modules are mounted in the SCC 2345 Signal Condition Connector block which is connected to the PCI 6229 mounted in the PC. In the following experiments all of the equipment is used except for the thermocouple modules since no thermocouple data was taken. The SCC-AI01 module was connected to the welding power supply to measure welding voltage used during testing. The SCC-AI03 was connected to the amp meter that measures the current drawn during welding. The SCC-FT01 modules handle the IR pyrometer temperature measurements. Motion control data is acquired using a separate set of hardware. All data related to the motion control is acquired directly from the NI PCI 7340 DAQ card. For more insight into the motion control system, interested readers are referred to Backlund (2008).

5.5.2 Experiments on six inch long specimens

Outlined in Sections 5.3.1and 5.3.2 were the use of models to predict the best controller constants for a Proportional, Integral and Derivative (PID) controller. Using the rough trends in the temperature dynamics observed through the use of analytical models such as the Rosenthal model and surrogate models, i.e. metamodels, control constants were found and simulated computationally to gauge their accuracy. In this section, experimental data is presented to corroborate the simulated data. From Section 5.3.1 , the Rosenthal model served as a potential bound on values for the proportional constant, K_p, and from Section 5.3.2, the metamodel paired with a controller provided controller tuning. In the following figures, similar logic as described in Section 5.3.2 to fine tune the control parameters applies to the experiments performed. As each parameter is tested, its performance is assessed to determine overall desirability in terms of performance. Shown in Figure 5-23 is the schematic of the test specimen used for the validation testing done on six inch long specimens. The specimens were single pieces of CuZn 90/10%wt with nominal dimensions of .0508m x 0.1524m x 0.00635m (2 inches x 6 inches x ¼ inches).

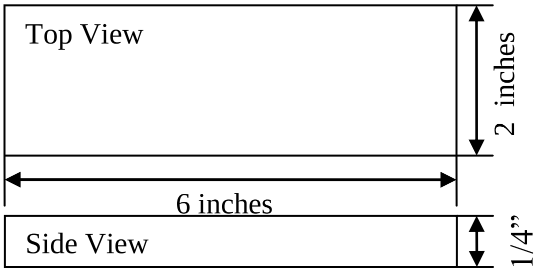

Figure 5-25: Schematic of six inch test specimen used for validation tests

Outlined in Table 5-4 and Table 5-5 are the welding test parameters and torch parameters used during validation testing. These parameters were used for both six inch and twelve specimens.

Table 5-4: Welding test parameters used for study

Voltage (V)	Feed (mm/s)	Speed (mm/s)	# Passes
22	169 (400 ipm)	2.117 (5 ipm)	1

Table 5-5: Torch Parameters

Argon Flow Rate	Head Angle	Distance to Work Height
40 cfh	71 degrees	9.65 mm (~0.38”)

Shown in Figure 5-26 is a plot of temperature and velocity vs. time for a controlled weld experiment using proportional control only. In this experiment, temperature, position and velocity data are taken every 50ms and control decision made every 50ms. The proportional constant is K_p = 1 inch per minute/Deg C (0.000423 m/sK) and chosen to be smaller than the proportional constant found using the metamodel (K_p = 0.001 m/sK) in order to characterize the region around K_p = 0.001 m/sK and to examine if there is any gain from decreasing the proportional constant on the physical system.

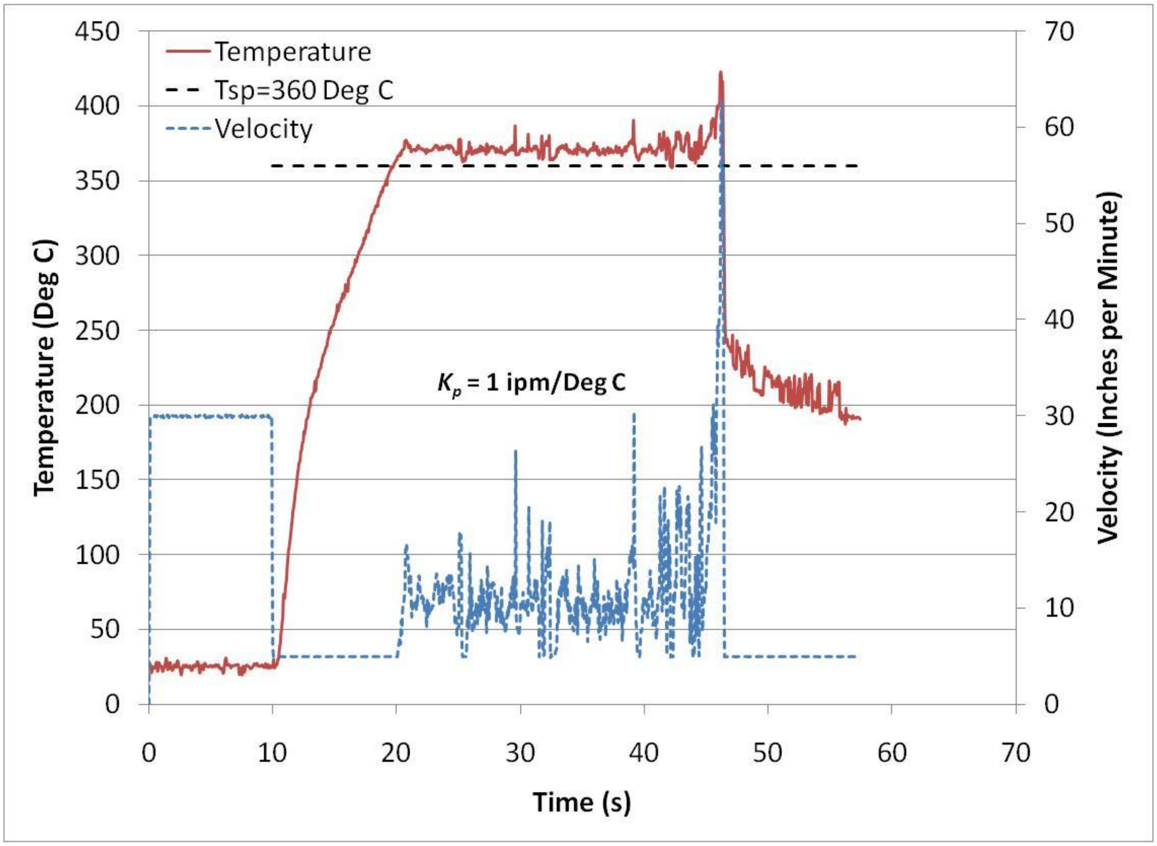

Figure 5-26: P controlled weld proportional control only, K_p = 1 inch per minute/ Deg C

As shown in Figure 5-26, the temperature response comes close to the set point temperature but is offset from it in the steady state portion of the weld. The controller does a fair job of regulating temperature but is not robust enough to control the temperature rise due to end of weld effects and not aggressive enough to curb the initial transients to reduce the initial offset from the set point temperature. This indicates that by increasing the proportional constant, it is possible to get a better control response in the temperature.

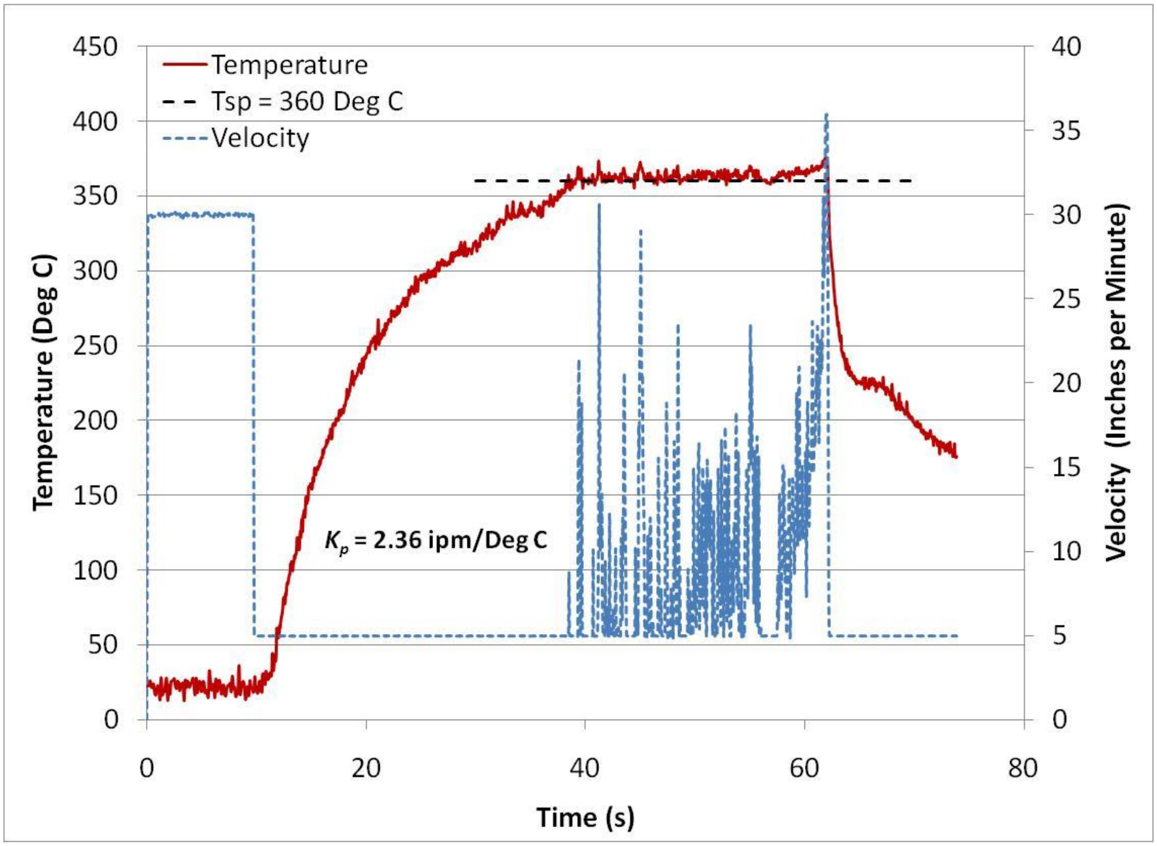

Figure 5-27: P controlled weld proportional control only, K_p = 2.36 inch per minute/ Deg C

Shown in Figure 5-27 is a plot of temperature vs. time and velocity vs. time for a controlled weld using proportional control only. In this experiment, temperature, position and velocity data are taken every 50ms and control decision made every 50ms. The proportional constant is K_p = 2.36 inch per minute/Deg C (K_p = 0.001 m/sK) which is identical to the tuned proportional parameter found from using the metamodel paired with a P controller, K_p = 0.001 m/sK. In comparision to the temperature plot in Figure 5-26, the temperature settles at the set point temperature during steady state and the controller does a better job of controlling the end of weld effects. There is a noticeable decrease in the temperature departure around 60 seconds whereas in Figure 5-26 the temperature departure at the end of weld is greater. This shows that the metamodel did a good job of predicting steady state behavior and served as a useful heuristic in designing a controller. One difference between the metamodel prediction and the physical system is that the metamodel predicted an overshoot with a K_p = 0.001 m/sK. This did not happen in the real system but the metamodel was able to represent the steady state conditions and end of weld conditions with fair agreement, this is corroborated by Figure 5-15. From the results of Figure 5-27, it is possible to increase K_p to force a faster dynamic and cause an overshoot. The results for K_p = 11.5 inch per minute/Deg C (K_p = 0.00487 m/sK) are shown in Figure 5-28.

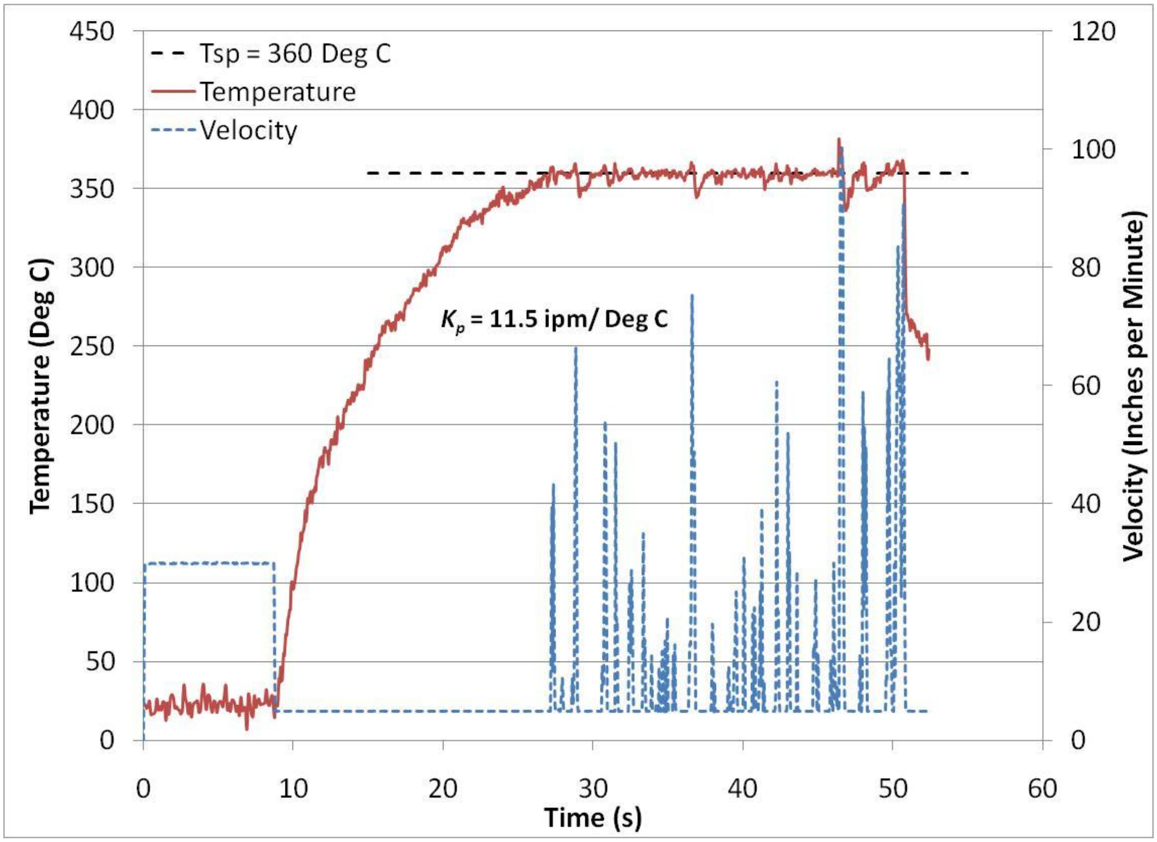

Figure 5-28: P controlled weld proportional control only, K_p = 11.5 inch per minute/ Deg C

Shown in Figure 5-28 is a plot of temperature and velocity vs. time for a controlled weld using proportional control only , where is K_p = 11.5 inch per minute/Deg C (0.00487 m/sK). In this experiment, temperature, position and velocity data are taken every 50ms and control decision made every 50ms. This value for the proportional constant was chosen since it corresponds to the value of the slope of the line of the first derivative of temperature vs. velocity from Figure 5-9. In contrast to the temperature curve in Figure 5-27, the controller with K_p = 11.5 inch per minute/Deg C (0.00487 m/sK) holds the temperature to the set point but is better able to control the temperature dynamics at the end of the weld than the previous value of K_p. As a result, the controller can hold the temperature in the welded workpiece to the set point temperature all the way to the end of the weld. Shown in Figure 5-29 is the temperature vs. time for a PI controlled weld that compares K_p = 2.36 inch per minute/Deg C (0.001 m/sK) and K_p = 11.5 inch per minute/Deg C (0.00487 m/sK) with integral action with τ_i = .02. In this experiment, temperature, position and velocity data are taken every 50ms and control decision made every 50ms. The functional form of the PI controller used corresponds to Eqn. 31 in Section 5.2.2. In both cases the controlled welds do not reach the temperature set point. The reason is because of how integral action is applied in the control system. Integral action will increase the control signal for any positive error signal and decrease the control signal for any negative error signal for a positive value of the proportional constant, K_p. In the LabView® program used to control the welding test station, there is a logic inverter in the control system hence for a positive error there is a decrease in control action. As a result, the integral action forced the velocity to increase at each integral kick hence is the reason why the welding test specimen never reached the setpoint temperature. As observed in Figure 5-27 and Figure 5-28, the P-controlled welds have exact set point tracking with no steady state offset. For this reason, there is no need for integral control action. One conclusion that is drawn from Figure 5-29 is the faster dynamics of the weld with K_p = 11.5 inch per minute/Deg C (0.00487 m/sK). The higher proportional constant causes a steeper temperature rise in the workpiece, yet from Figure

5-28 it has better steady state control dynamics since the controller is able to control the temperature through the end of the weld.

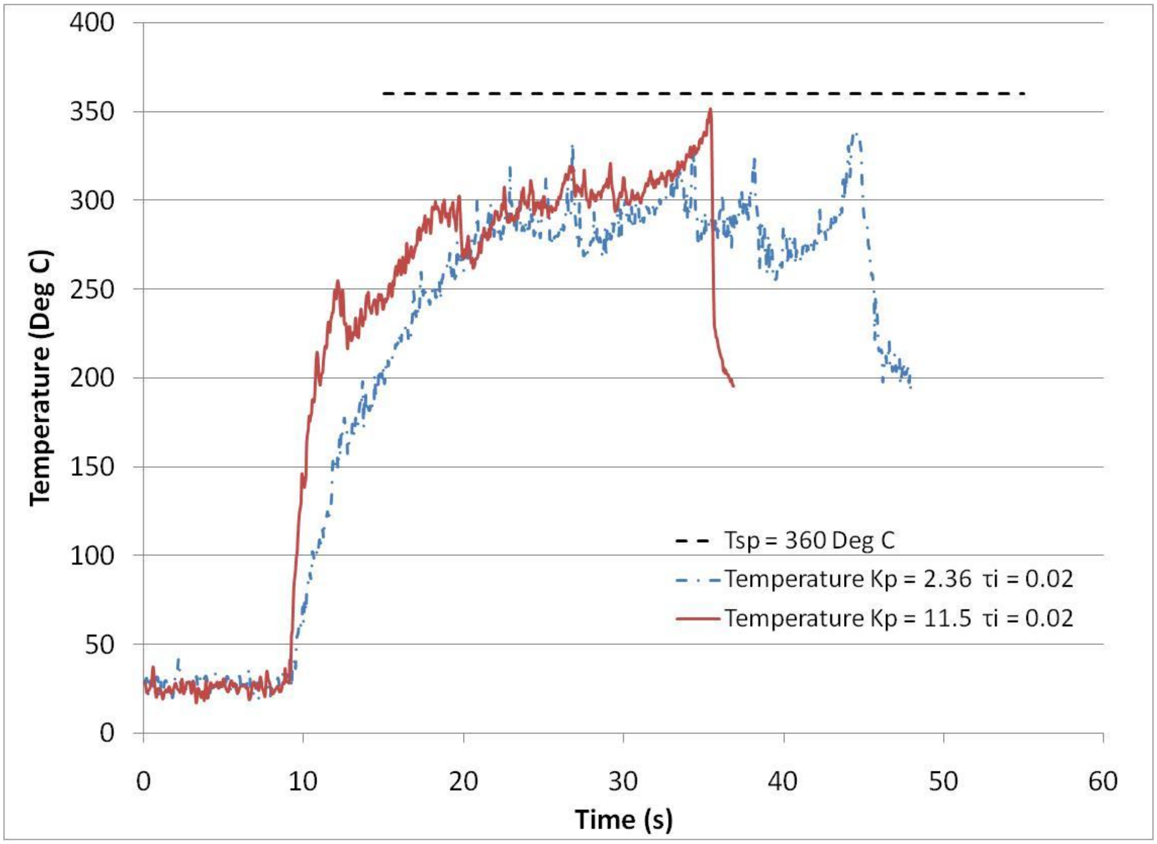

Figure 5-29: Temperature vs. Time for PI controlled weld, K_p = 2.36, K_p = 11.5 inch per minute/ Deg C and τ_i = 0.02

In the next section an experiment performed on an 1/8 inch thickness specimen to assess whether a proportional constant of K_p = 11.5 inch per minute/Deg C (0.00487 m/sK) will achieve the fastest dynamics for this system.

5.5.2.1 Validation test performed on 1/8 inch thickness specimen

An experiment was performed on a thin specimen to determine whether our controller is achieving the fastest dynamics possible. The specimens were single pieces of CuZn 90/10%wt with nominal dimensions of 0.0508m x 0.1524m x 0.003175m (2 inches x 6 inches x 1/8 inches). Shown in Figure 5-30 is a schematic of the one piece thin specimen used for validation testing of the PID controller.

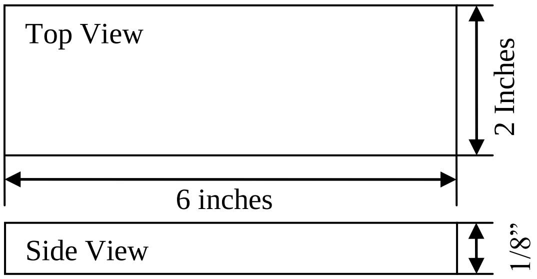

Figure 5-30: Schematic of thin six inch test specimen for validation testing

Shown in Figure 5-31 is a plot comparing temperature vs. time for an uncontrolled weld and a controlled weld with K_p = 11.5 inch per minute/Deg C (0.00487 m/sK). In this experiment, temperature, position and velocity data are taken every 50ms and control decision made every 50ms, for the uncontrolled weld temperature, position and velocity data are taken every 50ms. Eighth inch thick material was chosen for this experiment to assess the temperature dynamics in thin specimens. The use of thin specimens allows for the study of the temperature dynamics without the additional contribution of the material’s thermal `capacitance slowing down the dynamics of the temperature evolution. The uncontrolled weld shown in Figure 5-31 was performed using the welding parameters and torch parameters outlined in Table 5-4 and Table 5-5 and setup as outlined in Figure 5-10.

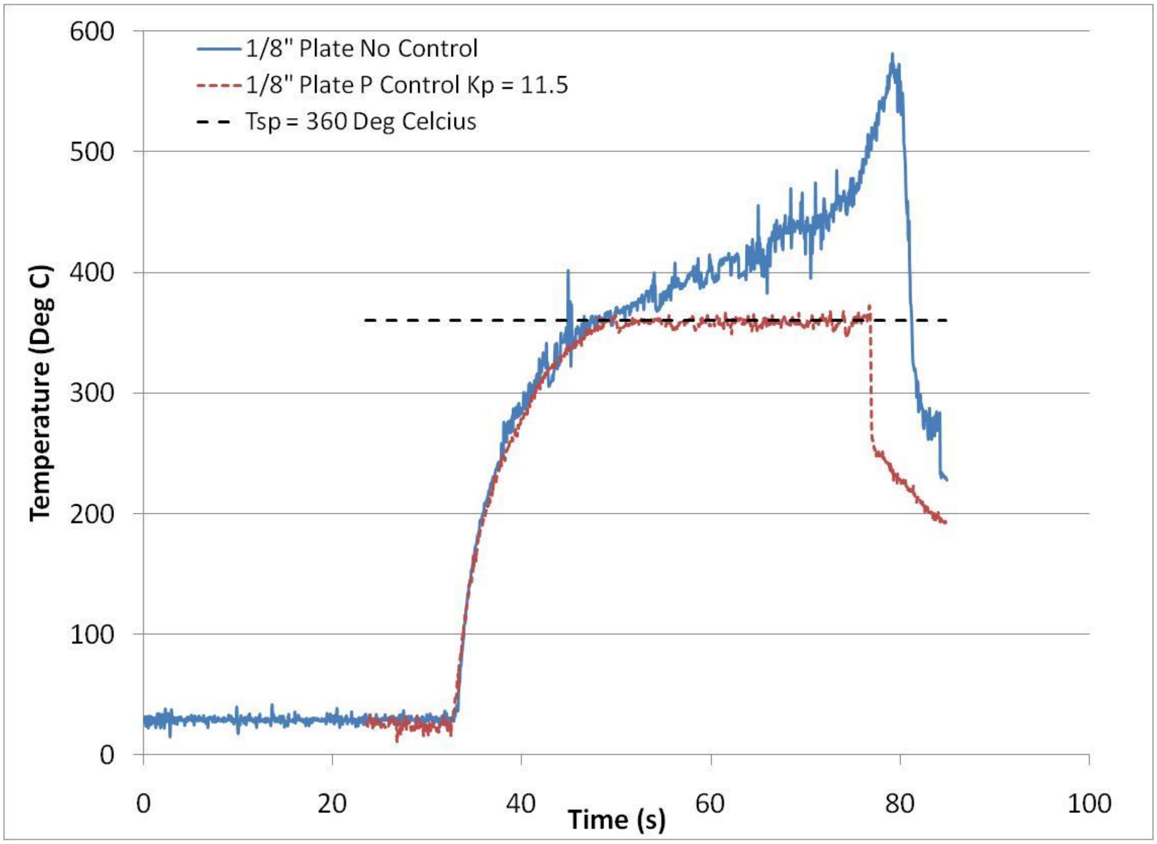

Figure 5-31: Temperature vs. time for P controlled weld and an uncontrolled weld on a 1/8 inch thick specimen

Comparing the temperature profiles of the controlled and uncontrolled weld in Figure 5-31 validates K_p = 11.5 inch per minute/Deg C (0.00487 m/sK). The uncontrolled weld on a 1/8 inch thick specimen represents the fastest thermal dynamic that could be observed for this system. The heat rate for both cases is the same and the uncontrolled weld is only hindered by the thermal resistivity of the welded metal. Additionally, since the specimens are thin the thermal dynamics are not slowed by additional thermal capacitance of the material, the system is lumped from a thermal standpoint, and hence this is the fastest dynamic possible for this system. Examining the temperature profile of the controlled weld it is seen in Figure 5-31 that the temperature profile of the controlled weld lays exactly on top of the uncontrolled weld up until reaching the set point temperature. At this point the temperature of the uncontrolled weld continues to grow and the controlled weld tracks the set point until the end of the weld. The observation that the controlled weld tracks exactly with the uncontrolled weld means that the controller is saturated and cannot push the dynamics of the system any faster since it is already matching the thermal dynamics of the uncontrolled system. This is the most desirable case; the dynamics of the system are developing as fast as possible and then adhering to the desired setpoint. The conclusion drawn from Figure 5-31 is that K_p = 11.5 inch per minute/Deg C (0.00487 m/sK) is the best control constant for this system and at the same time it was found by examining temperature vs. velocity data produced by thermal models.

With the establishment of the value of proportional constant that is appropriate for this system, the robustness of the controller is examined for specimens longer than six inches and to see if there is any improvement by including further prediction capabilities to the controller via data regression and extrapolation.

5.5.2.2 Experimental Validation of Regression and Extrapolation on six inch specimens

For this trial a change in procedure was introduced to implement a 1000 point average sampling at each discrete time step that data were taken. This feature was added to help smooth some of the random noise that was observed in previous trials in order to provide the controller a cleaner error signal on which to make control decisions and reduce the amount of sporadic over and under-correcting. An additional change was the inclusion of data regression and extrapolation to the P controllers. This was outlined in Sections 5.4.1 and 5.4.3. The investigation was to assess whether the use of regression and extrapolation of real time data enhances the predictive capabilities of controller to predict and correct for conditions happening one time step into the future. This implementation is to examine how the regression and extrapolation functions improve the capability of the P controller in a physical system on a six inch specimen.

Shown in Figure 5-32 is a plot that compares a standard P controller and a P controller with Regression and Extrapolation. The comparison metric is the standard deviation in the steady state region. For both controllers, K_p = 11.5 inch per minute/Deg C (0.00487 m/sK).

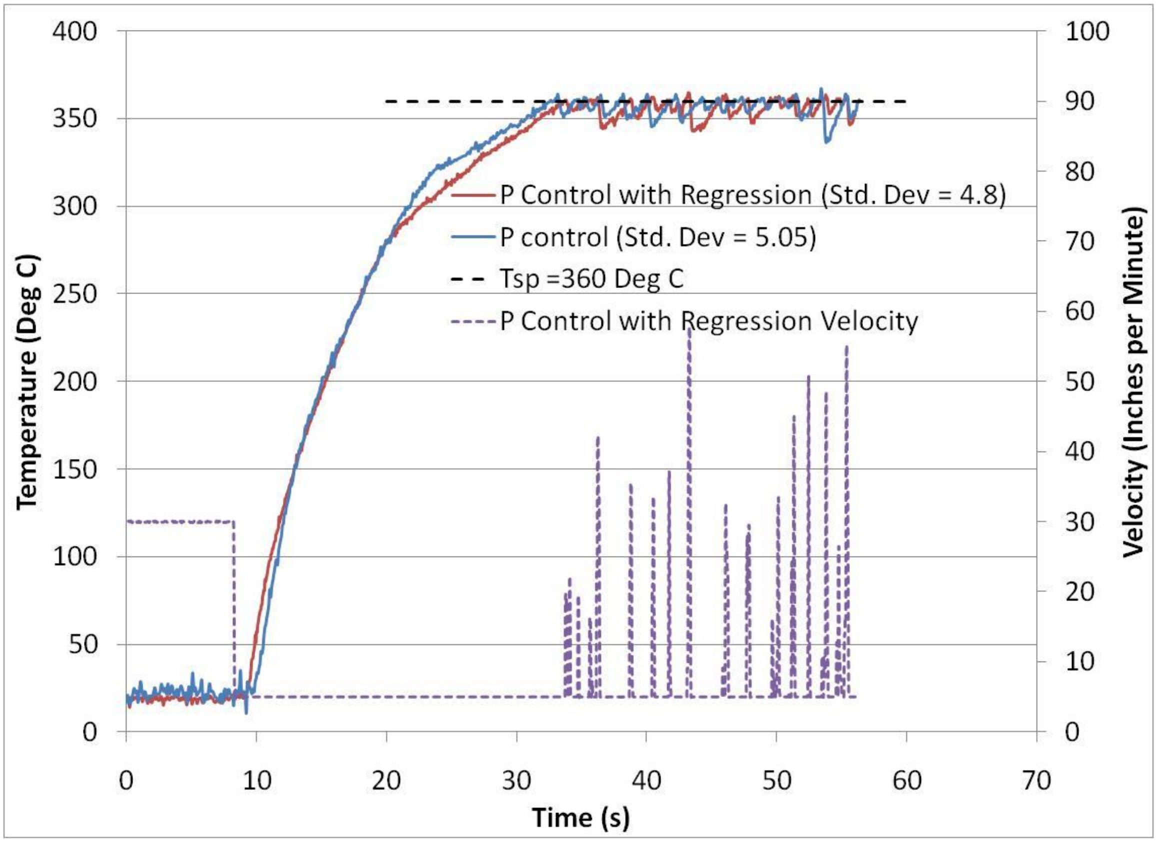

Figure 5-32: Temperature vs. Time for P controlled weld with regression and extrapolation, K_p = 11.5, Δ*t* = 25ms and a P controlled weld K_p = 11.5, Δ*t* = 75ms

In this trial the P controller is sampling every 75ms and making control decisions every 75ms. The P controller with regression and extrapolation samples data every 25ms and makes a control decision every 75ms using a regression of previous and current data and extrapolating 25ms (one time step) into the future. As annotated in Figure 5-32, the standard deviation for each method was tabulated for the steady state region of each weld and it was found that the standard deviation for the P controller with regression and extrapolation was 4.8 K and the standard deviation for the standard P controller was 5.05

K. The result is that the addition of Regression and Extrapolation to the controller adds a mild improvement.

5.5.3 Experiments on twelve inch long specimens

Shown in Figure 5-33 is the schematic of the test specimen used for the validation testing done on 12 inch long specimens. The specimens were single pieces of CuZn 90/10%wt with nominal dimensions of 0.0508m x 0.3048m x 0.00635m (2 inches x 12 inches x ¼ inches).

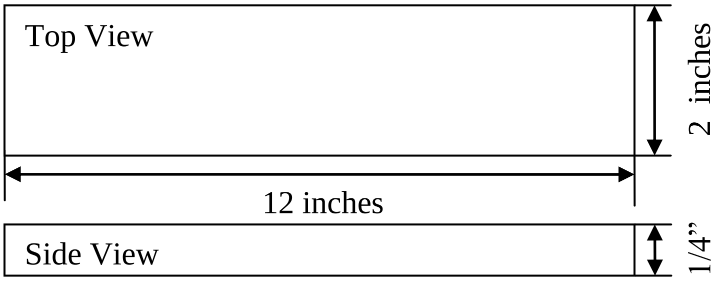

Figure 5-33: Schematic of twelve inch test specimen used for validation tests

One procedural change that took place for the validation testing of the twelve inch specimen was the implementation of 1000 point average sampling at each discrete time step that data were taken. This feature was added to help smooth some of the random noise seen in the data in order to provide the controller a cleaner error signal on which to make control decisions and reduce the amount of over and under-correcting. Testing the data regression and extrapolation feature on a longer test specimen was to assess whether there is addition benefit on a longer specimen and to investigate if there are any adverse effects of using the regression and extrapolation for longer periods of time. More specifically, it is important to know if there is any effect to the robustness of the control system.

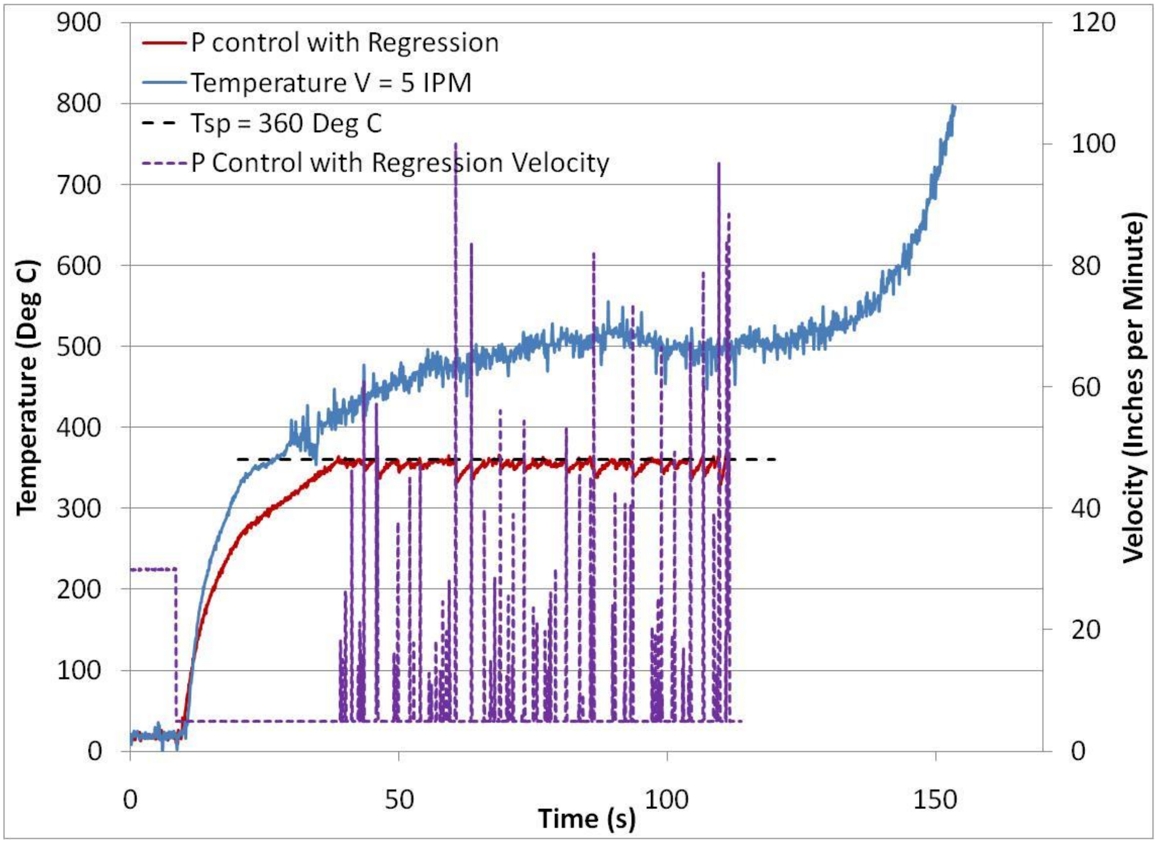

Figure 5-34: Temperature and Velocity vs. Time for P controlled weld with regression and extrapolation, K_p = 11.5, Δt = 25ms

Shown in Figure 5-34 is a graph of temperature vs. time and velocity vs. time for weld performed on a twelve inch long, one piece specimen. In this trial 1000 points were averaged every 25ms and a controller correction was made every 75ms using data that was extrapolated 25ms (one time step) into the future. In the comparison of the controlled weld vs. the uncontrolled welding it is observed that the controller was effective in controlling the temperature and holding it to the desired set point for the whole course of the weld. The next experiment gauges the effectiveness of the P controller with regression and extrapolation against a standard P controller.

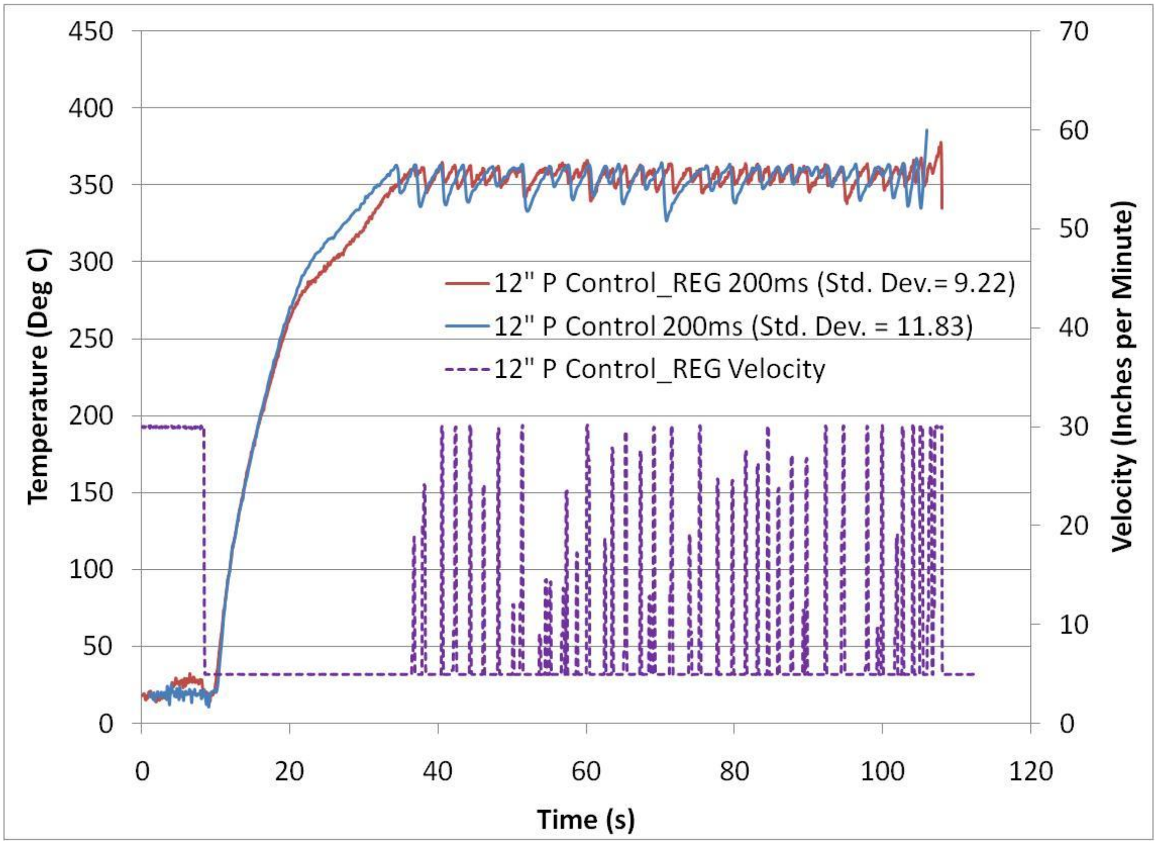

Figure 5-35: Temperature vs. Time for P controlled weld with regression and extrapolation, K_p = 11.5, Δ*t* = 50ms and a P controlled weld K_p = 11.5, Δ*t* = 200ms

Shown in Figure 5-35 is a plot that compares a standard P controller and a P controller with Regression and Extrapolation. Also plotted in Figure 5-35 is the velocity response for the P controller with Regression and Extrapolation. The comparison metric is the standard deviation in the steady state region. For both controllers, K_p = 11.5 inch per minute/Deg C (0.00487 m/sK) but one restriction for this trial was an upper and lower bound put on the controller of 30 inches per minute (0.0127 m/s) and 5 inches per minute (0.002117 m/s) respectively. Another change for this trial is that P controller is sampling every 200ms and making control decisions every 200ms. The P controller with regression and extrapolation samples data every 50ms and makes a control decision every 200ms using a regression of previous and current data and extrapolating 50ms (one time step) into the future. These changes were made to make use of the posit that the characteristic time to see a change at the location where the IR pyrometers are measuring are on the order of 136ms to 177ms (Ely, 2010). As annotated in Figure 5-35, the standard deviation for each method was tabulated for the steady state region of each weld and it was found that the standard deviation for the P controller with regression and extrapolation was 9.22 K and the standard deviation for the standard P controller was 11.83 K. The result is that the addition of regression and extrapolation to the controller adds a mild improvement but not one that is statistically significant when the pyrometer uncertainty is taken into account.

5.5.4 Metamodel Based Control

Outlined in this section is the experimental validation of the metamodel based process control using the metamodels that were outlined in Section 4.2.1. As outlined previously, a Support Vector Regression (SVR) metamodel was trained from FLUENT$^{\copyright}$

models to calculate temperature as a function of traverse speed and heat input, $T = f(V,Q)$. The metamodel is paired with a P controller that was previously tuned, as outlined in Section 5.5.2. In the following experiments the metamodel prescribes the temperature trajectory in the steady state region of the weld and the P controller drives the physical system to adhere to the metamodel trajectory.

5.5.4.1 Metamodel based controller

As discussed in Section 4.2, because of some of the differences in the FLUENT© model and the physical system, there are dissimilarities in the beginning of weld and end of weld transients. But because of the good agreement between the model and experimental data in the steady state region, metamodels may be employed as steady state controllers for the process.

Shown in Figure 5-36 is a schematic of the work piece that outlines the regions that the metamodel controls during the welding process. In order to effectively use the metamodels in the region where they are best suited, the first and last two inches of the work piece are controlled by a standard P controller as employed in Section 5.5.2. After 0.0508m (2 inches) the initial transients have died out and weld is into the steady state regime. After 0.254m (10 inches), the PID controller takes over the control and controls the dynamics until the end of the work piece is reached.

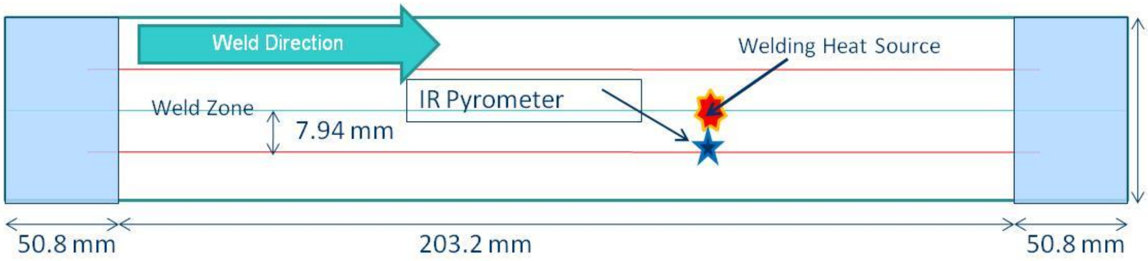

Figure 5-36: Schematic of area of the work piece controlled by metamodel

Shown in Figure 5-38 is the plot of temperature vs. time for a controller based on a metamodel trained from the data shown in Figure 4-6. The metamodel is paired with a P controller (K_p = 2.36 inch per minute/Deg C (0.001 m/sK)) and is used to control the regions of the weld specimen as outlined in Figure 5-36. The initial and final transient regions are governed by a P controller (K_p = 11.5 inch per minute/Deg C (0.00487 m/sK)). In all of the metamodel based control experiments, temperature, position, velocity, voltage and current are taken every 100ms. Every 100ms control decisions are made based on metamodel calculations that are also performed every 100ms.

Metamodels are capable of calculating temperature fields accurately and quickly but they do not take into account potential transient effects that can come about through process conditions or other dynamic changes that come about during welding. More specifically, the transient effects that manifest through the velocity changes that occur during a velocity controlled weld. Shown in Figure 5-37 are two plots of temperature vs. position that show separate metamodel calculations connected by transient response curves. During a velocity change the metamodel can calculate full temperature fields that pertain to the initial and final velocities of the velocity change.

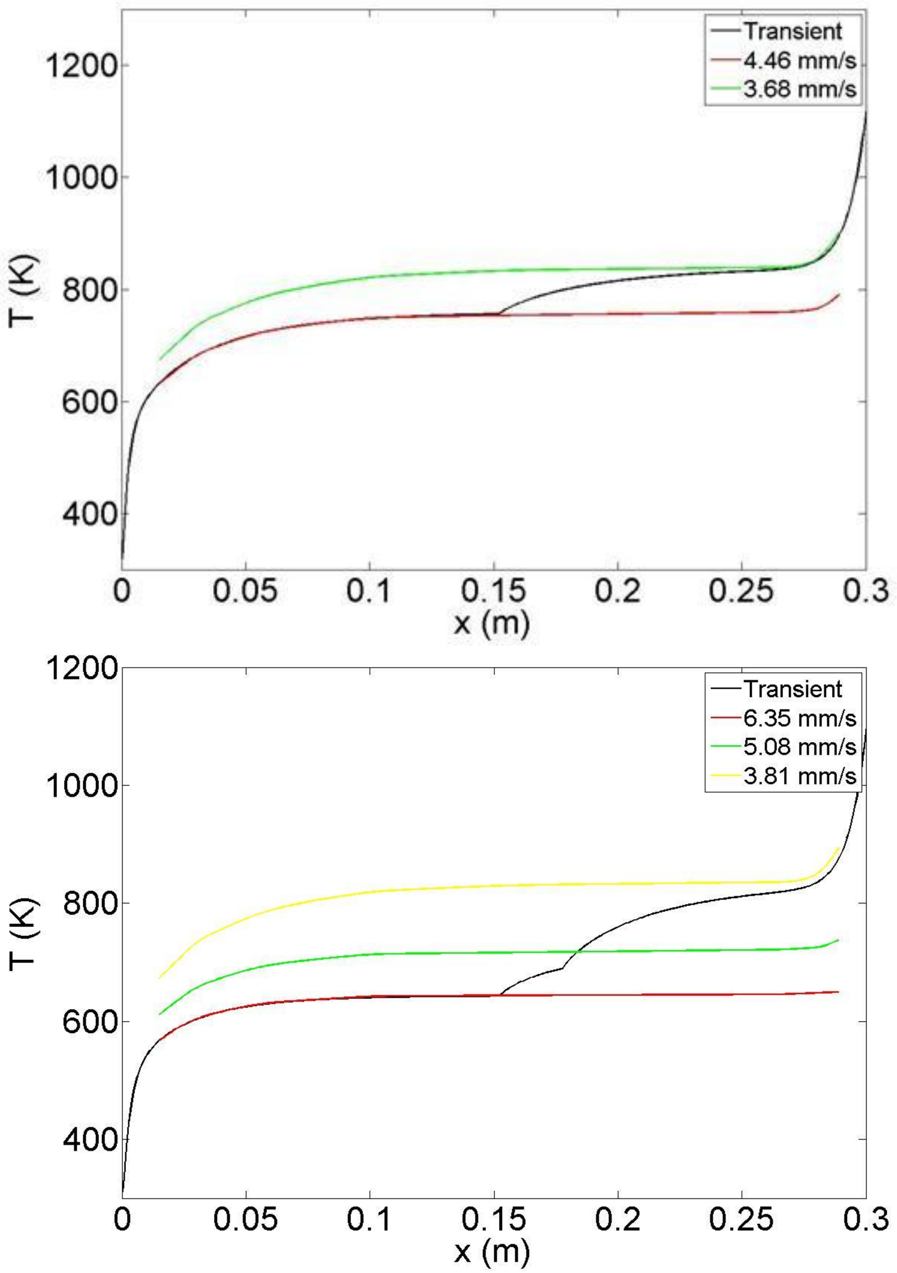

Figure 5-37: Plots of temperature vs. position that show transients that connect different metamodel trajectories (top) one velocity change (bottom) two velocity changes (Ely, 2010)

Reflected in Figure 5-37, the black lines are the transient temperature responses that the metamodel does not take into account when transitioning from one velocity to another. Shown in Figure 5-37 are plots that demonstrate a transient response for single and double velocity change. Since the metamodel does not take in account these intra-velocity transient effects, separate functions will be implemented in to the metamodels to take these effects into account. Shown in Figure 5-38 is a metamodel controlled weld that does not take into account transient effects.

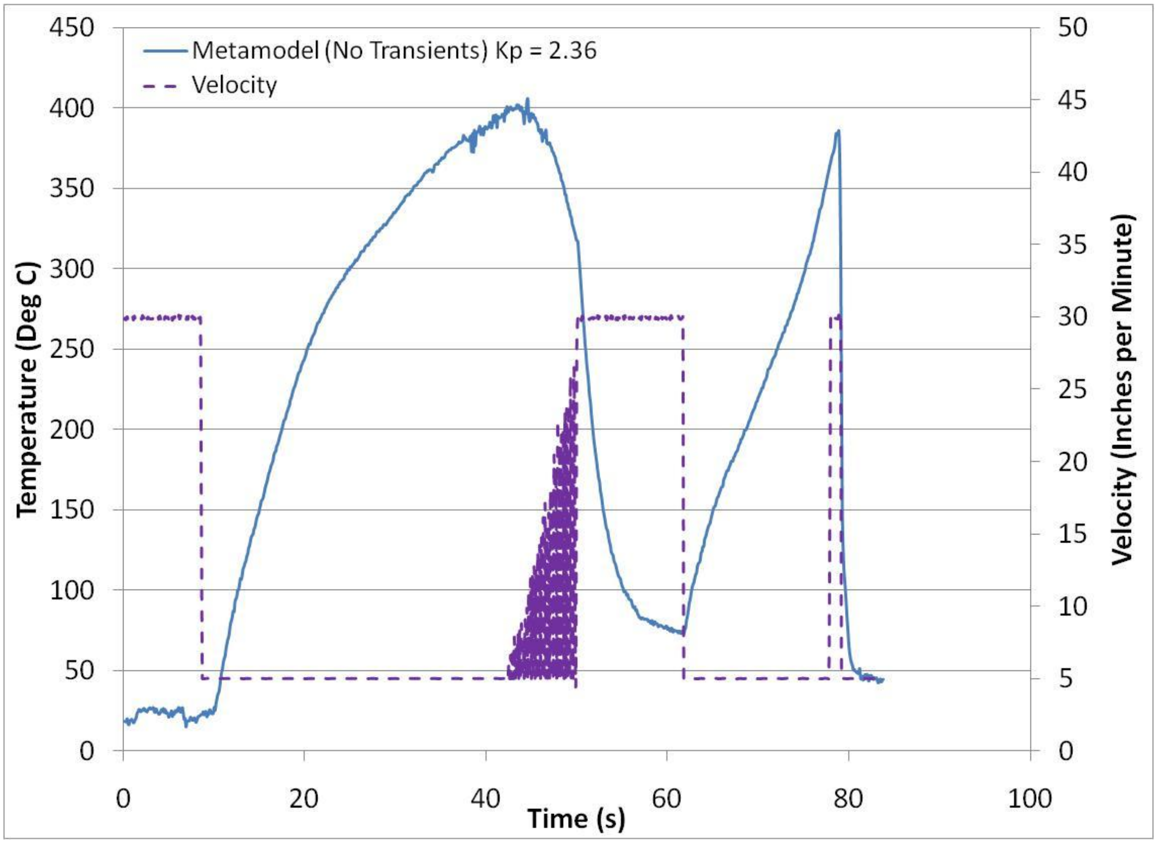

Figure 5-38: Temperature vs. time for metamodel based controller without transient effects, K_p = 2.36

As shown in Figure 5-38, the metamodel without transient effects does an unsatisfactory job of controlling the temperature of the weld in the steady state region. In the control scheme, the metamodel takes in traverse speed, *V* and heat input, *Q* and calculates the expected temperature. This temperature is sent to controller and the controller will react based on the estimated temperature. In this manner the temperature trajectory is based solely on the metamodel predictions. The poor performance of this control is explained by the fact that the metamodel responds to changes in velocity and estimates a new temperature based on velocity or perturbations in velocity and informs the controller of the new temperature without regard to temperature history. In essence the metamodel jumps from one temperature field based on traverse velocity to another temperature field without traveling along the path dictated by the transient temperature change as shown in Figure 5-37. A sensed change in the measured velocity of 0.00169 m/s (4 inches per minute) can cause the metamodel to predict a temperate that is 150 degrees lower than the current temperature and then inform the controller of an incorrect temperature change thus causing the controller to overreact. This is the case observed in Figure 5-38. After the metamodel takes over after 40s a perturbation in the velocity causes the metamodel to choose a temperature trajectory that causes the controller to overcorrect. This is remedied by introducing transient effects into the metamodel.

Shown in Figure 5-39 is a plot of a 0.3048m (12 inch) long and 0.00635m (1/4 inch) thick welding specimen that was run at a constant velocity of V = 0.002117 m/s (5 inches per minute) and a thinner, shorter specimen (0.003175 m (1/8 inch) thick and 0.1524 m (6 inches) long). The initial transient for both specimens is identical, shown boxed in dotted black. By looking at the initial transient, the time constant of the diffusion process may be ascertained. From this value of the time constant and initial transient, the metamodel is altered to include this transient response.

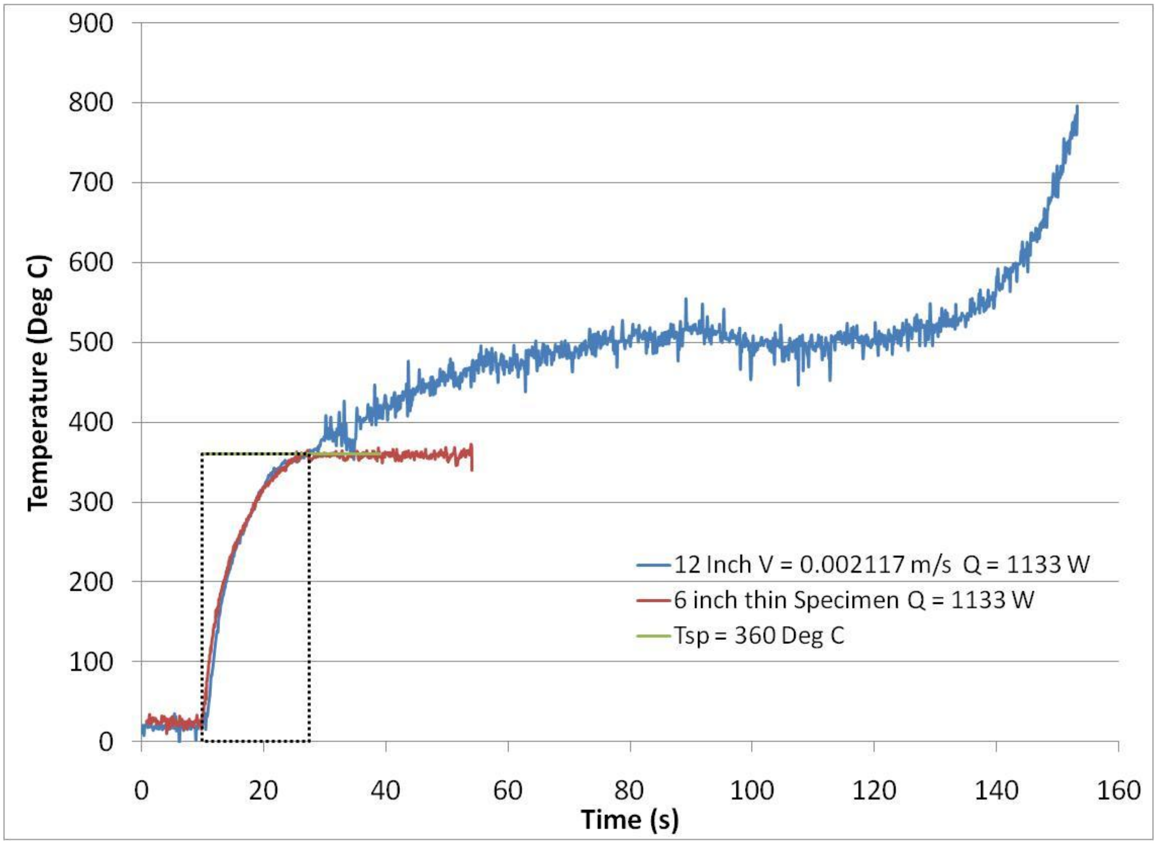

Figure 5-39: Temperature vs. time for two welding specimens that demonstrate initial transient effects

Shown in Figure 5-39 is the initial transient boxed in black. The transient is taken and curve fit to find the time constant. Plotted together in Figure 5-40 are the experimental data for the initial transient response and the curve fit to estimate the time constant.

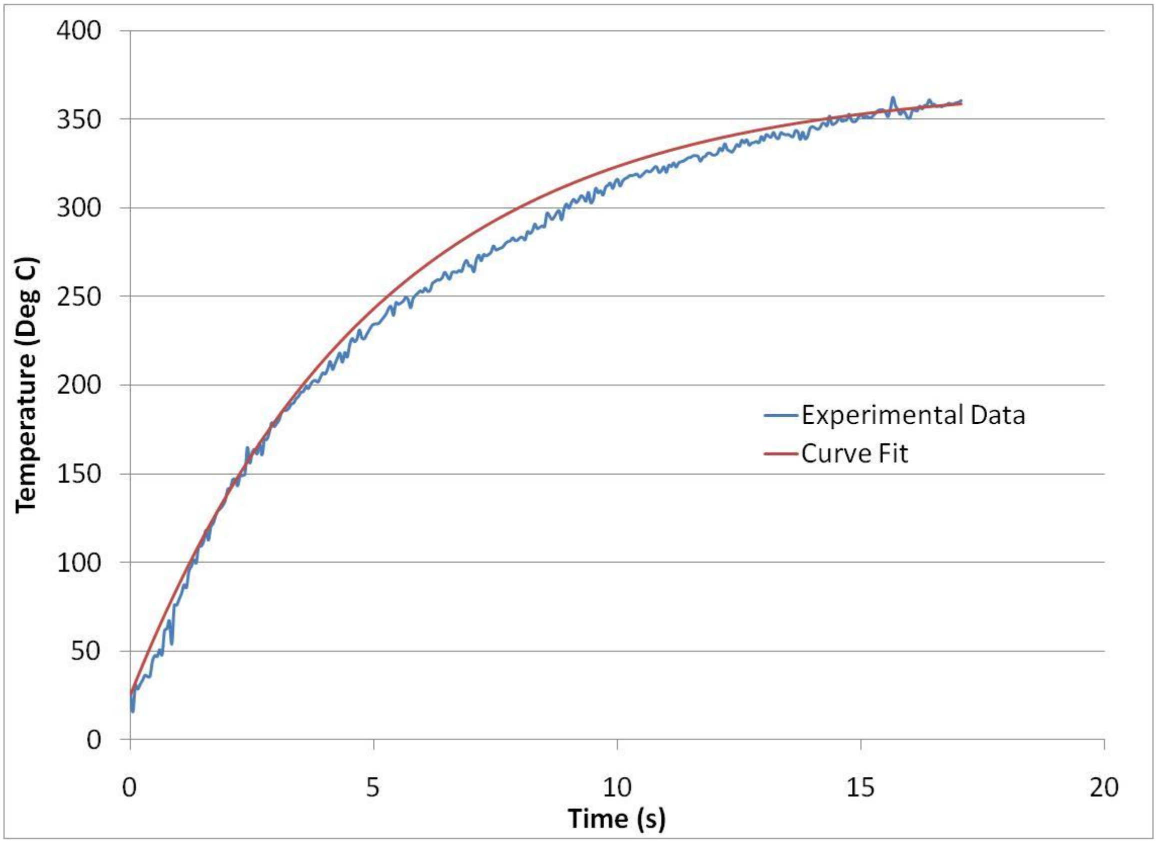

Figure 5-40: Temperature vs. time for initial transient from experimental data and the curvefit to estimate the time constant

It was found that the initial transient response of the system may be estimated by the following equation:

$$T_{new} = (T_{next} - T_{current}) * (1 - e^{-xt}) + T_{current} \tag{47}$$

where $T_{current}$ is the temperature at the current time step, T_{next} is the temperature that the system is trying to go to, x is a constant which is the reciprocal of the time constant, hence $x = 1/\tau$. T_{new} is the temperature that the system wants to go to at time t when taking into account the current temperature, $T_{current}$, the temperature that the system wants to go to, T_{next}, and the time constant, τ that constrains the system. Equation 47 is the dynamic equation that the metamodel will use in conjunction with the PID controller to help to tailor the trajectories that the metamodel estimates. For the integration into the physical welding system and integrating it with the metamodel, Equation 47 can be rewritten as:

$$T_{new} = (T_{metamodel} - T_{measured}) * (1 - e^{-.2\Delta t}) + T_{measured} \tag{48}$$

In Eqn. 48, the new temperature, T_{new} that is sent to the controller is based on the measured temperature at the current temperature, $T_{measured} = T_{current}$, the temperature that the system wants to go to which is calculated by the metamodel, $T_{metamodel} = T_{next}$ and governed by the time constant, τ and the time step Δt. It was found from Figure 5-40 that $x = 0.2$ or that $\tau = 5$. Equation 48 essentially recreates the curve from Figure 5-40 but in a piecewise manner. Equation 48 is the transient equation that was paired the metamodel for welding control. Shown in Figure 5-41 and Figure 5-42 are plots of temperature vs. time and velocity vs. time for metamodel controlled welds.

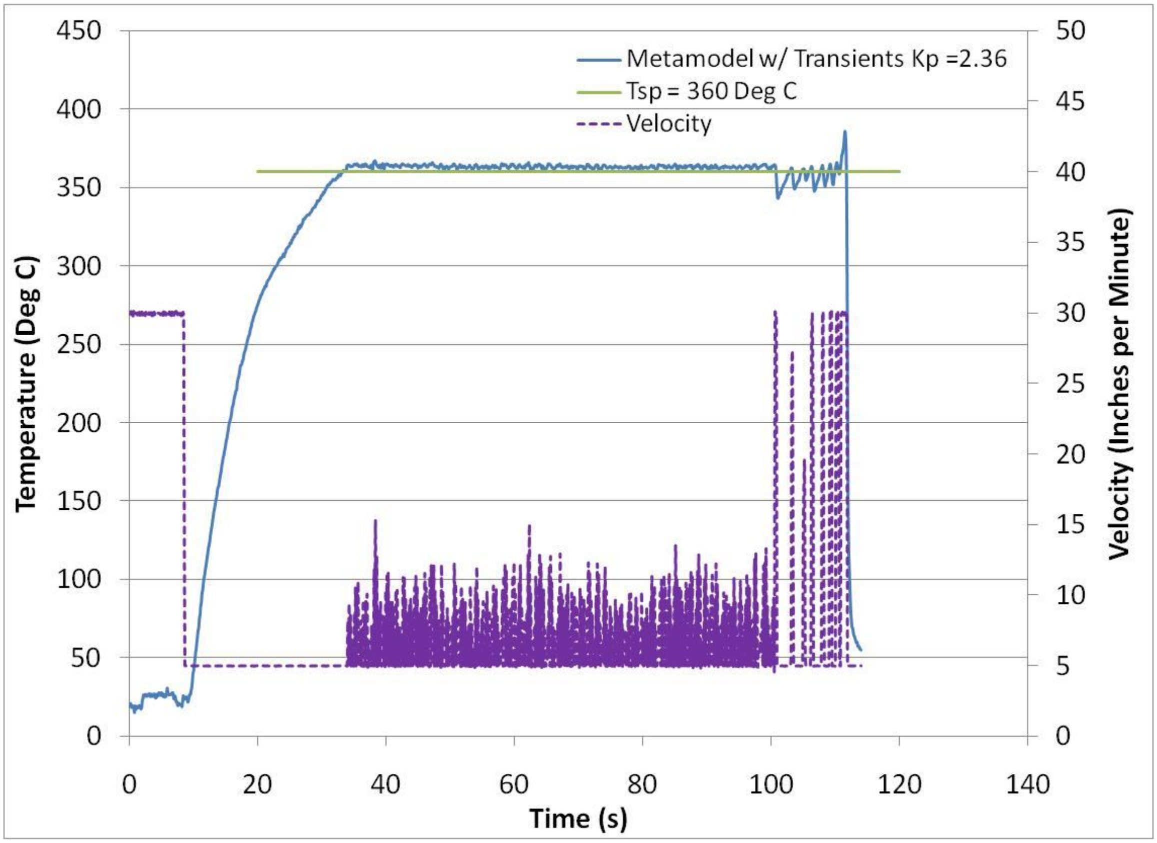

Figure 5-41: Temperature vs. Time and Velocity vs. Time for a controlled weld using a metamodel with dynamics, K_p = 2.36

Table 5-6: Performance metrics for the different control schemes, K_p = 2.36

Method	**Tavg**	**Standard Deviation**
P Control	353.3 Degrees C	7.6 Degrees C
P Control with Regression and Extrapolation	354.9 Degress C	5.3 Degrees C
Metamodel with P Control	362.1 Degrees C	2.0 Degrees C

Shown in Figure 5-41 is the temperature and velocity plot for a weld controlled by a metamodel with transients. K_p = 2.36 inch per minute/Deg C (0.001 m/sK) was chosen as the proportional constant as it found in Section 5.3.2 through computational modeling of the control system and tuning control models. As observed in Figure 5-41, the control response is smooth and controlled and there is less noise encountered than when using straight P control. Temperature data is used here in the piecewise treatment of the transient equation yet there is less noise affecting the system. The more jagged temperature response that occurs after 100s is attributed to the transition from the metamodel based controller to the straight P controller that controls the last two inches of the workpiece. For this experimental trial, it was found that the average temperature for the region of the workpiece that was controlled by the metamodel, T_{avg} = 362 Deg C. Shown in Table 5-6 are the performance metrics of the three different control scheme that were investigated. Although the P controller with regression and extrapolation shows a mild improvement, there is essentially no change from straight P control when taking into account the pyrometer uncertainty. On the other hand, taking into account the pyrometer uncertainty, the metamodel with P control is a clear improvement over the other two control schemes. This result experimentally validates the proportionality constant that was found in Section 5.3.2 and furthermore demonstrates the feasibility and capability of metamodel based process control. Although the result from this experiment was acceptable, curiosity implores whether a better result may be achieved through better tuning. As a result one final test was run to see whether a better result could be attained. These results are shown in Figure 5-42.

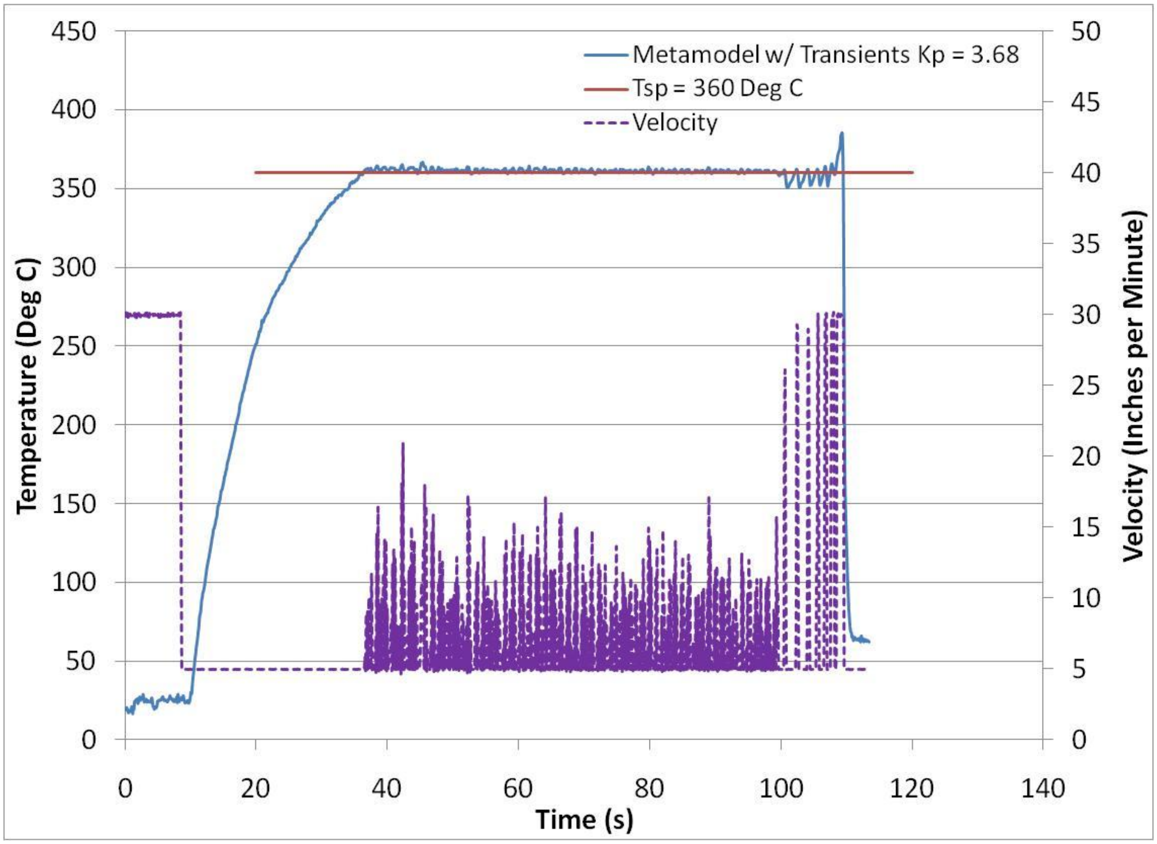

Figure 5-42: Temperature vs. Time and Velocity vs. Time for a controlled weld using a metamodel with dynamics, K_p = 3.68

Table 5-7: Performance metrics for the different control schemes, Kp = 3.68

Method	**Tavg**	**Standard Deviation**
P Control	353.3 Degrees C	7.6 Degrees C
P Control with Regression and Extrapolation	354.9 Degress C	5.3 Degrees C
Metamodel with P Control	362.1 Degrees C	3.4 Degrees C

Shown in Figure 5-42 is the temperature and velocity plot for a weld controlled by a metamodel with dynamics. K_p = 3.68 inch per minute/Deg C (0.00156 m/sK) was chosen as the proportional constant. Previous experience and intuition led to the value of this proportional constant. As observed in Figure 5-42, the control response is smooth and controlled similar to the control response observed in Figure 5-41. Compared to K_p = 2.36 inch per minute/Deg C (0.001 m/sK), K_p = 3.68 inch per minute/Deg C (0.00156 m/sK) has a noticeable improvement to previous proportional constant. It can be observed that the steady state response has less offset from the setpoint value and the end of weld transient is better controlled. For this experimental trial, it was found that the average temperature for the region of the workpiece that was controlled by the metamodel, T_{avg} = 360.2 Deg C. Shown in Table 5-7 are the performance metrics of the three different control scheme that were investigated. Although the P controller with regression and extrapolation shows a mild improvement, there is essentially no change from straight P control when taking into account the pyrometer uncertainty. On the other hand, taking into account the pyrometer uncertainty, the metamodel with P control is a clear improvement over the other two control schemes. Despite the slightly higher standard deviation for this case when compared to the case when K_p = 2.36 inch per minute/Deg C (0.001 m/sK), the average temperature in the steady state region is nearly exactly the desired setpoint value. The slight trade-off in standard deviation in the steady state region is worth the greater precision in achieving the setpoint temperature. The result of experiment is that by fine tuning the proportional parameter, better performance was achieved.

Chapter 6: Conclusions

This study examined the possibility and feasibility of predictive process control via the application of model based control concepts and using model based data whenever applicable to aid in the control process. The goal of this research was to implement models into the manufacturing process control space in order to lessen the need for stochastic data in manufacturing processes. For cases where the statistical database is either not available or not feasible to compile, the desire to use models becomes apparent. Situations where this could occur would be customized products or one-off builds where each manufacturing step is not fully characterized or the use of different or more expensive material would make the ability to compile a statistical database cost- prohibitive. For these reasons model- based control is very compelling.

This research covered several areas such as model selection and model verification and validation, controller design and controller implementation and design and integration of model based control using surrogate modeling techniques. The following sections outline the conclusions and salient points observed from each respective research area.

6.1 Thermal Modeling

In this study thermal models for welding and braze welding were examined and investigated. Analytical models were looked at for convenience and speed, and computational models were investigated for their ability to include sophisticated boundary conditions and couple multiple physical phenomenon within a model. Three models were explored, the Rosenthal analytical model, a custom finite difference model and a finite volume model done in FLUENT. All three models were used to model the heat evolution in a welded workpiece. In each model only conduction effects were considered since conduction was the physical phenomena of interest and the most principle effect in braze-welding. All models were validated and assessed against experimental data taken from thermocouples and IR pyrometers. It was found that the FLUENT model and Rosenthal model gave the best agreement to thermocouple data. It was found that FLUENT and the custom finite difference method had the best agreement with the IR pyrometer data. In both cases the FLUENT model provided the best match with the experimental data.

One of the metrics for thermal modeling was the speed at which the model can tabulate temperature fields for use in real time control. Despite being the highest fidelity model when compared to experimental data, the FLUENT was prohibitive based on calculation time. For real time control, fast calculation times and high accuracy are most desirable. This led to the adoption of surrogate models or metamodels to function as the process model of the welding process. The metamodels take large quantities of data and fit the databases using various techniques in order to retrieve and interpolate between parameters represented in the body of data. From research by others on the system used here, it was found that Support Vector Regression (SVR) and Multi Adaptive Regressive Splines (MARS) were the best methods to use to fit and predict data associated with welding or conduction equations with moving heat sources. FLUENT$^{©}$ was used to tabulate a large database of temperature fields that modeled a series of welding conditions and an SVR metamodel was used to fit all the data. The SVR model served as the process model for the controller and was used to design and fine tune the controller.

6.2 Control Design and Model based tuning

All experiments were performed on a custom-designed welding test station from the Seepersad Design Group. Automatic control capability was implemented on the welding test station and thermal feedback control was instituted on the welding test station to allow for the control of the stepper motor based on the thermal signals measured by the IR pyrometers. The dynamics of the welding process were controlled via classical control techniques, i.e. Proportional, Integral Derivative (PID) control. In order to find the PID control constants, the Rosenthal thermal model and the SVR metamodel were used to find and tune the control parameters (which is an ancillary benefit of model-based control development). The Rosenthal model was used to generate curves of temperature vs. velocity and the first derivative of temperature vs. velocity. The slopes of a linear curve fit to the temperature vs. velocity and first derivative of temperature vs. velocity were used as starting points for the proportional constant, K_p. The SVR metamodel was used as a plant model and paired with a PID controller. The system based on the SVR model was tuned using a technique based on Ziegler-Nichols tuning.

Different techniques were investigated to deal with measurement noise and a regression and extrapolation technique was adopted to deal with noise and also extrapolate into the future for predictive capability. The PID control parameters and noise filtering techniques were validated on the welding test station via experiments. It was found that the proportional constant found via tuning the SVR based system was a viable control constant, as it provided noticeable control action and exact set point tracking. It was also found that the proportional constant that corresponded to the slope of the line that approximated the first derivative of temperature vs. velocity based on the Rosenthal model was the best proportional constant since it provided exact set point tracking, control through the end of the weld and better initial dynamics. Noise filtering and future prediction were investigated through the inclusion of polynomial regression and extrapolation in the controller. When compared to a standard controller without regression and extrapolation it was found that the regression and extrapolation provided a mild improvement to the steady state control response. Both controllers were tested on six inch pieces and twelve inch pieces. In both cases the controller with regression and extrapolation had a lower standard deviation from the average steady state temperature.

Lastly metamodels are investigated to determine their ability to be used as process models in real time situations.

6.3 Metamodel based control

A metamodel was constructed from FLUENT© model data for a 0.3048m long (12 inch), 0.0508m (2 inch) wide and 0.00635m (1/4 inch) thick workpiece. The longer workpiece was chosen to test the robustness of the controller and also facilitate the testing and validation of metamodels and metamodel base control. A Hammersley sequence was used to determine all the different FLUENT© parameters that should be run to compile a thorough and complete set of training data on which to train metamodels. The FLUENT© training data was compared to experimental data to check for agreement with a physical system. It was found that the training data and experimental data agreed well in the steady state regime but has less agreement for the beginning of weld and end of weld transients. It was decided that the metamodel would be used as a steady state controller. The metamodel was built and used in a control system to assess how well it made decisions. It was found that the metamodel produced trajectories that the controller would over-correct. This caused poor weld performance. Since metamodels do not inherently have dynamics, the metamodel was coupled with a first order dynamic function to help with its decision making and trajectory projection. The metamodel based controller with dynamics was paired with a proportional controller and tested with a proportional constant of K_p = 2.36 inch per minute/Deg C (0.001 m/sK). This was the same value of the proportional constant found computationally by simulating the welding process with metamodels. It was found that the metamodel based controller was able to control the temperature to T_{avg} = 362 Deg C which was very close to the desired, T_{sp} = 360 Deg C. One last experiment was run with the metamodel based controller using a proportional constant of, K_p = 3.68 inch per minute/Deg C (0.00156 m/sK). The results turned out better than the first experiment, it was found that the metamodel based controller was able to controller temperature to T_{avg} = 360.2 Deg C and get better end of weld characteristics than with K_p = 2.36 inch per minute/Deg C (0.001 m/sK).

Chapter 7: Future Work

7.1 Metamodeling

In this body of research, it was seen that metamodel based control offered an improvement over traditional classical control. The metamodels proved that they are useful in controlling steady state phenomena but is yet to be tested to deal with transient phenomena like beginning of weld and end of weld transient effects. One way to deal with the initial transients encountered during test would be to preheat the specimen and hold the initial temperature at 635 K (360 Deg C) and thereby eliminating the initial transient. In this way the metamodel controller can start controlling the weld from the very beginning of the weld specimen instead of waiting to get to the steady state regime for the metamodel to take over. Another improvement that could be made to the metamodels is the fidelity of the training data. It was seen that the boundary conditions used FLUENT© model were an oversimplification of the real physical system.

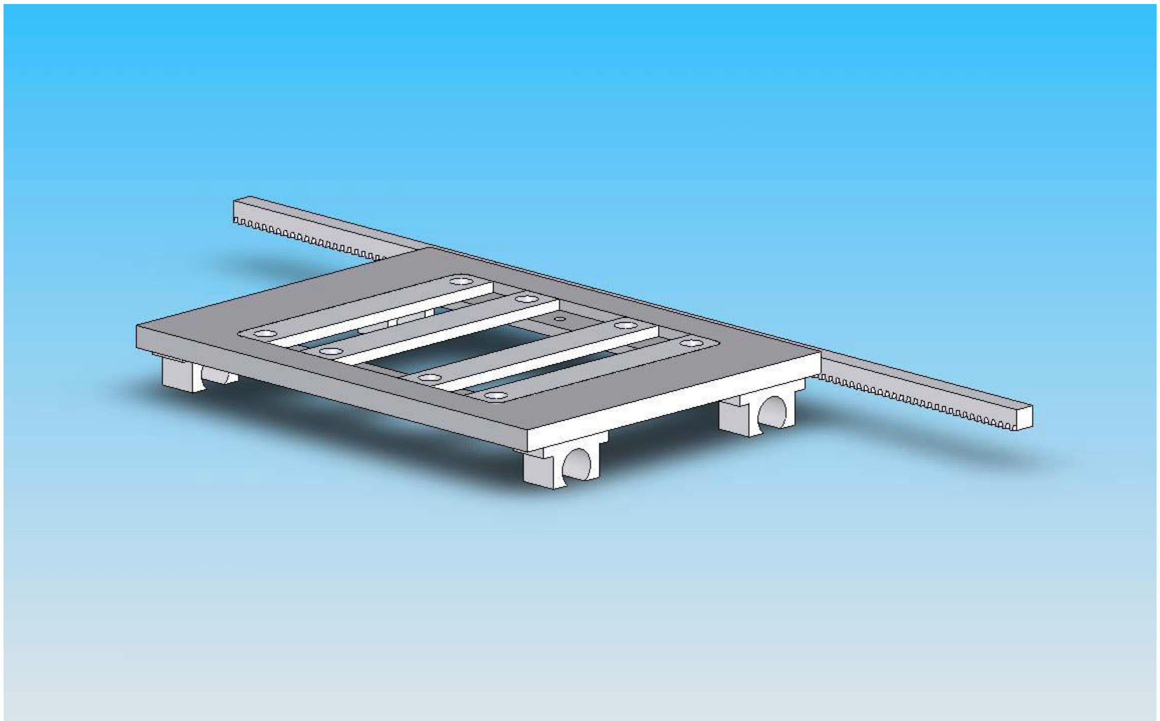

Figure 7-1: Schematic of the steel traverse platform that weld specimen rests on during testing (Backlund, 2008; Backlund, Ely, Seepersad, Taleff and Howell, 2009)

Shown in Figure 7-1 is a schematic of the steel platform that the weld specimen is fixture to during testing. Including the conduction path from this fixture and the impingement heat transfer from the argon shield gas would increase the accuracy of the FLUENT© training data and enhance the capabilities of metamodels to estimate transient phenomena in process control and manufacturing.

Secondly, in this research metamodels worked primarily as single input single output control systems. In reality, welding and other manufacturing processes have multiple parameters that can be controlled to obtain a desired outcome. Future research could explore the capabilities of multiple input metamodels. In the case of welding and braze welding, metamodels can be used to explore the space of multivariable control that includes several controllable parameters such as wire feed speed, voltage, current, and combinations of controllable parameters. Metamodels could also be developed to model inverse problems. For the case of welding, metamodels could be used to calculate the required power input for a weld based on temperature measurement.

Lastly, in this study metamodels proved that they have control capability but further research should be conducted to examine if metamodels could emulate controllers themselves in a similar manner in which neural networks function.

7.2 Analytical Modeling

As discussed in Section 2.3.4, several analytical models exist that describe the heat evolution in an irradiated solid. The two most recent models that have been developed were by Boo and Cho (1990) and Nguyen et al. (1999). Since then there has been a dearth of analytical development and more recent solutions are computational in formulation. Of the extant analytical solutions only a few attempt to put physical boundaries in the solution of the diffusion equation (Rosenthal, 1946; Jhaveri et al., 1961, Boo and Cho, 1990), all other formulations are done on a semi-infinite domain. While the semi-infinite solutions offer good approximations to the temperature fields closer to the weld zone, they become increasingly less accurate further away from the weld zone. One of the first attempts to move the analytical field forward in the modeling of welding would be to revisit some of the classical formulations and attempt to apply physical boundary conditions on the periphery of the domain and solve the finite domain problem.

In the literature, there has been an evolution in the types of boundary conditions from semi-infinite and adiabatic boundaries to dealing with convection and in a limited fashion, radiation. These improvements have been a step forward in attempts to accurately model the conduction based temperature evolution during welding. Yet one very significant physical phenomenon has been ignored in all of models that currently exist. Thus far, none of the analytical models take into account solid-liquid phase change in their formulation. In welding, the materials are bonded together through the addition of a molten filler metal and melted parent material (Holliday, 1993). Since the parent material of the workpiece undergoes significant melting, the inclusion of solid-liquid phase change would be a justifiable addition to the problem formulation. Illustrated in the following equations is an improvement to the Nguyen et al. (1999) model. These governing equations include the Stefan conditions to add phase change to the Nguyen model. In the following equations, α is thermal conductivity, T is temperature, L is latent heat of fusion, δ is solid –liquid interface position, ρ is density and x,y,z are the Cartesian coordinates of the reference frame.

Governing Eqn in 3-D that describes the temperature evolution in a solid

$$\frac{\partial T}{\partial t} - V_x \frac{\partial T}{\partial x} = \alpha\left(\frac{\partial^2 T}{\partial x^2} + \frac{\partial^2 T}{\partial y^2} + \frac{\partial^2 T}{\partial z^2}\right)$$

subjected to the double ellipsoidal moving heat source boundary condition

Front half of double ellipsoidal heat source:

$$Q(x,y,z)=\frac{6\sqrt{3}r_f Q}{a_h b_h c_{hf}\pi\sqrt{\pi}}\exp\left(-\frac{3x^2}{c_{hf}^2}-\frac{3y^2}{a_h^2}-\frac{3z^2}{b_h^2}\right)$$

Rear half of double ellipsoidal heat source:

$$Q(x,y,z)=\frac{6\sqrt{3}r_b Q}{a_h b_h c_{hb}\pi\sqrt{\pi}}\exp\left(-\frac{3x^2}{c_{hb}^2}-\frac{3y^2}{a_h^2}-\frac{3z^2}{b_h^2}\right)$$

where

$$r_f=\frac{2c_{hf}}{c_{hf}+c_{hb}} \quad \text{and} \quad r_b=\frac{2c_{hb}}{c_{hf}+c_{hb}}$$

An additional boundary condition is the Stefan condition in 3-D that describes the solid liquid interface that develops under the influence of the moving heat source.

$$-k\nabla T\big|_{x,y,z=\delta(t)}=\rho L\frac{d\delta(t)}{dt}$$

The development of this analytical model would be a significant advancement in the analytical welding model field. As part of the solution of the above equations, an expression for the eigenvalues of the governing equation will be found. The representation of those eigenvalues may be the basis for an optimal controller.

7.3 Controller Development

In this research, classical control was used to control the dynamics of the temperature evolution in workpiece during welding. The drawback to using classical control is that the research was limited to Single Input Single Output (SISO) systems (Seborg, Edgar and Mellichamp, 2004). In this research the equivalent weld head velocity was controlled in order to maintain the temperature of temperature points that were being monitored. But in reality, welding has several inputs that may be changed that can affect the quality of the weld and the resulting temperature field of the workpiece. An extension to work done here would be to use modern control theory i.e. state-space control to control our welding system. Modern control is the only way to control a Multiple Input Single Output (MISO) or Multiple Input Multiple Output (MIMO) system (Ogata, 2002; Friedland, 2005).

Classical PID controllers add or move poles to improve the steady state error and improve transient response independently (Åström and Hägglund, 1995). From a theoretical standpoint, controllers manipulate the placement of poles in the plane made up of the real and imaginary axis in the *s*-plane (Nise, 2002). With properly tuned PID constants the classical controller may find a solution to the control problem but that solution is not necessarily an optimal solution to the control problem. In classical control the movement of the poles of the system is constrained by the values of the PID constants. But in order to place the eigenvalues of the system anywhere in the *s*-plane modern controllers must be used (Friedland, 2005)

Outlined in Section 7.1were the details of a new analytical model that could be developed. As part of the solution of that model, an expression for the eigenvalues of the system would be obtained. With any eigenvalue problem, a modern control system may be designed with knowledge of the eigenvalues. Furthermore, recognizing that the eigenvalues come from an infinite dimensional linear system (Curtain and Pritchard, 1987 and Curtain and Zwart, 1995), an appropriate transfer function can be derived from the expression of the eigenvalues. Following the methods that Li, Farson and Richardson (2001) employed, an H^{∞} controller (an optimal controller) was derived to control welding depth penetration from temperature measurements.

By looking into state-space control techniques, this research could further progress by using new model formulations as mentioned in Section 7.1 or use existing models and recasting them for use with optimal controllers that use performance indexes for a more tailored dynamic response. This could be ported to take advantage of system dynamics described by lumped systems, distributed parameter systems and metamodels.

7.4 Weld Quality

Two questions that were answered through this research were 1) whether current physics based models are adequate for physics based control and 2) how would one implement physics those physics based models in a real time control system. In this research, analytical models, computational models and surrogate models were investigated and compared with experimental data to assess how well they match real world conditions. It was found that the current physics based models are adequate at representing the thermal phenomena observed during braze-welding. Metamodels trained with FLUENT simulation data were successfully implemented in a model predictive control scheme and showed improvement over classical control schemes.

Although thermally based control was successfully implemented to control temperature in a braze-welded workpiece, further research must be done in order to take the next step of residual stress reduction and weld quality control. With the ability to control temperature in a welded workpiece, thermally induced stresses and crack propagation can indirectly be controlled through temperature. Since temperature measurement is an indirect way of correlating weld quality, temperature control directly affects other phenomena that directly correlates to weld quality such as size of the heat effected zone, the formation of specific metallographic phases, secondary dendrite formation and residual stress to name a few.

The seminal research completed here can be used as vehicle to begin investigations in to areas auxiliary to weld quality. The control system developed here can be used to investigate how thermal control influences the formation of residual stress, metallographic phases and overall weld quality. The successful implementation of metamodels with a control system enables the possibility of training metamodels as structural or thermal-structural models that can predict residual stress or thermal deformation based on various welding input parameters. Then the structural metamodels can be pared with controllers and the structural phenomena can be directly controlled during welding or braze-welding.

Appendix A: Experimental Set-Up

In this appendix, the final design of the welding test station is outlined. The concept was designed and built by Peter Backlund of the Seepersad Design group as part of his Master's work (Backlund, 2008; Backlund, Ely, Seepersad, Taleff and Howell, 2009). This is the semi-automatic welding test station on which all of the data collection and control scheme testing took place. Details of the welding test station design, capabilities and physical margins are presented with photographs and detailed explanations of the workings of each module and subsystem.

A.1 Final Design

The final layout of the test station, shown in Figure A-1, is composed of five separate modules that carry out the main functions of the system. The frame assembly is the common platform to which all other modules connect. It is used for mounting any other equipment that must be interfaced with the system such as an infrared camera. The linear weld surface holds the test specimen and moves laterally to provide the desired process motion. The drive-shaft assembly, which is connected to the motor with a belt pulley system, drives the linear weld surface. The torch mount holds the welding torch in a specified position during the welding process. Lastly, the motor assembly holds the motor in place, and isolates it from the electrical current that is present during the welding process (Backlund, 2008; Backlund, Ely, Seepersad, Taleff and Howell, 2009).

A photograph of the final assembly of the welding test station is shown in Figure A-2. In the following subsections, the component materials and detailed features of each module are explained in detail (Backlund, Backlund et al.).

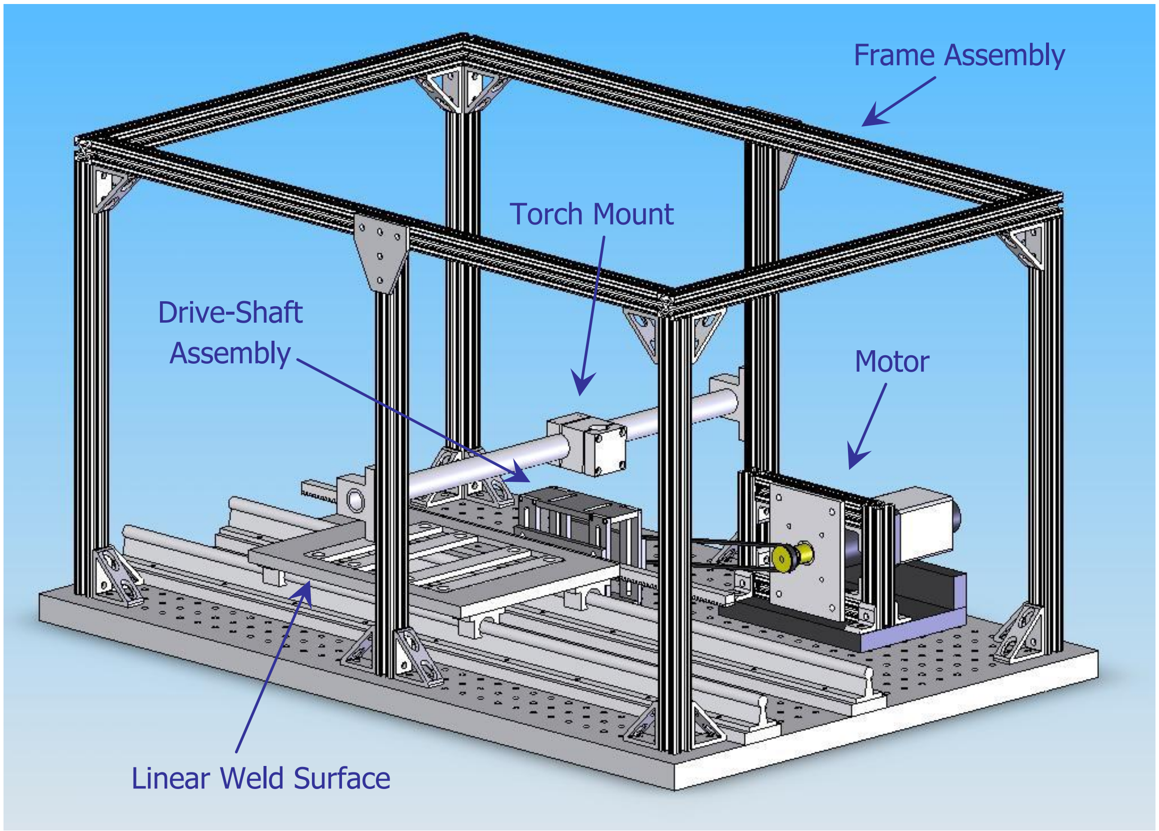
Frame Assembly
Torch Mount
Drive-Shaft Assembly
Motor
Linear Weld Surface

Figure A-1: Final test station layout

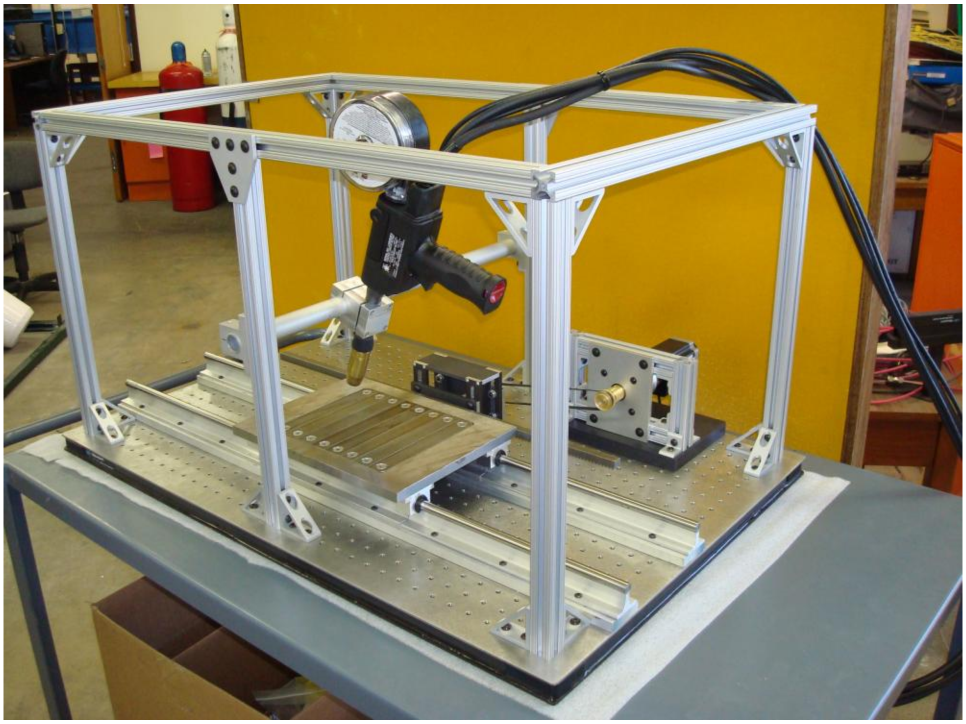

Figure A-2: Final assembly

A.1.1 Frame/Base Assembly

The frame/base assembly of the welding test station has two main features. The first is the optical breadboard that functions as the base of the system, Newport model TD-23. The outer dimensions are 2 ft. x 3 ft., and it features an array of 1” spaced ¼-20 threaded holes. It was decided to use an optical breadboard to increase the flexibility of the system. The pattern of threaded holes makes it very easy to add or subtract modules and components if the needs and functions of the system change in the future.

The second feature of the frame/base assembly is the structural mounting frame. The frame can be used to mount various components and modules and is constructed of 8020 brand T-Slotted aluminum. Due to the nature of the T-Slotted members, anything that is mounted to the frame can be secured in any desired position. This is very important since the position of the welding torch and the infrared camera will be critical process parameters (Backlund, Backlund et al.).

A.1.2 Linear Motion Table

The linear motion table, shown in Figure A-3, provides a moving surface to which the test specimens can be mounted. This surface moves beneath the welding torch which is held stationary during the welding process. The welding surface is designed with removable sections on the interior. This feature allows any test piece that is between 1 inch and 12 inches to be constrained from both ends with standard C-clamps. Furthermore, we may want to take temperature measurements from underneath the test piece. The option of an open section in the middle of the welding surface allows a clear line of sight to the underside of the test specimen. It also allows thermocouples to be attached to the underside of the work piece.

The linear welding surface and the removable table sections are made of 4140 alloy steel. This material has a high electrical conductivity, which is crucial so that the welding current can conduct to the ground cable with minimal resistance. Another advantage to using steel for this assembly is its relatively high melting temperature. This property prevents welding spatter from lower melting temperature filler metals, such as aluminum and silver, from sticking to the surface.

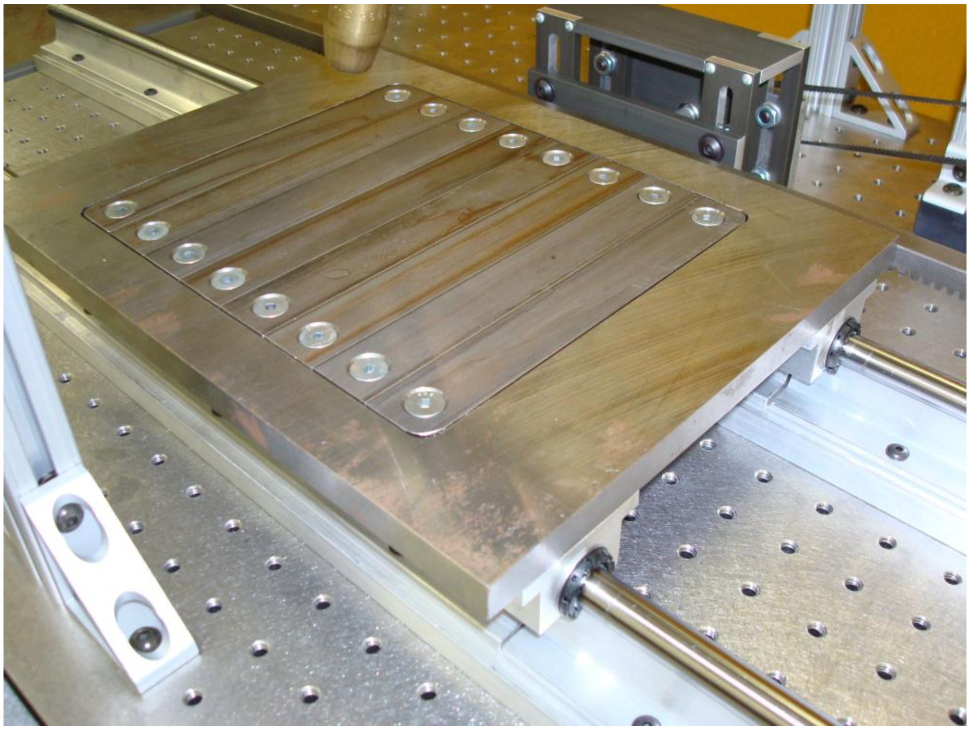

Figure A-3: Linear motion table

To allow the necessary lateral motion, the rectangular surface sits on four pillow blocks that house linear ball bearing elements. The pillow blocks were custom machined in-house to reduce costs. These linear bearing elements slide on two parallel rails that are screwed into the breadboard. Although the rails are made of case hardened steel, it was observed during preliminary tests that some of the welding spatter was beginning to pit the surface of the rails. To mitigate this problem, two protective brackets were designed and attached to the moving table that cover and protect the rails from welding spatter. The assembly has a 24 inch rack mounted along the back edge which is driven by a pinion gear in the shaft mount assembly to provide the desired motion (Backlund, Backlund et al.).

A.1.3 Torch Mount

The torch mount, which is shown in Figure A-4, is used to hold the welding torch in a preset position during the welding process. It consists of a circular tube that is supported by stanchions at each end. The stanchions are of the same brand as the T-slotted aluminum frame members and can be attached to the frame with the standard 8020 connectors. The stanchion can slide vertically in the frame assembly, thus providing the necessary height adjustment. The torch clamp is a three piece assembly with two orthogonal holes bored at each end. The larger hole is used to wrap around the circular beam support beam that spans the width of the station. It can be rotated to any angle, thus providing the necessary angle adjustment. The smaller hole is used to secure the welding torch. The stanchions and the cross beam were manufactured by the 8020 company, and the torch clamp was custom machined in-house (Backlund, Backlund et al.).

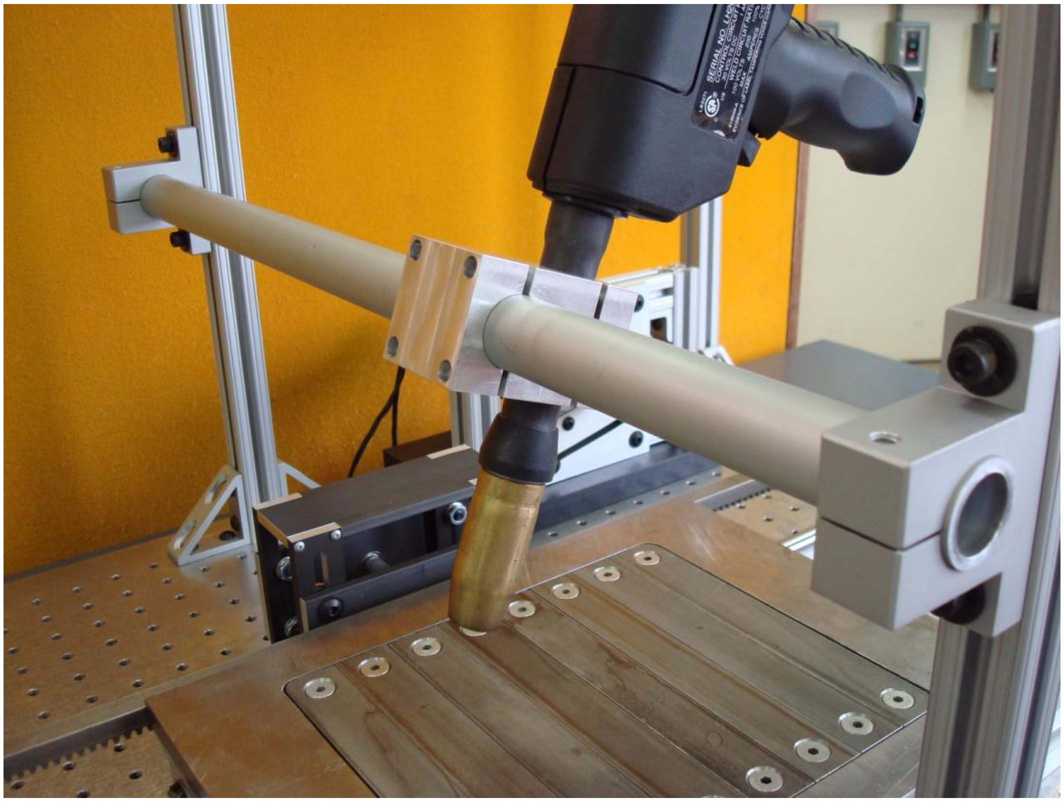

Figure A-4: Torch mount assembly

A.1.4 Drive Shaft Assembly

The drive shaft assembly, shown in Figure A-5 and Figure A-6, interfaces with the linear motion table and drives the sliding weld surface with rack and pinion style gearing. The drive shaft in the module is driven by a belt pulley system that connects directly to the motor. The rear of the assembly, Figure A-5, shows the belt pulley that connects to the belt from the motor. The pulley on the drive shaft is connected with set screws and can be replaced easily in the event that the gear ratio needs to be changed. The pinion gear is connected to the front end of a double ended shaft which runs from the front to the rear of the module. It is affixed to the shaft with an interference fit to make a secure, non-slipping connection.

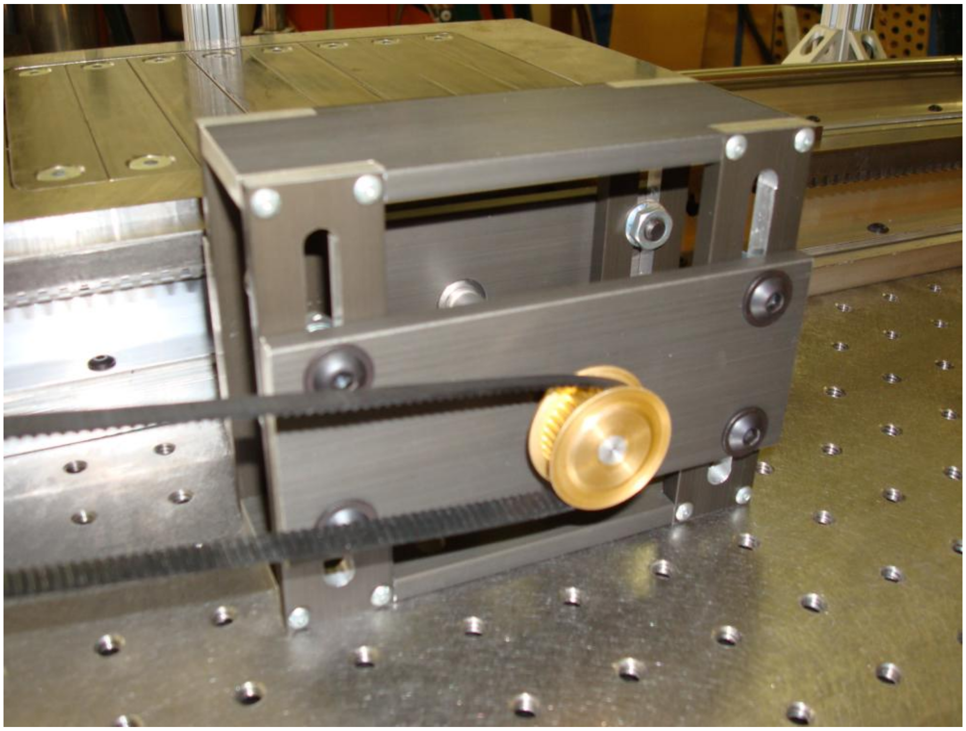

Figure A-5: Drive shaft assembly - rear view

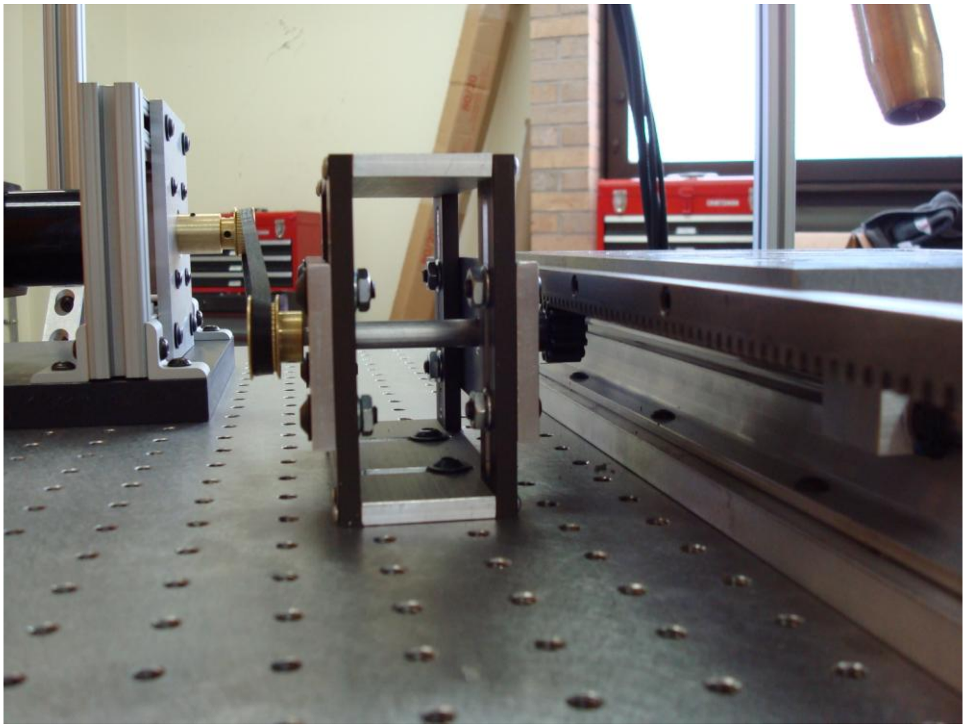

Figure A-6: Drive shaft assembly - side view

The entire length of the drive shaft can be seen in the side view of the assembly in Figure A-6. The drive shaft is supported by two plates that have flanged ball bearings mounted in them to provide low friction rotation of the shaft. The plates are mounted to the rest of the assembly in slotted holes for easy vertical adjustment of the shaft. This adjustability ensures a perfect mating between the pinion and the rack on the linear motion table (Backlund, Backlund et al.).

A.1.5 Motor Mount

The motion of the sliding table is driven by a stepper motor that is controlled with LabVIEW motion control software and hardware. The final design of the motor mount is shown in Figure A-7. This motor subsystem has two major design requirements. First, it must completely isolate the motor from the welding current. This is achieved by using a plastic, electrically insulating base to connect the motor to the frame base. Second, it must allow the motor to be adjusted horizontally, so that the drive belt can be tensioned. This is achieved by mounting the motor in slotted frame members (Backlund, Backlund et al.).

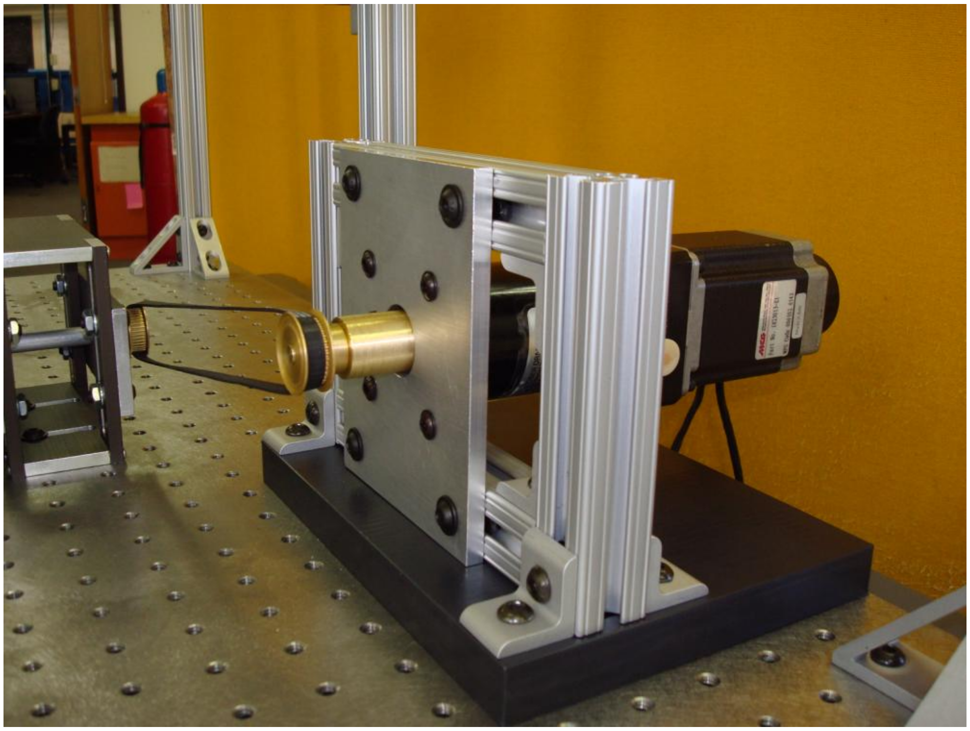

Figure A-7: Motor mount

For a detailed bill of materials for all of the test station parts and components, please refer to Backlund (2008).

A.2 Data Acquisiton and Motion Control

A.2.1 Temperature Measurement: Thermocouples

For the thermal analysis of the gas metal arc welding process, the test station includes a thermocouple measurement system. The type K thermocouples are combined with the signal conditioning block and 8 built-in cold-junction compensation modules. The system measures the temperature profiles of the specimen before, during, and after the weld. By using a data acquisition (DAQ) system from National Instruments, we are able to connect the temperature measurement to the motion control component. As a result, we know the precise location of the work piece relative to the welding torch when a temperature measurement is taken.

In Figure A-8, data from a preliminary test sample is shown. The red and blue lines indicate temperature readings from thermocouples that were placed on top of the specimen, one on each side of the weld, midway along the length of the specimen. The green line indicates the position of the torch relative to the leading end of the test specimen.

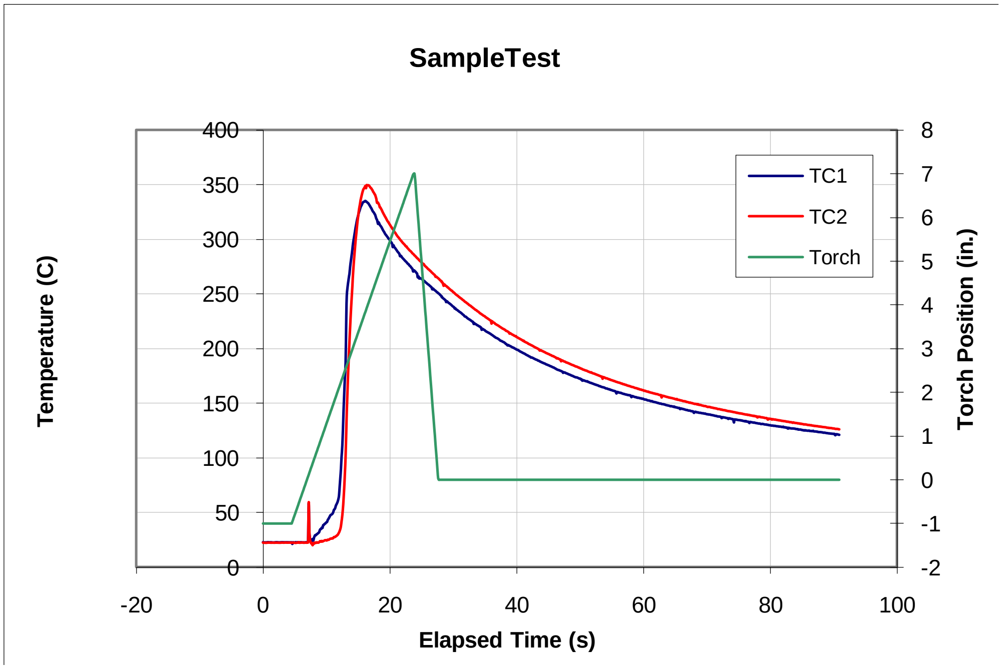

Figure A-8: Preliminary test data

Our virtual instrument starts with user input and begins taking samples of the specimen before it heats up. Once welding begins, the sampling rate increases and continues through multiple passes. When welding ceases, the rate of thermal acquisition decreases, but continues for a user specified cool down period. The DAQ assistant automatically converts the thermocouple voltage signals into temperatures ranging from 0 to 1500°C. However, it should be noted that the insulated type K thermocouples that we are currently using have a maximum rated temperature of 702°C. The LabVIEW program creates internal virtual channels to handle the physical thermocouple readings and stores the data for further thermal analysis of the welded specimen (Backlund, Backlund et al.).

A.2.2 Temperature Measurement: Infrared Pyrometers

As described in Section A.2.1, the welding station was originally configured to acquire temperatures exclusively from thermocouples facilitated by LabVIEW software and data acquisition hardware from National Instruments. Thermocouples have limitations for welding applications and Model Predictive Control (MPC). Concerns stem from the restrictions caused by welding the temperature sensor directly to the surface of the workpiece. Fixing the thermocouples directly to the workpiece forces the temperature measurements to be taken in relation to the fixed coordinate system of the workpiece instead of the moving coordinate system of the heat source. Previous studies have shown that temperature measurements that move along with the welding heat source are needed for welding control (McCampbell et al., 1965; Shah et al, 2009). Thermocouple data may assist in state measurement and the validation of thermal models but is less effective as the sole source for temperature data for use in MPC.

Infrared (IR) pyrometers were added to the welding test station as a source of non-contact temperature measurement. IR pyrometers measure the thermal power due to radiation given by the Stefan-Boltzmann equation:

$$I = \varepsilon\sigma(T^4 - T_\infty^4) \tag{A.1}$$

In Eqn. A.1 I is the thermal intensity, ε is the material's emissivity, σ is the Stefan-Boltzmann constant, T is the absolute temperature of the material, and T_∞ is the ambient temperature. By knowing the emissivity and ambient temperature, the IR pyrometer can then measure the temperature of the incident surface. This can be shown through rearranging Equation A.1 to solve for the temperature of the surface. Since IR pyrometers are non-contact, the IR pyrometers may be mounted to measure any temperature points on the workpiece.

The welding test station was outfitted with Omega OS554A Range 6 infrared pyrometers connected to a FT-01 analog input module. Custom mounting brackets were designed by George “Ray” Ely of the Seepersad Design group (Ely, 2010) to fixture the infrared pyrometers to move along with the weldhead. For convenience, the brackets are attached to the same circular beam as the weld torch. The brackets were designed to allow flexibility in the positioning of the pyrometer spots relative to the weld zone and weld head location. The final design, shown in Figure A-9 utilizes the circular beam to allow rotations and translations. These movements accommodate the desired coordinate location of the pyrometer’s focus relative to the center of the heat source (Ely). An additional degree of freedom is added to adjust the height of the pyrometer. The ability to change the height is essential because the field of view of the pyrometers is based on the distance from the work piece. To minimize the field of view and therefore measure the temperature over the smallest possible spot size, the height needs to be positioned at approximately 152.4 mm. Two channels with set screws are used to adjust the infrared pyrometer’s distance from the work piece without changing the coordinate location relative to the weld pool. Figure A-10 shows two infrared pyrometers integrated into the welding station.

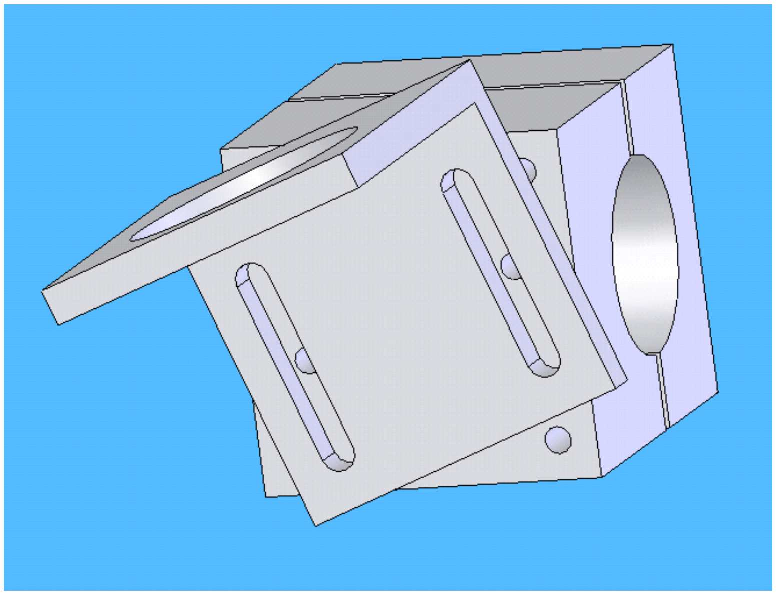

Figure A-9: Infrared pyrometer mount (Ely, 2010)

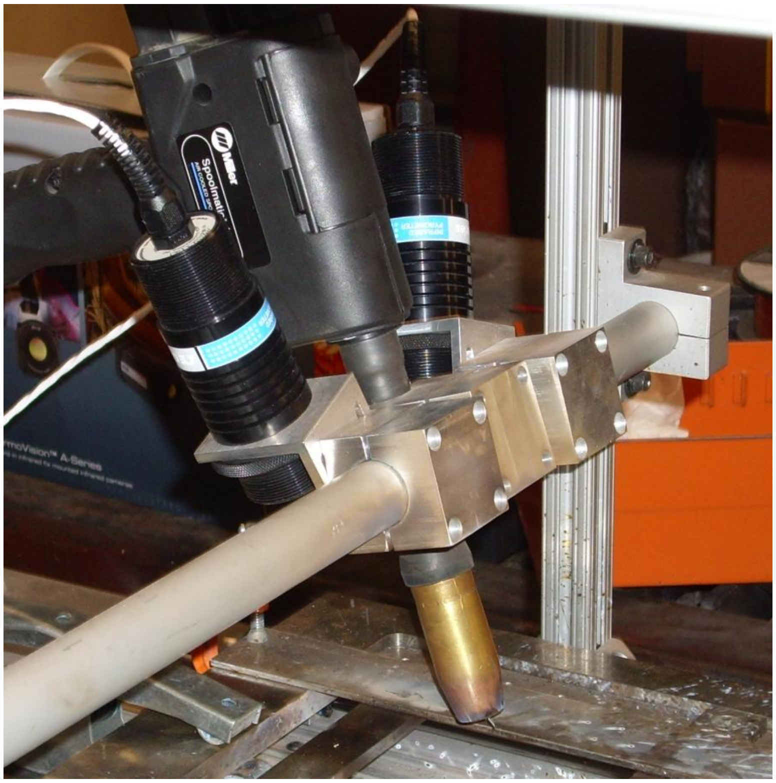

Figure A-10: IR pyrometers mounted to the welding test station (Ely, 2010)

A.2.3 Temperature Measurement: Infrared Camera

Another upgrade to the welding test station to extend its capabilities to acquire temperature data, an infrared (IR) camera was mounted to the test station. The infrared camera possesses a separate set of operational needs. Because of the value of the camera and its auto focus feature, it needs to be positioned at a greater distance from the welding torch to avoid weld splatter onto the lens. As shown in Figure A-11, the camera is mounted on t-slotted members that can attach to the frame of the welding station at numerous expansion points. Past experiments were performed with the camera positioned on the top of the frame in front of the torch as well as behind the torch as pictured in Figure A-11.

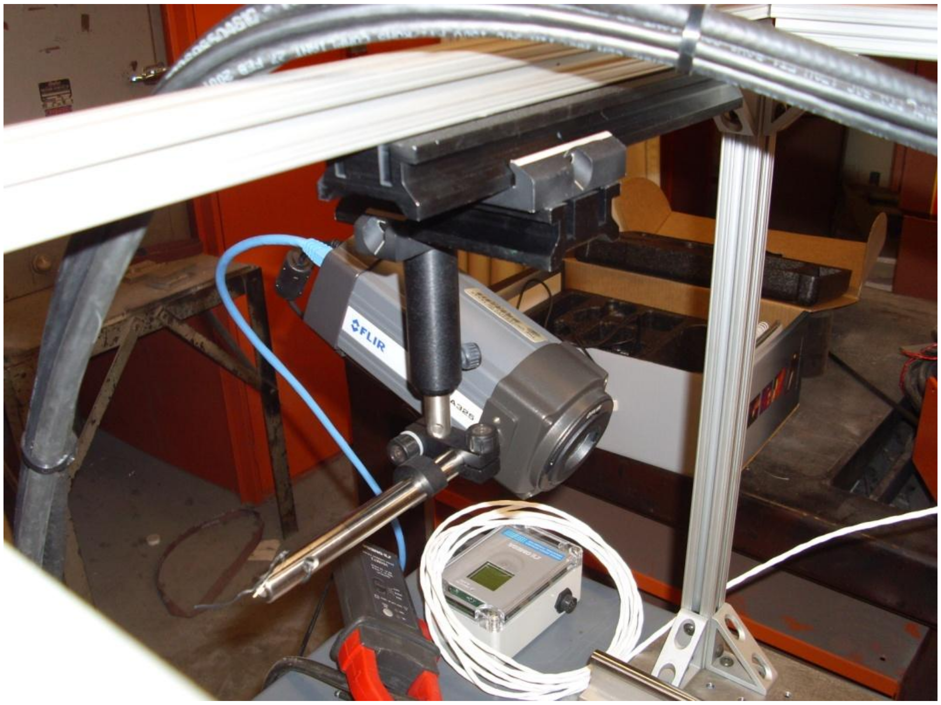
Figure A-11: Infrared camera mount

A.2.4 Motion Control

The motors on the test-bed are used to move the motion table and the test specimen across the path of the welding torch. For safety reasons, the trigger on the welding gun is manually operated to weld the test specimens. A program controls the welding table to move it exact distances in reference to a zero point or a current point. In Figure A-12, the graphical user interface (GUI) of the LabVIEW program is shown. The "Motion Status" and "Faults" boxes indicate to the user the status of the motor and any errors or faults in the system. The buttons in the "Jog" box allow the user to move the table in small amounts by clicking the left and right arrows. Clicking the zero button resets axis location so that the current position of the table becomes the zero point on the motion axis. The "GoTo (in)" box allows the user to move the table a specified distance at a specified speed. In the "Initial V" box allows a user to specify initial velocity that the motor will move for a distance of "PID Start Distance". After that distance the PID controller will turn on and initialize itself with a velocity of "2nd V". The motor controller will then adjust its velocity depending on what temperature the IR pyrometers measure and what the set point temperature is to be reached. The velocity will be controlled until the distance of "Total Distance" is reached. For safety reasons we have also built an emergency stop function into the user interface.

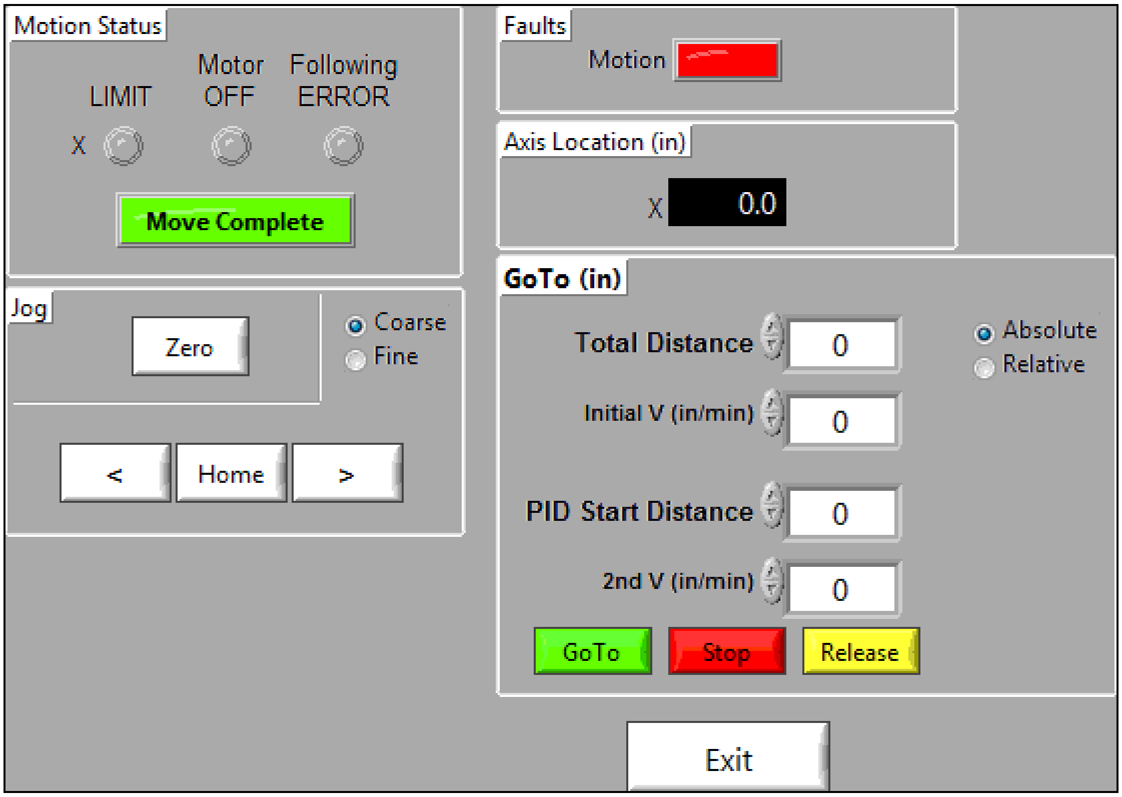
Motion Status
LIMIT
Motor OFF
Following ERROR
X
Move Complete
Faults
Motion
Jog
Zero
<
Home
>
GoTo (in)
GoTo
Stop
Release
Exit

Axis Location (in) X 0.0

● Coarse
○ Fine

Total Distance 0

Initial V (in/min) 0

PID Start Distance 0

2nd V (in/min) 0

● Absolute
○ Relative

Figure A-12: LabVIEW user interface

Along with the motion of the table, the program also controls the temperature data acquisition. The program takes temperature data from the 8 thermocouples for 10 seconds before the weld process, during the weld process, and for a user specified duration after the welding is completed. IR pyrometer data is taken before and during the weld but not after the weld schedule has completed. The data acquisition rate can also be adjusted for each DAQ time period (Backlund, Backlund et al.).

A.2.5 Variable Wire Feed Rate

Weld penetration and bead width are two aspects of welding that are directly affected by the wire feed rate and are tied to the current and voltage parameters. Controlling the wire feed rate requires adjustments to both the hardware (the weld gun) and the LabVIEW VI file. As sold by the manufacturer, the Miller Spoolmatic® 15A weld gun feeds the weld wire using a 24V DC motor. The wire feed rate is controlled by adjusting the voltage sent to the DC motor via a potentiometer that interacts with a controller to send the proper voltage to the motor and the corresponding feed rate to a digital display. The relationship between voltage and the feed rate that was output to the digital display was evaluated by George Ely (2010). Shown in Figure A-13is a plot of feed rate vs. voltage. As shown, the feed rate of the weld gun is strongly linearly dependent on voltage (Ely).

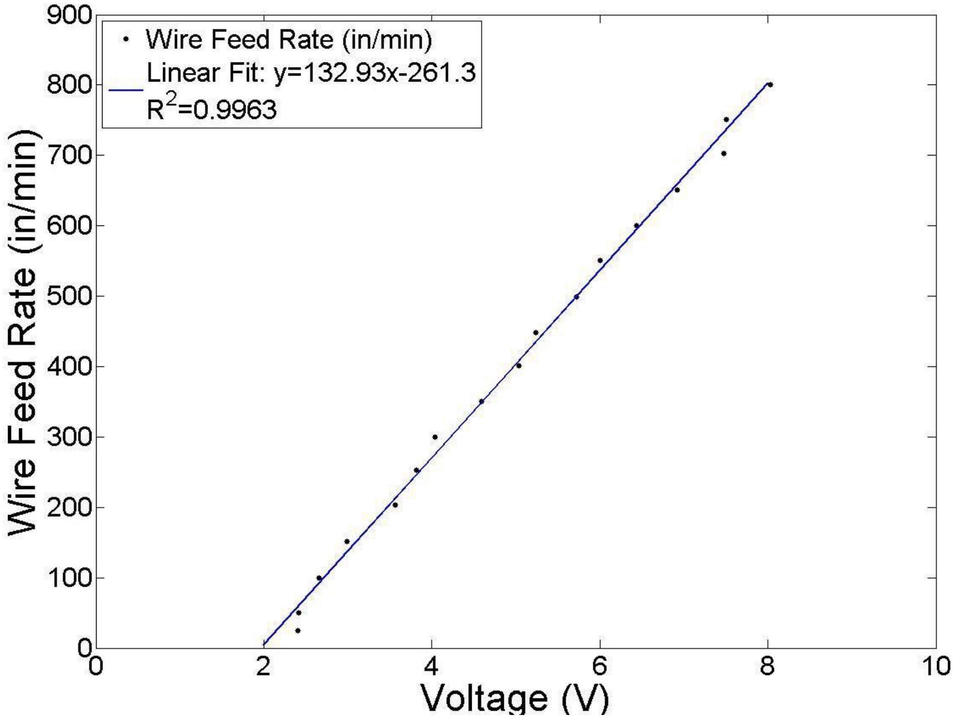

Figure A-13: Relationship between wire feed rate and voltage (Ely, 2010)

The linear relationship between wire feed rate and voltage makes the control of the DC feed motor amenable through LabVIEW. A NI SCC-FT01 feed through module is added to the output channel of an NI SC-2345 signal conditioning connector block. The feed through module allows access to an analog voltage output channel of the NI PCI-6229 data acquisition board. The hardware allows LabVIEW to output a voltage between 0 and 10 volts. The weld gun requires a range of approximately 2 to 8 volts, hence may be controlled directly from the SCC-FT01 on the output channel of the SC-2345. For further details of the design, construction and testing of the variable wire feed rate welding gun, readers are referred to Ely (2010).

A.3 Final Test Station Parameters

In this section, the final operating parameter margins of the welding test station are presented. The test station meets all of the immediate experimental needs of the project and operates with excellent reliability. There are many parameters that can be adjusted with the welding test station to investigate the effects on various measures of weld quality. In Table A-1, the test parameters and corresponding ranges of the complete experimental setup, including the welding power supply, are listed.

Table A-1: Welding test station parameters

Test Parameter	**Range**
Traverse speed	0-120 in/min
Pass length	0-12 inches
Torch height	Any
Torch angle	± 90°
Number of passes	1 – 3
Specimen length	1 – 12 inches
Wire feed rate	50-700 in / min
Weld voltage	17 – 32 VDC

Appendix B: Finite Difference Temperature Model

The Finite Difference Model (FDM) is based on Eqn. 1b from Section 2.3.5 and uses a 2-D, implicit method. This formulation was done by Carlos Rios-Perez (2009) as part of his Master's research. Eqn. 1b is simplified by retaining the terms that correspond to a 2-D diffusion process and adding terms that account for radiative and convective losses from the top and bottom surfaces of the work piece, yielding the following energy balance equation:

$$\frac{\partial T}{\partial t} = \alpha\left(\frac{\partial^2 T}{\partial x^2} + \frac{\partial^2 T}{\partial y^2}\right) - 2\left[\frac{h}{\Delta z \rho C_p}(T - T_\infty) + \frac{\varepsilon\sigma}{\Delta z \rho C_p}(T^4 - T_\infty^4)\right] + \frac{\dot{Q}'''(x,t)}{\rho C_p} \qquad \text{(B.1)}$$

Defining the non-dimensional parameter, θ, as follows:

$$\theta = \left(\frac{T - T_\infty}{T_\infty}\right)$$

yields the following energy balance equation:

$$\frac{\partial \theta}{\partial t} = \alpha\left(\frac{\partial^2 \theta}{\partial x^2} + \frac{\partial^2 \theta}{\partial y^2}\right) - 2\left[\frac{h}{\Delta z \rho C_p}\theta + \frac{\varepsilon\sigma T_\infty^3}{\Delta z \rho C_p}((\theta+1)^4 - 1)\right] + \frac{\dot{Q}'''(x,t)}{\rho C_p T_\infty} \qquad \text{(B.2)}$$

After applying a second-order central difference discretization scheme to the space derivatives and a backwards difference scheme to the time derivatives (implicit method), Eqn. B.2 and the associated boundary conditions yield a set of discretized equations upon which the FDM is based. Equations B.3, B.4 and B.5 are examples of the equations that apply to a corner node (opposite to where the coordinate system is located), border node and body node on the interior of the plate:

$$\begin{aligned}\frac{\theta_{i,j}^{k+1}-\theta_{i,j}^{k}}{\Delta t} &= \alpha\left(\frac{\theta_{i,j-1}^{k+1}-\theta_{i,j}^{k+1}}{\Delta x^2}+\frac{\theta_{i+1,j}^{k+1}-\theta_{i,j}^{k+1}}{\Delta y^2}\right)\\ &\quad -\left[\frac{\theta_{i,j}^{k+1}h}{\rho C_p}+\frac{\varepsilon\sigma T_\infty^3}{\rho C_p}((\theta_{i,j}^{k+1}+1)^4-1)\right]\left(\frac{2}{\Delta z}+\frac{1}{\Delta y}+\frac{1}{\Delta x}\right)+\frac{\dot{Q}'''^{k+1}_{i,j}}{T_\infty \rho C_p}\end{aligned} \tag{B.3}$$

$$\begin{aligned}\frac{\theta_{i,j}^{k+1}-\theta_{i,j}^{k}}{\Delta t} &= \alpha\left(\frac{\theta_{i,j-1}^{k+1}-2\theta_{i,j}^{k+1}+\theta_{i,j+1}^{k+1}}{\Delta x^2}+\frac{2\theta_{i-1,j}^{k+1}-2\theta_{i,j}^{k+1}}{\Delta y^2}\right)\\ &\quad -\left[\frac{\theta_{i,j}^{k+1}h}{\rho C_p}+\frac{\varepsilon\sigma T_\infty^3}{\rho C_p}((\theta_{i,j}^{k+1}+1)^4-1)\right]\left(\frac{2}{\Delta z}\right)+\frac{\dot{Q}'''^{k+1}_{i,j}}{T_\infty \rho C_p}\end{aligned} \tag{B.4}$$

$$\begin{aligned}\frac{\theta_{i,j}^{k+1}-\theta_{i,j}^{k}}{\Delta t} &= \alpha\left(\frac{\theta_{i,j-1}^{k+1}-2\theta_{i,j}^{k+1}+\theta_{i,j+1}^{k+1}}{\Delta x^2}+\frac{\theta_{i-1,j}^{k+1}-2\theta_{i,j}^{k+1}+\theta_{i+1,j}^{k+1}}{\Delta y^2}\right)\\ &\quad -\left[\frac{\theta_{i,j}^{k+1}h}{\rho C_p}+\frac{\varepsilon\sigma T_\infty^3}{\rho C_p}((\theta_{i,j}^{k+1}+1)^4-1)\right]\left(\frac{2}{\Delta z}\right)+\frac{\dot{Q}'''^{k+1}_{i,j}}{T_\infty \rho C_p}\end{aligned} \tag{B.5}$$

where the subscripts *i* and *j* are indices that correspond to the location of the node along the *x* and *y* axes while *k* represents the time index. (Rios-Perez, 2009)

Appendix C: Modern Control: State Space Analysis

C.1 Abstract

During the welding process it is advantageous to resolve the temperature field in a work piece, as the temperature evolution in the base material will have a direct effect on the size of the heat affected zone (HAZ), the weld fatigue life and the amount of residual stresses left in the work piece after welding. Having knowledge the temperature field will also serve as the basis for specific types of welding control. For these reasons it is necessary to be able to deduce the temperature field in a welded material. In this work, a state-space model of a welding process is used to formulate a Kalman estimator to estimate the temperature field in a welded piece of CuZn10.

C.2 Introduction

In the manufacturing process of welding, two pieces of metal are joined by locally heating the material in the presence of a filler material. The induced melting mixes the workpiece metal and filler material to form a cohesive bond. One parameter of importance during the welding process is the temperature field that develops in the workpiece as it has direct influence on the resulting microstructure and strength of the welded joint. Several efforts have been made to accurately model the temperature evolution in the welded metal, yet because of the calculation time associated with sophisticated models, they become increasingly less amenable for use in real-time, automatic control. An alternate method upon which to resolve a temperature field without the use of a complex model is needed. One way to achieve this is through the use of state estimation. In a real system, not all state variables are available for direct measurement or only a few state variables of a given state are measurable like the output variables and the rest are not. For the remaining states that are not measurable, it is necessary to estimate those state variables using a state estimator or a state observer. The state observer is a subsystem in the control system that performs an estimation of the state variables based on the measurements of the output and control variables.

In this work, a piece of CuZn10 is welded and temperature measurements are taken at four points on the top surface of the work piece. This temperature data are used in conjunction with a Kalman filter to estimate the temperatures in the remainder of the work piece. Additional measurements that serve as inputs to the system that are taken during the welding experiment were current and voltage. These values for current and voltage are used to calculate the assumed power input of the plasma arc during the weld. The Kalman gain is calculated from a state-space model derived from a physical model that describes the phenomenon of heat evolution in an irradiated material subjected to moving heat source. Such a phenomenon occurs in welding and will serve as the basis for the state model.

C.3 Theory, Background and Experimental Setup

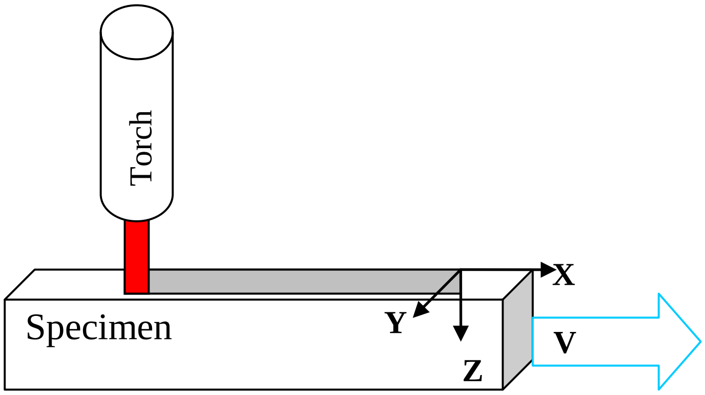

Figure C-1: Schematic of Welding Problem

An elementary schematic of the welding process is shown in Figure C-1. From a thermal conduction perspective, the temperature evolution in the solid irradiated by a moving heat source may be described as the material derivative of the temperature, which is equal to the thermal diffusivity, alpha (α), times the Laplacian of the temperature plus any volumetric heat sources that may be present from chemical reactions or heating sources as shown in Equations 1a & 1b from Section 2.3.4 and repeated here for convenience as Equations C.1a and C.2a.

$$\frac{DT}{Dt} = \alpha \nabla^2 T + \dot{Q}''' \tag{C.1a}$$

$$\frac{\partial T}{\partial t} + u\frac{\partial T}{\partial x} + v\frac{\partial T}{\partial y} + w\frac{\partial T}{\partial z} = \alpha\left(\frac{\partial^2 T}{\partial x^2} + \frac{\partial^2 T}{\partial y^2} + \frac{\partial^2 T}{\partial z^2}\right) + \dot{Q}''' \tag{C.1b}$$

In Equations C.1a and C.1b, T is temperature, x,y,z are the Cartesian coordinates of the system and u,v,w are the components of the velocity of the moving solid and $\dot{Q}'''$ is the heat per unit volume in the solid. By canceling the appropriate terms and aligning the coordinate system with the moving heat source as pictured in Figure C-1, Equation C.1b reduces to the following:

$$\frac{\partial T}{\partial t} - u\frac{\partial T}{\partial x} = \alpha\left(\frac{\partial^2 T}{\partial x^2} + \frac{\partial^2 T}{\partial y^2} + \frac{\partial^2 T}{\partial z^2}\right) + \dot{Q}''' \tag{C.2}$$

Equation 2 may be solved analytically, depending on the types of boundary conditions placed on the problem. Analytical solutions of Equation C.2 consider only the problem of heat conduction. Other physical phenomena may be coupled with the welding process, such as fluid dynamics or electro-magnetism, but they require additional equations that become intractable to solve analytically. One of the earliest solutions to the welding equation, Equation C.2, was presented by Rosenthal (Rosenthal, 1946). In Rosenthal's solution, the moving point source is modeled as fixed at the origin, and the material properties are assumed to be temperature independent. Since this represents one of the most fundamental solutions of the parabolic diffusion equation with and advection term (Equation C.2), the same assumptions will be applied to the present state-space model for simplicity. Additional boundary conditions placed on the domain upon which Equation C.2 pertains are adiabatic boundaries.

Applying a 2nd order central difference discretization scheme to Equation C.2 and the associated boundary conditions yields the follow state-space representation in continuous space.

$$\frac{\partial T}{\partial t} = \alpha\left(\frac{T^n_{i+1,j,k} - 2T^n_{i,j,k} + T^n_{i-1,j,k}}{(\Delta x)^2}\right) + \alpha\left(\frac{T^n_{i,j+1,k} - 2T^n_{i,j,k} + T^n_{i,j-1,k}}{(\Delta y)^2}\right) + \alpha\left(\frac{T^n_{i,j,k+1} - 2T^n_{i,j,k} + T^n_{i,j,k-1}}{(\Delta z)^2}\right) + u\left(\frac{T^n_{i+1,j,k} - T^n_{i-1,j,k}}{2\Delta x}\right)$$

(C.3)

Equation C.3 does not include the volumetric heating term, $\dot{Q}'''$ since it will be represented as a heat input and will be represented in a separate matrix equation. For the current treatment, the domain of the welded specimen will be modeled as a 2-D surface with temperature lumped in the Z-direction. Only the temperature distribution on the top surface of the weld specimen will be modeled. The terms in Equation C.3 that correspond to a 2-D formulation and will represent the *A* matrix in the state-space model are the following:

Tridiagonal terms

$$\left(\frac{\alpha}{(\Delta x)^2} - \frac{u}{2\Delta x}\right)T^n_{i-1,j} \quad \left(\frac{-2\alpha}{(\Delta x)^2} - \frac{2\alpha}{(\Delta y)^2}\right)T^n_{i,j} \quad \left(\frac{\alpha}{(\Delta x)^2} + \frac{u}{2\Delta x}\right)T^n_{i+1,j} \qquad \text{(C.4a,b,c)}$$

Penta-diagonal terms

$$\left(\frac{\alpha}{(\Delta y)^2}\right)T^n_{i,j-1} \qquad \left(\frac{\alpha}{(\Delta y)^2}\right)T^n_{i,j+1} \tag{C.5a,b}$$

Boundary Conditions

$$\frac{\partial T}{\partial x}=0 \qquad \frac{\partial T}{\partial y}=0 \quad \text{Insulated boundaries applied at x =0, X and y=0,Y} \tag{C.6a,b}$$

$$\left(\frac{T^n_{i+1,j}-T^n_{i-1,j}}{2\Delta x}\right)=0 \qquad \left(\frac{T^n_{i,j+1}-T^n_{i,j-1}}{2\Delta y}\right)=0 \tag{C.7a,b}$$

Equations C.4a,b,c and C.5a,b make up the interior points of the *A* matrix and Equations C.7a,b make up the periphery of the *A* matrix to enforce the insulated boundaries found on the edges of the domain of the weld specimen.

The dynamic model represented by the state and output equations:

$$\begin{aligned} x(k+1) &= Ax(k)+Bu(k) \\ y(k) &= Cx(k) \end{aligned} \tag{C.8a,b}$$

Equation 8a is used to calculate the states, *x(k)* (temperatures) in the work piece based on the power input at each time step, *u(k)*. The *B* vector in Equation C.8a represents the position of the weld head and changes with each time step.

$$\begin{bmatrix}1\\0\\0\\0\\0\\0\end{bmatrix}\rightarrow\begin{bmatrix}0\\1\\0\\0\\0\\0\end{bmatrix}\rightarrow\begin{bmatrix}0\\0\\1\\0\\0\\0\end{bmatrix}\rightarrow\begin{bmatrix}0\\0\\0\\1\\0\\0\end{bmatrix}\rightarrow\begin{bmatrix}0\\0\\0\\0\\1\\0\end{bmatrix}$$

Figure C-2: Diagram of how *B* vector changes at each time step

Collectively the term, *Bu(k)* represents the volumetric heat source term, $\dot{Q}'''$ in Equation C.2 and hence was the reason why it was omitted in the formulation of the state matrix, *A* in Equation C.3.

The dynamic model outlined in Equations C.8a,b does not make use of the measured output, *y(k)*. The performance of this dynamic model can be improved if the difference between the measured output, *y(k)* and the estimated output $\hat{y}(k) = C\hat{x}(k)$ which is used to monitor the state $\hat{x}(k)$, that approximates the state in Equations C.8a,b. The dynamic model of Equations C.8a,b are modified to include the difference in the outputs and takes on the following form:

$$\begin{aligned}\hat{x}(k+1) &= A\hat{x}(k) + Bu(k) + K_e[y(k) - \hat{y}(k)]\\ \hat{y}(k) &= C\hat{x}(k)\end{aligned} \qquad \text{(C.9a, b)}$$

In Equation C.9a the K_e matrix is the weighting matrix on the discrepancy between the measured output and the estimated output. By including the difference between the measured output and the estimated output will help reduce the differences between the dynamic model and actual system. For the state estimator utilized here, K_e the noise on the measured outputs and estimated states is considered such that the gain filter is designed to minimize the mean square of the estimation error. This is the Kalman filter approach to determining the gain matrix, K_e hence the state estimator utilized here is a Kalman filter. In Equation 9b the *C* matrix corresponds to location of the all the outputs that are measured during the experiment.

One way to derive the Kalman gain, K_e is outlined below:

$$\begin{aligned} N &= Q + ANA^T - ANC^T(R + CNC^T)^{-1}CNA^T \\ K_e &= N\hat{C}^T(\hat{R} + \hat{C}N\hat{C}^T)^{-1} \end{aligned} \qquad \text{(C.10a, b)}$$

N may be solved using the *DARE* function in MatLab.

In Equations 10a, b, matrix *Q* is the covariance on the noise of the model of the states and matrix *R* is the covariance on the noise of the measurements. Values for those matrices will be determined from the experimental data.

Experimental Setup

Eight thermocouples were placed on the top surface of each of the test specimens as shown in Figure C-3. The weld began at the origin and moved along the positive x direction. The thermocouples were spaced 3.175mm (1/8") apart in both the x and y directions, as shown in Table C-1.

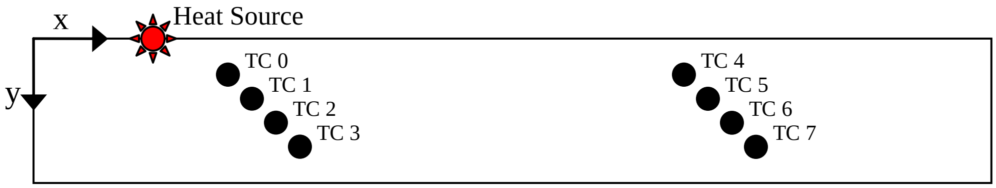

Figure C-3: Thermocouple Layout (½ of actual domain)

Table C-1: Thermocouple placement

	x (mm)	y (mm)			x (mm)	y (mm)
TC 0	41.3 (1.625”)	9.53 (0.375”)		**TC 4**	101.6 (4”)	9.53 (0.375”)
TC 1	44.5 (1.75”)	12.7 (0.5”)		**TC 5**	104.6 (4.125”)	12.7 (0.5”)
TC 2	47.6 (1.875”)	15.9 (0.625”)		**TC 6**	108 (4.25”)	15.88 (0.625”)
TC 3	50.8 (2”)	19.1 (0.75”)		**TC 7**	111.1 (4.375”)	19.1 (0.75”)

Table C-2: Material Properties for CuZn10 (UNS C22000)

ρ (Kg/m^3)	K (W/mK)	Tm (ºC)	Cp (J/KgK)	α (m^2/s)
8712	188.5	1308	382.3	5.66E-05

Table C-3: Welding Test Parameters

Trial	Voltage (V)	Feed (mm/s)	Speed (in/min)	# Passes
1	24.0	254 (600 ipm)	8.47 (20 ipm)	1

Shown in Figure C-3 is half of the actual domain of the experimental work piece. Since the problem is symmetric only one half of the physical domain is considered as this will speed up computation time between calculations. The physical size of the domain being modeled is 152.4 mm (6”) long by 25.4 mm (1”) wide; the material properties of the workpiece metal are outlined in Table C-2 and the welding parameters are outlined in Table C-3.

C.4 Data and Results

Shown below are plots for power input and comparisons for the physics model estimated temperature states and Kalman filter model estimated states. The method for determining the noise in the system is outlined in this section.

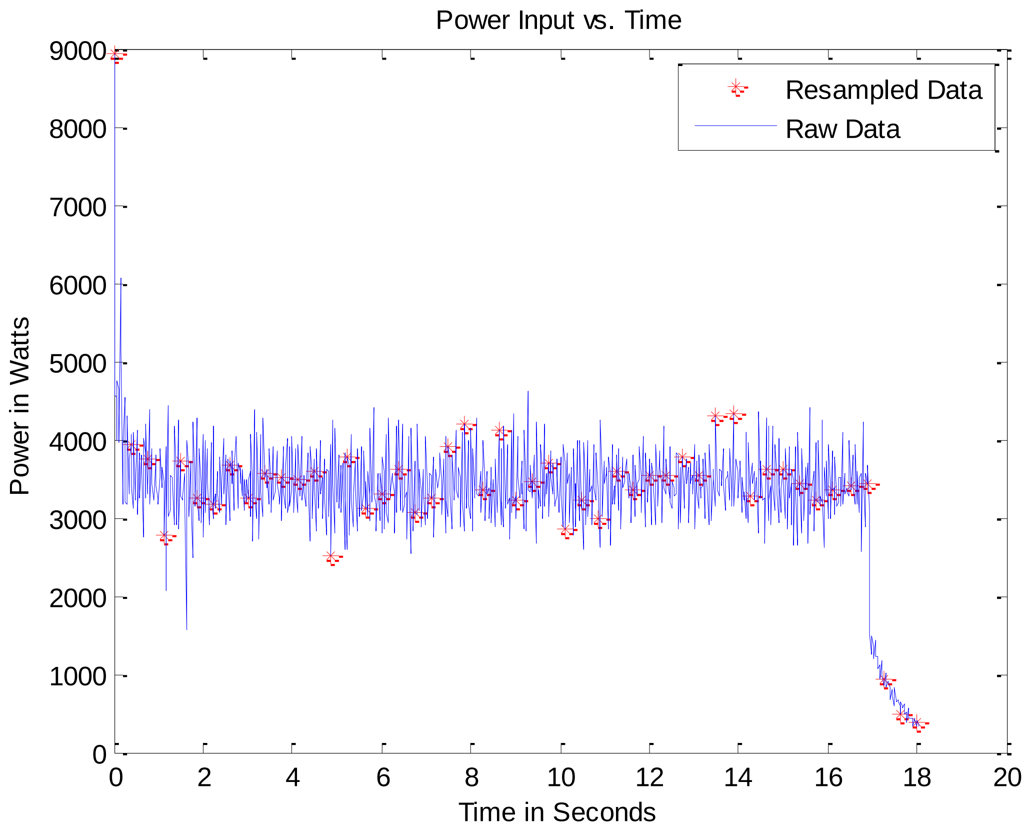

Figure C-4: Measured power input during welding

Shown in Figure C-4 is a plot of the power data taken over time during the welding experiment. The blue line represents all the data points taken during the experiment. The issue with this data is that measurements were not on regular time intervals hence the time signatures on the data alternate between 30Hz and 60Hz. In order for the data to be utilized in our dynamic models it was necessary to resample the data in regular time intervals. The data were resampled with a regular time interval of Δt =.375 seconds. These points are represented in Figure C-4 by the red star points.

Determination of the Noise in the System

As shown in Figure C-3, data was taken at eight points on the surface of the weld specimen via thermocouples. Those eight points would correspond to eight outputs being monitored. In our Kalman estimate, four outputs corresponding to thermocouples 0-4 were monitored and used to estimate the remaining states in the work piece. Using four outputs translates to a *C* matrix with four rows by N columns (number of states). The matrix *R* in Equation C.10a,b is the covariance on the noise of the measurements. The measurement noise was estimated by taking 0.1 percent of the difference between the measured output at the four locations in consideration and the estimated output from Equations C.8a,b and averaging all of those values at each location considered.

$$[R] = .001 * \frac{\sum (y(k) - \hat{y}(k))}{N\# ofstates} \qquad \text{(C.11)}$$

From Matlab,

```
R =

   0.0432        0        0        0

        0   0.0552        0        0

        0        0   0.0612        0

        0        0        0   0.0709
```

Matrix Q is the covariance on the noise of the model of the states and will be approximated by populating the diagonal elements of the Q matrix with the diagonal elements of the R matrix continuously until all the diagonal elements of the Q matrix are filled. Now that matrices Q and R are defined, the Kalman filter gain was calculated using a Matlab command, *[Ke,S,e] = dlqr(Ad,Cd',Q,R,0);* and the Kalman gain, K_e was then used in Equations C.10a,b to calculate the new states and outputs.

Results

In this section, results from a study comparing the effects of matrices Q and R on the estimation of the temperature field. Six plots will be compared varying the magnitude of the elements in matrix Q from .001 of matrix R to 100 times matrix R. This corresponds to having a high penalty on matrix R and then increasing the penalty on matrix Q. A comparison between the physical model state estimate and the Kalman filter state estimate will be made at a specific snapshot in time and the largest percent error will be reported that is found in the domain.

$Q = .001*R$

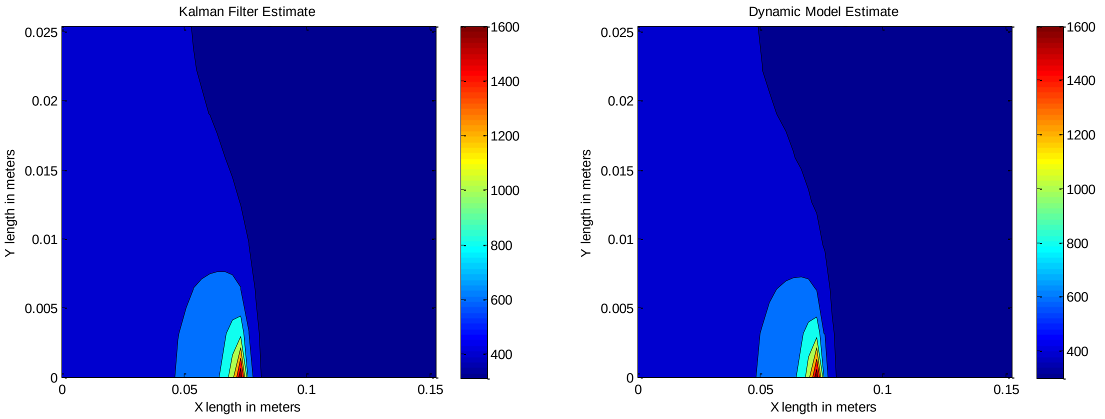

Figure C-5: Comparison of Kalman Model with Regular Model for Q = .001*R

Maximum percent difference throughout the domain = 0.0410 or 4.10%

Q = .01**R*

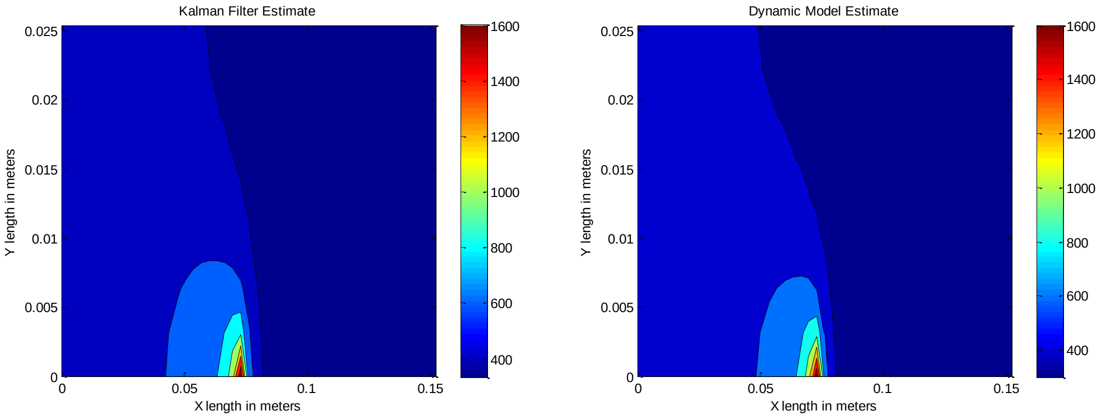

Figure C-6: Comparison of Kalman Model with Regular Model for Q = .01*R

Maximum percent difference throughout the domain = 0.1024 or 10.24%

Q = .1**R*

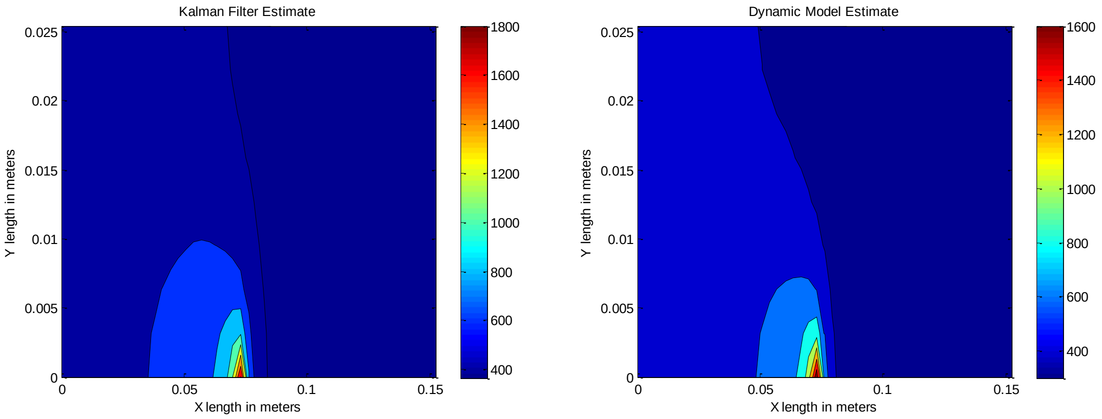

Figure C-7: Comparison of Kalman Model with Regular Model for Q = .1*R

Maximum percent difference throughout the domain = 0.1797or 17.97%

Q = R

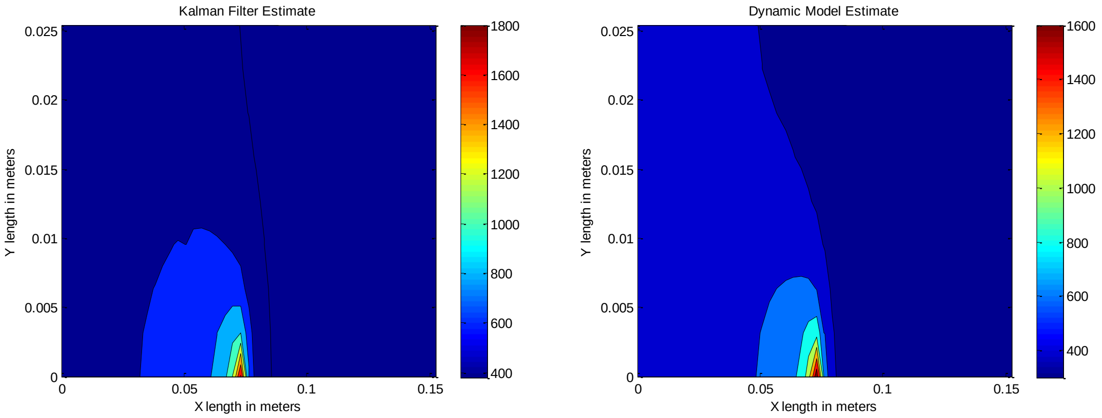

Figure C-8: Comparison of Kalman Model with Regular Model for Q = R

Maximum percent difference throughout the domain = 0.2125 or 21.25%

Q = 10**R*

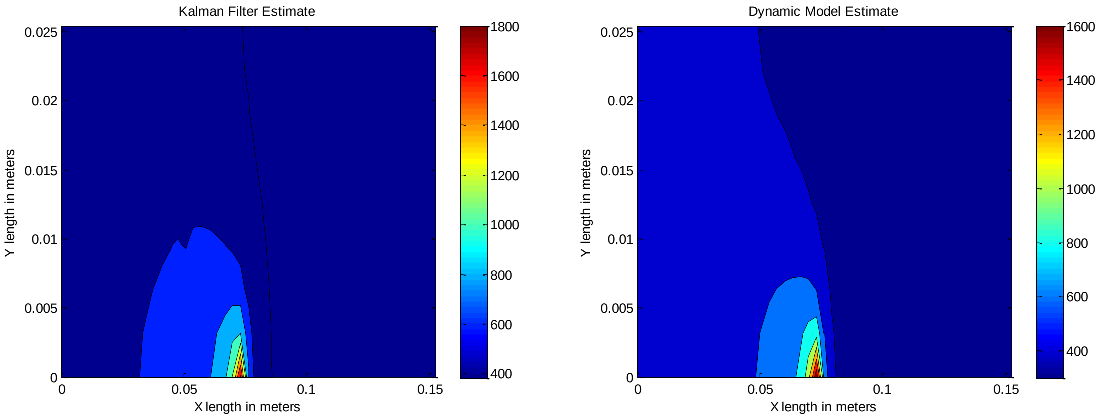

Figure C-9: Comparison of Kalman Model with Regular Model for Q = 10*R

Maximum percent difference throughout the domain = 0.2176 or 21.76%

Q = 100**R*

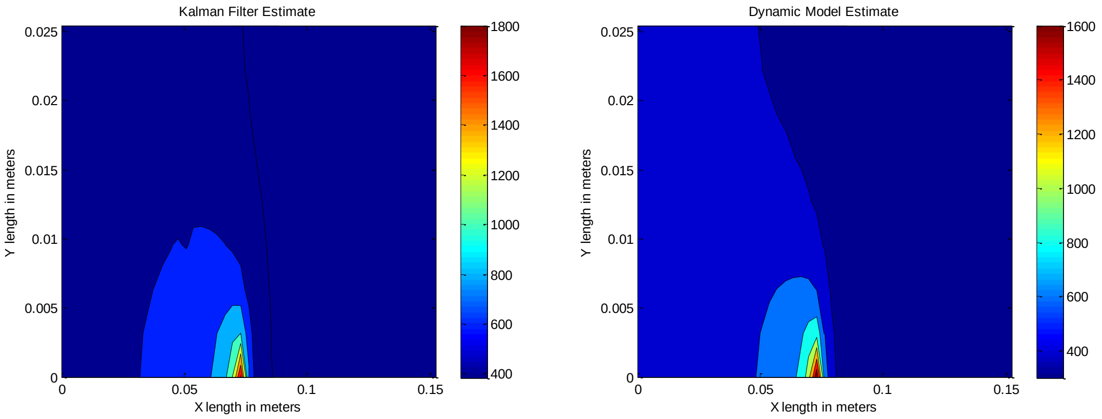

Figure C-10: Comparison of Kalman Model with Regular Model for Q = 100*R

Maximum percent difference throughout the domain = 0.2180 or 21.80%

Q = 1000**R*

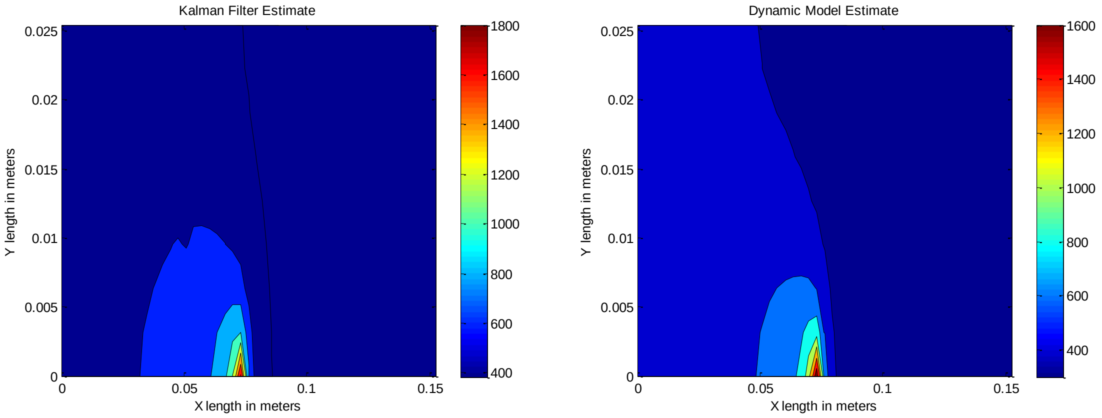

Figure C-11: Comparison of Kalman Model with Regular Model for Q = 1000*R

Maximum percent difference throughout the domain = 0.2180 or 21.80%

Examining the results from Figures C-11, it is apparent that the difference between the Kalman Model and the regular dynamic model becomes greater with increasing penalty on the *Q* matrix. This means that as you increase the weight on the noise of the measurements that the agreement between the two models decreases. In the case where *Q* = .001**R*, the largest %difference in the domain at the 25th time step was only 4.1%. This means that the agreement between the two models increases with higher weighting on the *Q* matrix and greater penalty on the *R* matrix. This also infers that the noise on the physical model is less than the noise on our measurements, so with higher weighting the on the *Q* matrix yielding better agreement to the dynamic model means that we can trust our model more than our measurements. From Figures 9-11, the maximum percent difference throughout the domain was 21.80%, this appears to be a threshold on the amount of error between the two models regardless of how heavily the *Q* matrix is penalized.

C.5 Conclusion

A Kalman estimator was created based on a physical model that describes the heat evolution in an irradiated material. The model utilized only considered the phenomenon of heat evolution and neglected other contributions from other phenomena inherent in welding such as fluid convection and electromagnetism. Based on the conduction model and insulated boundary conditions, a state-space model was constructed and used as a dynamic model to estimate the states (temperature field of the welded work piece). During welding, temperature measurements were taken and monitored as the measured outputs. A state observer was built from the state-space model using the Kalman approach and the resulting Kalman filter gain was used to refine the state estimation between the dynamic model and the measured outputs. A study was conducted to examine the effects of penalizing the *Q* matrix or the covariance of the noise of the model. It was found that the higher the penalty on the *Q* matrix the higher the difference error became. The difference error was found to be as high as 21.8% on a heavily penalized *Q* matrix. This infers that covariance of the noise on the measurements is less than the covariance of the noise on the measurements. When the *R* matrix carried a higher penalty the largest percent difference between the dynamic model and the Kalman model was found to be 4.1%. In addition, this infers that the model is more trustworthy than the measurements and having a higher weighting on the Q matrix will give us a better agreement with the physical model.

REFERENCES

Thermal Modeling

Bertram, L.A., 1996, "A Digital Rykalin Function for Welding", Report No. SAND97-8225, Sandia National Laboratory, Albuquerque, NM.

Boo, K.S. and Cho, H.S., 1990, "Transient Temperature Distribution in Arc Welding of Finite Thickness Plates", *Proceedings of the Institution of Mechanical Engineers. Part B, Journal of Engineering Manufacture*, **204**, pp. 75-83.

Carslaw, H.S. and Jaeger, J.C., 1967, *Heat Conduction in Solids*, 2nd Ed., Oxford University Press, Cambridge, UK, p. 255.

Chang, C.C., and Lin, C.J., 2001, *LIBSVM: A Library for Support Vector Machines*.

Clark, S.M., Griebsch, J.H., and Simpson, T.W., 2005, "Analysis of Support Vector Regression for Approximation of Complex Engineering Analyses," *Journal of Mechanical Design*, **127**, No. 6, pp. 1077-1087.

Chapra, S.C. and Canale, R.P., 1988, *Numerical Methods for Engineers*, 2nd Ed., McGraw-Hill, New York, pp. 138-143.

Christensen, N., Davies, V. de L. and Gjermundsen, K., 1965, "Distribution of Temperatures in Arc Welding", *British Welding Journal*, **54**, No. 2, pp. 54-75.

Davies, A. C., 1977, *The Science and Practice of Welding*, 7th Ed., Cambridge University Press, Cambridge, UK.

Deng, D. and Murakawa, H.,2005, "Numerical Simulation of Temperature Field and Residual Stress in Multi-Pass Welds in Stainless Steel Pipe and Comparison with Experimental Measurements", *Computational Materials Science*, **37**, pp. 269-277.

Eagar, T.W. and Tsai, N.S., 1983. "Temperature Fields Produced by Traveling Distributed Heat Sources", *Welding Journal*, **62**, No. 12, pp. 346s-355s.

Easterling, K.E., 1992, *Introduction to the Physical Metallurgy of Welding*, 2nd Ed., Butterworth & Heinemann, Oxford, UK, pp. 38-43.

Ely, G.R. and Seepersad, C.C., 2009, "A Comparison of Metamodeling Techniques for

Predictive Process Control of Welding Applications", *Proceedings of the ASME 2009 International Manufacturing Science and Engineering Conference*, Paper No. MSEC2009- 84189.

Fan, H.G. and Kovacevic, R., 2006, "Three-Dimensional Model for Gas Tungsten Arc Welding with Filler Metal", *Proceedings of the Institution of Mechanical Engineers. Part B, Journal of Engineering Manufacture*, **220**, pp. 1107-1115.

Friedman, E., 1975, "Thermomechanical Analysis of the Welding Process Using the Finite Element Method", *Journal of Pressure Vessel Technology*, **97**, pp. 206-213.

Friedman, J.H., 1991, "Multivariate Adaptive Regression Splines," *Annals Statistics*, **19**, pp. 1-141.

Giunta, A., Watson, L.T., and Koehler, J., 1998, "A Comparison of Approximation Modeling Techniques: Polynomial Versus Interpolating Models," *Proceedings of 7th AIAA/USAF/NASA/ISSMO Symposium on Multidisciplinary Analysis and Optimization*, **1**, pp. 392-404. AIAA-98-4758.

Goldak, J., Chakravarti, A. and Bibby, M., 1984, "A New Finite Element Model for Welding Heat Sources", *Metallurgical and Materials Transactions B*, **15B**, pp. 299-305.

Goldak, J., Chakravarti, A. and Bibby, M.,1985, "A Double Ellipsoid Finite Element Model for Welding Heat Sources" *IIW-85, International Institute for Welding*, Strasbourg, France.

Holliday, D.B., 1993, "Gas Metal Arc Welding", *Welding, Brazing and Soldering, ASM Handbook*, 10th Ed., **6**, ASM International, Metals Park, Ohio, pp. 567-570.

Hu, J. and Tsai, H.L., 2007a, "Heat and Mass Transfer in Gas Metal Arc Welding. Part II: The Metal", *International Journal of Heat and Mass Transfer*, **50**, pp. 808-820.

Hu, J. and Tsai, H.L., 2007b, "Heat and Mass Transfer in Gas Metal Arc Welding. Part I: The Arc", *International Journal of Heat and Mass Transfer*, **50**, pp. 833-846.

Hu, J. and Tsai, H.L., 2008, "Modeling of Transport Phenomena in 3D GMAW of Thick Metals with V Groove", *Journal of Physics D: Applied Physics*, **41**, pp. 1-10.

Jhaveri, P., Moffatt, W. G., and Adams, C.M., 1962, “The Effect of Plate Thickness and Radiation on Heat Flow in Welding and Cutting”, *Welding Journal,* **41,** No. 1, pp. 12s-16s.

Jin, R., Chen, W., and Simpson, T.W., 2001, “Comparative Studies of Metamodeling Techniques Under Multiple Modeling Criteria,” *Structural and Multidisciplinary Optimization,* **23**, pp. 1-13.

Jones, D.R., 2001, “A Taxonomy of Global Optimization Methods Based on Response Surfaces”, *Journal of Global Optimization,* **21**, pp. 345-383.

Jönsson, P.G., Szekely, J., Choo, R. T. C. and Quinn, T.P., 1994, “Mathematical Models of Transport Phenomena Associated with Arc-Welding Processes: A Survey”, *Modelling and Simulation in Materials Science and Engineering,* **2,** No. 5, pp. 995-1016.

Kearns, W.H., and Weisman, C., 1978, *Welding Processes-Arc and Gas Welding and Cutting, Brazing and Soldering, Welding Handbook*, 7th Ed., **2**, American Welding Society, Miami, FL, p. 434.

Kim, I. S., and Basu, A., 1998, “A Mathematical Model of Heat Transfer and Fluid Flow in the Gas Metal Arc Welding Process”, *Journal of Materials Processing Technology*, **77**, pp. 17-24.

Komanduri, R. and Hou, Z.B., 2000, “Thermal Analysis of the Arc Welding Process: Part I. General Solutions”, *Metallurgical and Materials Transactions B,* **31B,** pp. 1353 – 1370.

Kumar, S. and Bhaduri, S.C., 1994, “Three-Dimensional Finite Element Modeling of Gas Metal-Arc Welding”, *Metallurgical and Materials Transactions B,* **25B**, pp. 435-441.

Larson, R., and Taylor, D.L.,2008, “Thermophysical Properties of C22000 Commercial Bronze”, Report No. TRPL 4179, TPRL, Inc., West Lafayette, IN.

Mackle, J., 1996, “Finite Element Analysis and Simulation of Welding: A Bibliography (1976 – 1996)”, *Modelling and Simulation in Materials Science and Engineering,* **4,** No. 5, pp. 501-533.

Mackle, J., 2002, “Finite Element Analysis and Simulation of Welding – An Addendum: A Bibliography (1996 – 2001)”, *Modelling and Simulation in Materials Science and Engineering,* **10,** No. 3, pp. 295-318.

Mickley, H.S., Sherwood, T.K., and Reed, C.E., 1957, *Applied Mathematics in Chemical Engineering*, 2nd Ed., McGraw-Hill Book Company, New York, NY, p. 66.

Nguyen, N.T., Ohta, A., Matsuoka, K., Suzuki, N., and Maeda, Y., 1999, “Analytical Solutions for Transient Temperature of Semi-Infinite Body Subjected to 3-D Moving Heat Sources”, *Welding Journal,* **78,** No. 8, pp. 265s-274s.

Queipo, N.V., Haftka, R.T., Shyy, W., Goel, T., Vaidyanathan, R., Tucker, P.K., 2005, “Surrogate-based Analysis and Optimization”, *Progress in Aerospace Sciences,* **41,** pp. 1-28.

Rios-Perez, C. A. (2009). *Finite difference model of a welding process on flat plate and semi-infinite cylinder geometries*. The University of Texas at Austin, Austin, TX.

Rosenthal, D., 1946, “The Theory of Moving Sources of Heat and Its Application to Metal Treatments”, *Transactions of the ASME,* **68**, pp. 849-866.

Swift-Hook, D.T. and Gick, A. E. F., 1973, “Penetration Welding with Lasers”, *Welding Journal*, **52**, No. 11, pp. 492s-499s.

Schwartz, M.M., 1993, “Introduction to Brazing and Soldering”, *Welding, Brazing and Soldering, ASM Handbook*, 10th Ed., **6**, ASM International, Metals Park, Ohio, pp.124-125.

Shah, S.E., Lee, J.C., Rios-Perez, C., and Seepersad, C.C., 2009, “Comparison of Analytical and Computational Thermal Models for Gas Metal Arc Braze Welding”, *Proceedings of the ASME 2009 Summer Heat Transfer Conference*, Paper No. HT2009- 88491.

Simpson, T.W., Mauery, T.M., Korte, J.J., and Mistree, F., 1998, “Comparison of Response Surface and Kriging Models for Multidisciplinary Design Optimization,” *Proceedings of 7th AIAA/USAF/NASA/ISSMO Symposium on Multidisciplinary Analysis and Optimization*, **1**, pp. 381-391.

Simpson, T.W., Poplinski, J.D., Koch, P.N., and Allen, J.K., 2001, "Metamodels for Computer-based Engineering Design: Survey and Recommendations," *Engineering with Computers,* **17,** No. 2, pp. 129-150.

Song, J. B. and Hardt, D.E., 1993, "Closed-Loop Control of Weld Pool Depth Using a Thermally Based Depth Estimator", *Welding Journal*, **72,** No. 10, pp. 471s-478s.

Taylor, G.A., Hughes, M., Strusevich, N., Pericleous, K., 2002, "Finite Volume Methods Applied to the Computational Modelling of Welding Phenomena", *Applied Mathematical Modeling,* **26**, No. 2, pp. 309-320.

Wahab, M. A. and Painter, M. J.,1997, "Numerical Models of Gas Metal Arc Welds Using Experimentally Determined Weld Pool Shapes as the Representation of the Welding Heat Source", *International Journal of Pressure Vessels and Piping,* **73**, pp. 153-159.

Wahab, M. A., Painter, M. J. and Davies, M. H., 1998, "The Prediction of the Temperature Distribution and Weld Pool Geometry in the Gas Metal Arc Welding Process", *Journal of Materials Processing Technology,* **77**, pp. 233-239.

White, D. and Jones, J., 1997, "Process Modeling with Neural Networks for Pulsed GMAW Braze Welds", *Journal of Minerals, Metals and Materials Society,* **49**, No. 9, pp. 49-53.

Vapnik. V., 1998, *The Nature of Statistical Learning Theory*. New York: Wiley.

Varadarajan, S., Chen, W., and Pelka, C., 2000, "The Robust Concept Exploration Method with Enhanced Model Approximation Capabilities," *Engineering Optimization,* **32**, pp. 309-334.

Yaghi, A. and Becker, A., 2004, "State of the Art Review – Weld Simulation Using Finite Element Methods", Report No. FENET-UNOTT-DLE-08, FENET EU Thematic Network.

Yang, R.J., Gu L., Liaw, L., Gearhart, C., Tho, C.H., Liu, X., and Wang, B.P., 2000, "Approximations for Safety Optimization of Large Systems," *ASME Design Automation Conference,* Paper No. DETC-00/DAC-14245.

Yang, Z and Debroy, T., 1999, "Modeling Macro- and Microstructures of Gas-Metal-Arc Welded HSLA-100 Steel", *Metallurgical and Materials Transactions B*, **30B**, pp. 483-493.

Welding Procedures

Davies, A. C., 1977, *The Science and Practice of Welding*, 7th Ed., Cambridge University Press, Cambridge, UK.

Dawson, R. J. C., 1973, *Fusion Welding and Brazing of Copper and Copper Alloys*, Newnes-Butterworths, London, UK.

HCP [Picture file]. (n.d.). Retrieved from http://www.benbest.com/ cryonics/HCP.gif

Kearns, W.H., and Weisman, C., 1978, *Welding Processes-Arc and Gas Welding and Cutting, Brazing and Soldering, Welding Handbook*, 7th Ed., **4**, American Welding Society, Miami, FL, p. 434.

Lincoln Electric Company, 1978, *The Procedure Handbook of Arc Welding*, 12th Ed., The Lincoln Electric Company, Cleveland, OH.

Properties of pure metals. (2003). *ASM handbooks online*. Retrieved May 10, 2007, from http://products.asminternational.org.ezproxy.lib.utexas.edu.content.lib.utexas.edu:2048/hbk/index.jsp

Russell, A.M. and Lee, K.L. (2005). *Structure-Property Relations in Nonferrous Metals.* (p. 157). Hoboken, New Jersey: John Wiley & Sons, Inc.

Control

Åström, K.J. and Hägglund, T., 1995, *PID Controllers: Theory, Design, and Tuning*, 2nd Ed., International Society for Measurement and Control, Research Triangle Park, NC, pp. 59 – 116.

Backlund, P.B., 2008, *Flexibility for Future Evolution: Validation and Development of Design Guidelines*, The University of Texas of Austin, Austin, TX.

Backlund, P.B., Ely, G.R., Seepersad, C.C., Taleff, E. and Howell, J.R., 2009, “Design and Construction of an Automated Gas Metal Arc Welding Test Station”, *International Manufacturing Science and Engineering Conference*.

Curtain, R. F. and Pritchard, A. J., 1978, *Infinite Dimensional Linear System Theory*, Springer-Verlag, Berlin.

Curtain, R. F. and Zwart, H. J., 1995, *An Introduction to Infinite Dimensional Linear System Theory*, Springer-Verlag, Berlin.

Ely, G.R., 2010, *An Analysis of the Feasibility of Predictive Process Control of Welding Applications Using Infrared Pyrometers and Thermal Metamodels*, The University of Texas of Austin, Austin, TX.

Ferziger, J., 1981, *Numerical Methods for Engineering Application*., John Wiley & Sons, Inc, New York, p. 124.

Ferziger, J and Peric, M., 2002, *Computational Methods for Fluid Dynamics*, 3rd Ed., Springer-Verlag, Berlin, p. 36.

Friedland, B., 2005, *Control System Design: An Introduction to State-Space Methods*, Dover Publications, Mineola, NY, p. 234.

Fornberg, B., 1988, "Generation of Finite Difference Formulas on Arbitrary Spaced Grids", *Mathematics of Computation*, **51**, No. 184, pp. 699 – 706.

Jiluan, P., 2003, *Arc Welding Control.* Boca Raton, FL, CRC Press.

Kreysig, E., 1999, *Advanced Engineering Mathematics*, 8th Ed., John Wiley & Sons, Inc., New York, p. 1145.

Li, X.C., Farson, D., and Richardson, R., 2001, "Welding Penetration Control System Design and Testing", *Journal of Manufacturing Systems*, **19**, No. 6, pp. 383 – 392.

McCampbell, W.M., Cook, G.E., NordHolt, L.E. and Merrick, G.J., 1965, "The Development of a Weld Intelligence System", *Welding Journal*, **40**, No. 3, pp. 139s – 144s.

Montgomery, D.C., Peck, E.A. and Vining, G.G., 2001, *Introduction to Linear Regression Analysis*, 3rd Ed., John Wiley & Sons, Inc., New York, pp. 13-15; 67-71.

Naidu, D.S., Ozcelik, S. and Moore, K.L., 2003, *Modeling, Sensing and Control of Gas Metal Arc Welding*, Elsevier Science Ltd., Oxford, pp. 100-101.

Ngo, M. D., Duy, V. H., Phuong, N. T., Kim, H. K., and Kim, S. B., 2006, "Development of Digital Gas Metal Arc Welding System", *Journal of Materials Processing Technology*, **189,** pp. 384 – 391.

Nise, N.S., 1995, *Control Systems Engineering*, 2nd Ed., Addison-Wesley, Menlo Park, CA, p. XX.

Ogata, M., 1987, *Discrete-Time Control Systems*, 1st Ed., Prentice-Hall, Inc., Englewood Cliffs, NJ, pp. 681-720.

Seborg, D.E., Edgar, T.F. and Mellichamp, D.A., 2004, *Process Dynamics and Control*, 2nd Ed., John Wiley & Sons, Inc., Hoboken, NJ, pp. 185- 200.

Smartt, H. B. and Einerson, C. J., 1993, "A model for Heat and Mass Input Control of Gas Metal Arc Welding", *Welding Journal,* **72**, No. 5, pp. 217s – 229s.

Song, J., Peters, J., Noor, A., Michaleris, P., 2003, "Sensitivity Analysis of the Thermomechanical Response of Welded Joints". *International Journal of Solids and Structures,* **40**, pp. 4167-4180.

Wikle III, H. C., Zee, R. H. and Chin , B. A., 1999, "A Sensing System for Weld Process Control", *Journal of Materials Processing Technology,* **89-90,** pp. 254 – 259.

VITA

Sanjiv Edlagan Shah was born in Springfield, MA and had the opportunity of living in several interesting cities in the North-East United States until his family settled in Midland, TX. By chance, he was able to attend high school in a suburb of Baltimore, MD and received his High School Diploma in 1995 from Dulaney High School. After attending Emory University in Atlanta, GA for one year, he transferred to Tulane University where he majored in Mechanical Engineering and Spanish. He received a Bachelor of Science in Mechanical Engineering in May of 2000 and a Master of Science in Mechanical Engineering in December of 2002. After working for a few years for the Hewlett-Packard Corporation, he entered the doctoral program in Mechanical Engineering at the University of Texas at Austin in the fall of 2005. As a graduate student in the Thermal Fluids Systems area of the Mechanical Engineering Department, his research was supervised by John R. Howell, Ph.D and co-advised by Carolyn C. Seepersad, Ph.D of the Manufacturing and Design area. His research focused on the modeling of Gas Metal Arc Welding and Gas Metal Arc Braze-Welding, the application of Model Predictive Control to the welding problem and model reduction.

Permanent address: 410 Towne Park Trail, Austin, TX 78751
This dissertation was typed by the author.